CIVIL ENGINEERING STUDIES
Illinois Center for Transportation Series No. 21-035
UILU-ENG-2021-2035
ISSN: 0197-9191

The Impact of Wide-Base Tires on Pavement—A National Study

Prepared By
Imad L. Al-Qadi
Jaime A. Hernandez
Angeli Jayme
Mojtaba Ziyadi
Erman Gungor
Seunggu Kang
John Harvey
Rongzong Wu
James Greene
Bouzid Choubane
Morris De Beer
Tom Scarpas

Research Report No. ICT-21-035

https://doi.org/10.36501/0197-9191/21-035

Illinois Center for Transportation

September 2016

FOREWORD

This project was conducted in cooperation with the Illinois Center for Transportation; the U.S. Department of Transportation, Federal Highway Administration; Rubber Manufacturers Association, and the following state departments of transportation: Florida, Illinois, Minnesota, Montana, New York, Ohio, Oklahoma, South Dakota, Texas, and Virginia. The feedback and input of the following are greatly appreciated: John Bowman, Keith Brewer, Steve Butcher, Larry Buttler, Shongtao Dai, Brian Diefenderfer, Dan Hill, Terri Holley, David Huft, Sam Khoury, Stan Lew, David Lippert, Shad Sargand, Chuck Wienrank, and Wes Yang. This project is managed by Eric Weaver, who has been instrumental in providing directions and input.

The contents of this report reflect the view of the authors, who are responsible for the facts and the accuracy of the data presented herein. The contents do not necessarily reflect the official views or policies of the Illinois Center for Transportation, the Federal Highway Administration, or the participating partners. This report does not constitute a standard, specification, or regulation.

Jorge E Pagan-Ortiz
Director, Office of Infrastructure
Research and Development

TECHNICAL REPORT DOCUMENTATION PAGE

1. Report No. ICT-21-035	2. Government Accession No.	3. Recipient's Catalog No.
4. Title and Subtitle The Impact of Wide-Base Tires on Pavement – A National Study		5. Report Date September 2016
		6. Performing Organization Code:
7. Author(s) Imad L. Al-Qadi, Jaime A. Hernandez, Angeli Jayme, Mojtaba Ziyadi, Erman Gungor, Seunggu Kang, John Harvey, Rongzong Wu, James Greene, Bouzid Choubane, Morris De Beer, Tom Scarpas		8. Performing Organization Report No. ICT-21-035 UILU-ENG-2021-2035
9. Performing Organization Name and Address Illinois Center for Transportation University of Illinois at Urbana-Champaign 1611 Titan Drive Rantoul, IL 61866		10. Work Unit No.
		11. Contract or Grant No. DTFH61-11-C-00025
12. Sponsoring Agency Name and Address Office of Insert Office Name Here Federal Highway Administration 6300 Georgetown Pike McLean, VA 22101-2296		13. Type of Report and Period Covered Final Report; April 2011− December 2015
		14. Sponsoring Agency Code HRDI-20
15. Supplementary Notes https://doi.org/10.36501/0197-9191/21-035		

16. Abstract

Researchers have been studying wide-base tires for over two decades, but no evidence has been provided regarding the net benefit of this tire technology. In this study, a comprehensive approach is used to compare new-generation wide-base tires (NG-WBT) with the dual-tire assembly (DTA). Numerical modeling, prediction methods, experimental measurements, and environmental impact assessment were combined to provide recommendations about the use of NG-WBT. A finite element approach, considering variables usually omitted in the conventional analysis of flexible pavement was utilized for modeling. Five hundred seventy-six cases combining layer thickness, material properties, tire load, tire inflation pressure, and pavement type (thick and thin) were analyzed to obtained critical pavement responses. A prediction tool, known as ICT-Wide, was developed based on artificial neural networks to obtain critical pavement responses in cases outside the finite element analysis matrix. The environmental impacts were determined using life cycle assessment. Based on the bottom-up fatigue cracking, permanent deformation, and international roughness index, the life cycle energy consumption, cost, and green-house gas (GHG) emissions were estimated. To make the outcome of this research effort useful for state departments of transportation and practitioners, a modification to AASHTOWare is proposed to account for NG-WBT. The revision is based on two adjustment factors, one accounting for the discrepancy between the AASHTOware approach and the finite element model of this study, and the other addressing the impact of NG-WBT.

17. Key Words new-generation wide-base tires, dual-tire assembly, NG-WBT, DTA, life-cycle assessment, LCA, numerical modeling, neural networks	18. Distribution Statement No restrictions. This document is available through the National Technical Information Service, Springfield, VA 22161.		
19. Security Classif. (of this report) Unclassified	20. Security Classif. (of this page) Unclassified	21. No. of Pages 276	22. Price N/A

Form DOT F 1700.7 (8-72) Reproduction of completed page authorized

SI* (MODERN METRIC) CONVERSION FACTORS

APPROXIMATE CONVERSIONS TO SI UNITS

Symbol	When You Know	Multiply By	To Find	Symbol
		LENGTH		
in	inches	25.4	millimeters	mm
ft	feet	0.305	meters	m
yd	yards	0.914	meters	m
mi	miles	1.61	kilometers	km
		AREA		
in^2	square inches	645.2	square millimeters	mm^2
ft^2	square feet	0.093	square meters	m^2
yd^2	square yard	0.836	square meters	m^2
ac	acres	0.405	hectares	ha
mi^2	square miles	2.59	square kilometers	km^2
		VOLUME		
fl oz	fluid ounces	29.57	milliliters	mL
gal	gallons	3.785	liters	L
ft^3	cubic feet	0.028	cubic meters	m^3
yd^3	cubic yards	0.765	cubic meters	m^3
	NOTE: volumes greater than 1000 L shall be shown in m^3			
		MASS		
oz	ounces	28.35	grams	g
lb	pounds	0.454	kilograms	kg
T	short tons (2000 lb)	0.907	megagrams (or "metric ton")	Mg (or "t")
		TEMPERATURE (exact degrees)		
°F	Fahrenheit	5 (F-32)/9 or (F-32)/1.8	Celsius	°C
		ILLUMINATION		
fc	foot-candles	10.76	lux	lx
fl	foot-Lamberts	3.426	$candela/m^2$	cd/m^2
		FORCE and PRESSURE or STRESS		
lbf	poundforce	4.45	newtons	N
lbf/in^2	poundforce per square inch	6.89	kilopascals	kPa

APPROXIMATE CONVERSIONS FROM SI UNITS

Symbol	When You Know	Multiply By	To Find	Symbol
		LENGTH		
mm	millimeters	0.039	inches	in
m	meters	3.28	feet	ft
m	meters	1.09	yards	yd
km	kilometers	0.621	miles	mi
		AREA		
mm^2	square millimeters	0.0016	square inches	in^2
m^2	square meters	10.764	square feet	ft^2
m^2	square meters	1.195	square yards	yd^2
ha	hectares	2.47	acres	ac
km^2	square kilometers	0.386	square miles	mi^2
		VOLUME		
mL	milliliters	0.034	fluid ounces	fl oz
L	liters	0.264	gallons	gal
m^3	cubic meters	35.314	cubic feet	ft^3
m^3	cubic meters	1.307	cubic yards	yd^3
		MASS		
g	grams	0.035	ounces	oz
kg	kilograms	2.202	pounds	lb
Mg (or "t")	megagrams (or "metric ton")	1.103	short tons (2000 lb)	T
		TEMPERATURE (exact degrees)		
°C	Celsius	1.8C+32	Fahrenheit	°F
		ILLUMINATION		
lx	lux	0.0929	foot-candles	fc
cd/m^2	$candela/m^2$	0.2919	foot-Lamberts	fl
		FORCE and PRESSURE or STRESS		
N	newtons	0.225	poundforce	lbf
kPa	kilopascals	0.145	poundforce per square inch	lbf/in^2

*SI is the symbol for the International System of Units. Appropriate rounding should be made to comply with Section 4 of ASTM E380.
(Revised March 2003)

TABLE OF CONTENTS

LIST OF FIGURES

LIST OF TABLES

EXECUTIVE SUMMARY

Researchers have been studying wide-base tires for over two decades, but no evidence has been provided regarding the net benefit of this tire technology. The present study reflects a relevant step forward, where a comprehensive approach is used to compare new-generation wide-base tires (NG-WBT) with the dual-tire assembly (DTA). Numerical modeling, prediction methods, experimental measurements, and environmental impact assessment were combined to provide recommendations about the use of NG-WBT.

Numerical modeling allows the calculation of pavement responses for an ample combination of variables, which would be expensive, time-consuming, and impractical if performed as part of any experimental program. A finite element approach, considering variables usually omitted in the conventional analysis of flexible pavement, such as dynamic analysis, continuously moving load, linear viscoelastic asphalt materials, nonlinear anisotropic granular materials, interaction between pavement layers, and three-dimensional contact stresses/loads, was utilized for modeling. Five hundred seventy-six cases combining layer thickness, material properties, tire load, tire inflation pressure, and pavement type (thick and thin) were analyzed to obtained critical pavement responses. The numerical model comprised an experimental measurement of three-dimensional contact stresses/loads, material properties from nation-wide databases, and pavement structures as part of the road infrastructure. Based on the pavement responses, current transfer functions used in the Mechanistic-Empirical Pavement Design Guide (MEPDG) were used for comparing the damage resulting from NG-WBT with that from DTA. In addition, a new procedure is introduced to quantify the three-dimensional stress and strain states.

The experimental program aimed to validate the results of the numerical model. It could also be used to experimentally verify the trends inferred from the finite element model for the scenarios of the testing program. Stress, strain, and temperature were measured at various locations in the pavement structure in sections subjected to accelerated pavement testing (Florida and California) and controlled truck loading (Ohio). In addition, measurements from previous projects were used by the research team (California, Florida, Illinois, Ohio, and Virginia). The information was compiled in a database that users could access to retrieve experimental results.

Even though the numerical and experimental testing program was broad and robust, it did not cover all possible scenarios. Consequently, a prediction tool based on artificial neural networks was developed to obtain critical pavement responses in cases outside the finite element analysis matrix. The tool, known as ICT-Wide, can promptly predict critical pavement responses without performing finite element calculations.

The environmental impacts were determined using life cycle assessment. Based on the bottom-up fatigue cracking, permanent deformation, and international roughness index, the life cycle energy consumption, cost, and green-house gas (GHG) emissions were estimated. Three scenarios were established with different levels of market penetration of NG-WBT: i) NG-WBT and dual tires demonstrating equivalent fatigue and international roughness index (IRI) performance; ii) design life determined by fatigue performance; and iii) design life determined by IRI performance.

Finally, to make the outcome of this research effort readily implementable for state departments of transportation and practitioners using AASHTOWare, a modification to AASHTOWare is proposed to account for NG-WBT. The revision is based on two adjustment factors, one accounting for the discrepancy between the AASHTOware approach and the finite element model of this study, and the other addressing the impact of NG-WBT.

CHAPTER 1. INTRODUCTION

BACKGROUND

After more than two decades of research by the tire industry and pavement researchers, a new generation of wide-base tires (NG-WBT) (445/50R22.5 and 455/55R22.5) was introduced to improve safety, reduce the impact on the environment, and provide cost savings. The introduced NG-WBT is wider, has improved structure and design, and offers a rolling tread width increase of 15 to 36% compared with the first generation wide-base tires (FG-WBT). In addition, the new tires adhere to the "inch-width" rule applicable all over the U.S. for 5-axle, 79.8 kip gross-vehicle-weight trucks.

In Europe, wide-base tires (having a different design than the ones introduced in the U.S.) have been used successfully on trucks since the early 1980s. In 1997, around 65% of trailers and semi-trailer tires in Germany used wide-base tires (COST 334, 2001). In April 2008, Canada increased the allowable weight limit on axles with wide-base tires. Per the new guidelines, axle loads may not exceed 17 kip for single axles and 34 kip for tandem axles when an axle is fitted with two single tires (each 445 mm wide or greater), compared with 20.2 and 37.4 kip, respectively, for dual-tire assemblies (DTA).

The impact NG-WBT on trucking operations has also been evaluated. Fuel economy improved when NG-WBT was used. NG-WBT reduced the rolling resistance coefficient to 0.005, which is translated in fuel efficiency of 10% higher than that of DTA, according to a fuel consumption model (Muster, 2000). In addition, in combination of aerodynamic devices, WBT improved fuel economy by 18% for a truck traveling on a highway at 65 mph according to field testing (Bachman et al., 2005). Moreover, based on data collected from hauling companies, the use of WBT translated into fuel savings ranging between 3.5 and 12% (GENIVAR Consulting Group, 2005). In 2010, the improvement of fuel economy resulting from the use of NG-WBT was reported at approximately 10% (Franzese et al., 2010).

Other benefits of using WBT have been reported. Since a WBT is lighter than DTA, the hauling capacities of trucks equipped with WBT increases (Markstaller et al., 2000). WBT is easier to inspect, repair, and maintain, (ENIVAR Consulting Group, 2005) uses less rubber material, and decreases the amount of disposable materials (Environmental Protection Agency, 2004). Furthermore, WBT has similar or slightly better performance than DTA with regard to safety and comfort (Markstaller et al., 2000).

WBT is more environmentally friendly than DTA; using WBT leads to lower consumption of gas, which also leads to a reduction in gas-emission. Moreover, since the amount of materials needed to produce a WBT is less than that for DTA, the material disposed at the end of the life cycle of the tire is relatively less (GENIVAR Consulting Group, 2005). In addition, it is worth mentioning that WBT produces slightly less noise (Markstaller et al., 2000). More recently, WSP Canada, Inc. (WSP) reported that eliminating earlier weight limitation on NG-WBT compared to DTA can provide benefits such as increase competitiveness due to lower fuel consumption and greenhouse gas emissions (Xue & Weaver, 2015).

OBJECTIVE AND SCOPE

The objective of this study was to quantify the impact of vehicle-tire interaction on pavement damage for various pavement structures using advanced theoretical modeling and to validate this impact by performing full-scale pavement testing based on available data. In addition, the study aimed to further assess the economic and environmental effects of using NG-WBT as related to pavement performance. Finally, to allow for the use and implementation of NG-WBT by state departments of transportation, a simple user-friendly tool was introduced to assess the impact of NG-WBT on pavement networks and to facilitate decision-making.

The main objectives of this project include the following:

- Develop a tool and methodology that allow state departments of transportation and practitioners to assess the impact of NG-WBT on the pavement network.
- Perform an analysis of the economic and environmental effects of using NG-WBT relative to their impact on pavement performance.
- Quantify the impact of NG-WBT compared with DTA using validated finite element model. The comparison was performed not only to investigate critical pavement responses, but also the corresponding distresses and environmental and economic impacts. Appropriate and accurate input for the three-dimensional finite element model was determined including contact stresses/loads and material properties.

NG-WBT 445/50 R22.5 and DTA 275/80 R22.5 tires were considered. The three-dimensional contact stresses/loads were measured for a wide range of loads and tire inflation pressures, and a subset of the testing matrix was used in the finite element analysis. Material selection was made using extensive databases of material test results and material characteristics. The finite element model, which was validated using the experimental measurements, provided critical pavement responses for comparing NG-WBT with DTA. In addition, the outcome of numerical modeling was used to develop a prediction tool based on artificial neural networks. Life cycle cost analysis (LCCA) and life cycle assessment (LCA) were performed to complement the mechanistic comparison between the two investigated tires for a holistic evaluation. Finally, a methodology based on two adjustment factors, considering the finite element analyses and the relative effect of wide-base tires, was proposed to account for the effect of NG-WBT using the current pavement design guide (AASHTOware).

OVERVIEW OF THE REPORT

The body of the report consists of eleven chapters and eight appendices. Chapter 2 presents a concise background on WBT and their applications and impact. Chapter 3 expands on the measurement of the three-dimensional tire-pavement contact stresses/loads, where the measuring equipment and data processing and analysis are detailed. Details of the developed finite element model are discussed in Chapter 4, which also includes the definition of input parameters. The effect of tire configuration on critical pavement responses is presented in Chapter 5, which is the foundation for developing the prediction tool introduced in Chapter 6. Chapter 7 explains the development of two adjustment factors that would allow using AASHTOWare for NG-WBT loading. Chapters 8 and 9 present the experimental pavement sections (pavement structure, instrumentation, and testing matrix), and the quantification of pavement damage, respectively.

Finally, the life cycle assessment (LCA) of using NG-WBT is introduced in Chapter 10, and conclusions and recommendations are provided in Chapter 11.

The eight appendices provide samples of three-dimensional (3-D) tire contact stresses/loads, modeling results of thin and thick pavements, and a user guide of the prediction tool. In addition, the design and material characteristics of the pavement sections built and tested in Florida and California are presented in the appendices, which also include details about the data processing of pavement instrument responses of the experimental pavement sections and database management.

CHAPTER 2. LITERATURE REVIEW

Research conducted to date on WBT can be divided into two time periods. The first period focused on the first generation of wide-base tires (FG-WBT) and spanned from early 1980s to 2000. The second period started in early 2000 with the introduction of the NG-WBT after it became evident that FG-WBT was more damaging to the pavement infrastructure than the conventional DTA.

Studies of WBT may be divided into four impact categories: impact on road infrastructure, dynamic tire loading, trucking operations, and the environment. To investigate the effect of WBT on road infrastructure, researchers followed three main approaches: accelerated pavement testing, numerical modeling and analytical methods, and evaluation of in-service field data.

Accelerated pavement testing was used in Finland to study the effect of tire type and axle configurations (Huhtala et al., 1989; Huhtala, 1986). Flexible pavements with thicknesses of 2, 3, and 6 in were instrumented and subjected to various axle configurations and tire types. The study concluded that FG-WBT was more damaging than DTA; the amount of damage caused by these two types of tires decreased as the thickness of the asphalt concrete (AC) layer increased (Huhtala, 1986). Furthermore, FG-WBT was reported to cause between 1.2 and 4 times more damage than DTA (Huhtala et al., 1989).

In 1992, studies conducted in Virginia and Pennsylvania reported several findings related to FG-WBT. In Virginia, FHWA compared DTA and FG-WBT through performance and response analysis (Bonaquist, 1992). Twelve pavement sections were tested at various environmental conditions, axle loads, and tire inflation pressures. FG-WBT was found to be more damaging than DTA as it demonstrated two times more permanent deformation and 25% less fatigue life than DTA. On the other hand, a study led by Pennsylvania State University test track used trucks traveling at 40 mph with various tire inflation pressures, tire types, axle loads, and axle configurations. The study showed that the damage caused by FG-WBT was 50-70% greater than the damage caused by DTA (Sebaaly & Tabatabaee, 1992).

FG-WBT was also evaluated in overlay systems. A study in California compared the performance of dense-graded AC and asphalt-rubber hot-mix gap-graded (ARHM-GG). The accelerated pavement testing was carried out at high temperature, including aircraft tires. The number of repetitions to failure (excessive rutting) of FG-WBT ranged between 10 and 60% of DTA (Harvey & Popescu, 2000).

Several countries in Europe also studied WBT at the beginning of the previous decade (COST 334, 2001). The study included WBT 495/45R22.5, which was referenced as the new generation of WBT. In the United Kingdom, a comparison between WBT-385 and WBT-495 concluded that WBT-385 produced 70 and 50% more rutting in medium-thick and thin flexible pavements, respectively. Thick pavements were tested in Germany, and the ratio between the rutting generated by WBT-495 and DTA (315/80R22.5) was around 1.3. Very thick and stiff pavement structures were built and tested in France. No significant difference was found between measurements of both tires at the bottom of the AC. Finally, the difference in dynamic loading between various types of tires was investigated in Finland. Measurements were taken of a truck

traveled at 50 mph. The WBT-495 originated a greater response (COST 334, 2001). Some analytical method considered rectangular contact area for wide-base tire and concluded that it created more damage than dual-tire assembly (Maina et al., 2012).

Twelve different pavement sections were built, heavily instrumented, and tested in Virginia in the past decade. The testing program included various tire types, loading configurations, and speeds (See Al-Qadi et al., 2004; Al-Qadi et al., 2005a; Al-Qadi et al., 2005b; Elseifi et al., 2006). Transfer functions were used to link pavement response to damage. The comparison between the combined damage ratio of NG-WBT and DTA showed that NG-WBT is, in general, less damaging.

Research on WBT has also been conducted in Canada (Pierre et al., 2003). Strains near the surface of a flexible pavement with 4 in AC layer were measured and compared considering different tire types, speeds, loads, and tire inflation pressures. The damage of NG-WBT and DTA was found to be dependent on environmental conditions and location. For instance, strains at the base resulting from NG-WBT and DTA loading during summer were close in magnitude. However, NG-WBT produced higher strains in the spring (Pierre et al., 2003). The National Center for Asphalt Technology (NCAT) also reported that the horizontal strains at the bottom of the AC and the stresses on top of the subgrade produced by NG-WBT and DTA are comparable (Priest & Timm, 2006).

The effect of DTA, FG-WBT, and NG-WBT on full-depth pavements was compared in a study at the University of Illinois at Urbana-Champaign (Al-Qadi & Wang, 2009a, 2009b; Dessouky, et al., 2014). The thickness of the flexible pavements varied between 6 and 16.5 in After testing at various tire inflation pressures, axle loads, and temperatures, it was observed that WBT-425 (FG-WBT) is more damaging than WBT-455 (NG-WBT). Similar tests carried out on low-volume road test sections showed that NG-WBT is more damaging to this type of pavement (Al-Qadi & Wang, 2009c).

A study performed in Florida that focused on permanent deformation compared WBT-445, WBT-455, WBT-425, and DTA. Foil strain gauges close to the surface were installed, and the pavement was tested at high temperatures (Greene et al., 2009). DTA had the highest number of passes to reach 0.5 in rutting, and WBT-425 needed the least number of passes. More recently, it was shown that NG-WBT created 30% higher tensile strain at the bottom of the AC and "likely reduced" tensile strain near the surface and the edges of the tire (Grellet et al., 2012; Grellet et al., 2013). Similarly, impact of six tires (DTA 11R22.5, DTA 275/80R22.5, DTA 295/75R22.5, 285/70R22.5 tires, and WBT 455/55R22.5 and WBT 445/50R22.5) was measured in Ontario for two AC thicknesses, 7.3 and 8.8 in. (Bayat & Knight, 2012). Although experimental data were presented, no analysis was performed on the collected data. In addition, it was difficult to perform comparison between tires because as different testing parameters and scenarios were used (i.e., speed, load, temperature, and tire inflation pressure). Finally, it was recently reported that WBT 495 performed equal or better than DTA 295, while WBT 425 caused more damage at the pavement surface and the bottom of the AC (Xue & Weaver, 2015). A summary of field and accelerated pavement testing for quantifying the impact of WBT is presented in Table 1.

Numerical models have also been used to evaluate the effect of WBT. Radial, bias ply, and FG-WBT in thin (2 in) and thick (8 in) flexible pavements (Sebaaly & Tabatabaee, 1989) were

compared using BISAR. The study concluded that FG-WBT (15R22.5 and 18R22.5) generated the greatest strain at the bottom of the AC and stress on top of the subgrade, respectively. VESYS-DYN was used to assess fatigue damage and rutting. It was reported that FG-WBT caused wider and shallower rut depth than DTA (Gillespie et al., 1992). In addition, no influence of the tire inflation pressure on rutting was observed. FG-WBT produced 15-40% greater critical strain when using CIRCLY, software that considers shear contact stresses and friction between layers (Perdomo & Nokes, 1993). The relevance of the shear contact stresses was highlighted in the study.

A continuum-based finite-layer method was used to show that for FG-WBT traveling at high speed, the transverse tensile strain was more critical when predicting fatigue life (Siddharthan et al., 1998). The study also reported the importance of nonuniform 3-D contact stresses. ABAQUS was used to conclude that the contact stresses between the tire and the pavement were independent from the material of the layer in contact with the tire (Myers et al., 1999). Also, BISAR was used to highlight the importance of lateral contact stresses and their influence on surface cracking and near-surface rutting. Finally, the software 3D-MOVE was used to evaluate the shape of the contact area for different types of tires on pavement response (Siddharthan et al., 2002). FG-WBT with circular contact area provided the highest longitudinal strain at the bottom of AC and vertical strain on top of the subgrade. The study also found that lateral contact stresses were relevant only close to the surface.

The application of general-purpose software ABAQUS has been continuously improved to address details in the modeling of flexible pavements response. The software was used to include viscoelastic material characteristics (Elseifi et al., 2006), dynamic analysis (Yoo & Al-Qadi, 2008), 3-D contact stresses analysis (Yoo & Al-Qadi, 2008), continuous moving loading and layer interaction (Zhang et al., 2009), and nonlinear granular material (Al-Qadi et al., 2010; Kim, et al., 2005). All these effects have proven relevant when evaluating the response of flexible pavements. Table 2 presents a summary of the modeling conducted to date on this topic.

Regulations on using NG-WBT vary between agencies. For example, Mexico in 2008 approved using 9000 kg/axle on the tractor-single trailer. The Canadian Council of Ministers Responsible for Transportation and Highway Safety increased the axle load from 6,000 kg/axle to the US load of 7,700 kg/single axle and 15,400 kg/tandem axle.

The environmental benefits provided by NG-WBT are due to reduction in fuel consumption, savings in material needed to fabricate the tires, and producing lower noise levels. Fuel savings between 3.5 and 12% have been reported (WSP Canada, 2015), while reduction in emission can reach 1.1 million metric tons of carbon equivalent (MMTCE) in 8 years (Ang-Olson & Schroeer, 2002). In addition, savings of $415,900/year have been reported for material disposal at the end of life (GENIVAR Consulting Group, 2005).

Available literature suggests that FG-WBT causes more pavement damage. The impact of NG-WBT on pavement is inconsistent according to the findings in the literature. Hence, a gap exists in the current state of knowledge; specifically, with regard to pavement responses to loaded by NG-WBT. In addition, there are significant variations caused by the inconsistency in load modeling (including tire configuration, axle loading, and contact stresses) and use of material models. Therefore, accurate models of pavement responses to tire loading are needed and must be validated with in-situ measured data.

Table 1. Summary of Field and Accelerated Pavement Testing

Source	Pavement Structure	Instrumentation	Tire Type	Load (kip)	Tire Pressure (psi)	Outcome
Finland (Huhtala et al., 1989; Huhtala, 1986)	AC: 2, 3, and 6 in; base: 22 in; subgrade: fine sand	Strain gauges at bottom of AC and pressure cells on top of subgrade	12R22.5, 265/70R19.5, 445/65R22.5, 385/65R22.5, and 350/75R22.5	8.8, 11, and 13.2	69.6 to 156.5	• WBT caused 1.2-4 times more damage • The wider the WBT, the less the damage
Virginia (Bonaquist, 1992)	12 sections. AC: 3.5 and 7 in; base: 12 in; subgrade: silty fine sand	Strain gauges at bottom of AC, and LVDT at different depths	425/65R22.5 and 11R22.5	9.2, 12.1, 14.4, and 16.6	75.4, 103, and 140	• WBT produced two times more permanent deformation and 25% less fatigue life than DTA
Texas (Akram et al., 1992)	2 sections: i) AC: 1.5 in; base: 10 in.; ii) AC: 7 in; base: 14 in; subbase: 6 in stabilized w/ lime; Subgrade: sandy clay	Multi-depth deflectometers	425/65R22/5 and 11R22.5	16.5 and 18.5	130 and 120	• Maximum shear at edge of WBT • WBT produced higher deflections • WBT caused 2.8 more damage for thin and 2.5 for thick AC pavements
Pennsylvania (Sebaaly & Tabatabaee, 1992)	Thin section: AC: 6 in; base: 8 in Thick section: AC: 10 in.; base: 10 in.	Strain gauges at bottom of AC (instrumented core); geophones	11R22.5, 245/75R22.5, 385/65R22.5, and 385/65R22.5	7.3, 8.6, 8.8, and 10.8	75, 90, 100, 105, 120, and 130	• WBT resulted in more fatigue damage (between 0.5 and 2.8 times) • WBT caused 30 to 60% more rutting
California (Harvey & Popescu, 2000)	Overlays: 1.5 and 2.5 in DGAC, and 2.5 and 3 in ARGM-GG. Preexisting: AC: 6 in; base: 10.8 in, subbase: 9 in 3-in ATPB under AC in some sections	Thermocouples	Bias ply 10.00-20, 11R22.5, 425/65R22.5, and Aircraft 46x16	9 and 22.5	90, 105, 110, and 150	• Aircraft tire showed the worst rutting performance followed by WBT. • WBT required 10-60% the number of repetitions to failure (0.5 in rutting)
Europe (COST 334, 2001) England	Two AC thicknesses: 4 and 8 in; subbase: 9 in.; subgrade: 3-4% CBR	LVDTs and strain gauges	295/60R22.5, 295/80R22.5, 315/70R22.5, 315/80R22.5, 385/65R22.5, and 495/40R22.5	6.7, 9.69, and 12.7	72-145	• Ratio of rutting between 385/65R22.5 and 495/45R22.5 was 1.7 for 8 in pavement and 1.5 for 4 in pavement

Source	Pavement Structure	Instrumentation	Tire Type	Load (kip)	Tire Pressure (psi)	Outcome
Europe (COST 334, 2001) Germany	Four sections with: AC: 10.6 in; base: 10 in; subgrade: clay/peat	N/A	385/65R22.5, 315/80R22.5, 495/45R22.5, and 295/60R22.5	10.1 and 12.9	101.5 and 130.5	• Ratio of rutting between WBT-385 and DTA-315: 1.94 to 2.73 • Ratio of rutting between WBT-495 and DTA-315: 1.32 to 1.34
Europe (COST 334, 2001) France	AC: 3.2 in; AC base: 16 in; subbase: 12 in; subgrade: sandy clay	Strain gauges and thermocouples at different depths	385/65R22.5, 495/45R22.5, 315/80R22.5, and 295/60R22.5	10.1 and 12.9	116, 145, 166, and 87-167	• Similar vertical and longitudinal strains for WBT-495 and WBT-385
Europe (COST 334, 2001) Finland	AC: 6 in.; base: 6 in; and subbase: 16 in	7 long strain gauges at bottom of AC and three pressure cells at various depths	315/70R22.5 495/45R22.3	12.8	110 130	• At 50 mph, WBT-495 induced 17% more strain at bottom of AC than DTA-315 • 21 and 14% greater stress on top of the base and subbase, respectively. Almost the same on top of subgrade
Canada (PRe Constultants, 2013)	AC: 4 in; base: 8 in; subbase: 19 in; subgrade: silty	Distortion gauges, multi-depth deflectometer; slab built and instrumented in laboratory	11R22.5, 12R22.5, 385/65R22.5, and 445/55R22.5	6.6, 8.8, 11, 13.2, and 15.4	81.2, 105.9, and 130.5	• WBT-385 was more damaging than the other tires • Similar strain at base for WBT-455 and DTA during summer • WBT performed better in rutting • Less deflection for DTA
Virginia. (Al-Qadi et al., 2004; Al-Qadi et al., 2005a; Al-Qadi et al., 2005b; Elseifi et al., 2006)	12 pavement structures	Strain gauges and pressure cells at different depths. Thermocouples and TDRs	275/8R22.5 445/50R22.5	17.0 and 8.5	90/90, 90/60 and 90/30 105	• Combined pavement damage for WBT-445 was less than that for DTA-275
Alabama (Romanoschi & Metcalf, 2001)	AC: 6.7 in; base: 6 in; 17 in compacted subgrade	Long and transverse strain gauges at bottom of AC and pressure cells on top of subgrade	275/80R22.5 445/50R22.5	9.25 and 7.8	100 120	• Insignificant difference at the instrumented location between both tires

Source	Pavement Structure	Instrumentation	Tire Type	Load (kip)	Tire Pressure (psi)	Outcome
Illinois (Al-Qadi & Wang, 2009a, 2009b)	AC: 16.5, 10, and 6 in; lime modified subgrade	Two long and one transverse strain gauge at bottom of AC	425/65R22.5, and 455/55R22.5 11R22.5	6, 8, 10, 12 and 14	80, 100, and 110 110./30, 110/50, 110/70, 110/90, and 110/110,	• WBT-425 showed higher response than WBT-455 • Difference between WBT and DTA was relevant close to surface • WBT-425 was more damaging for fatigue cracking
Illinois (Al-Qadi et al., 2008; Al-Qadi & Wang, 2009c)	AC: 3 and 5; base: 8, 12, and 18 in; subgrade silty sand @4%. geogrid in 5 sections	Strain gauge at bottom of AC; LVDTs in 3directions. Pressure cells; TDR, thermocouples	11R22.5 and 455/55R22.5	6, 8, and 10	80, 100, and 110 and differential tire pressure	• WBT-455 caused more damage to low-volume roads than DTA
Florida (Greene et al., 2009)	AC: 5.1 in dense-graded and open-graded; base: 10.5 in; subbase: 12 in; subgrade: A-3	Foil gauges at the wheel path and 2 and 5 in from the edge of the tire	11R22.5 425/65R22.5 445/50R22.5 455/55R22.5	9	100 115	• DTA showed the best and WBT-425 the worst performance with respect to rutting. • WBT-425 generated the highest transverse strain at the surface • WBT-455 generated the lowest shear strain at edge of the tire; WBT-445 and DTA generated similar values
Ohio (Xue &Weaver, 2011; Yoo & Al-Qadi, 2007)	AC: 4 and 8 in; base: 6 in DGAB	Strain gauges rosettes and longitudinal and transverse strain gauges at the bottom of AC and close to the surface	275/80R22.5 295/75R22.5 425/65R22.5 495/45R22.5	5.05 4.2 5 5	70, 100, and 120	• WBT-425 produced higher response (shear strain) than the other tires • WBT-495 performed equal or better than DTA 295
Canada (Grellet et al., 2013; Bayat & Knight, 2012; Hallin et al., 1983)	AC: 2, 3, 4, 5, 7.3, 8, and 8.7 in; base: 8, 12, 19	Strain gauges installed on extracted core and polymeric plate	11R22.5 12R20.0 275/80R22.5 285/70R22.5 295/75R22.5 445/50R22.5 455/55R22.5	8.8-11.0	100	• NG-WBT created 30% higher tensile strain at the bottom of the AC than DTA • Higher fatigue damage and secondary rutting for NG-WBT

Table 2. Summary of Numerical Modeling and Analytical Methods

Study	Pavement Structure	Tire	Load Configuration	Tire pressure (psi)	Material Characterization	Outcome
Hallin et al. (1983)	AC: 3, 6, and 9.5 in; base: 8 in	Dual and single (width between 10 and 18 in)	Circular contact area: constant radius-variable pressure, double circle constant pressure, and single circle constant pressure	80	Resilient modulus test. Effect of temperature considered	• The difference in equivalent loading factor decreased as the tire width increased
Sebaaly and Tabatabaee (2002)	AC: 2, 4, 6, and 8 in; base: 8 in	11R22.5, 11-22.5, and 385/65R22.5	Measured contact stresses inputted as concentric circles with different pressures	DTA: 80-130; WBT: 105-145	Linear elastic	• Inflation pressure affected thin pavement, mainly for WBT-385 • WBT-385 generated the greatest strain at the bottom of AC and compressive stress on top of subgrade
Gillespie et al. (1992)	AC: 2 - 6.5 in; base: 4 - 11 in	215/75R17.5, 245/75R19.5; 11R22.5, 10.0-20, 11R24.5, 295/75R22.5; 15R22.5, 18R22.5, 385/65R22.5, and 445/65R22.5	Circular area with uniform pressure	75-120	Linear elastic	• WBT was more damaging than DTA for typical highway pavement • WBT caused wider but shallower rut profile than DTA; WBT 15R22.5 produced nine times more fatigue damage after changing tire inflation pressure from 75 to 120 psi
Perdomo and Nokes (1993)	AC: 6.6 in; base: 3 in	WBT and DTA (specific models not provided)	Circular contact area. Shear and nonuniform vertical contact stresses were considered	Maximum contact stress: WBT: 220; DTA: 160	Linear elastic	• WBT resulted in 15-40% higher critical strains, and 30-115% higher strain energy of distortion • Shear contact stresses had a high impact on tensile strain and strain energy

Study	Pavement Structure	Tire	Load Configuration	Tire pressure (psi)	Material Characterization	Outcome
Siddhartan et al. (2002) and Siddhartan et al. (1998)	AC: 6 and 10 in; base: 8 and 10 in	425/65R22.5 and DTA	Moving load with any shape of contact area. 3D contact stresses	123-130	Linear elastic and linear viscoelastic AC layer	• 16 and 33% higher strain at the bottom of AC for thin and thick pavement, respectively • When using WBT, transverse normal strain should be used
Myers et al. (1999)	AC: 8 in; base: 12 in	Bias ply, Radial, and WBT	Measured 3D contact stresses incorporated in BISAR	90-140	Linear elastic	• WBT at high values of load and inflation pressure were considerably more damaging than DTA (surface rutting and cracking) • Surface cracking and near-surface rutting were mainly influenced by lateral stresses
Siddharthan et al. (2002)	AC: 6 and 10 in; base: 8 and 10 in	425/65R22.5	Circular, elliptical, and rectangular contact area. Uniform and nonuniform pressure. 3D contact stresses	125	Elastic and viscoelastic AC layer	• For WBT, greater long strain at the bottom of AC and vertical strain on top of subgrade • Response at a depth of 2 in was greater for WBT with circular contact area • Shear contact stresses were relevant and close to the surface only
Al-Qadi et al. (2005a), Elseifi et al. (2006)	AC: 7.4 in; OGDL: 3 in; base: 6 in; subbase: 7 in	11R22.5, 445/50R22.5 and 455/55R22.5	Exact contact area and 3D contact stresses	104.4	Viscoelastic AC (creep test)	• WBT-445 was more damaging than DTA for subgrade and surface rutting • WBT-455 caused as much damage as DTA • Both WBTs were less damaging than DTA and

Study	Pavement Structure	Tire	Load Configuration	Tire pressure (psi)	Material Characterization	Outcome
						might cause more fatigue cracking
Kim et al. (2005)	AC: 6 in; base: 6.7 in	425/65R22.5 and conventional 5R17.5DTA	Rectangular contact area. Uniform contact stress and equal to maximum vertical contact stress	125	Subgrade: Druvker-Prager model. Linear elastic AC	• WBT produced the highest vertical stress on top of subgrade • WBT produced four times more permanent strain
Yoo et al. (2006)	AC: 7.4 in; OGDL: 3 in; base: 6 in; subbase: 7 in	445/50R22.5 and DTA	Continuous moving load. Measured 3D contact stresses	104.4	Viscoelastic AC, linear granular material	• Continuous moving load, interface friction, and 3-D contact stresses improve accuracy of modeling
Priest & Timm (2006)	AC: 6.7 in; base: 6 in	445/50R22.5 and 275/80R22.5	Comparison between experimental results at NCAT and mechanistic calculation using WESLEA (properties backcalculated by EVERCALC 5.0)	120	Linear elastic (backcalculation from FWD)	• Measurement showed similar stresses and strain for WBT and DTA; based on analytical result, WBT response was higher • Based on WESLEA: WBT created 69% less fatigue life
Al-Qadi et al. (2008), Al-Qadi and Wang (2009a, 2009b, 2009c)	Thin and thick	455/55R22.5, 445/50R22.5, and 425/65R22.5,	Dynamic analysis, continuous moving load, and measured 3D contact stresses	80-110	Viscoelastic AC, and nonlinear granular material	• WBT produced higher long strain at bottom of AC and higher vertical stress on top of subgrade, and less compressive and vertical shear strains close to surface • WBT-445 created less damage on highway pavements, but more on low-volume roads

CHAPTER 3. MEASURED TIRE-PAVEMENT CONTACT STRESSES/LOADS

The contact stresses/forces of the tires were measured by the Council for Scientific and Industrial Research (CSIR) in South Africa. A representative DTA, a set of two new tires of size 275/80 R22.5 and NG-WBT of size 445/50 R22.5, selected by the Rubber Manufacturer Association, were used in this study. This chapter describes the measuring equipment and testing program and provides an analysis of contact stresses.

STRESS-IN-MOTION EQUIPMENT

The dual Stress-In-Motion (SIM) (De Beer et al., 1997) Mk IV system used in this study for contact stress/load measurement consists of two SIM pad assemblies, each 33 × 18.5 in in nominal area. The single SIM pad assembly of the SIM Mk IV tire contact load/stress measurement system consists of an array of 21 instrumented pins installed across the center portion of the SIM pad assembly. In addition to the instrumented pin assemblies, supporting pins bore the test tire on both sides of the instrumented pins (approximately 1020 for each SIM pad) during SIM testing. These conical-shaped pins of an approximate height of 1.97 in were fixed to a 1.77-in-thick rigid steel base plate. Figure 1 and Figure 2 show the SIM system and sign convention.

Figure 1. Photo. Dual SIM Mk IV pad assembly.

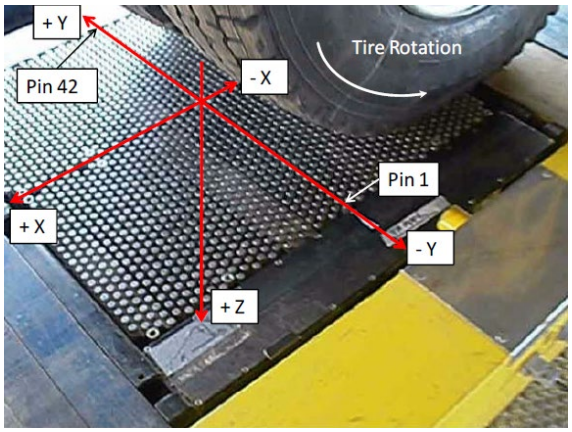

Figure 2. Photo. Sign convention of contact stresses.

In the current study, the test tires were fixed to the axle on the hydraulic loading test carriage of the Heavy Vehicle Simulator (HVS Mk III). The test tires were also fixed in the lateral position over the dual SIM pads for all measurements in the test series. Therefore, no lateral shifts were allowed during SIM testing. The vertical contact stresses were assumed positive in the vertical downward direction, while positive longitudinal contact stresses pointed in the traffic direction. The direction of positive transverse contact stresses can be inferred from the right-hand rule (Figure 1). The average tire speed was 0.75 mph and sampling frequency was 1001 Hz.

Static tire ink imprints were made using black roof paint on white paper under the HVS Mk III (Figure 3 - Figure 6) to obtain prints for the target loads indicated in the test matrix. Photos were then taken of each case (per the test matrix) and scaled in Excel spreadsheets. To calculate the contact area, tire footprints were imported and properly scaled in AutoCAD.

TEST TIRES AND TEST MATRIX

Three-dimensional (3-D) tire-pavement contact stresses/loads were measured for the NG-WBT (445/50R22.5) and DTA (275/80R22.5). Four values of tire inflation pressure (S) at 80, 100, 110, and 125 psi, and five tire loadings (*P*) at 6, 8, 10, 14, and 18 kip, were applied to the tires to measure the 3-D contact stresses. In addition, differential tire inflation pressure was applied to DTA; one tire of the assembly was kept at 110 psi while two values, 60 and 80 psi, were applied to the other. Figure 7 and Figure 8 present the test tires, and Table 2 summarizes the test matrix.

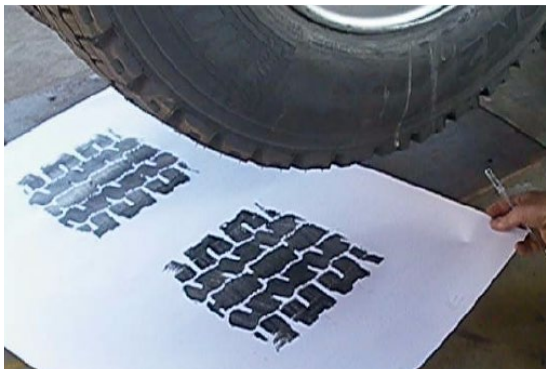

Figure 3. Photo. Measured Typical tire footprint for DTA.

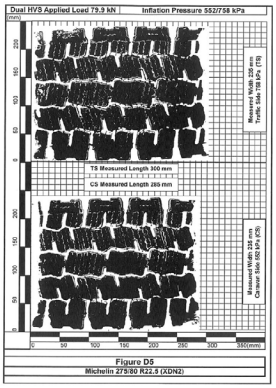

Figure 4. Photo. Processed Typical tire footprint for DTA.

Figure 5. Photo. Measured Typical tire footprint for NG-WBT.

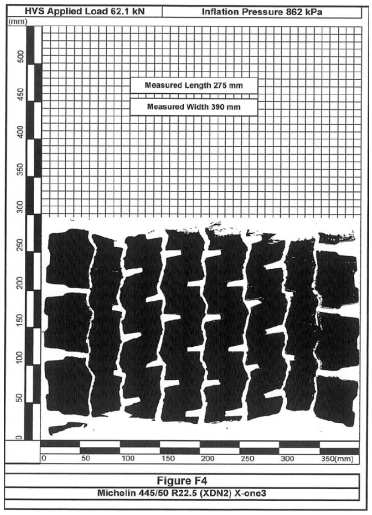

Figure 6. Photo. Processed Typical tire footprint for NG-WBT.

THREE-DIMENSIONAL CONTACT STRESSES/LOADS

The SIM measurements were reported in .txt format. Each file included the readings of the 42 instrumented pins in one of the three directions and its own measuring test speed and applied SIM total load (in kN). Three repetitions of each loading case were reported. SIM load distribution measurements were reported in load units (N). Load values were converted to "effective contact stress" values by applying the "effective area" geometrical conversion factor of 0.388 in^2 to the load data. The conversion factor assumed full contact between the tire and the measuring pins (no treads) (De Beer et al., 1997).

Figure 7. Photo. Test tires NG-WBT.

Figure 8. Photo. Test tires DTA.

Table 3. Test Matrix for WBT and DTA

Tire Type	Tire Inflation Pressure (psi)	Tire Loading (kip)				
NG-WBT and Dual	80	6.0	8.0	10.0	14.0	18.0
NG-WBT and Dual	100	6.0	8.0	10.0	14.0	18.0
NG-WBT and Dual	110	6.0	8.0	10.0	14.0	18.0
NG-WBT and Dual	125	6.0	8.0	10.0	14.0	18.0
Dual Only	60/110*	6.0	8.0	10.0	14.0	18.0
Dual Only	80/110*	6.0	8.0	10.0	14.0	18.0

The three repetitions of the experimental readings were filtered using the moving average method with a window size of 20 measurements. The same value was used for all data files, and it was selected based on the final smoothness and small shift of the data. After each repetition was filtered, average measurements were calculated. The distance along the tire contact patch was obtained using the sampling frequency and the speed of tire in each case. The filtered data and the three repetitions are given in Figure 9 and Figure 10 along with a zoomed view showing the effect of the filter.

In general, the shape of distribution of the vertical and transverse contact stresses σ_z and σ_y respectively) was very similar, even though their magnitudes were different. σ_z and σ_y were zero at the beginning and end of the contact length and had a maximum value around the center of the tire. The location of the maximum of the vertical contact stresses were consistently close to the center. In some cases, σ_y showed a negative peak at the end of the contact length, whose magnitude was small when compared with the positive peak.

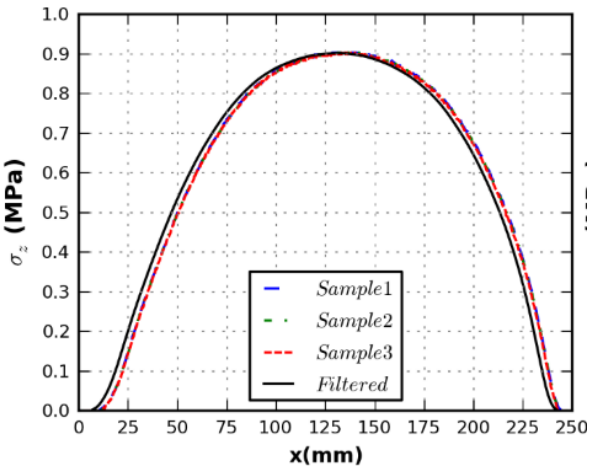

Figure 9. Graph. Three repetitions and filtered output.

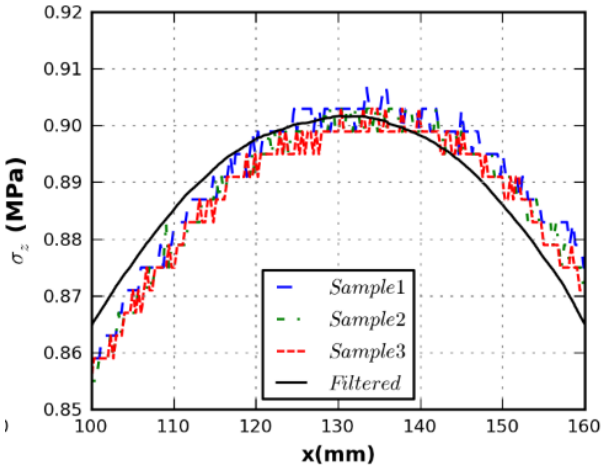

Figure 10. Graph. Three repetitions and filtered output – detail around peak.

The variation of the longitudinal contact stresses σ_x varied according to the rib's location. When the rib was at the edge of the tire, the distribution had three peaks, two negative and one positive. The first negative peak was located at the tire's front part and its magnitude was comparable to the positive peak. The second negative peak was greater than the other two extreme values, and it was located at the end of the contact length. For non-edge ribs, the negative peak at the tire's end vanished and the distribution of σ_z had two peaks only, one

positive and one negative. In this case, the magnitude of the positive peak (rear part of the tire) was significantly higher than that of the negative peak. The value and location of the described peaks for each entry of the test matrix were extracted from every measuring pin. A graphical representation of typical distribution of 3-D contact stresses is shown in Figure 11 through Figure 13. The contact length used in the analysis was determined based on σ_z, and it was defined as the distance at which σ_z is not equal to zero in each measurement. For each loading case, the maximum value of contact length was selected.

Once the measurements of each pin were filtered, a summary plot was created for each loading case. These plots included the variation of the 3-D contact stresses in every rib of NG-WBT and DTA. It is important to notice the presence of more than one pin in one rib. A calculated contact patch is also included. Based on the contact area from AutoCAD and the contact length from the vertical contact stresses, the width of each rib was obtained. This width was divided by the number of pins in the corresponding rib to determine the influence width of a pin. A sample of the mentioned summary plots is presented in Appendix A. A total of 50 graphics was elaborated corresponding to 20 loading cases (four tire inflation pressure cases and five applied load cases) per tire (NG-WBT and DTA) plus ten cases of differential tire inflation pressure.

In converting forces to stresses, the use of 0.388 in^2 as the influence area assumes that the tire is smooth (no ribs) and in full contact (tire rubber covers pin's influence area). However, these assumptions are invalid for the tires under analysis. Each tire comprises a number of ribs (8 and 10 ribs for NG-WBT and DTA, respectively). Moreover, each tread pattern is nonuniform. For instance, if a pin is located at a rib edge with partial contact, the area in contact between the pin and tire could potentially be half that of a pin at the middle of the rib, resulting in stress values double the ones computed with 0.388 in^2 as the contact area. To overcome the issue, the measurements were converted to nonuniform force per unit length variations along the length of the tire x in the longitudinal $q_x(x)$ transverse $q_y(x)$, and vertical $q_z(x)$ directions. It is important to note that the shape of $q_x(x)$, $q_y(x)$, and $q_z(x)$ is the same as the contact stresses; however, the unit is force over distance.

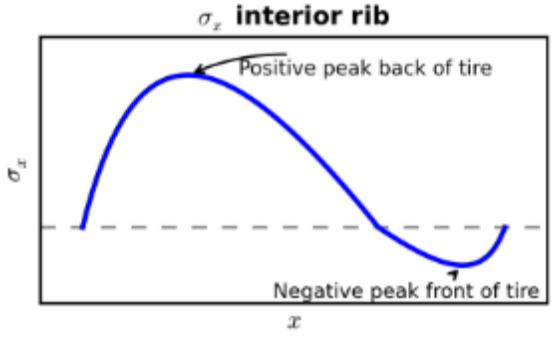

Figure 11. Graph. Typical distribution of longitudinal contact stresses for interior ribs.

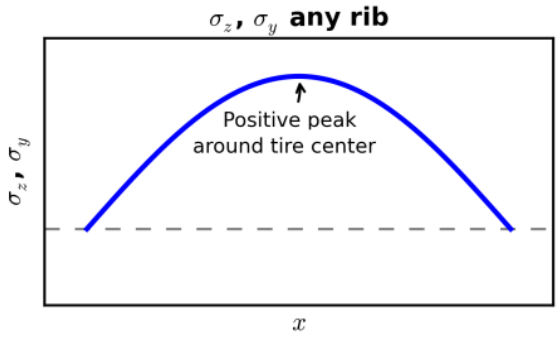

Figure 12. Graph. Typical distribution of vertical contact stresses.

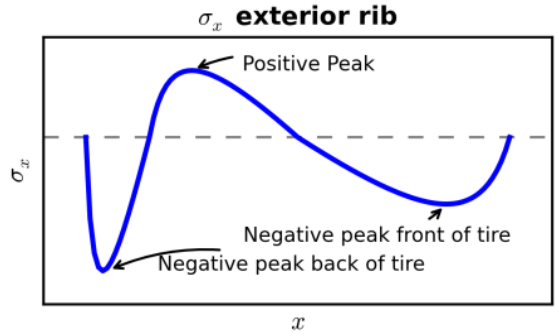

Figure 13. Graph. Typical distribution of longitudinal contact stresses for exterior ribs.

The ratio of the load carried by each rib P_i (i=1 to 8 for NG-WBT and 1 to 10 for DTA) with respect to the applied load P is presented in Figure 14 through Figure 19 for three P values (6, 10, and 18 kip) and four S values (80, 100, 110, and 125 psi). For both tires, the shape of the distribution across the tire width changed as P increased. when P was low, the center ribs carried more load than the ones at the edges of the tire (n shape distribution across the patch). On the other hand, when P was high, the center ribs carried less load than the ones at the edges of the tire (m shape distribution across the patch). The patterns were observed for all tire inflation pressure values considered. As the load increased, the percentage of load carried by the edge ribs became significantly higher for NG-WBT than for DTA. This was due to the higher number of sidewalls of DTA compared with NG-WBT (4 vs. 2). Furthermore, the variations of P_i/P across all the ribs with various S values for NG-WBT were relatively close to each other for a given P value. This finding indicates that the percentage of P carried by each rib was not significantly affected by S. For DTA, however, the observation is valid only if the tire inflation pressure was less than or equal to 100 psi. Finally, it was noted that P_i/P was generally higher for NG-WBT than for DTA because of the lower number of ribs.

The magnitudes of the measured forces in three directions were also compared. Ratios of the maximum transverse $q_{y,max}$ and longitudinal $q_{x,max}$ forces per unit length with respect to vertical force $q_{z,max}$ for each rib are illustrated in Figure 20 through Figure 23. The horizontal axis represents the combination of the number of ribs with various S (e.g., NG-WBT: 8 ribs by 4 S equates to 32 case indicators). Even though a distinct relationship between the aforementioned

ratios, tire type, *P*, and *S* was not identified, two observations can be made regarding the relative magnitude of $q_{x,max}$ and $q_{y,max}$ with respect to $q_{z,max}$. On one hand, 85% of the data points fall in the range of $0.05 < q_{x,max}/q_{z,max} < 0.32$ for NG-WBT, whereas the range changes to $0.05 < q_{x,max}/q_{z,max} < 0.26$ in the case of DTA. On the other hand, the variation range for $q_{y,max}/q_{z,max}$ becomes narrower in comparison with $q_{x,max}/q_{z,max}$. The tighter band enables a greater number of data points to be considered. For NG-WBT, 90% of the data varies between 0.16 and 0.35, while the lower and upper limits change to 0.10 and 0.28 for DTA.

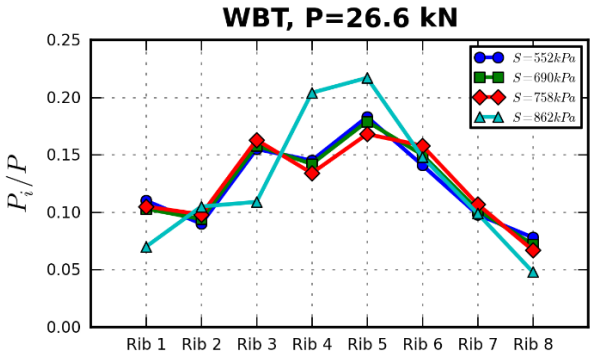

Note: 1 kPa=0.145 psi, 1 kN=224.8 lb

Figure 14. Graph. Percentage of load carried by each rib for NG-WBT and 26.6 kN.

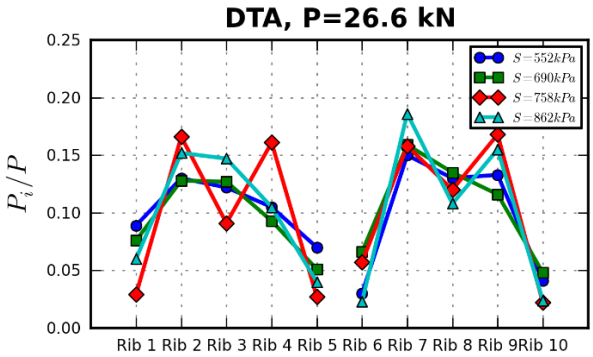

Figure 15. Graph. Percentage of load carried by each rib for DTA and 26.6 kN.

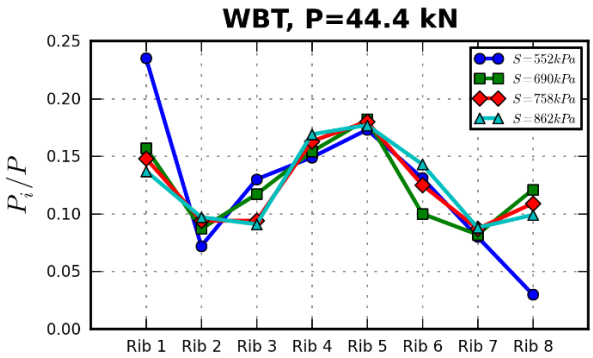

Figure 16. Graph. Percentage of load carried by each rib for NG-WBT and 44.4 kN.

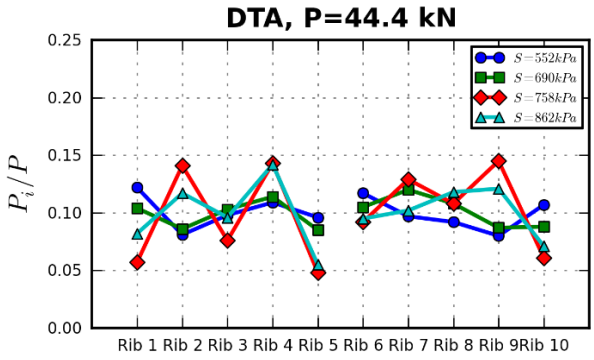

Figure 17. Graph. Percentage of load carried by each rib for DTA and 44.4 kN.

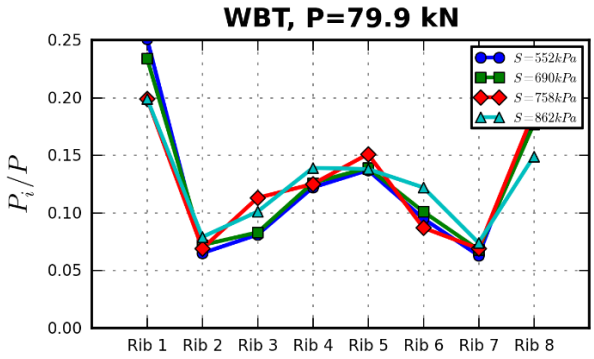

Figure 18. Graph. Percentage of load carried by each rib for NG-WBT and 79.9 kN.

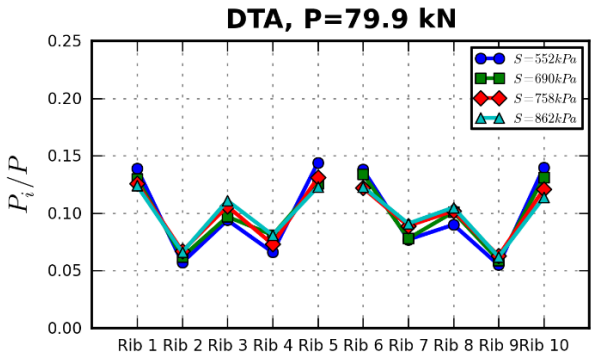

Figure 19. Graph. Percentage of load carried by each rib for DTA and 79.9 kN.

Based on these remarks, it can be concluded that the peak transverse and longitudinal forces per unit length (or contact stresses) are relatively higher for NG-WBT than DTA. Additionally, regardless of the tire type, the magnitude of the tangential contact stresses are considerably high, thereby highly influencing pavement responses. Previous research has indicated the importance of considering transverse contact stresses, which have been linked to near-surface cracking and shear flow. [48] Since ratios $q_{x,max}/q_{z,max}$ and $q_{y,max}/q_{z,max}$ are different for both tires, same effect on pavement responses and performance may not be assumed, although both tires have the same applied load and tire inflation pressure.

CONTACT AREA AND CONTACT LENGTH

Characterization of the 3-D tire-pavement contact stresses/loads was completed by accurate contact area and length. The contact area was obtained from static imprints, whereas the contact length was determined based on the variation of vertical contact stresses/loads. Figure 24 and Figure 25 compares the change of the contact area *Ac* and the average contact length *l* of both tires, respectively. As expected, the contact area increased as *P* reached 18 kip. In addition, *Ac* was greater for DTA than WBT for all loading cases, and the contact area ratio between DTA and NG-WBT was as high as 1.3. Regarding the average contact length, a strong linear relationship was found when comparing *l* of both tires. The average contact length for DTA was approximately 8% shorter than the contact length for NG-WBT.

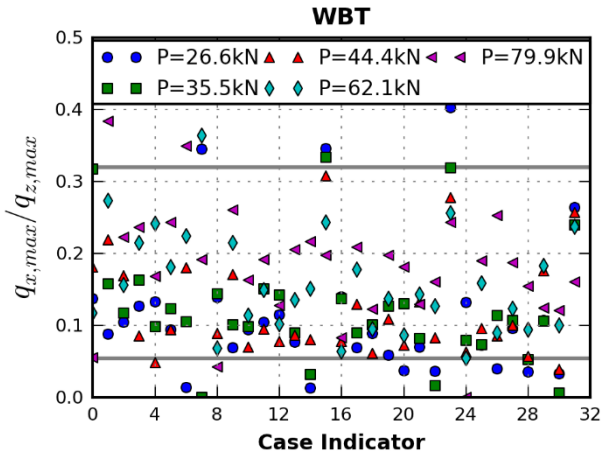

Figure 20. Graph. Ratio of maximum longitudinal to vertical contact forces for NG-WBT.

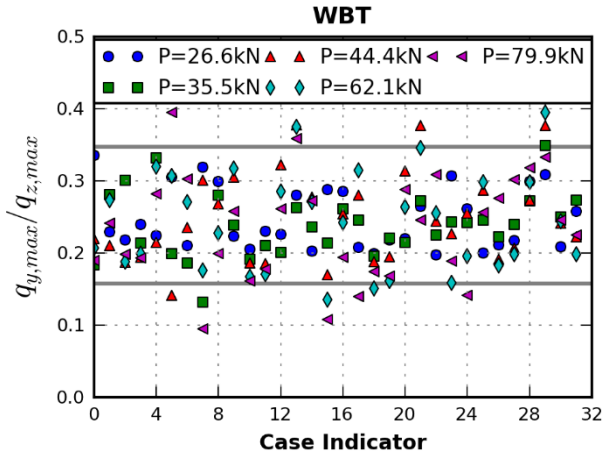

Figure 21. Graph. Ratio of maximum transverse to vertical contact forces for NG-WBT.

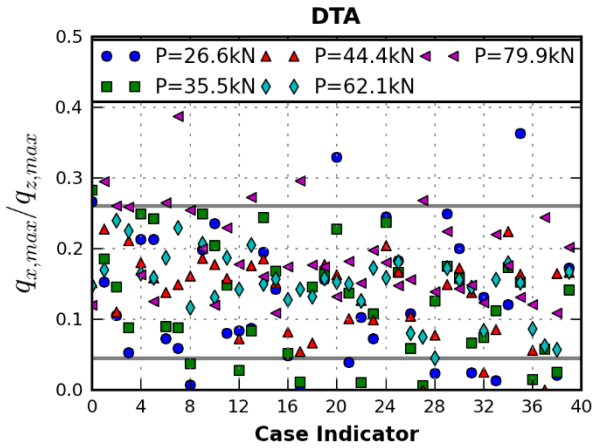

Figure 22. Graph. Ratio of maximum longitudinal to vertical contact forces for DTA.

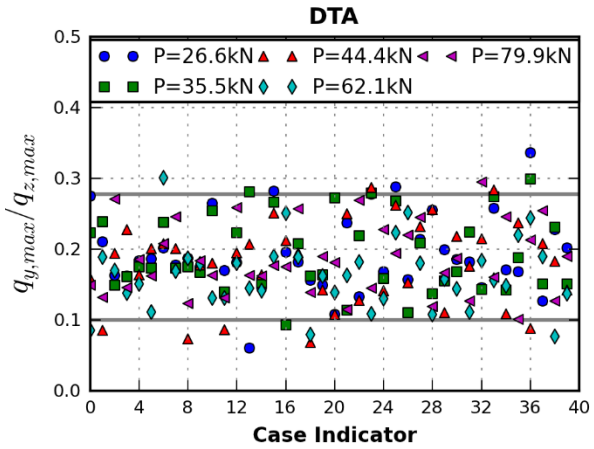

Figure 23. Graph. Ratio of maximum transverse to vertical contact forces for DTA.

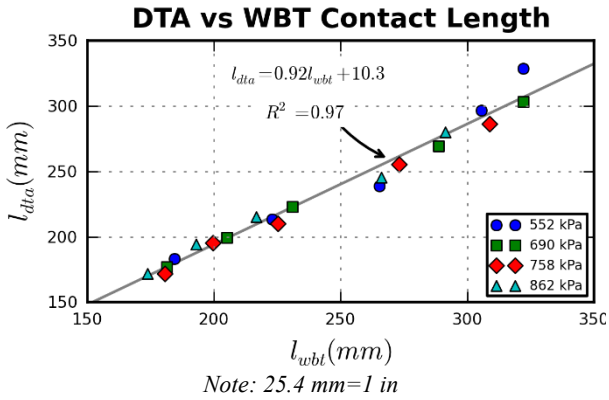

Figure 24. Graph. Average contact length.

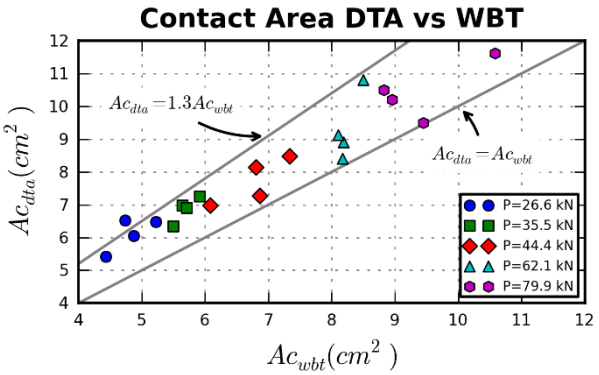

Figure 25. Graph. Contact area.

SUMMARY

Tire-pavement contact stresses/loads possess two important characteristics that significantly affect pavement responses: non-uniformity and three dimensionality. Experimental data for two truck tires, NG-WBT and DTA, were measured and analyzed to emphasize the importance of considering realistic contact loads. The ratio of transverse and longitudinal contact forces with respect to the vertical contact force was found to be higher for NG-WBT than DTA. The results also indicated considerably high magnitudes of the transverse contact load, regardless of the tire type, which asserts its relevance in pavement analysis. Finally, the contact area of the DTA was as much as 30% higher than NG-WBT. The transfer-load mechanism of each tire is very different, and it is expected not to be constant across various geometries of NG-WBT.

CHAPTER 4. NUMERICAL MODELING OF PAVEMENT STRUCTURES

The current design method for flexible pavements is based on the structural response that uses inappropriate assumptions. Static analysis of multilayer elastic systems simulates the tire load as a uniformly distributed vertical pressure on a circular contact area with the contact pressure equal to the tire inflation pressure, which does not accurately represent the actual phenomenon of a flexible pavement subjected to truck loading. Therefore, a numerical model was generated to mend the gap between reality and the current representation of a flexible pavement loading. This enabled a more robust analysis of pavement responses under various combinations of tire load and tire inflation pressure, pavement structure, and pavement material properties.

DEVELOPMENT OF THREE-DIMENSIONAL FINITE ELEMENT MODEL

One of the key aspects of the loading configuration highlighted in the analysis below is the three-dimensionality and non-uniformity of contact stresses, which is the main excitation for pavement responses. Other important factors considered in the simulations include linear viscoelastic material characterization of AC, nonlinear anisotropic behavior of the granular base (thin pavement only), dynamic analysis, contact stress measurements, continuous moving load, layer interaction, temperature profile in the AC layer, and an optimized mesh discretization with infinite elements.

Viscoelastic Asphalt Materials

The U.S. Federal Highway Administration (FHWA) Long-Term Pavement Performance (LTPP) Standard Release 26.0 provides material characterization of the AC layers. The group of tables used for this project are named, 'TST_ESTAR,' indicating the dynamic modulus, $|E^*|$ data of AC mixtures.

Dynamic modulus is a fundamental material property that defines AC stiffness as a function of temperature and loading time. The test data collected at different temperatures were shifted relative to the time of loading or loading frequency to align various curves to form a single master curve (FHWA, 2012). Using a sigmoidal fitting function solves shift factors simultaneously with the coefficients of the fitting function. It also eliminates irrational modulus value predictions when extrapolating outside the range of data, which occurs when a single polynomial model is used at high and low temperatures. Below is the sigmoidal function that the MEPDG uses to fit the dynamic modulus test data.

$$log(|E^*|) = \delta + \frac{\alpha}{e^{\beta - \gamma \log(\xi)}}$$

Figure 26. Equation. Shifted dynamic modulus data.

where: $|E^*|$ = dynamic modulus

ξ = reduced angular frequency in Hertz

δ = minimum modulus value
α = span of modulus values
β, γ = shape parameters

Additionally, the 'TST_ESTAR_MODULUS_COEFF' table contains the coefficients for the time-temperature shift factor function for $|E^*|$ as indicated in the following equation:

$$log(|E^*|) = \delta + \frac{\alpha}{e^{\beta - \gamma \log(\xi)}}$$

Figure 27. Equation. Time-temperature shift factor.

where: a_T = AC time-temperature shift factor
T= temperature of interest
$\alpha_1, \alpha_2, \alpha_3$= regression coefficients

For initial filtration of the data provided, a 'MASTERCURVE_QUALITY' check was included in the 'TST_ESTAR_MODULUS_COEFF' table to differentiate between passing and failing data. A pass was assigned whenever the confidence level was greater than 0.99 and ratio of standard error to standard deviation was less than 0.05. Data were further filtered to appropriately choose material properties through statistical analysis, wherein the minimum modulus value became the controlling factor as it represents the behavior of the material under slow loading condition and/or high temperature.

The remaining data, approximately 1000 data sets, was sorted in an increasing order according to the minimum modulus value. Using normal distribution, three tolerance intervals were considered: 95.4%, 97.5%, and 99.8%. The chosen intervals denoted the percentage of values lying within their respective standard deviations. The three tolerance intervals determined the minimum and maximum modulus values for the wearing surface, intermediate, and base layers, respectively. Another parameter, the nominal maximum aggregate size (NMAS), was used to further refine the data. For the wearing surface, typical NMAS had to be 0.37 in or 0.5 in to be acceptable; whereas, typical NMAS had to be 1 in or 0.77 in for the intermediate layer and 1 in or 1.5 in for the base layer.

With the combination of the statistical tolerance level and typical layer NMAS, the data were refined to the most appropriate material properties. Based on the remaining data passing the multiple criteria, graphical comparison of the master curves led to the determination of appropriate material properties for the three AC layers to represent the 'weak' and 'strong' sets that will be used for numerical analysis. Additionally, based on visual inspection, an intersection and/or overlap between the data sets was prevented. Six appropriate data sets were finalized, wherein the top three master curves were chosen for the 'strong' set and the bottom three represented the 'weak' set (Figure 28). The corresponding sigmoidal function coefficients are presented in Table 4.

Granular Material

For the simulated interstate highway, the base and subgrade materials were considered linear elastic. The assumed behavior was considered appropriate as thickness of the AC layer reduces the stress-dependency of the granular layers. On the other hand, for the low-volume pavement cases, the base layer materials were considered nonlinear anisotropic, and the subgrade was assumed to be linear elastic.

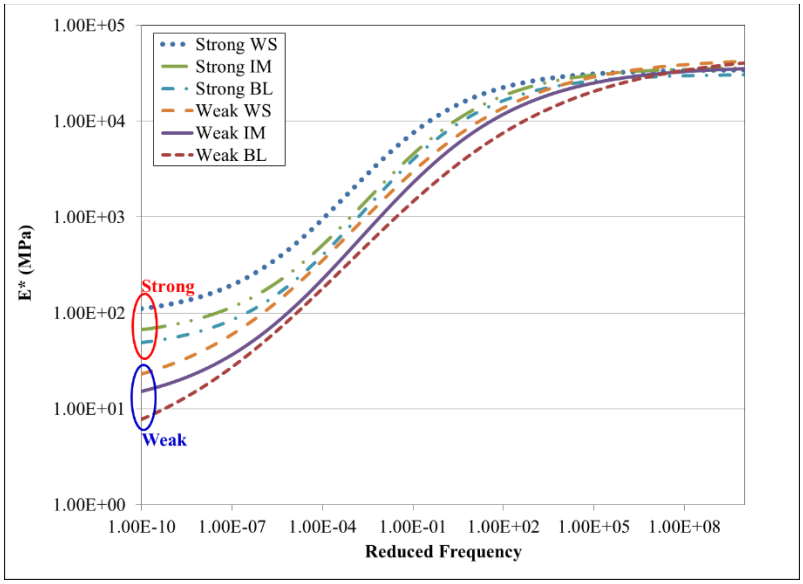

Note: 1 MPa=145 psi

Figure 28. Graph. AC linear viscoelastic material characterization.

Table 4. Sigmoidal Function Coefficients Representing AC Material Properties

Mix Type	Layer	δ	α	β	γ	α_1	α_2	α_3
Strong	WS*	1.9654	2.5711	-1.5622	0.4982	0.0002	-0.1053	6.3104
Strong	IM*	1.7370	2.8245	-1.2149	0.4656	0.0002	-0.1053	6.3104
Strong	BL*	1.6067	2.8820	-1.2840	0.4812	0.0004	-0.1533	8.6010
Weak	WS	1.0967	3.5621	-1.0530	0.3572	0.0002	-0.1169	6.9827
Weak	IM	0.9694	3.6050	-1.0560	0.3825	0.0001	-0.0962	6.1900
Weak	BL	0.3505	4.3576	-0.8800	0.2829	0.0009	-0.2285	11.6836

**Note: WS = Wearing Surface, IM = Intermediate Layer and BL = Base Layer*

To select appropriate strong and weak base layers, a database of 114 materials with appropriate nonlinear cross-anisotropic laboratory characterization was considered (Tutumluer, 2008). Pulse load was applied in the vertical and radial directions. Hence, cross-anisotropic characterization was possible. As part of the database, *k*-values were reported based on the Uzan model:

$$M_{rv} = k_1 \left(\frac{\theta}{p_o}\right)^{k_2} \left(\frac{\sigma_d}{p_o}\right)^{k_3}$$

Figure 29. Equation. Vertical resilient modulus of granular materials.

where: M_{rv} = resilient modulus in the vertical direction
k_1, k_2, k_3 = regression coefficients
$\theta = \sigma_1 + \sigma_2 + \sigma_3$ = bulk stresses
σ_d = deviator stress
p_o = unit reference pressure

It is known that the resilient modulus of granular materials depends on the stress level. To select appropriate weak and strong base materials, two stress levels (Table 5) were defined based on the field condition of base materials (Xiao et al., 2011).

Table 5. Stress Level for Low and High Base Material Resilient Moduli

	Low (kPa)	Low (psi)	Low (kPa)	Low (psi)
$\boldsymbol{\sigma_3}$	34.9	5.0	104.8	15.0
$\boldsymbol{\sigma_d}$	104.8	15.0	209.5	30.0
$\boldsymbol{\sigma_1}$	139.7	20.0	314.3	45.0
$\boldsymbol{\sigma_2}$	34.9	5.0	104.8	15.0
$\boldsymbol{\theta}$	209.5	30.0	523.9	75.0

Using the aforementioned stress levels and the *k*-values from the database, the resilient modulus for each material was calculated. The resilient moduli obtained for both stress states are presented in Figure 31. Assuming a normal distribution, the weak base material was selected as the one corresponding to the average minus two standard deviations ($\mu - 2\sigma$ = 9.8 ksi) of the set of resilient modulus corresponding to low-stress level. Similarly, the strong base material corresponded to the closer value of the vertical resilient modulus of $\mu + 2\sigma$ = 47.3 ksi. After materials selection, the laboratory data were used to determine the *k*-values based on the MEPDG model used in AASHTOWare.

Pulse loading was not applied in the shear direction during laboratory testing; hence, a simplified procedure proposed by Tutumluer and Thompson (1998) was used to determine the *k*-values in the shear direction. The procedure is summarized as follows:

- In case of cross-anisotropy, the Uzan model becomes (note that the database provides values for k_1 through k_6.):

$$M_{rv} = k_1 \left(\frac{\theta}{p_o}\right)^{k_2} \left(\frac{\sigma_d}{p_o}\right)^{k_3}$$
$$M_{rh} = k_4 \left(\frac{\theta}{p_o}\right)^{k_5} \left(\frac{\sigma_d}{p_o}\right)^{k_6}$$
$$M_{rs} = k_7 \left(\frac{\theta}{p_o}\right)^{k_8} \left(\frac{\sigma_d}{p_o}\right)^{k_9}$$

Figure 30. Equation. Vertical, horizontal, and shear resilient modulus of cross-anisotropic granular materials, respectively.

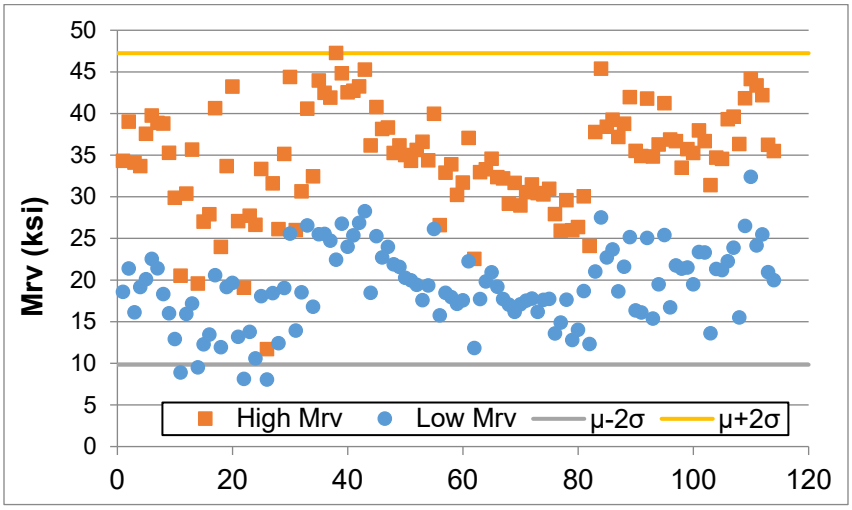

Figure 31. Graph. Resilient modulus for low and high granular base stress levels.

- Using the simplified method, the shear *k*-values for the shear direction are calculated as follows:

$$k_7 = -90.92 + 0.27k_1 + 305.34k_2 + 158.22k_3 \ (psi)$$
$$k_8 = 0.2 + k_2$$
$$k_9 = -0.2 + k_3$$

Figure 32. Equation. Calculating the coefficients k_7, k_8, and k_9.

- Using *k7,k8, and k9* and the stress levels of the vertical resilient modulus, the shear resilient modulus data can be computed.
- Regression parameters of the MEPDG model are obtained from the resilient moduli in the vertical, horizontal, and shear directions. The MEPDG version of the nonlinear cross-anisotropic model is as follows:

$$M_{rv} = k_1 p_a \left(\frac{\theta}{p_a}\right)^{k_2} \left(\frac{\tau_{oct}}{p_a} + 1\right)^{k_3}$$
$$M_{rh} = k_4 p_a \left(\frac{\theta}{p_a}\right)^{k_5} \left(\frac{\tau_{oct}}{p_a} + 1\right)^{k_6}$$
$$M_{rs} = k_7 p_a \left(\frac{\theta}{p_a}\right)^{k_8} \left(\frac{\tau_{oct}}{p_a} + 1\right)^{k_9}$$

Figure 33. Equation. MEPDG model for the vertical, horizontal, and shear resilient modulus of cross-anisotropic granular materials.

The regression parameters for the selected materials are summarized in Table 6. In addition, Table 7 details calculation of the resilient modulus for both stress levels and materials, while Figure 34 through Figure 37 compare the measured and calculated resilient moduli of the selected materials. The resilient modulus was 42.7 ksi in the vertical direction for the strong material at high stress level and 9.9 ksi for the weak material at low stress level. For thick pavements, the resilient modulus for weak and strong granular base was 20.0 ksi and 60.0 ksi, respectively.

Table 6. Regression Parameters of the MEPDG Model for Weak and Strong Granular Materials

Direction	Weak	Weak	Weak	Strong	Strong	Strong
Vertical	k_1=453.3	k_2=0.8858	k_3=-0.5713	k_1=869.6	k_2=0.9785	k_3=-0.5673
Horizontal	k_4=282.4	k_5=0.6701	k_6=-1.1341	k_4=596.6	k_5=1.1419	k_6=-1.3464
Shear	k_7=310.3	k_8=1.0297	k_9=-1.1036	k_7=389.1	k_8=0.9083	k_9=-0.2409

Table 7. Summary Results of Resilient Moduli in the Vertical, Horizontal, and Shear Directions at Two Stress Levels

	Weak Low (MPa)	Weak High (MPa)	Weak Low (psi)	Weak High (psi)	Strong Low (MPa)	Strong High (MPa)	Strong Low (psi)	Strong High (psi)
$\sigma 3$	0.0349	0.1048	5.0	15.0	0.0349	0.1048	5.0	15.0
σd	0.1048	0.2095	15.0	30.0	0.1048	0.2095	15.0	30.0
σ_1	0.1397	0.3143	20.0	45.0	0.1397	0.3143	20.0	45.0
σ_2	0.0349	0.1048	5.0	15.0	0.0349	0.1048	5.0	15.0
θ	0.2095	0.5239	30.0	75.0	0.2095	0.5239	30.0	75.0
p_a	0.1000	0.1000	14.3	14.3	0.1000	0.1000	14.3	14.3
t_{oct}	0.0494	0.0988	7.1	14.1	0.0494	0.0988	7.1	14.1
Mrv	69.41	132.75	9937.2	19006.3	142.8	297.7	20447.4	42624.8
M_{rh}	29.41	39.30	4210.0	5626.9	80.88	156.75	11579.9	22442.3
M_{rs}	42.68	80.00	6110.7	11453.4	69.16	148.40	9901.9	21246.4
M_{rh}/M_{rv}	0.42	0.30	0.42	0.30	0.57	0.53	0.57	0.53
M_{rs}/M_{rv}	0.61	0.60	0.61	0.60	0.48	0.50	0.48	0.50

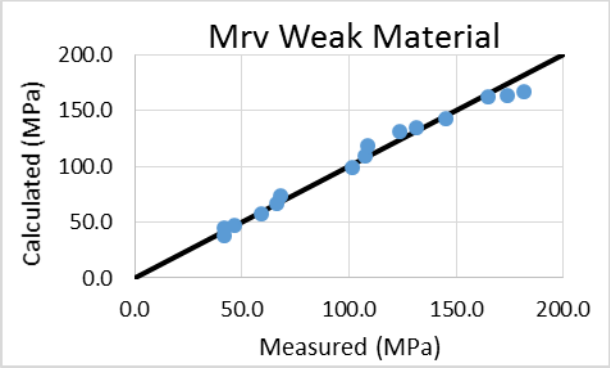

Note: 1 MPa=145 psi

Figure 34. Graph. Comparison between measured and calculated vertical resilient moduli for weak base.

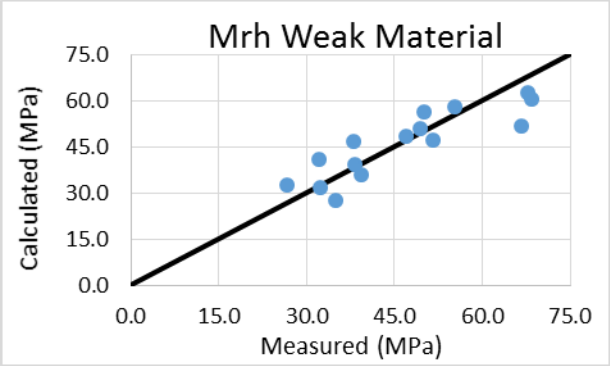

Figure 35. Graph. Comparison between measured and calculated horizontal resilient moduli for weak base.

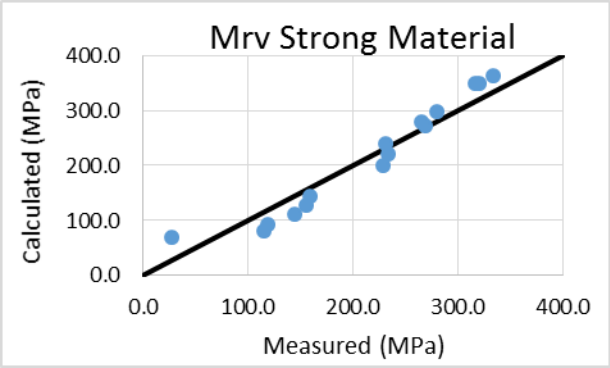

Figure 36. Graph. Comparison between measured and calculated vertical resilient moduli for strong base.

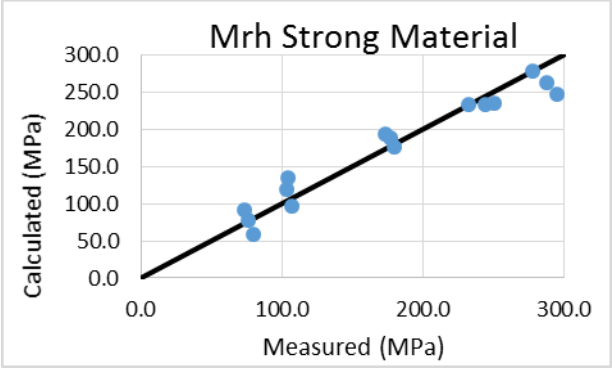

Figure 37. Graph. Comparison between measured and calculated horizontal resilient moduli for strong base.

Implicit Dynamic Analysis

In pavement analysis, three approaches are used to consider truck loading: i) static, ii) quasi-static, and iii) dynamic transient analysis. Conventionally, static loading is considered in multilayer elastic analysis. The quasi-static approach, on the other hand, incorporates the moving load concept at subsequent positions along the pavement at a given time step, wherein each load step is assumed to be one position. However, neither the inertial or damping effect nor the frequency-dependence of the material properties are considered in this approach. Therefore, the most suitable approach is the dynamic transient analysis, which takes into account the aforementioned factors.

When considering dynamic transient loading on a pavement system, a structural dynamic problem, rather than a wave propagation problem, arises as the wave propagation speed in a flexible pavement structure is significantly less than vehicle speed (OECD, 1992). This calls for a dynamic equilibrium equation, which can be solved using either an implicit or explicit direct integration method. For the frequencies given in this study, an implicit method would be more effective (Bathe, 1982).

For a dynamic analysis, the energy dissipation mechanisms dictate that a damping factor, friction factor, or viscoelastic material behavior be implemented. Hence, the AC layers do not require a damping factor due to the given linear viscoelastic material characterization. On the contrary, Rayleigh damping is used for the granular materials, where the mass proportional damping, α, and stiffness proportional damping, β, are assumed to be 3.1416 and 7.95×10^{-4}, respectively (Wang, 2011).

Three-Dimensional Contact Stresses

Measured contact loads/stresses were used in the pavement model to represent the three-dimensionality and non-uniformity of tire loading. In conventional pavement analysis, only vertical pressure is considered and is made equal to the tire inflation pressure. Traditionally, the contact area is also assumed to be circular, which leads to poor correspondence to the reality of

pavement loading. A detailed analysis and description of the contact stresses are provided in the previous chapter.

Continuous Moving Load

In order to simulate a continuous tire movement over the pavement structure at a specified speed, the tire loading was gradually shifted over the total loading area in the longitudinal direction (simulated traffic direction) until a single pass was completed. As indicated in Figure 38, the initial step included the span of the varying contact stresses over the tire imprint area, which then shifted over onto the next set of elements, while maintaining the same number of elements governed by the load.

Based on Yoo et al. (2007), the moving wheel load length in the longitudinal direction needs to be approximately 39.4 in to appropriately observe the continuous moving load effect on the pavement structure. To define the length of the loading area, the element size in the loading area was determined to be 0.79 in and the number of element steps was determined to be 16, moving three elements in every step. Additionally, the length of the tire was considered in the total length of the loading area.

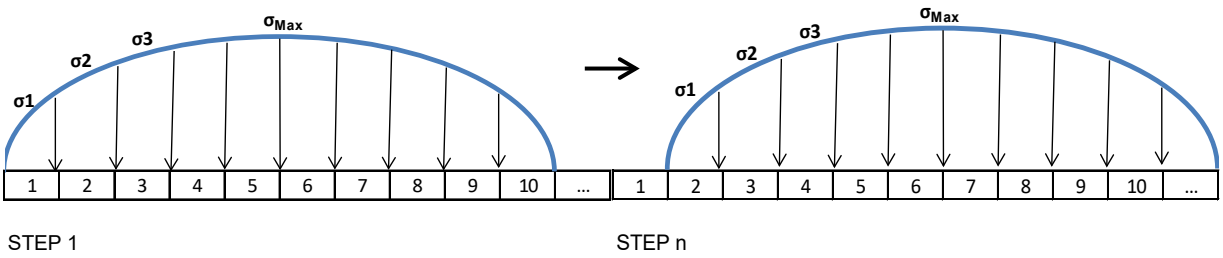

Figure 38. Graph. Step loading of the tire imprint over 3D-FE model.

Initially, tire loading was shifted one element at a time. However, it was necessary to evaluate the effect of load shifting over a larger span of elements to reduce computational time. Six cases were considered: 1, 2, 3, 4, 6 and 12 elements span. Moving the load one element at a time captured the most detailed and least incremental step; therefore, it was considered as a reference case. Table 8 indicates the results of an example analysis including the 'wall time' and percentage of error between the critical strains. Although the percentage of error between the cases did not exceed 5%, it was necessary to capture the utmost accuracy of the critical responses. The critical strain responses are presented in Figure 40 through Figure 45. With the balance of low computational time and accuracy, the number of loading steps chosen for the 3-D FEM model was 16, wherein each step spans over three elements.

Table 8. Effect Step Element Span for a Continuous Moving Load on the Critical Strains

Steps	No. of Elements	Wall Time	Diff. (%)	Diff. (%)	Diff. (%)	Diff. (%)	Diff. (%)	Diff. (%)
		(hr.)	$\varepsilon_{11botAC}$+	$\varepsilon_{33botAC}$	$\varepsilon_{11topAC}$	$\varepsilon_{33topAC}$	$\varepsilon_{23midAC}$	$\varepsilon_{22topSG}$
4	12	2.79	0.353	-0.101	0.135	-1.383	-0.878	-0.233
8	6	5.01	0.583	1.764	0.599	0.352	0.169	4.345
12	4	7.16	0.474	1.719	0.741	0.464	0.455	3.179
16	**3**	**9.09**	**0.416**	**1.653**	**0.857**	**0.499**	**0.686**	**3.021**
24	2	13.23	0.381	1.228	0.962	0.366	0.816	2.411
48	1*	21.27	--	--	--	--	--	--

**Assumed Reference*
+Parameters defined in Chapter 5

Layer Interaction

Defining the interaction between pavement layers is critically important as it affects pavement response to load excitation. The interface reflected a tied interaction between the AC layers. A Coulomb friction model was implemented for the AC to base and base to subgrade interfaces. The model assumes that the resistance of movement is proportional to the normal stress at the interface. A tolerance level was set for the shear strength, and when the two bodies passed the tolerance level, they slid relative to each other. For this scenario, the frictional stress was assumed to be constant. The proportionality of the friction coefficient to the allowed maximum shear stress (strength) and normal stress is defined by the following equation:

$$\mu = \frac{\tau_{max}}{\sigma}$$

Figure 39. Equation. Defining friction coefficient.

where: τ_{max}= the allowed maximum shear stress prior to relative sliding of layers
σ = the normal stress at the interface
μ= friction coefficient

Temperature Profile

The viscoelastic material characterization of AC invokes the importance of temperature in this study. Depending on the environmental conditions, pavement responses vary significantly in the asphalt layer. At low temperature, AC stiffness tends to increase, whereas it decreases at high temperature. Hence, temperature directly affects pavement responses.

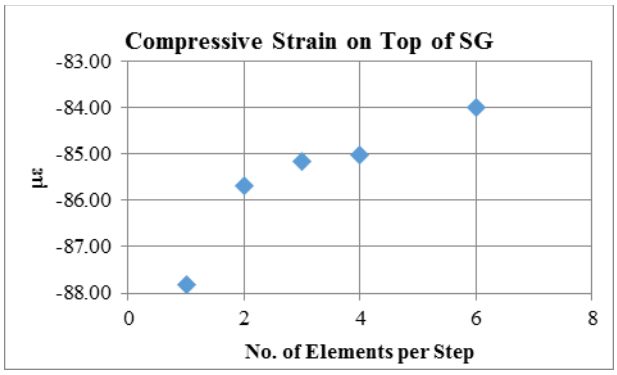

Figure 40. Graph. Effect of the number of elements per step on compressive strain on top of the subgrade.

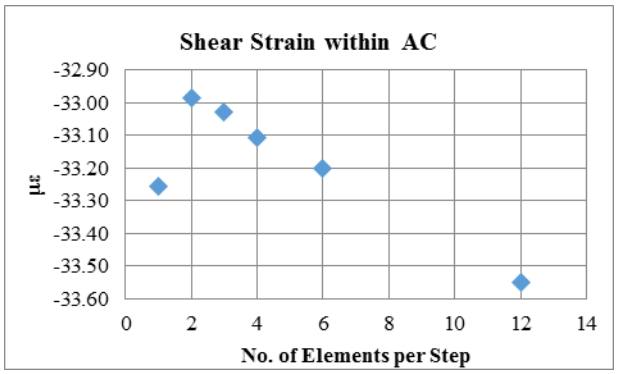

Figure 41. Graph. Effect of the number of elements per step on shear strain within the AC.

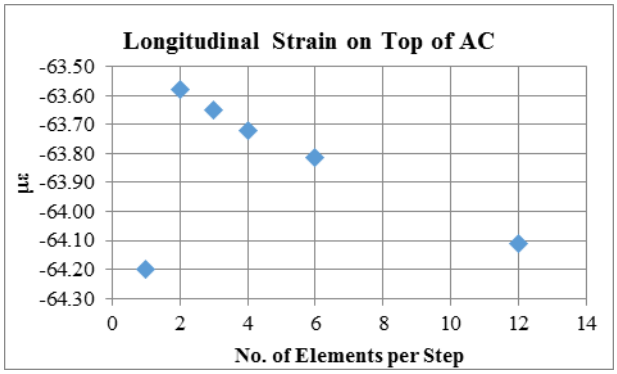

Figure 42. Graph. Effect of the number of elements per step on longitudinal strain on top of AC.

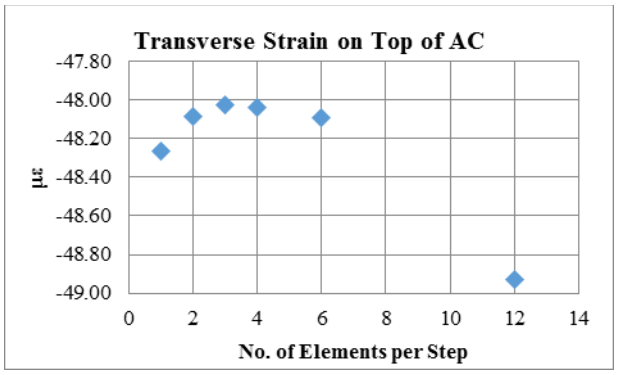

Figure 43. Graph. Effect of the number of elements per step on transverse strain on top of AC.

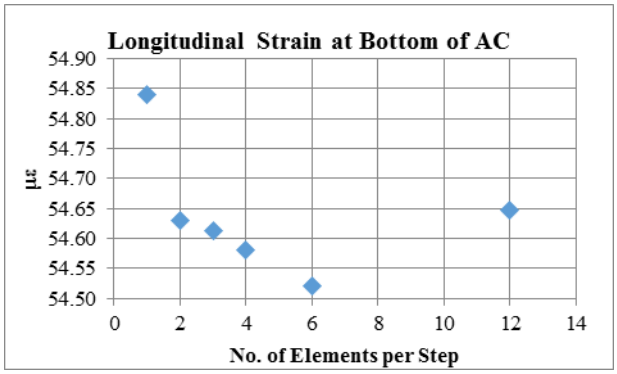

Figure 44. Graph. Effect of the number of elements per step on longitudinal strain at the bottom of AC.

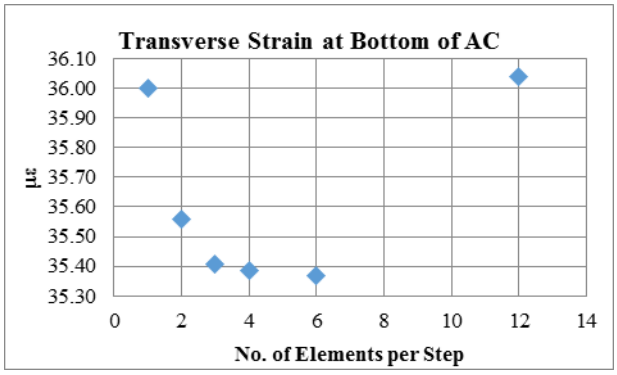

Figure 45. Graph. Effect of the number of elements per step on transverse strain at the bottom of AC.

However, imposing a constant temperature throughout the AC layers inaccurately bounds the problem and can lead to erroneous results. Aside from capturing sensitivity to temperature, it is also pertinent to consider the temperature gradient within the AC layer. In addition, the time of the day significantly impacts pavement temperature. Based on a two-layer system analysis, consisting of AC and granular base, a temperature profile was derived (Wang et al., 2009). An

initial temperature was defined on the surface of the AC layer as the reference temperature. The resulting temperature distribution is a function of the AC layer thickness, initial temperature, thermal conductivity and diffusivity of the AC and granular material, and discrete pavement depths.

SIMULATED PAVEMENT STRUCTURES

The pavement structure factorial consists of two conventional roadway types, low-volume road and interstate highway. The thicknesses vary between two extreme conditions, as the artificial neural network (discussed later) has a robust capability to accurately interpolate within the problem domain. Thickness variations for the two structures are summarized in Table 9.

Table 9. Pavement Structure Factorial

	Low-Volume	Interstate Highway
Wearing Surface	3.0 and 5.0 in*	1.0 and 2.5 in
Intermediate	3.0 and 5.0 in*	1.5 and 4.0 in
Binder	3.0 and 5.0 in*	2.5 and 10.0 in
Granular Base	6.0 and 24.0 in	6.0 and 24.0 in

**Note: Low-volume road cases consider only one AC layer*

MESH VERIFICATION

To achieve an acceptable level of accuracy, the three-dimensional finite element (3-D FE) solution must converge into a continuum model solution and the stress transition across element must be adequately continuous. One measure that may help meet the aforementioned criteria is mesh refinement. Selection of the element thickness at the interface between layers of a pavement system affects the continuity of stresses. Therefore, a robust sensitivity analysis must be carried out.

The first task in the mesh sensitivity analysis is to determine the element size in the tire loading area. It is worth noting that the element size can be analogous to the computational time in the sense that a decrease in element size will generate an increase in computational time. In addition, infinite boundary must be used around the sides and bottom of the 3-D FE model to simulate the stresses and strains dissipating to nearly zero at the boundary.

Vertical Mesh Refinement

It was previously determined that the mesh thickness of the first element, from the top surface of the AC layer, should be 0.4 in or smaller, and that the top element of the subgrade layer must range between 1.2 and 2.0 in. (Al-Qadi et al., 2008).

Although most critical strain results indicate that decrease of the element size leads to more accurate results, throughout the iterations, a plateau value was reached wherein the difference in the strain value from BISAR and FEM model became negligible. Therefore, it was decided that the range of the element size on top of the subgrade should be reduced to 2 in or less for higher accuracy. It was also decided that appropriate transitions between the elements throughout the

remaining layers should be considered; the element thickness from one layer to another should be almost equal. Iterations consist of altering the number of elements and bias until the desired convergence is reached for the "coarsest" mesh. A relatively coarse mesh would limit computational time while maintaining accuracy within acceptable limits.

Longitudinal and Lateral Mesh

Tire-pavement contact area, which initially defined the longitudinal and lateral mesh properties, was extended using mesh sensitivity analysis to ensure that the responses tended to zero on the model boundaries. Based on previous studies, the element length of 0.79 in. along the 39.4-inch wheel path is adequate for the critical strain values to become nil (Yoo & Al-Qadi, 2008). However, the selected wheel path length of 39.4 in was inadequate for capturing a full pulse duration. Two models were generated to investigate the impact of wheel path length on pavement responses, wherein the length varied between 39.4 and 78.7 in. Specifically, the pavement structure was held constant with an AC thickness of 16.2 in and a base of 5.9 in. The load and tire inflation pressure applied were 18 kip and 125 psi, respectively.

The results revealed a shift in the vertical stress as the wheel path increased from 39.4 to 78.7 in. The model with 78.7 in wheel path failed to capture the full pulse duration as the tail of the corresponding curve in Figure 46 did not reach zero, thereby implying that a larger wheel path is needed for this purpose. It is worth noting that the spike near time, t=0, for the vertical compressive stress is induced by the initial impact of loading the model.

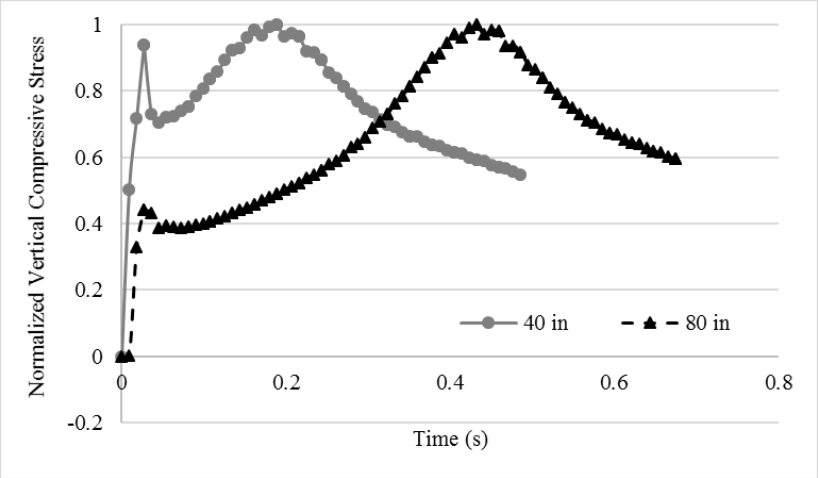

Figure 46. Graph. Pulse duration results for the two varied wheel paths.

However, to simulate full pulse duration, starting from zero and tending back to zero after a peak, significant computational effort was required. For this criteria, increasing the wheel path further than 78.7 in. was not feasible for all simulation cases considered in this study. In addition, because the maximum pavement response values were not significantly affected by the assumed wheel path length of 39.4 in, the FE model was reasonably accurate as the remainder of the analysis would be based on critical/maximum point responses.

As shown in Figure 47, the difference was generally low, except for the shear strain in the base layer, which differed up to 12.6%. Therefore, a wheel path length of 39.4 in was appropriate as it did not adversely impact critical pavement responses, which are required inputs for pavement damage quantification. In terms of pulse duration, the truncated version was used wherein the ascending part only fits the revised haversine equation, and data were extrapolated to a normalized vertical compressive stress of 0.1. Duration of the half pulse was then multiplied by two under the assumed pulse symmetry (Fakhri & Ghanizadeh, 2014).

The lateral meshing was controlled by the width of the rib and groove partition of the specified tire pressure and loading condition. Longitudinal and lateral meshing was further refined by altering the dimensions of the biased elements surrounding the loading area and narrowing the thickness of the element across the depth of the pavement structure.

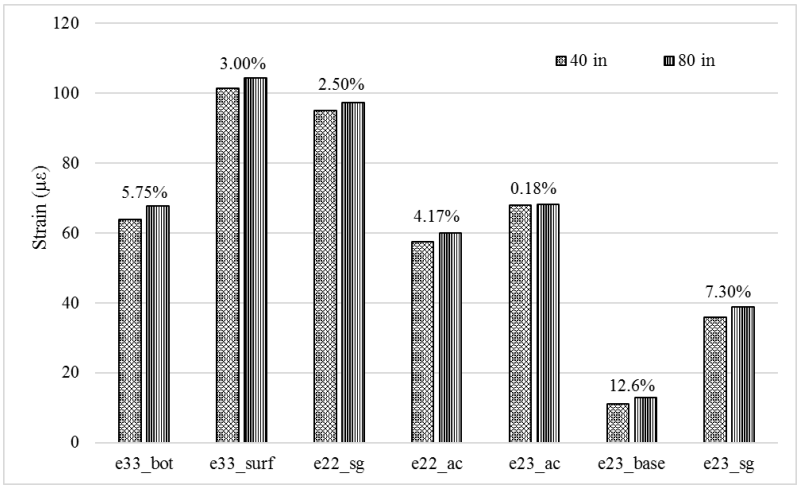

Figure 47. Graph. Pavement response comparison for varying wheel path lengths.

To simulate the characteristics of perpetual interstate roadways, a finite element model with a significantly large domain must be created, but it is computationally inefficient. Therefore, infinite elements, which simulate far-field boundary conditions, were placed on the vertical external sections and the bottom of the subgrade. Proper transitions from the finite section of the model to the infinite elements were also implemented.

Following a multitude of iterations, it was determined that reduction of the elements with bias in both longitudinal and lateral directions would be appropriate to create a smooth transition to the infinite boundary, while still maintaining accuracy and reducing computational time (Figure 48). There were two transition zones from the loading area. The first transition included biased elements in the longitudinal and transverse directions, with lengths *L*1 and *B1*, respectively. The second transition area consisted of a single finite element around the model in the longitudinal and transverse directions, which were defined as *L2* and *B2* lengths, respectively, and were placed adjacent to the infinite boundary. The transitional area reduced the required finite elements as the bias imposed larger sized elements towards the infinite boundary.

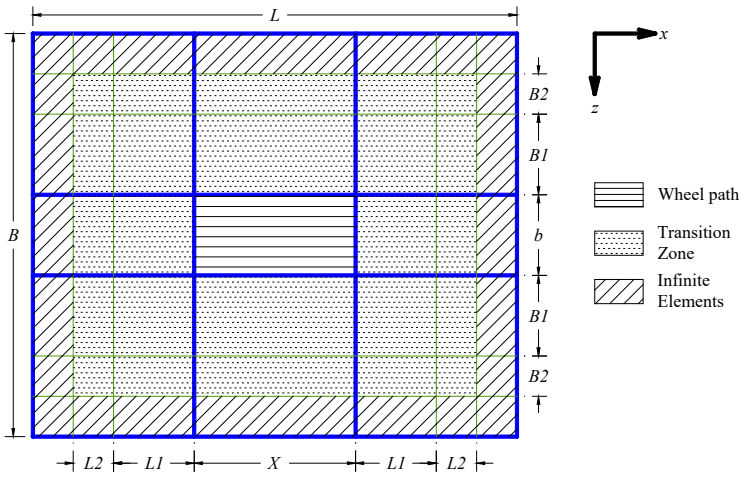

Figure 48. Illustration. Mesh definition in plan view.

Verification of the Constructed Mesh Combination

Based on the continuum model theory, vertical stresses should be continuous between pavement layers. Computational time and data storage space requirements should be considered, provided that the results stay within acceptable bounds of accuracy. As the element size within the domain decreased, computational time and data storage space increased. To evaluate accuracy of the results, the FE model with varying mesh element thicknesses throughout different pavement layers was compared with the results obtained from BISAR, which is based on the multilayer elastic theory that uses an axisymmetric model. The two approaches followed the same vehicular loading, material properties, and pavement structure.

The comparison was simplified with a static and uniform load over a circular contact patch and linearly elastic material to minimize possible computational errors. In order for the FE model to be directly comparable to BISAR, layer interactions were tied to preserve continuity between layers for convergence purposes. The results of the statically linear elastic case showed negligible errors, thus indicating that the constructed meshing combination is appropriate.

BISAR is considered inadequate for simulating the cross-anisotropic behavior of granular layers, continuous moving load, and realistic interfacial friction properties between pavement layers. In BISAR, the response locations must be determined a priori to running the analysis, whereas the FE model is capable of simulating the analysis and responses throughout the entire model without being pre-defined.

The goal was to reach a level of accuracy of 5% or better. Using BISAR solution as reference, the pavement responses of the two methods were compared at the same location. Being the main inputs in the transfer functions for pavement damage evaluation, critical strains were investigated. The vertical and longitudinal mesh parameters were altered at each iteration until the relative comparison of strain values met the defined level of accuracy.

To compare the results obtained from the FE software, ABAQUS, and BISAR, an axisymmetric model was implemented in ABAQUS. The final mesh was then transformed into the 3-D domain and a similar check was done. The results are presented in Table 10 through Table 13. Generally, the percentage of difference was less than 5%. The final mesh configuration (i.e., layer thickness, number of elements, and bias) for the interstate and low-volume pavement structures are presented in Table 14 and Table 15.

Table 10. Comparison of Results from BISAR and ABAQUS Simulations for Interstate Highway Pavements and AC=5 in

	ABAQUS *B*=6 in	BISAR *B*=6 in	Diff. (%) *B*=6 in	ABAQUS *B*=24 in	BISAR *B*=24 in	Diff. (%) *B*=24 in
Tensile strain at bottom of AC (με)	65.6	68.1	3.7	61.1	63.8	4.2
Vertical strain top of subgrade (με)	300.0	295.5	1.5	157.4	159.7	1.4
Shear in AC (με)	19.4	19.2	1.0	19.8	19.4	1.8
Shear in base (με)	73.3	70.0	4.7	74.9	74.7	0.3
Shear in subgrade (με)	83.2	88.2	5.7	53.7	56.6	5.1

Table 11. Comparison of Results from BISAR and ABAQUS Simulations for Interstate Highway Pavements and AC=16.2 in

	ABAQUS *B*=6 in	BISAR *B*=6 in	Diff. (%) *B*=6 in	ABAQUS *B*=24 in	BISAR *B*=24 in	Diff. (%) *B*=24 in
Tensile strain at bottom of AC (με)	9.9	9.4	5.2	9.1	9.7	6.3
Vertical strain top of subgrade (με)	36.0	36.1	0.3	27.9	27.8	0.3
Shear in AC (με)	7.3	7.6	4.0	7.6	7.3	4.2
Shear in base (με)	6.8	6.6	3.3	7.9	8.0	1.3
Shear in subgrade (με)	8.5	8.1	5.0	7.8	8.2	4.8

PAVEMENT RESPONSE

The numerical model produces a database of stresses and strains at any location within the problem domain. However, the essential output values were the maximum and minimum strains at each layer, vertical compressive pressure at every layer, and von Mises stress within the AC layer. Within this subdomain, the critical responses include the following:

- Tensile strain at the surface of AC for near-surface cracking
- Tensile strain at the bottom of the AC for bottom-up cracking
- Compressive strain for rutting (AC and granular layers)
- Shear strain within the AC layer

Table 12. Comparison of Results from BISAR and ABAQUS Simulations for Low-Volume Roads and AC=3 in

	ABAQUS *B*=6 in	BISAR *B* 6 in	Diff. (%) *B*=6 in	ABAQUS *B*=24 in	BISAR *B*=24 in	Diff. (%) *B*=24 in
Tensile strain at bottom of AC (με)	126.5	133.8	5.5	105.4	111.3	5.3
Vertical strain at top of subgrade (με)	817.9	836.8	2.3	354.6	364.4	2.7
Shear in AC (με)	27.0	27.4	1.4	25.5	26.1	2.3
Shear in base (με)	193.0	190.4	1.4	179.1	170.7	4.9
Shear in subgrade (με)	269.9	276.6	2.4	128.7	135.1	4.8

Table 13. Comparison of Results from BISAR and ABAQUS Simulations for Low-Volume Roads and AC=5 in

	B=6 in			*B*=24 in		
	ABAQUS	BISAR	Diff. (%)	ABAQUS	BISAR	Diff. (%)
Tensile strain at bottom of AC (με)	63.9	67.2	4.9	56.6	59.5	4.9
Vertical strain at top of subgrade (με)	341.0	348.9	2.3	206.5	212.6	2.9
Shear at AC (με)	17.0	17.0	0.2	16.4	16.5	0.7
Shear at base (με)	68.4	67.9	0.8	75.2	73.0	3.0
Shear at subgrade (με)	101.6	103.9	2.2	70.6	75.8	6.9

Table 14. Interstate Highway Mesh Configuration

	AC=5 in, *B*=6 in	*AC*=5 in, *B*=24 in	*AC*=16.2 in, *B*=6 in	*AC*=16.2 in, *B*=24 in
Wearing course (in)	1.0	1.0	2.5	2.5
Intermediate course (in)	1.5	1.5	4.0	4.0
Binder course	2.5	2.5	10.0	10.0
Base (in)	6.0	24.0	6.0	24.0
Subgrade (in)	167	149	155	137
Wearing course (# elements @ bias)	4 @ 1	4 @ 1.1	5 @ 1.2	5 @ 1.2
Intermediate course (# elements @ bias)	5 @ 1.2	5 @ 1.0	6 @ 1.4	6 @ 1.4
Binder course (# elements @ bias)	7 @ 1.15	7 @ 1.2	12 @ 1.0	9 @ 1.0
Base (# elements @ bias)	12 @ 1.5	25 @ 1.0	7 @ 1.0	22 @ 1.0
Subgrade (# elements @ bias)	15 @ 75.0	15 @ 30.0	15 @ 30.0	15 @ 25.0

Table 15. Low-Volume Road Mesh Configuration

	AC=3 in, B=6in	AC=3 in, B=24 in	AC=5 in, B=6 in	AC=5 in, B=24 in
Surface (in)	3.0	3.0	5.0	5.0
Base (in)	6.0	24.0	24.0	24.0
Subgrade (in)	168	151	166	149
Surface (# elements @ bias)	12 @ 1.0	12 @ 1.0	15 @ 1.2	15 @ 1.2
Base (# elements @ bias)	12 @ 1.7	25 @ 1.3	12 @ 1.7	25 @ 1.0
Subgrade (# elements @ bias)	15 @ 70.0	15 @ 30.0	15 @ 50.0	15 @ 30.0

Thick Pavement Damping

After simulations for the thick pavement were completed, it was determined that appropriate damping parameters were not adequately applied to the thick pavement model. This section explains the correction process.

To account for damping and mass inertia effect, damping properties must be defined for all pavement layers in the finite element model. The sources of damping could be an arbitrary damping factor, friction factor, or viscoelastic material behavior. Given that the asphalt layers are characterized by viscoelasticity, the structural damping is appropriately accounted for. However, the granular layers are defined with elastic moduli values, which does not consider dissipation.

Using the Rayleigh damping model in ABAQUS, energy dissipation can be considered for the elastic granular base and subgrade layers. Two damping coefficients are required for the Rayleigh model, α_d and β_d, which are dependent on a proper damping ratio. Based on Wang (2011), the critical damping ratio for soils range from 2% to 5%. For this study, 5% is used. In addition, the typical natural frequency of 62.8 rad/sec (10Hz) is assumed.

Given the aforementioned parameters, α_d=3.1416 and β_d=7.95×10^{-4} were selected. However, the thick pavement cases were run using 0.02 and 0.06. For the same damping ratio of 5%, this corresponds to 0.695 rad/sec, a significantly low natural frequency. The difference in Rayleigh damping coefficients result in inaccurate material property representation. In addition, these parameters are not held constant for thin and thick pavements, so a direct comparison between the two cannot be conducted appropriately. Due to the fact that the relationship between damping influence and pavement layer thickness is inversely proportional, the simulation case selected as an initial check includes a combination of lowest pavement layer thicknesses, highest applied load, tire inflation pressure, and weak material properties from the thick pavement matrix.

The load case considered the applied load of 18 kip and the tire inflation pressure of 125 psi. The selected structure had layer thicknesses of 5 in and 6 in, for the total AC and granular base layers, respectively. Material characterizations were assumed weak for both AC and base layers. Table 16 shows that the difference between the baseline and corrected values ranged from 2.2% to 8.6%, wherein the maximum stemmed from the shear strain values of the granular base layers.

It was also considered that 5% variation for the horizontal strain in the AC layers, connected to fatigue distresses, can have a significant impact, especially when considering the number of loading repetitions.

Table 16. Difference in Responses Using Correct Damping Parameters

Pavement Response	Corrected	Base	Diff. (%)
Long strain, surface of AC	372.7	352.9	5.3
Trans strain, surface of AC	332.4	320.8	3.5
Long strain, bottom of AC	321.5	305.4	5.0
Trans strain, bottom of AC	318.1	307.8	3.2
Vertical strain, AC	324.2	311.4	3.9
Vertical strain, base	795.9	778.4	2.2
Vertical strain, subgrade	975.4	949.9	2.6
Shear strain, AC	145.9	142.5	2.3
Shear strain, Base	242.1	221.4	8.6
Shear strain, subgrade	288.7	277.7	3.8
Mises stress, AC	4.1	4.0	2.4

However, due to the fact that the impact of damping decreases as pavement thickness increases, it was deemed appropriate to perform a repetition of the extreme cases to adequately cover the scope of the thick simulation matrix. From this approach, 24 cases were rerun. The factorial included:

- Two pavement structures: *AC*=5 in and *B*=6 in; and *AC*=16.2 in and *B*=24 in
- Two material properties: weak and strong for both AC and base layers
- Six loading conditions: *L1, L5, L4, L9, L11*, and *L12* (Table 23)

Figure 49 through Figure 59 illustrate the relationship between the baseline and corrected cases for all critical pavement responses. The terms in the title of each figure are defined in Chapter 5.

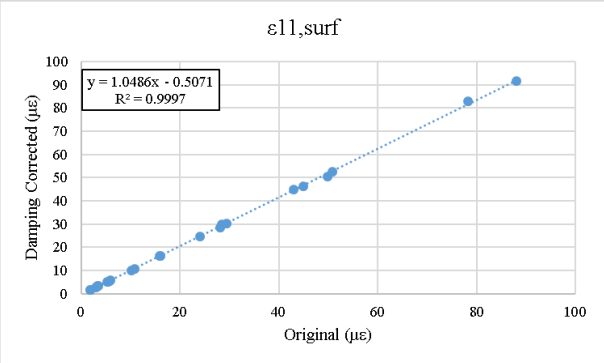

Figure 49. Graph. Longitudinal strains at the AC surface.

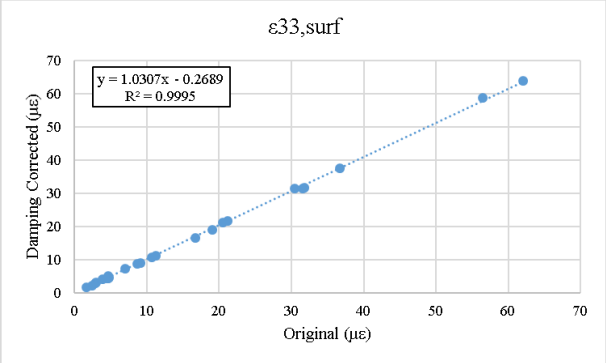

Figure 50. Graph. Transverse strains at the AC surface.

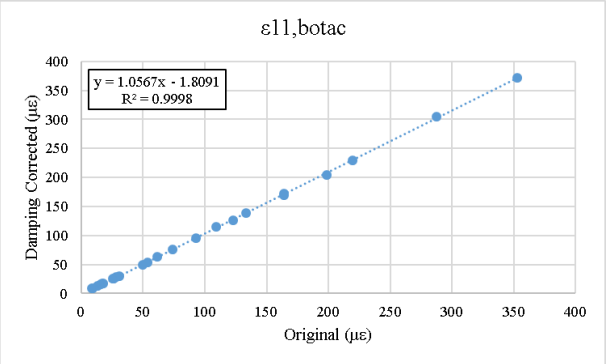

Figure 51. Graph. Longitudinal strains at the bottom of the AC.

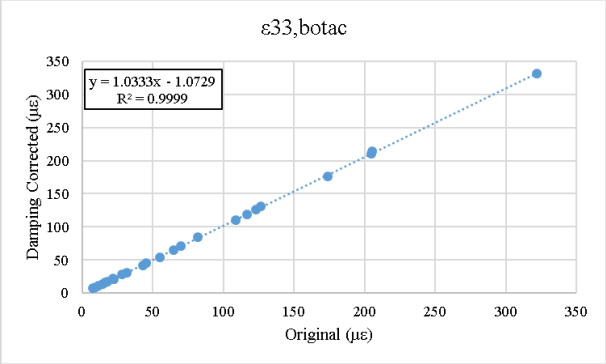

Figure 52. Graph. Transverse strains at the bottom of the AC.

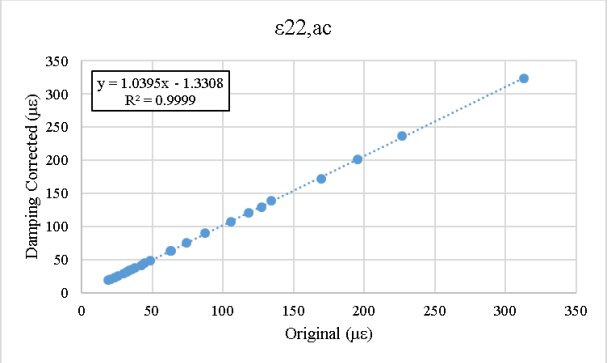

Figure 53. Graph. Vertical compressive strain within the AC.

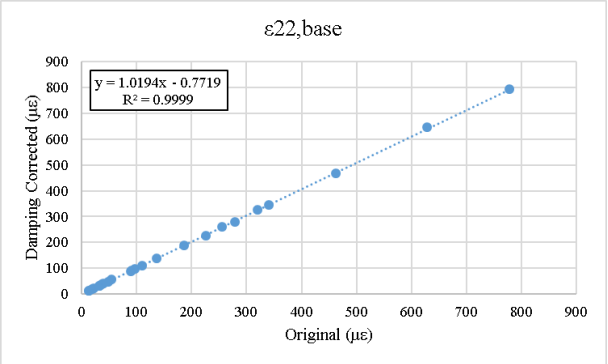

Figure 54. Graph. Vertical compressive strain within base.

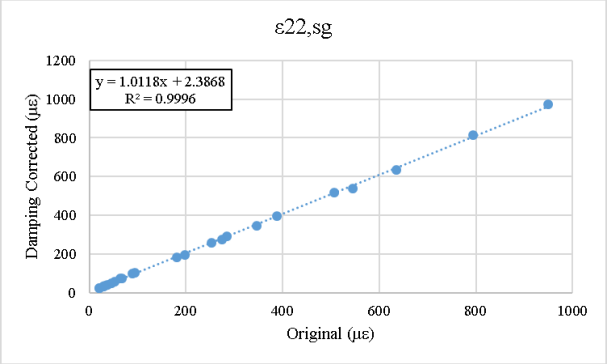

Figure 55. Graph. Vertical compressive strain within the subgrade.

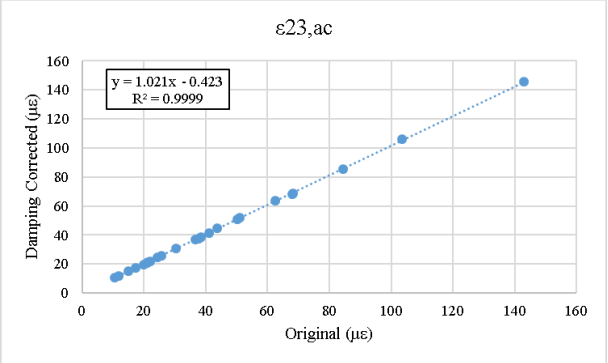

Figure 56. Graph. Shear strain in the AC.

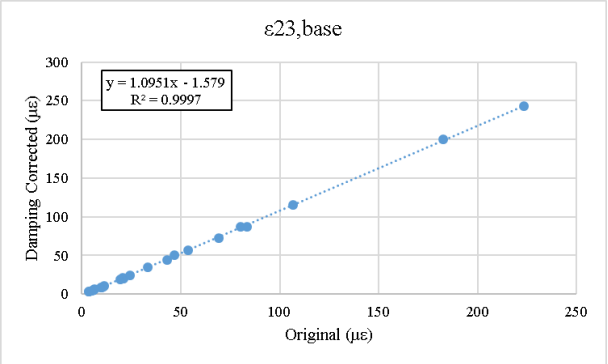

Figure 57. Graph. Shear strain in the base.

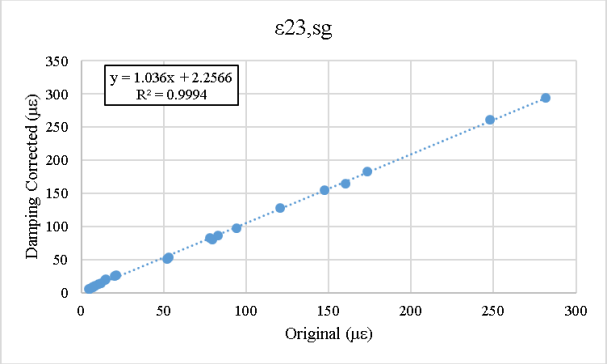

Figure 58. Graph. Shear strain in the subgrade.

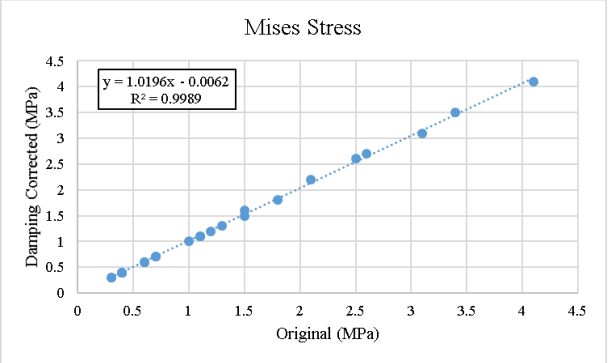

Figure 59. Graph. Mises stress in the AC layer.

Based on the plots comparing baseline values to the same cases with corrected damping parameters, a linear relationship can be observed. For the rerun cases, all pavement responses were underestimated ranging from 1.2% to 9.5%, as indicated in Table 17. Therefore, the slopes can be treated as damping adjustment factors for all critical responses. The finite element model represented the granular materials more accurately when these factors were applied on the remainder of the database, and a direct comparison between the thin and thick cases could thus be appropriately performed.

Table 17. Damping Adjustment Factors (Slope and RMSE) for Critical Pavement Responses

Response	Slope	RMSE
Long strain, surface of AC	1.049	0.687
Trans strain, surface of AC	1.031	0.459
Long strain, bottom of AC	1.057	2.221
Trans strain, bottom of AC	1.033	1.413
Vertical strain, AC	1.039	1.607
Vertical strain, base	1.019	2.365
Vertical strain, subgrade	1.012	5.882
Shear strain, AC	1.021	0.541
Shear strain, base	1.095	1.906
Shear strain, subgrade	1.036	2.991
Mises stress, AC	1.020	0.036

VALIDATION OF THE FINITE ELEMENT MODEL

After developing the 3-D FE pavement model, the model was validated against results of accelerated pavement testing that were conducted on a number of pavement sections built in participant states. Details about the sections and FE validations are given below.

Thin Section at Illinois Center for Transportation

FEM was validated for a thin section that was built at the Illinois Center for Transportation testing facility, the Advanced Transportation Research and Engineering Laboratory (ATREL). Nine thin pavement sections were constructed and heavily instrumented. A section with 5 in of AC layer and 12 in of base layer was used. Loading conditions were 8 kips tire load and 100 psi tire inflation pressure for DTA. Two pressure cells were installed at the bottom of the base. Data were collected for four runs. The eight pressure measurements are given in Table 18.

Table 18. Field Pressure Measurements at the bottom of the Base

Pressure Cell 1 (psi)	Pressure Cell 2 (psi)
1.53	2.10
2.00	2.33
2.31	2.16
2.83	2.5

The mean of these eight field vertical pressure measurements was 2.2 psi with a standard deviation of 0.38 psi. On the other hand, the FEM model predicted the vertical pressure as 2.44 psi at the bottom of base. FEM provided accurate approximation for vertical pressure at the bottom of the base layer. The transverse strain at the bottom of AC was also used for validation. There were four strain measurements for this section because one strain gauge was installed (1x4 pass), as shown in Table 19.

Table 19. Field Strain Measurements at the bottom of the AC

Transverse Strain (με)
68.6
59.4
76.3
79.3

The means of the four field transverse strain measurements were calculated as 70.9 με with 8.9 με standard deviation. FEM resulted in 53.3 με. This variation could be attributed to the bending of the strain gauge in the field as a result of loading thin AC layer and because the strain gauge was supported by a weak platform.

Thick Section at the Virginia Smart Road

Section B of the Virginia Smart Road project was used to validate the finite element model of thick pavement. This section is considered as a thick section and has the input parameters in Table 20 (Al-Qadi et al., 2008).

Table 20. Smart Road Pavement Input Parameters

Layer	Thickness (in)	Instantaneous Modulus (ksi)	Poisson's Ratio	Density (lb/ft^3)	Rayleigh Damping Parameters (α)	Rayleigh Damping Parameters (β)
SMA-9.5*	1.5	613.5	0.2	143.3	N/A	N/A
BM-25*	6.0	689.0	0.2	143.3	N/A	N/A
OGDL*	3.0	350.3	0.3	130.8	0.107	0.015
CTB*	6.0	1500.0	0.2	124.6	0.024	0.0015
Subbase	7.0	450.0	0.35	93.4	0.02	0.06
Subgrade	-	38.0	0.35	93.4	0.02	0.06

**Note: SM-9.5: AC Surface Mix with NMAS of 9.5mm, BM-25: AC Base Mix with NMAS of 25mm, OGDL: Open-Graded Drainage Layer, and CTB: Cement-Treated Base*

The top two layers, SM-9.5 and BM-25, were characterized as viscoelastic and defined using the Prony series from Table 21 Al-Qadi et al. (2008) shifted the Prony series to 77 °F and therefore the William-Landel-Ferry coefficients were omitted. In this scenario, the two layers are assumed to be subjected to uniform temperature condition of 77 °F. In addition, the optimized mesh for the corresponding section resulted in the configuration presented in Table 22.

Table 21. Viscoelastic Material Characterization of SM-9.5 and BM-25

i	G_i (SM-9.5)	K_i (SM-9.5)	τi (SM-9.5)	G_i (BM-25)	K_i (BM-25)	τi (BM-25)
1	7.7465×10^{-1}	7.7471×10^{-1}	1.00×10^{-2}	6.49899×10^{-1}	6.49562×10^{-1}	1.00×10^{-2}
2	1.6498×10^{-1}	1.6493×10^{-1}	1.00×10^{-1}	2.24921×10^{-1}	2.25154×10^{-1}	1.00×10^{-1}
3	3.9793×10^{-2}	3.9752×10^{-2}	1.00	8.51861×10^{-2}	8.53679×10^{-2}	1.00
4	1.3829×10^{-2}	1.3822×10^{-2}	1.00×10^{1}	2.46542×10^{-2}	2.46481×10^{-2}	1.00×10^{1}
5	2.7364×10^{-3}	2.7285×10^{-3}	1.00×10^{2}	1.07095×10^{-2}	1.07301×10^{-2}	1.00×10^{2}
6	1.7106×10^{-3}	1.7133×10^{-3}	1.00×10^{3}	1.79179×10^{-3}	1.79305×10^{-3}	1.00×10^{3}
7	2.0405×10^{-3}	2.0364×10^{-3}	1.00×10^{4}	7.27802×10^{-4}	7.27326×10^{-4}	1.00×10^{4}
8	1.6524×10^{-5}	1.6487×10^{-5}	1.00×10^{5}	-	-	-
9	6.8306×10^{-6}	6.9430×10^{-6}	1.00×10^{6}	-	-	-

Moreover, the loading condition was defined with a half-axle load of 7.8 kip and 105 psi for the DTA 275/80R22.5. The contact stresses used in the model were based on previous experimental measurements and the same input definition (details in Chapter 3) was applied. Given the input parameters, three critical responses were extracted from the FE model and compared with field data, as shown in Table 21. Based on the resulting difference, the vertical pressure on top of the subgrade and the transversal and longitudinal strain underneath the AC layers varied by 2.36%, 12.06%, and 2.14 %, respectively. This exercise ensures that the models used in this study to evaluate the impact of NG-WBT are representative of field conditions and are suitable for completing the selected analysis matrix.

Table 22. Section B Mesh Details

	Length (in)	252.7
	Width (in)	219.3
	Depth (in)	177.1
	L1=B1 (in)	70.9
	L2=B2 (in)	12.0
SM-9.5	No. of Elements	4
SM-9.5	Bias	1.20
BM-25	No. of Elements	12
BM-25	Bias	1.20
OGDL	No. of Elements	5
OGDL	Bias	1.00
CTB	No. of Elements	10
CTB	Bias	1.00
Subbase	No. of Elements	10
Subbase	Bias	1.30
Subgrade	No. of Elements	18
Subgrade	Bias	35.00
L1=B1	No. of Elements	18
L1=B1	Bias	18.0
L2=B2	No. of Elements	1
L2=B2	Bias	1.0

Table 23. Comparison of Simulation Results and Field Measurements

Depth (in)	Location Definition	Pavement Response	Simulation Results	Field Measurement	Difference (%)
23.0	Top of subgrade	Vertical Pressure (psi)	5.28	5.42	2.36
7.5	Bottom of AC (BM-25)	Transversal Strain (με)	103.8	92.6	12.06
7.5	Bottom of AC (BM-25)	Longitudinal Strain (με)	116.1	118.6	2.14

Thin Section at Florida

Results of the Accelerated Pavement Test conducted at the Florida Department of Transportation (FDOT) were used to validate FEM pavement model. A Test Pit section with 3 in of AC, 10.5 in of limerock base and 12 in of subbase was selected for the validation. The load condition was 80 psi tire inflation pressure with 6 kips tire load for DTA.

Four pressure cells were installed in this section, two of which are located at the bottom of AC and the other two at the bottom of the base layer. While the average pressure was measured as 24.5 psi at the bottom of AC, it was 4.5 psi at the bottom of the base layer. FEM computed those stresses as 24.2 psi and 3.8 psi. Six strain gauges were installed at the bottom of the AC layer, three in the traffic direction and three in the transverse direction. The average tensile strain was measured as 21.1 and 98.0 με for transverse and traffic directions, respectively. On the other hand, FEM predicted these strains at 18.5 and 43.0 με.

FEM results are in general similar in the case of vertical pressures and tensile strains in the transverse direction. However, the prediction of the strain in traffic direction was off by a factor of 2. The base material is characterized as stress-dependent nonlinear material. However, since the resilient modulus test was only conducted using vertical load, it was not possible to obtain nonlinear material characterization parameters for all three dimensions. Therefore, the base material was assumed isotropic; this resulted into underestimation of the tensile strains in the traffic direction.

Thin Section at UC-Davis

Another section used for FEM validation was built at the University of California Pavement Research Center facility in Davis, California. Section 671HC was selected for FEM validation. This section has two AC layers, each at 2.4 in-thick. While the top layer is warm-mix asphalt, the bottom later is AC. Underneath the two AC layers are recycled base and subbase layers with 9.8 and 10.6 in layer thicknesses, respectively.

Four pressure cells were installed in this section, two of them are located at the top of the recycled base layer and the other two at the bottom of the recycled base layer. While the average pressure was measured as 12.3 psi at the top of the base layer, it was 5.8 psi at the bottom of base layer. FEM computed those stresses as 8.6 psi and 4.5 psi. There was a total of eight strain gauges installed in this section. Four of them were placed at the bottom of the top AC layer as two strain gauges are oriented for each direction (traffic and transverse directions). The other four strain gauges are located at the bottom AC layer in a same way. The transverse strains at the bottom of top and bottom AC layers measured 59.2 and 11.57 με, respectively. On the other hand, FEM predicts those strains as 4.3 and 16.9 με.

FEM prediction for vertical pressure at the top and bottom of the base layer was much lower than field responses, which appear to be high. The base material was characterized as linear elastic material due to the lack of resilient modulus data. As reported in the literature (Kim et al., 2009), linear elastic characterization of base results in stiffer behavior in pavement simulation. The effect gets even more significant for the pavement with thinner AC layer as in this section. In addition, the stain gauge measurements are dependent on installation and type of the strain gauge used.

Thick Section at Ohio

The last validation of the developed FEM was done on a thick driving mainline section in Ohio. This section has a total of six layers including subgrade: 1 in of fine graded polymer AC, 2 in of AC intermediate course, 8 in of AC base, 4 in of fatigue resistant base layer, 6 in of aggregate base. The load case selected was DTA with axle load of 10 kip and tire pressure of 110 psi.

The AC was characterized by the Prony series, which were derived from the complex modulus test. However, the information provided for base material characterization was not sufficient for obtaining the model parameters needed by a nonlinear cross-anisotropic model. The elastic modulus values were assumed to be 74.4 ksi and 111 ksi for base and subgrade, respectively.

These values were reported by Xue and Weaver (2011). Despite the differences that might exist between these sections, it was considered an appropriate approximation.

A total of four pressure cells were installed in the section, two were located at the bottom of the fatigue-resistant base layer and the other two cells were installed at the bottom of the aggregate base layer. The average vertical pressure measurement for these two locations is 7.0 psi and 4.5 psi. The FEM approximation for these responses is 8.4 psi and 7.3 psi, respectively.

Additionally, transverse strain measurements were used to validate the FEM. Transverse strains were measured at three different locations: bottom of AC layer, bottom of AC base, and bottom of fatigue-resistant base layer. There were 300 measurements for transverse strain at the bottom of AC showing great variability. The measurements varied between 50 με and 350 με with an average of 173 με and a standard deviation of 76 με. The FEM predicted this strain at 40.2 με. The measured transverse strains at the bottom of the AC base and fatigue resistant layers were 46 με and 123 με, respectively. FEM's predictions, on the other hand, were 27 and 15 με. High discrepancy between the measurement and FEM results was alluded to the unavailability of data for the base and subgrade material characterizations.

SUMMARY

In order to perform accurate FE simulations of the loaded pavement, an adequate numerical model must be generated. Based on the assumptions made in this study with regard to model geometry, material characterization, temperature profile, layer interaction, and boundary conditions, the FE models used in this study are considered appropriate. Model accuracy was further supported by the validation phase of various field test sections across the U.S., wherein sample critical responses compared relatively well to measured field responses, except for the sections that were lacking some material characteristics data.

CHAPTER 5. EFFECT OF TIRE CONFIGURATION ON PAVEMENT RESPONSE

The FE analysis matrix included pavement structure (thin and thick pavements), thickness of pavement layers (see Table 9), material properties, and 12 loading conditions for a total of 576 cases. The loading conditions consisted of very high and low loads (6 and 18 kip) and tire inflation pressure (80 and 125 psi) for developing the artificial neural network model. A loading case with *P*=10 kip and *S*=110 psi was included to evaluate the pavement responses at normal loading conditions. Finally, two loading cases with differential tire inflation pressure were added to the loading matrix. Table 24 shows the 12 loading cases, type of tire, applied load, tire inflation pressure, and the resultant. The resultant was obtained as the reaction force of the measured vertical contact stresses/forces.

Table 24. Loading Cases Used in Finite Element Analysis

Loading Case	Tire	*P* (kip)	*S* (psi)	Resultant (kip)
L1	NG-WBT	6.0	80	5.5
L2	NG-WBT	6.0	125	6.0
L3	NG-WBT	18.0	80	17.8
L4	NG-WBT	18.0	125	17.8
L5	DTA	6.0	80	5.8
L6	DTA	6.0	125	5.7
L7	DTA	6.0	80/110	5.9
L8	DTA	18.0	80	17.5
L9	DTA	18.0	125	17.4
L10	DTA	18.0	80/110	17.2
L11	NG-WBT	10.0	110	9.8
L12	DTA	10.0	110	8.8

The studied pavement responses are linked to various pavement distresses. The tensile surface strain in the longitudinal $(\varepsilon_{11,surf})$ and transverse $(\varepsilon_{33,surf})$ direction is associated with near-surface cracking. In addition, the tensile strain at the bottom of the AC in the longitudinal $(\varepsilon_{11,AC})$ and transverse $(\varepsilon_{11,AC})$ direction relates to the pavement's fatigue life (bottom-up fatigue cracking). Permanen was included, even though it is not formally related to any pavement distress in the Mechanistic-Empirical Pavement Design Guide (MEPDG) AASHTOWare procedure.

The effect of pavement structure, layer thickness, material properties, and type of tire on critical pavement responses was studied. Under the same loading condition and layer thicknesses, the change in critical pavement responses with various material properties was plotted, as shown in Figure 60 for the Mises stresses. In this figure, the horizontal axis represent the various material properties (*W*=weak and *S* =strong), with the top letter corresponding to the AC, the middle to the base, and the bottom one to the subgrade. The values considered an adjustment caused by the small difference between the applied load and the resultant (compared columns 3 and 5 in Table

23). Similar drawings were prepared for each one of the 576 analysis cases, and a sample of the results are provided in Appendices B and C.

Box plot were used to have a global assessment of the difference between NG-WBT and DTA (Figure 61). For each pavement response under a fixed loading case, the percentage difference was calculated using DTA as reference. The box plot shows the first and third quartile along with the median of the percentage difference. In addition, the disparity between the maximum and minimum difference with the third and first quartiles, respectively, are shown. For instance, in the case shown in Figure 61, there are more values with difference less than the median, with a minimum difference of 15.8% and a maximum difference of 45.6%. In addition, the mean and the median are close to one another (34.0% vs. 34.8%).

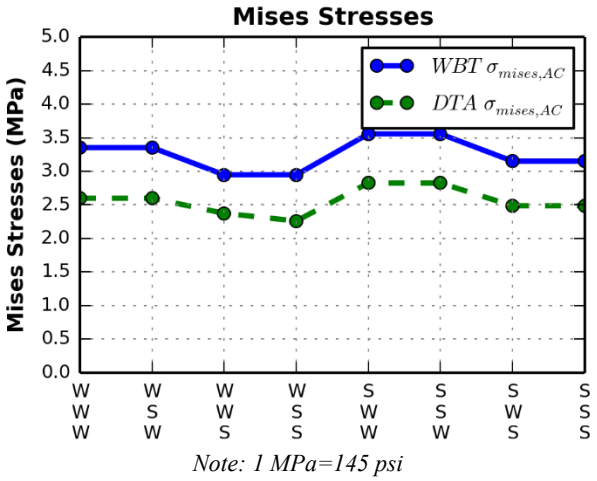

Figure 60. Graph. Variation of Mises stresses in thin pavement for *AC*=5 in, *B*=6 in, *P*=10 kip, and *S*=110 psi (L11 and L12).

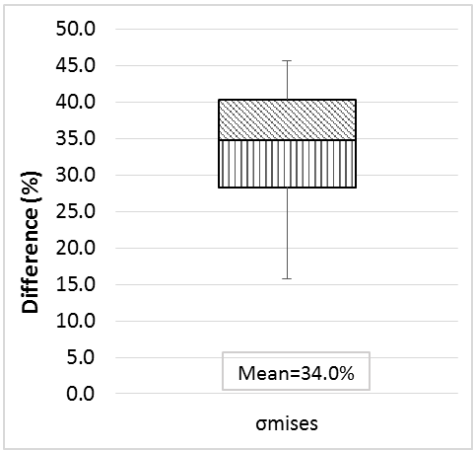

Figure 61. Graph. Box chart for the Variation of Mises stresses in thin pavement for *AC*=5 in, *B*=6 in, *P*=10 kip, and *S*=110 psi (L11 and L12).

THIN PAVEMENT STRUCTURES

Longitudinal and Transverse Strains at the Surface and Bottom of the AC

Figure 62 and Figure 63 show the variation of the longitudinal and tensile strains on the surface and at the bottom of the AC for NG-WBT and DTA. This figure corresponds to *P*=10 kip and *S*=110 psi. The magnitude of the surface strain did not significantly change between weak and strong base when its thickness was 6 in; however, when the base thickness was 24 in, the only material significantly affecting the surface strain was the AC layer. The effect of tire inflation pressure on surface strain was not important for almost any combination of the considered variables, but the effect of applied load was clear.

The tensile strain at the bottom of the AC, in both the longitudinal and transverse directions, was higher for NG-WBT than DTA. The $\varepsilon_{33,AC}$ for NG-WBT was also higher than $\varepsilon_{11,AC}$ and $\varepsilon_{33,AC}$ for DTA. The tire inflation pressure had more influence on $\varepsilon_{33,AC}$ than on $\varepsilon_{11,AC}$ for both tires, but again, load was the most relevant factor. For the thickest layers (*AC*=5 in and *B*=24 in), the only parameter affecting the tensile strain at the bottom of the AC was the AC material, but this behavior changed as the thickness of AC and base changed.

Figure 64 summarizes the behavior of the percentage difference between NG-WBT and DTA for the longitudinal and transverse tensile strains at the pavement surface and at the bottom of the AC. For $(\varepsilon_{33,surf})$, a reduction in the difference was observed as the AC thickness increases. If the AC thickness was 5 in, the difference tended to be higher for the weak AC; however, if *AC*=3 in the difference was not as sensitive.

The fact that the tensile strain at the bottom of the AC was not greatly affected by tire inflation pressure translated into relatively constant difference between both tires as the inflation pressure changed. The highest discrepancy between both tires for $\varepsilon_{11,AC}$ was observed at loads of small magnitude. In addition, the impact of the tire type on $\varepsilon_{11,AC}$ did not depend on the material property of any layer. On the other hand, $\varepsilon_{33,AC}$ showed the highest average difference among all the pavement responses, 49.3%, ranging between 33.8 and 67.7%. The information in Figure 64 also allows to conclude that: i) the tensile strain at the surface of the AC had a smaller range of values; ii) for $(\varepsilon_{33,surf})$, more values above the mean than below; and iii) the average difference in the longitudinal strain at the bottom of the AC, which was consistently higher than the transverse strain, was 20.5%.

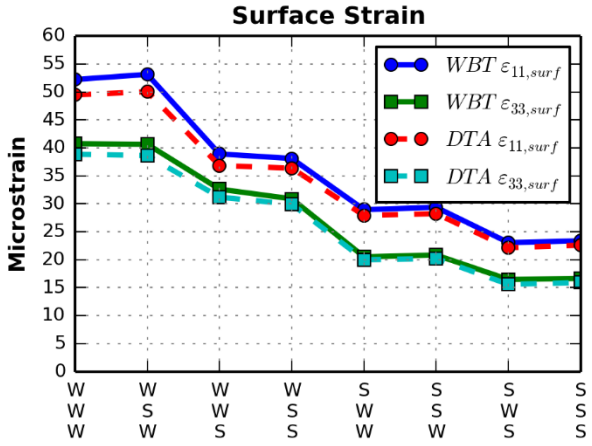

Figure 62. Graph. Longitudinal and transverse strains at the pavement surface for *AC*=5 in, *B*=6 in, *P*=10 kip, and *S*=110 psi.

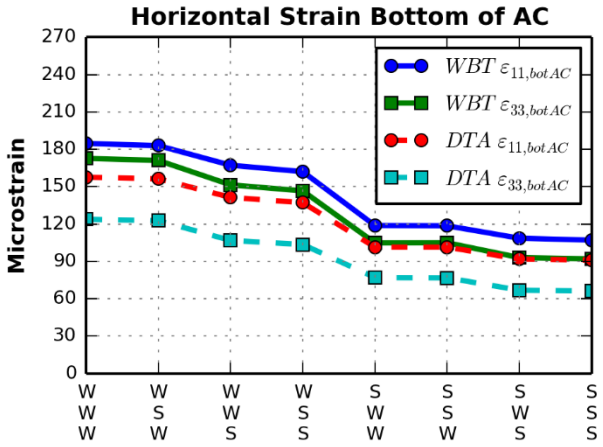

Figure 63. Graph. Longitudinal and transverse strains at the bottom of AC for *AC*=5 in, *B*=6 in, *P*=10 kip, and *S*=110 psi.

Shear Strain in the AC, Base, and Subgrade

Figure 65 shows the same variation as in Figure 62 and Figure 63; but for the vertical shear strain in each layer. The tire inflation pressure slightly affected the vertical shear strain in the pavement layers for NG-WBT more than for DTA, and this effect was more noticeable in the subgrade and base. Conversely, the effect of *S* on $\varepsilon_{23,subg}$ was almost nonexistent in the thickest pavement structure, regardless of the material properties. The shear strain in the AC was mainly affected by the AC material, but $\varepsilon_{23,base}$ was sensitive to change in material properties in any layer for both type of tires for thin AC layer, *AC*=3 in and *B*=24 in. Furthermore, the shear strain in the subgrade was not only affected by the subgrade but also by the AC. As in tensile strain, the load was the most relevant parameter, and the tire inflation pressure played a secondary role.

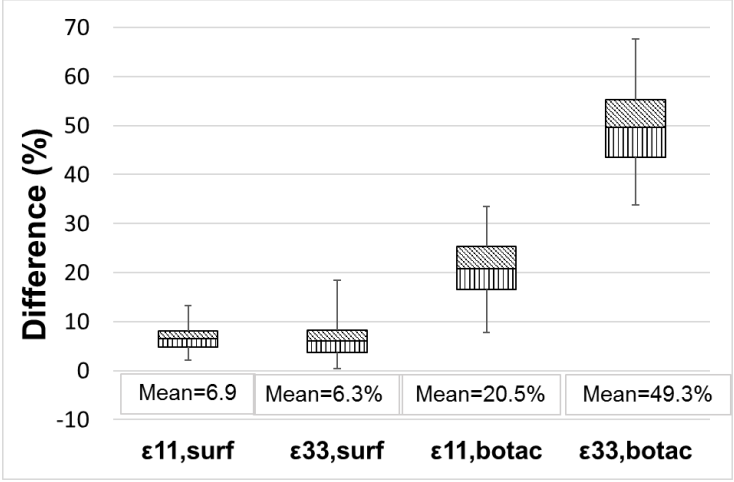

Figure 64. Graph. Box plots for difference between NG-WBT and DTA for tensile strain on the surface and bottom of the AC.

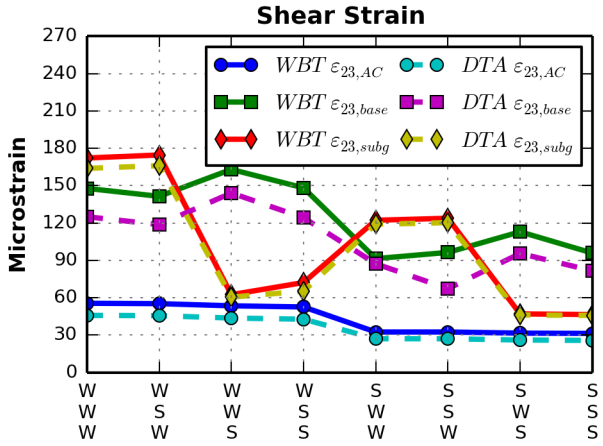

Figure 65. Graph. Vertical shear strain in the AC, base, and subgrade for *AC*=5 in, *B*=6 in, *P*=10 kip, and *S*=110 psi.

The variation of the percentage difference between NG-WBT and DTA is provided in Figure 66 for vertical shear strain. Once more, the mean difference decreased with depth from 23.6% in the AC to 8.8% in the subgrade. However, the range of values in the AC was the smallest. The difference in the $\varepsilon_{23,AC}$ was mainly affected by load and tire inflation pressure, and material properties did not significantly affect the results once thicknesses were fixed. In some cases, the shear strain in the subgrade was smaller for NG-WBT than for DTA (negative difference). Specifically, for high load and the AC thickness of 125 mm, the difference was small (less than 10%), and sometimes negative (as low as -4.4%).

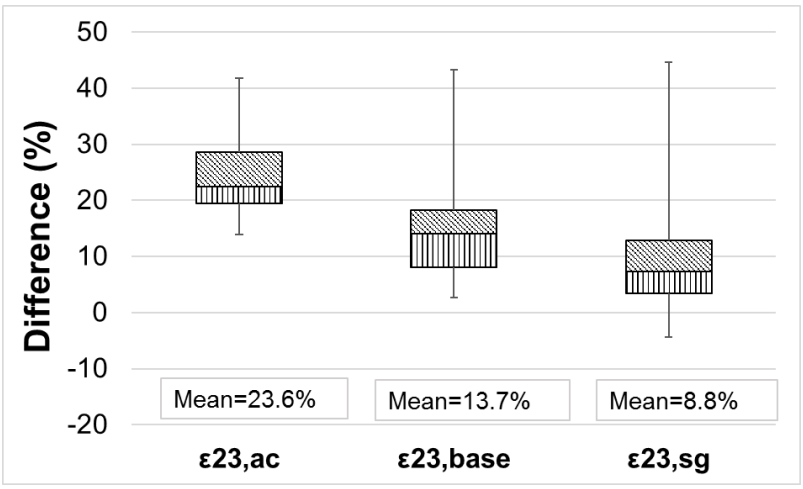

Figure 66. Graph. Box plots for difference between NG-WBT and DTA for shear strain in each layer.

Vertical Strains in the AC, Base, and Subgrade

The variation of the vertical strain in each layer for loading cases *L11*and *L12* when *AC*=5 in and *B*=6 in is shown in Figure 67. The applied load was the most relevant factor. Tire inflation pressure affected $\varepsilon_{22,base}$ base when the applied load was high. The base layer showed the highest vertical compressive strain, and $\varepsilon_{22,AC}$ was mainly defined by the applied load. Regarding the vertical strain on top of the subgrade, the material of each layer affected its magnitude differently, with subgrade being the most important, followed by AC, and base being the least important. Base properties had a slight effect when its thickness was 24 in.

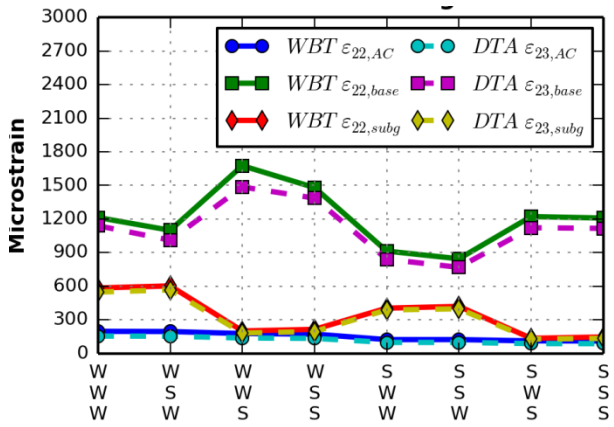

Figure 67. Graph. Vertical strain in the AC, base, and subgrade for *AC*=5 in, *B*=6 in, *P*=10 kip, and *S*=110 psi.

Figure 68 shows the behavior of the difference between NG-WBT and DTA for the vertical strains in each layer. The highest average difference was 33.4%, which corresponded to the AC. This average difference decreased with depth, reaching 12.0% in the base and 10.4% in the

subgrade. For $\varepsilon_{22,subg}$, smaller difference occurred for thickest AC, and the difference was more sensitive to the material property selection when *AC*=3 in. It was also noticed that, even though the subgrade had the smallest average percentage difference, it had the largest range (44.5%). In addition, the difference in the vertical strain was more uniform closer to the surface and the average difference decreased with depth, for all thicknesses, loads, tire inflation pressures, and materials.

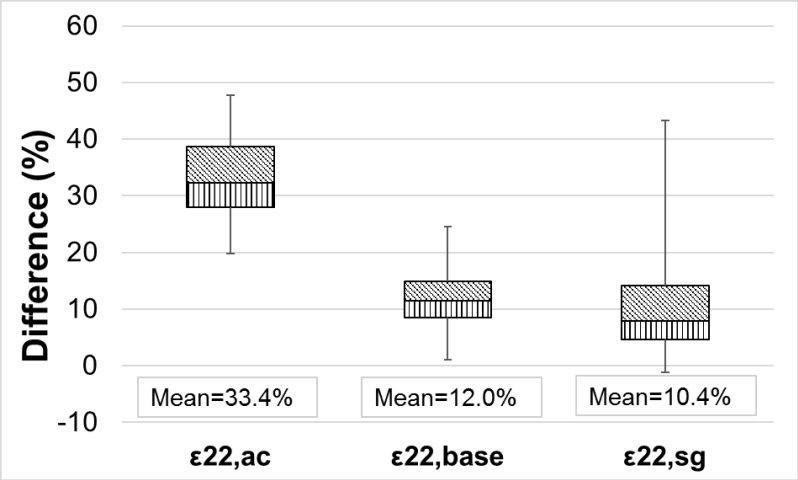

Figure 68. Graph. Box plots for difference between NG-WBT and DTA for vertical strain in each layer.

THICK PAVEMENT STRUCTURES

The simulation factorial for the thick pavement consisted of 192 cases with varied input parameters. Only selective cases are analyzed to present the key findings as the general trends for the same categories are similar. The plots presented in this section reflects the NG-WBT (*L11*) and DTA (*L12*) cases with *P*=10 kip and *S*=110 psi.

Longitudinal and Transverse Strains at the Surface and Bottom of the AC

AC and granular base material characterization varied by using weak and strong properties. In Figure 69 and Figure 70, the top row on the horizontal axis denotes the AC materials, whereas the bottom row indicates the granular base layer materials.

As expected, the transition of AC material properties from strong to weak increased the strain magnitudes. Moreover, AC material property induced a higher change in responses than base material alteration. Similar strain response evolution was evident for NG-WBT and DTA cases, although NG-WBT had a higher magnitude than DTA. In addition, the disparity between the NG-WBT and DTA responses increased as both AC and granular base layers were characterized as weak materials and even more significantly for the $\varepsilon_{33,AC}$ at the surface, and $\varepsilon_{11,AC}$ at the bottom of the AC.

The horizontal strains at the surface and bottom of the AC were more significantly impacted when the AC layer thickness varied than the base thickness was altered. For AC layer thickness of 16.2 in, the strain magnitudes for both NG-WBT and DTA were relatively similar, whereas the NG-WBT responses were evidently greater than the DTA for a 5-in-thick AC layer.

Comparing the impact of the applied load and tire inflation pressure, it was observed that the applied load governs the change in pavement response. In comparison with tire inflation pressure variation, there was a steeper increase in the strains when the applied load increased. Moreover, a notable difference between the NG-WBT and DTA cases became apparent as the applied load was altered from 6 to 18 kip, specifically for the $\varepsilon_{33,AC}$ at the surface, and $\varepsilon_{11,AC}$ at the bottom of the AC.

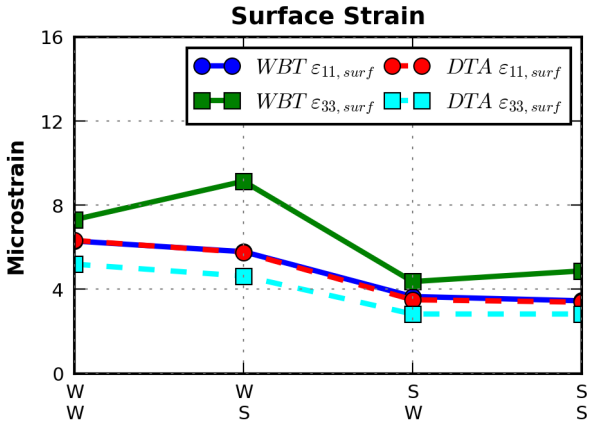

Figure 69. Graph. Longitudinal and transverse strains at the pavement surface *AC*=16.5 in, *B*=24 in, *P* =10 kip, and *S*=110 psi.

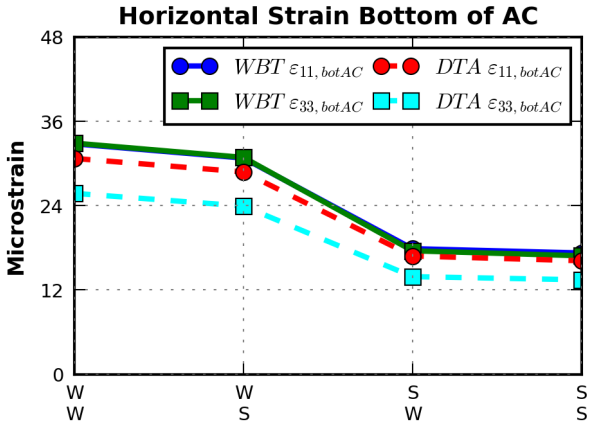

Figure 70. Graph. Longitudinal and transverse strains at the bottom of *AC*=16.5 in, *B*=24 in, *P*=10 kip, and *S*=110 psi.

Figure 71 presents the percentage difference between NG-WBT and DTA responses. $\varepsilon_{11,AC}$ were impacted less as the mean difference was 10.8% and 14.7% for the surface and bottom of the AC, respectively. On the other hand, not only the percent difference increased for $\varepsilon_{33,AC}$, with 20.3% and 39.6% for the surface and bottom of the AC, respectively, but the spread was also greater. It is also worth noting that the large error bar for accounts for high percentage differences between NG-WBT and DTA cases, considering *AC*=16.5 in, and corresponds to absolute strain value differences up to 5 microstrains (with the highest value of 9.1 microstrains). Hence, the percentage difference was high but the actual strain values were significantly low. This finding coincides with field observations wherein thick pavements typically do not fail due tensile strains within the AC surface.

Shear Strains in the AC, Base, and Subgrade

Similar to the horizontal strains at the surface and bottom of the AC, the shear strains for all three pavement layers increased as their materials were characterized from strong to weak. However, only the vertical shear strain of the AC layer changed significantly throughout the material progression in contrast with the coincidental and almost flat evolution of the strains for the granular base and subgrade layers. The disparity between the NG-WBT and DTA cases also increased as the material became weaker (Figure 72). It was observed that the effect of the applied load on the vertical shear strain response exceeded that of the tire inflation pressure variation.

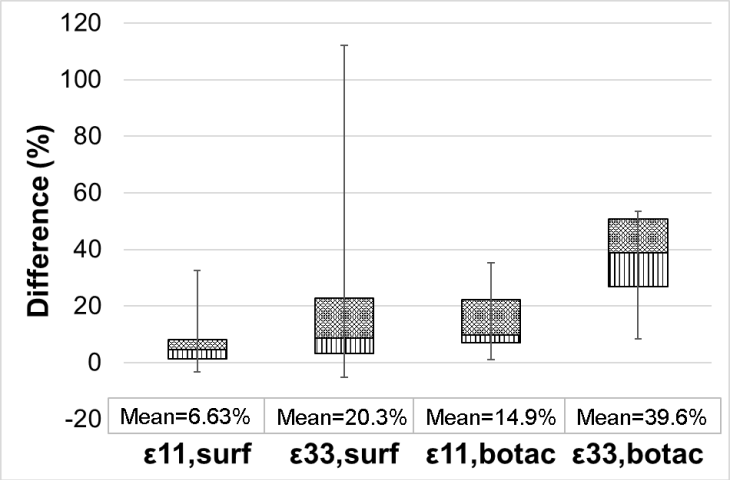

Figure 71. Graph. Box plots for difference between NG-WBT and DTA for tensile strains on the surface and bottom of the AC.

The impact of varying the pavement layer thickness also indicated that the structure with *AC*=16.2 in and *B*=24 in induced the highest vertical shear strain in the AC. The subgrade vertical shear strain also resulted in higher strain magnitudes than the AC and granular base layers, when the base layer thickness was reduced to 6 in (with *AC*= 5 in). On the other hand, the base layer shear strain was significantly greater than that of the AC layer and subgrade for *AC*= 5

in and *B*= 24 in. In addition, the NG-WBT responses became significantly greater than the DTA cases as the AC and granular base layer thicknesses decreased.

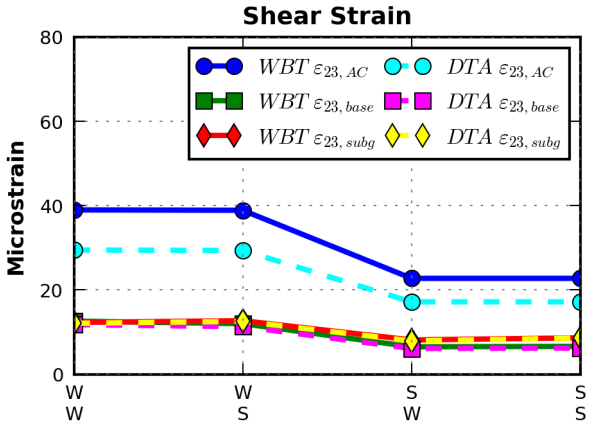

Figure 72. Graph. Vertical shear strain in the AC, base, and subgrade for *AC*=16.2 in, *B*=24 in, *P*=10 kip, and *S*=110 psi.

In comparison with the NG-WBT impact on vertical shear strains, Figure 73 indicates that the percentage difference for the base and subgrade layers was less affected than the ones in the AC layer, wherein the average percentage difference were 14.8% and 4.38%, respectively. This behavior was anticipated as at a greater pavement depth, the applied load becomes the significant factor, whereas contact stresses have a greater effect at the near-surface region of the AC layer leading to an average percent difference of 34.6% and higher difference between the first and third quartile (19.6% and 37.0%).

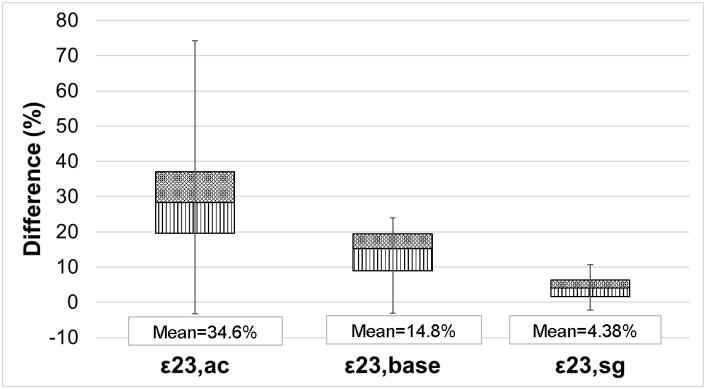

Figure 73. Graph. Box plots for difference between NG-WBT and DTA for shear strains in each layer.

Vertical Strains in the AC, Base, and Subgrade

For the last critical pavement response considered, the vertical strains of the subgrade layer were generally higher than the ones in the AC and base layers; this difference is more significant when the base layer is characterized as strong. The trends presented in Figure 74 are even more

exacerbated when the pavement layer thickness is lower. In addition, when the AC layer material was held constant and the base layer material varied, the difference between the vertical compressive strains in the subgrade and base layers did not change significantly.

Additionally, at a high AC layer thickness of 16.2 in, the strain magnitude range between the AC, base, and subgrade layers was significantly limited compared with that of a 5-in-thick AC layer. The case of *AC*=5 in and *B*=24 in generated the highest vertical compressive strain in the base layer more than the ones in the AC and subgrade layers, whereas the subgrade response became significantly greater than the other layers when *AC*=5 in and *B*=6 in Moreover, as the AC and base layer thicknesses were reduced, the responses from the NG-WBT cases increases more significantly than that of the DTA.

In contrast with the percentage difference of the NG-WBT and DTA vertical compressive strain responses in the AC and base layers, the range of the ones for the subgrade layer was significantly less with an average of 6.6%. On the other hand, the average percent difference for the AC and base layers increased to 30.3% and 17.1%, respectively, with a larger spread as well.

Based on the impact of the loading conditions, the applied load was most influential for both the pavement structures in contrast with the tire inflation pressure. In addition, for both cases, the factors inducing higher disparity between the NG-WBT and DTA responses, included an increase in the applied load, reduced pavement layer thicknesses, and weak material characterization.

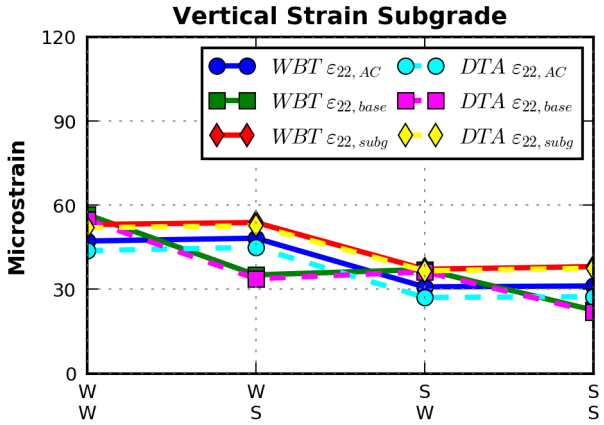

Figure 74. Graph. Vertical compressive strain in the AC, base, and subgrade for *AC*=16.2 in, *B*=24 in, *P*=10 kip, and *S*=110 psi.

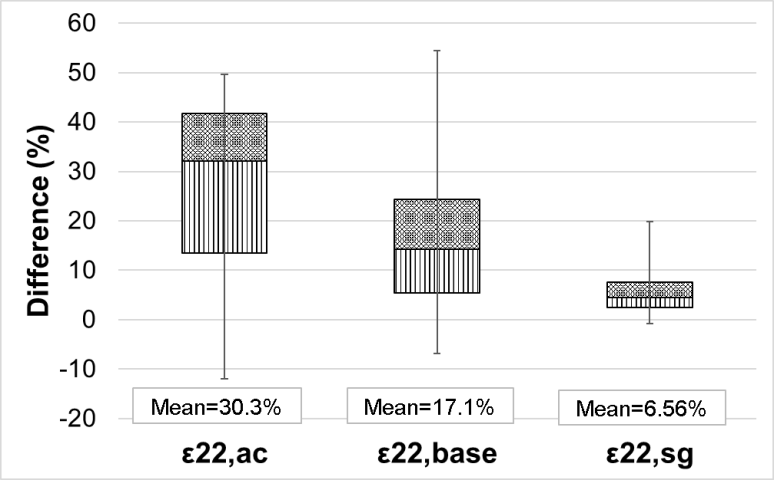

Figure 75. Graph. Box plots for difference between NG-WBT and DTA for vertical compressive strain in each layer.

SUMMARY

The influence loading conditions on critical pavement responses for various pavement structures was studied. Special focus was given to the comparison between NG-WBT and DTA not only for the magnitude of the responses but also the percentage difference.

For thin pavements, the difference decreased with depth, as the influence of the contact stresses decreased. It was also observed that the highest average difference was in the transverse strain at the bottom of the AC. In general, the difference was greater close to the surface. Shear strain in the subgrade had small difference, and in some cases it was smaller for NG-WBT than for DTA.

On the case of thick pavement, the combination of the low thickness and weak pavement material characterization induced the highest strain values for the thick pavement structure. For instance, the transition of AC material properties from strong to weak and the reduction in AC layer thickness increased the strain magnitudes. Moreover, changes in the AC material property would generate a greater impact on responses compared with altering the base material.

Comparing NG-WBT and DTA cases, similar strain response evolution was evident, although NG-WBT had a higher magnitude than DTA. In addition, the disparity between the NG-WBT and DTA cases also increased as the material became weaker and AC thickness was reduced to 5 in. It was also observed that the applied load governs the change in pavement response more significantly than the tire inflation pressure. Lastly, the relative percentage difference between the NG-WBT and DTA responses revealed the following:

- The transverse strains at the pavement surface and bottom of AC layer are more affected compared with the strain in the longitudinal direction,
- The shear strain in the AC layer revealed a higher mean difference and spread than that in the base and subgrade, and
- The vertical strain in the AC resulted in a greater percentage difference than that in the two supporting granular layers.

CHAPTER 6. ARTIFICIAL NEURAL NETWORKS (ANN)

Calculation of pavement responses to the applied loading condition is a key step in the pavement design procedure, where these responses are used to quantify the pavement damage, which is the final criterion in the mechanistic-empirical pavement design procedure. Pavement damage quantification is typically done using empirical equations while response prediction is carried out based on mechanistic models. As explained earlier, FE modeling provides realistic consideration of 3D tire loading and nonlinear pavement structure. However, running FE models is computationally expensive, and, depending on the complexity of the models, can take days to run and obtain the responses of the pavement structure. Also, the user must have technical knowledge about FE and details of the modeled pavement structures.

Considering these difficulties for pavement designers, it is necessary to have a simple model to replace this procedure, provided that the model maintains a high level of accuracy and robustness. The recently developed nonlinear, mathematical data-driven models seem to provide the tool needed by researchers to infer data and establish a model that captures underlying nonlinear relationships. Artificial neural networks (ANN) are a soft computing technique introduced in past decades for providing rapid solutions to complex problems. Soft computing techniques, in general, and ANN, in specific, have been increasingly used for solving complex civil engineering problems.

ANN modeling was used in this project to predict pavement responses for a given loading condition. FE database was used for developing neural network models. The developed FE models covered the material properties and loading of the extreme pavement structures for two typical DTA and NG-WBT. Given these extreme cases, ANN models would interpolate the responses for any arbitrary intermediate cases in a fraction of a second without the need for running FE models.

Unlike regression methods, ANN is highly nonlinear. ANN is a statistical learning technique that infers from data and can efficiently handle noisy and erroneous data to describe the underlying phenomena. In fact, ANN is a mathematical representation of human neurons; it is a layered structured of parallel processing units called neurons. A number of neurons are arranged in layers to make a network. A typical three-layer ANN is shown in Figure 76.

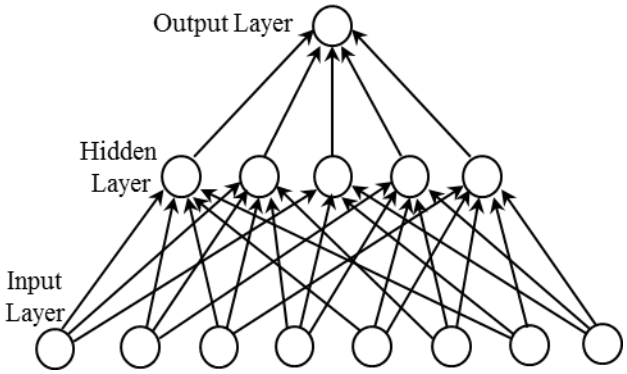

Figure 76. Illustration. Typical three-layer ANN model structure.

The first layer is called the input layer and has as many neurons as the same number of independent variables defined in the problem. The middle layer is called the hidden layer and contains an arbitrary number of neurons, defined by trial and error. And the last layer is called the output layer and has the same number of neurons as the dependent variables of the problem. Neurons in one layer are connected to the neurons in the next layer through links called weight factors. ANN modeling is used for determining the weight factors in a way so that the output of the ANN network is as close as possible to the target value for a specific set of input variables. This is accomplished through an optimization algorithm which adjusts the weights to minimize error between the output and the target. Neurons receive the weighted inputs from previous layer and pass them through a function called activation function; then, the weighted inputs are summed up and passed to the next layer.

Development of an ANN model involves three steps: training, validation, and testing. Accordingly, the database is divided into three datasets. Training data are used to train the network and acquire the weights. Cross-validation data are used for testing the network during training, this dataset represents a measure for training termination, overtraining, and overall generalization ability of the network. Finally, network performance is checked with test data that the network has not seen; this dataset represents a measure for network generalization ability.

In general, training the network consists of the following steps:

1. Weights are randomly generated in each link
2. Each data sample is set to the input layer
3. Value of each independent variable x_i in each neuron of the input layer is multiplied by the weight links to the next layer ($w_{ij}x_i$ for $j= 1,2, \ldots, m$)
4. Each neuron in hidden layer calculates the weighted sum as:

$$net_j = \sum_{i=1}^{n} w_{ij}x_i + bias_j$$

Figure 77. Equation. Weighted sum of the *j*-th neurons.

Where net_j is the weighted sum of the j-th neuron and w_{ij} is the weight between neuron i in the preceding layer and the neuron j

5. The output of the j-th neuron is calculated with an activation function:

$$out_j = F(net_j)$$

Figure 78. Equation. Calculation of the output of j-th neuron.

where F is the activation function. Two of the most popular activation functions based on their simplicity in calculations are:

$$out_j = F(net_j) = \frac{1}{1 + e^{-net_j}}$$

Figure 79. Equation. Sigmoidal function.

$$out_j = F(net_j) = \tanh(net_j)$$

Figure 80. Equation. Hyperbolic tangent.

6. The output of the hidden layer proceeds forward to the output layer and Steps 4 and 5 are repeated to calculate the final outputs in the output layer
7. The output of the network is compared with a target (desired) value to produce an error. The performance function for feed forward networks is the sum of square errors (*SSE*):

$$SEE = \sum_{k=1}^{l} (target_k - out_k)^2$$

Figure 81. Equation. Sum of square errors.

8. The error is back-propagated to the network and weights are altered until the desired sum of square errors is reached.

The performance function shown in the equation presented in Figure 81 is a minimization problem where the weights are the decision variables. Several training algorithms are implemented for solving this problem, including gradient descent and gradient descent with momentum, which are popular, but slow (Caglar et al., 2008). An adaptive fast training algorithm known as Levenberg-Marquardt is also available. For more details on ANN methodology, one may refer to Schalkoff (1997), Tabatabaee et al. (2013), and Moghaddam et al. (2011).

DATABASE

ANN modeling data include thin and thick pavement structures. According to FE test matrix, the database for ANN modeling consists of 12 load cases. Each load case has 16 and 32 cases (data samples) for thick and thin structures, respectively, totaling 192 thick and 384 thin case data samples. Also, eight cases of medium structure were added to the database to account for some intermediate cases. Table 25 through Table 28 show the pavement structure for thin, thick, and medium cases, respectively. Two different materials were defined as part of the test matrix to represent weak and strong material limits. Figure 82 shows dynamic modulus, $|E^*|$, master curve for weak and strong materials for different layers obtained from analysis of hundreds of mixes from LTPP database (same as Figure 28). Weak and strong cases were selected to represent extreme cases, where all materials in the analyzed LTPP database fall within the ranges defined by strong and weak materials. Medium cases are basically a combination of weak and strong cases.

Table 25. Weak and Strong Cases - Thin Pavement Structures

	Materials	Thicknesses (in)
AC Layer	WS-Weak WS-Strong	3 and 5
Base Granular	20 and 60 ksi	6 and 24
Subgrade	5 and 20 ksi	--

Table 26. Weak and Strong Cases - Thick Pavement Structures

	Materials	Thicknesses (in)
AC Wearing Surface	WS-Weak WS-Strong	1.0 and 2.0
AC Intermediate Layer	IM-Weak IM-Strong	1.5 and 4.0
AC Binder Layer	BM-Weak BM-Strong	2.5 and 10.0
Base Granular	20 and 60 ksi	6.0 and 24
Subgrade	10 ksi	--

Table 27. Medium Cases – Thin Structures

Layer	Materials	Thickness (in)
AC	IM-Strong	4.0
Base Granular	40.2 ksi	8.0
Subgrade	9.4 ksi	--

Table 28. Medium Cases –Thick Structures

Layer	Materials	Thickness (in)
AC Wearing Surface	WS-Weak	2.0
AC Intermediate	IM-Strong	2.0
AC Binder	BM-Weak	10.0
Base Granular	40.2 ksi	12.0
Subgrade	10.1 ksi	--

MODEL DEVELOPMENT AND TRAINING

For each pavement response, an ANN model was developed based on FEM results. Eleven responses, including longitudinal and transverse strains at surface and bottom of AC and vertical and shear strain in base and top of subgrade, were modeled. Critical variables affecting the responses were used as input variables. Variables are categorized under loading or structure. Table 29 summarizes the dependent and independent variables.

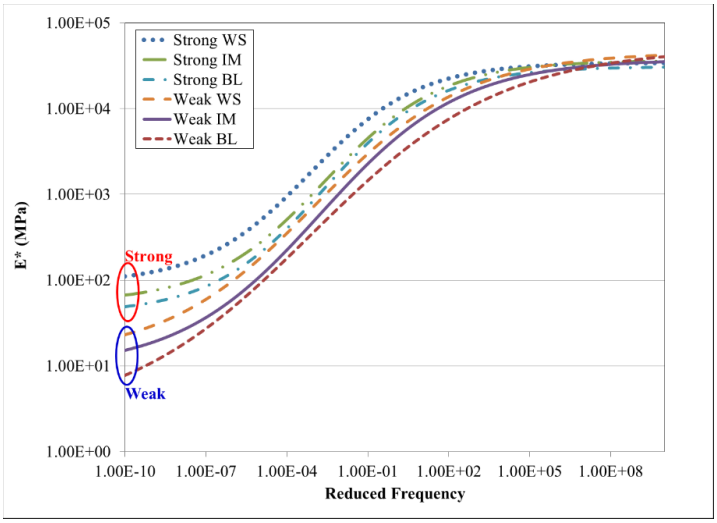

Note: 1 MPa = 145 psi

Figure 82. Graph. Dynamic modulus $|E^*|$ master curve for weak and strong AC layers.

Table 29. Dependent and Independent Variables Defined for Modeling

Category	Independent Variable	Type	Range	Dependent Variable	Type
Loading	Tire Type (NG-WBT/DTA)	Binary	0-1	Long-Strain-Surface	Continuous
Loading	Differential Tire Pressure	Binary	0-1	Trans-Strain-Surface	Continuous
Loading	Axle Load (kip)	Continuous	5.5-18.0	Long-Strain-BttmAC	Continuous
Loading	Tire Pressure (psi)	Continuous	80-125	Trans-Strain-BttmAC	Continuous
Thin Structure	AC Thickness (in)	Continuous	3-5	Vert-Strain-AC	Continuous
Thin Structure	AC Material Properties	Continuous	Weak-Strong (master curve)	Vert-Strain-Base	Continuous
Thin Structure	Base Thickness (in)	Continuous	6-24	Vert-Strain-SG	Continuous
Thin Structure	Base Material (modulus ksi)	Continuous	20-60	Shear-Strain-AC	Continuous
Thin Structure	Subgrade Material (modulus ksi)	Continuous	5-20	Shear-Strain-Base	Continuous
Thick Structure	Wearing Surface Thickness (in)	Continuous	1-2.5	Shear-Strain-SG	Continuous
Thick Structure	Intermediate Course Thickness (in)	Continuous	1.5-4.0	Mises-Stress-AC	Continuous
Thick Structure	Binder Course Thickness (in)	Continuous	2.5-10.0		
Thick Structure	Wearing Surface Material Properties	Continuous	Weak-Strong (master curve)		
Thick Structure	Intermediate Course Material Properties	Continuous	Weak-Strong (master curve)		
Thick Structure	Binder Course Material Properties	Continuous	Weak-Strong (master curve)		
Thick Structure	Base Thickness (in)	Continuous	6.0-24.0		
Thick Structure	Base Material (modulus ksi)	Continuous	20-60		

As part of the material property inputs for ANN modeling, three representative dynamic modulus values were used at reduced frequencies of 100, 0.01, and 1E-9 Hz from the master curves. The material properties for the medium cases are a combination of weak and strong cases. For thin structure, the corresponding AC material property is IM-Strong. Conversely, for thick structure, WS-Weak, IM-Strong and BM-Weak were used for wearing surface, intermediate layer, and binder layer, respectively, as shown in Figure 82.

The material properties, especially complex modulus, are not readily available. Therefore, two levels of input properties were defined to account for data availability issues, Level 1 for detailed material properties and Level 2 for receiving modulus of each layer at room temperature only. Level 1 is the most detailed input level where $|E^*|$, in terms of sigmoidal function coefficients, is required as input. $|E^*|$ is a fundamental material property that defines the stiffness as a function of temperature and loading time. Details are presented in section Chapter 4. For each response, a separate ANN model was designed and named Net1, Net2, and so on. All networks have three layers with one hidden layer. Levenberg-Marquardt was chosen as the training algorithm for all models. The number of neurons in the hidden layer was chosen on trial-and-error basis. A different number of neurons was tried, and the network with the least error in training was selected as the optimum number of neurons for that model. Figure 83 shows the variation of a sample training error versus the number of neurons, which was used as a criterion for selecting the number of neurons in the hidden layer for Net3 (Long-Strain-BttmAC). Sixteen is the optimum number of neurons for Net3. Similarly, the optimum number of neurons was determined for all networks.

After deciding on each network configuration, training data were fed into the model. Using the Levenberg-Marquardt algorithm, the network was trained to build the input-output realtionship. The next step was performance evaluation of models. In this step, prediction accuarcy was measured. The normalized root mean square error *(NRMSE)* and R-square were used as the performance measure for the models.

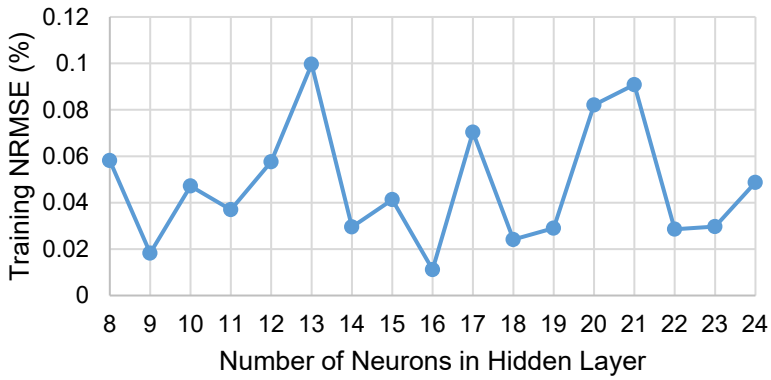

Figure 83. Graph. Number of neurons in hidden layer versus training error for Net3 (long-strain, bottom of AC).

$$NRMSE = \frac{N^2 \cdot RMSE}{N\sum_{i=1}^{N} d_i^2 - (\sum_{i=1}^{N} d_i)^2}$$

Figure 84. Equation. Normalized root mean square error.

where:

$$RMSE = \sqrt{\frac{\sum_{i=1}^{N}(d_i - y_i)^2}{N}}$$

Figure 85. Equation. Root mean square error.

and: d_i= desired output of i-th data
y_i= Network output of i-th data
N= number of data set.

Training data were used to train the networks, and test data were used to evaluate the networks' performance and validate the models. Therefore, the *k*-fold cross-validation technique was implemented.

K-fold Cross-Validation

The *k*-fold cross-validation technique was used to evaluate performance of the trained networks. In this technique, the database is divided into number of folds, and each fold is used as the test set one at a time. The best model is considered the one demonstrating the best performance on test data. Data are usually divided randomly into different folds to ensure unbiased comparison of models. In this study, however, unlike random approach, 12 folds corresponding to 12 load cases were used. If test and training sets were randomly assigned, some data samples from a load case would be part of the training dataset while others from the same load case would be part of the test dataset. During training, the model adapts itself to the load cases in the training set. Since data samples in each load case has identical loading information and only some of the variables have varying values, this would cause overtraining and better performance on the test data from the same load case and poor performance on the other load cases, thus adversely affecting the generalization ability of the model.

RESULTS

For each response, an ANN model was developed and tested for validation. Figure 86 shows sample performance results for all responses using thick and thin pavement models with one standard deviation band. Vertical axis is the average percentage of error on all test folds. Figure 87 shows the scatter plot and R-square result of the thick and thin models for three responses. Figure 87 is based on the best trained model and corresponding load case. Table 30 summarizes the test results for all models based on average performance on all 12 folds.

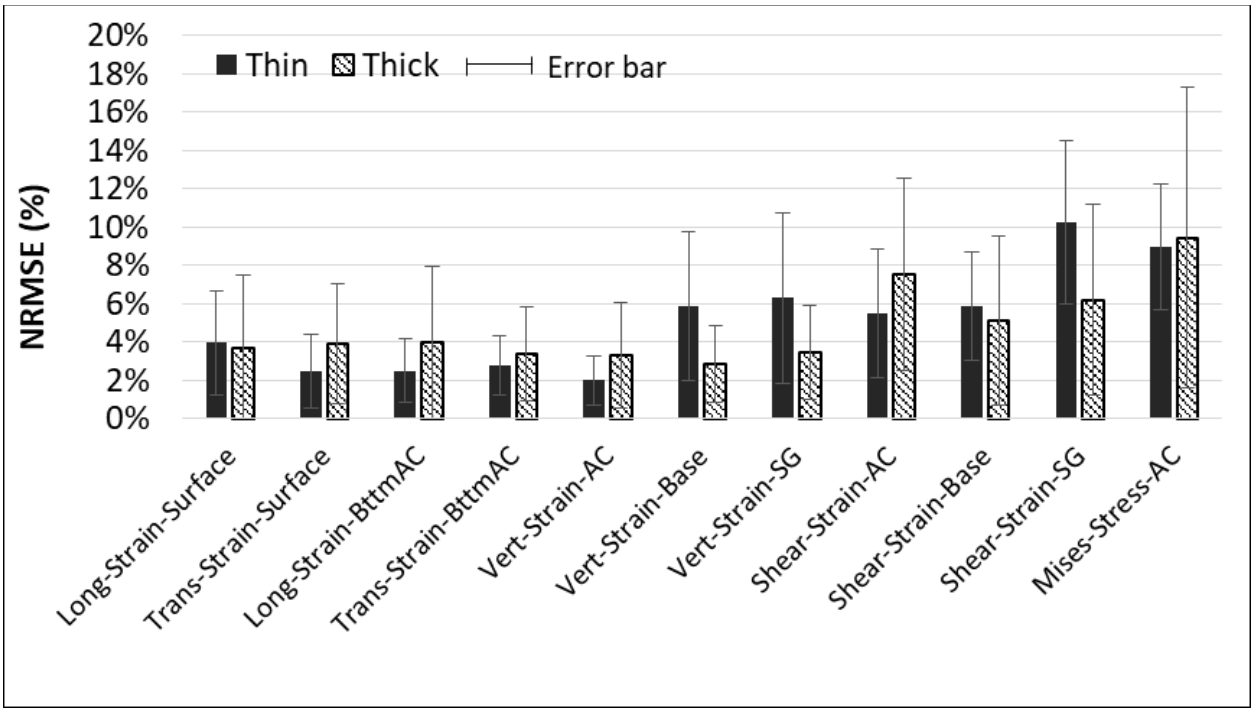

Figure 86. Graph. Sample prediction error for all responses using thin and thick pavement models with Level 1 inputs.

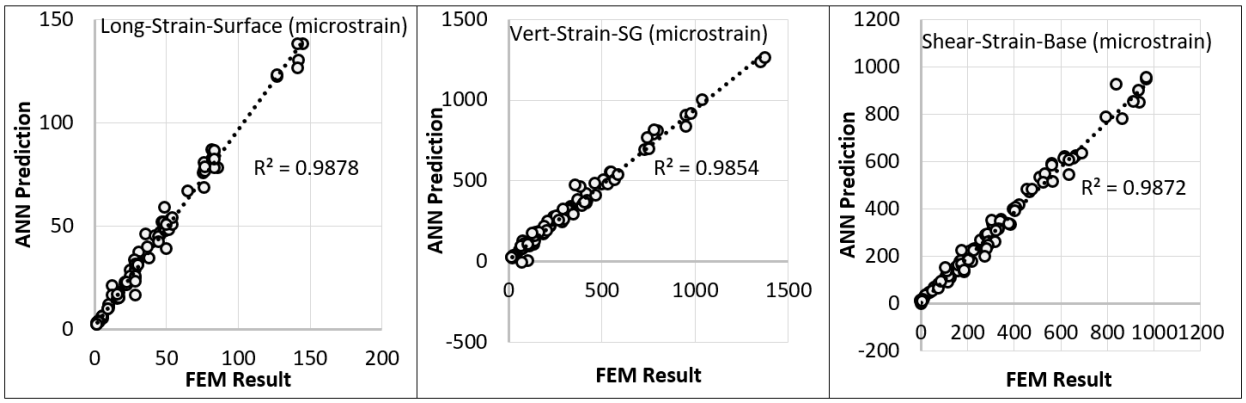

Figure 87. Graph. Scatter plot of FEM simulation versus ANN prediction for thick pavement Level 1 model.

Table 30. Summary of Average Performance of Models for All Folds

	Thick Level 1	Thick Level 1	Thick Level 2	Thick Level 2	Thin Level 1	Thin Level 1	Thin Level 2	Thin Level 2
	R^2	NRMSE (%)	R^2	NRMSE (%)	R^2	NRMSE (%)	R^2	NRMSE (%)
Long-Strain-Surface	0.9921	2.08	0.9977	2.82	0.9855	4.08	0.9970	1.65
Trans-Strain-Surface	0.9960	2.25	0.9922	2.72	0.9971	2.46	0.9789	3.09
Long-Strain-BttmAC	0.9888	1.72	0.9980	2.34	0.9953	2.52	0.9906	2.56
Trans-Strain-BttmAC	0.9965	1.23	0.9894	4.85	0.9995	2.90	0.9984	2.33
Vert-Strain-AC	0.9592	2.48	0.9975	3.76	0.9974	1.99	0.9994	1.73
Vert-Strain-Base	0.9981	2.35	0.9973	3.33	0.9993	6.58	0.9991	4.04
Vert-Strain-SG	0.9955	3.17	0.9877	4.12	0.9990	6.77	0.9960	5.48
Shear-Strain-AC	0.9661	4.62	0.9967	4.07	0.9977	6.35	0.9980	5.19
Shear-Strain-Base	0.9978	3.10	0.9986	2.50	0.9740	6.34	0.9657	4.59
Shear-Strain-SG	0.9984	2.81	0.9859	2.20	0.9844	11.37	0.9997	4.19
Mises-Stress-AC	0.9553	5.79	0.9621	4.46	0.9839	9.66	0.9884	6.14
Average	**0.9858**	**2.87**	**0.9911**	**3.38**	**0.9921**	**5.55**	**0.9919**	**3.73**
STD	**0.0161**	**1.25**	**0.0101**	**0.8788**	**0.0082**	**2.94**	**0.0103**	**1.48**

According to the results, the models trained well and no overtraining was observed . The average error for all models was 3.85% with standard deviation of 1.38. In general, the prediction error for shear strains was the highest, which might be attributed to the complex nature of the shear strians within the pavement structure. No specific trends were obsererved for thin and thick pavement cases and between Level 1 and Level 2. Although Level 1 models are more informative about material properties than Level 2 models, this does not neccesserly lead to better performance. Level 1 used three variables to describe material properties while Level 2 used one material property only. Additional information means more input variables added to the model (in this case 2 and 6 additional variables for thin and thick cases, respectively) without adding extra observations (data samples), thus increasing the complexitiy of the model. Furthermore, all material propeties correlate with each other, which in modeling prospective does not necessarly result in better performance. However, using three variables is a good representation of a viscoleastic material when dealing with data other than that used for modeling. In this case, two materials with the same modulus at room temperature, may have completely different viscoelastic behavior.

SENSITIVITY ANALYSIS

To investigate the importance of the input variables in ANN modeling scheme, a series of sensitivity analyses were conducted. The missing data problem and incremental sensitivity [also called one-at-a-time (OAT) analysis] method were implemented to analyze sensitivity. In the former, one variable was removed from the model at a time and output error was calculated. The relative importance of the variables was evaluated by comparing the output errors. The higher the error, the more important the variable. Figure 88 shows the missing data sensitivity results for thin and thick structures with variables aggregated into four categories: pavement structure, load, tire type, and tire pressure.

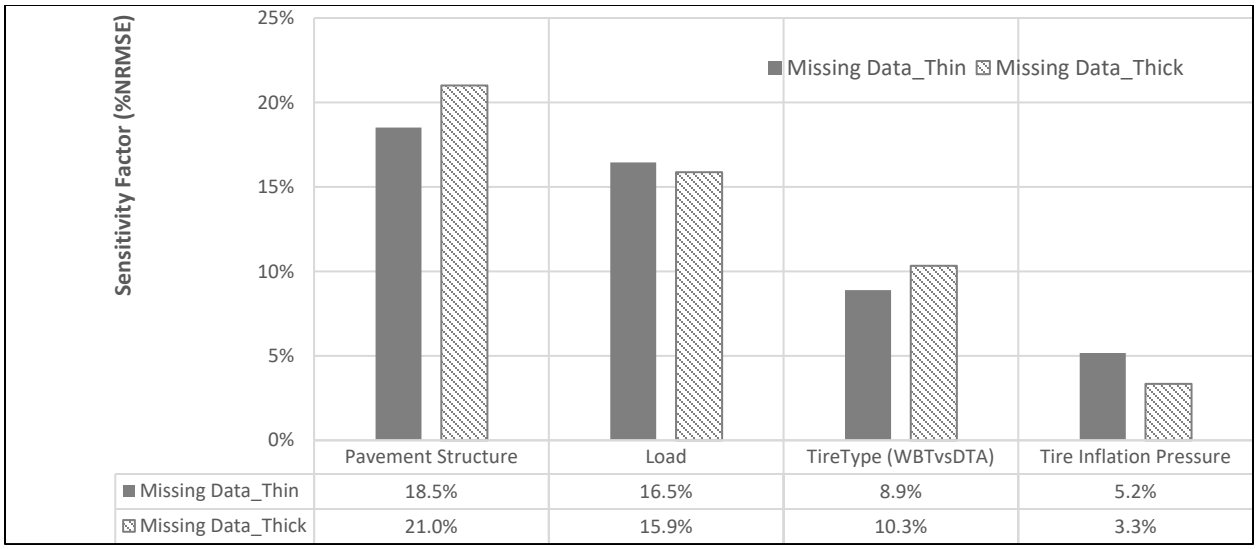

Figure 88. Graph. Missing data sensitivity analysis results for thin and thick pavement structures averaged over all responses and Level 1 and Level 2 models.

The vertical axis shows the amount of error incurred as a result of a missing variable, such as in the thick structures case. If there were no information about "pavement structure," the error would be 20.9%, making "pavement structure" the most important variable. It should be noted that, missing a specific variable is conditional on knowing the variable range; otherwise, it would be impossible to know the response without knowing, for instance, how much load is applied.

In OAT analysis, each variable gradually increases one step at a time from low to high values in the input range. The change in output is recorded while all other variables are kept at baseline values. Step length may vary for different variables depending on the unit, but the same number of steps should be used for all variables to obtain consistent results. At each step, a normalized sensitivity ratio (*SR*) was calculated using the following equation:

$$SR = \% \frac{\frac{y_{i+1}(x) - y_i(x)}{y_i(x)}}{\frac{x_{i+1} - x_i}{x_i(x)}}$$

Figure 89. Equation. Sensitivity ratio.

where: $y_{i+1}(x)$= model output in step $i + 1$ due to variable x
$y_i(x)$= model output in step i due to variable x
x_{i+1}= value of variable in step $i + 1$
x_i= value of variable in step i

The *SR* average over all steps is an indicator of the effect of the input on output; the higher the *SR*, the more important the variable. Figure 90 shows variable importance for thick and thin pavements in terms of *SR*. Twenty steps were used for this study.

According to the results of OAT analysis, an example trend analysis is provided in Figure 91 through Figure 94 for one of the responses. This example shows the change of longitudinal strain at the bottom of the AC wearing surface layer with change of tire inflation pressure, load, and AC layer thickness.

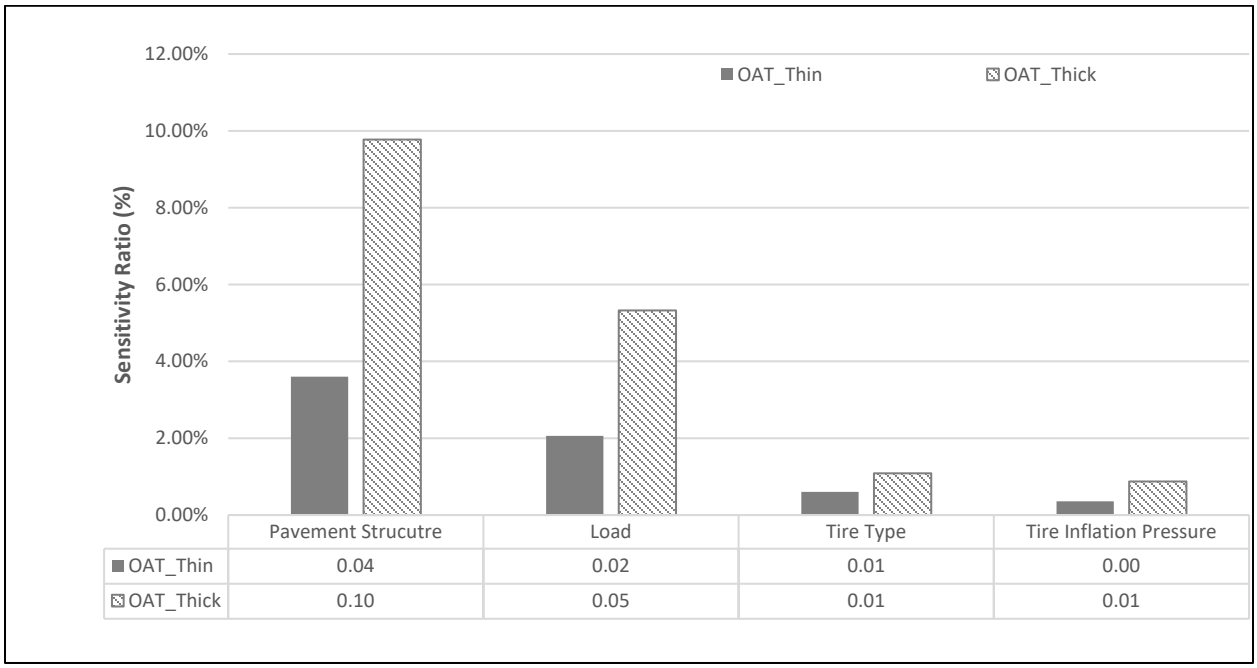

Figure 90. Graph. OAT sensitivity analysis results for thin and thick pavement structures averaged over all responses and Level 1 and Level 2 models.

Both sensitivity methods use different scales to determine the importance of variables; therefore, a sensitivity factor in a scale from 0 to 1 was defined, and the results were normalized to this scale. Figure 94 shows a comparison of the sensitivity factor from both methods in one scale averaged over thin and thick pavement structures, all responses, and all levels. According to sensitivity factor results, the pavement structure had the highest effect in both cases. Load is a little more emphasized in the missing data problem. It can also be noted that tire type plays an important role in pavement response calculation. This means that 10 to 30% influence on responses is caused by wide-base tire versus dual-tire, which is somewhat equal to the effect of tire pressure.

ICT-WIDE TOOL

To assist agencies and designers in the evaluation of the effect of NG-WBT on pavements, all trained models as well as damage calculations were incorporated into a tool called the Illinois Center for Transportation wide-base tool (ICT-Wide tool). The tool is a stand-alone Matlab-based tool that can be installed on any Windows operating system. Snapshots and a step-by-step procedure to use the tool are provided in Appendix D.

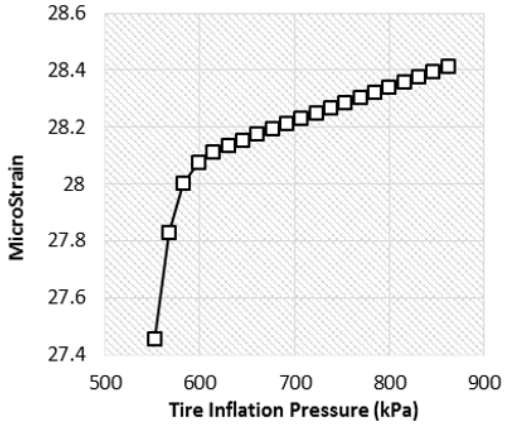

Note: 1 kPa = 0.145 ksi

Figure 91. Graph. Change of longitudinal strain at bottom of surface layer with change in tire inflation pressure.

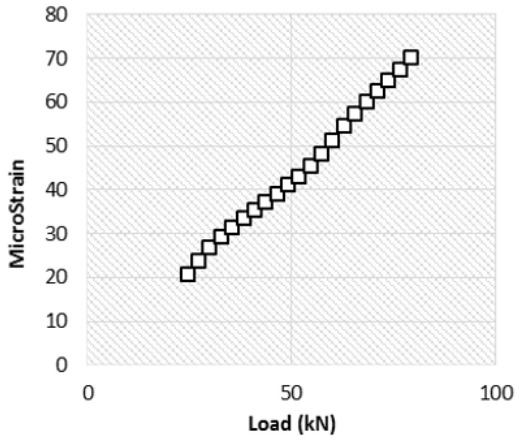

Figure 92. Graph. Change of longitudinal strain at bottom of surface layer with change in load.

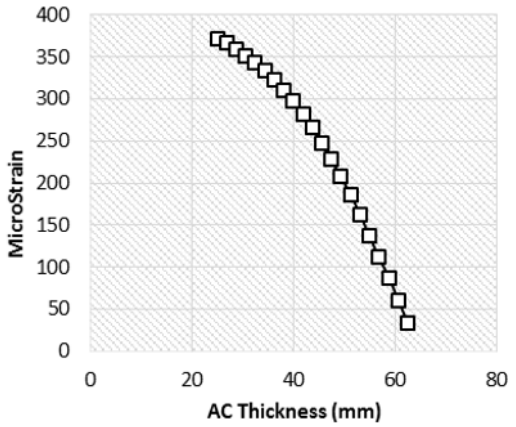

Figure 93. Graph. Change of longitudinal strain at bottom of surface layer with change in AC layer thickness.

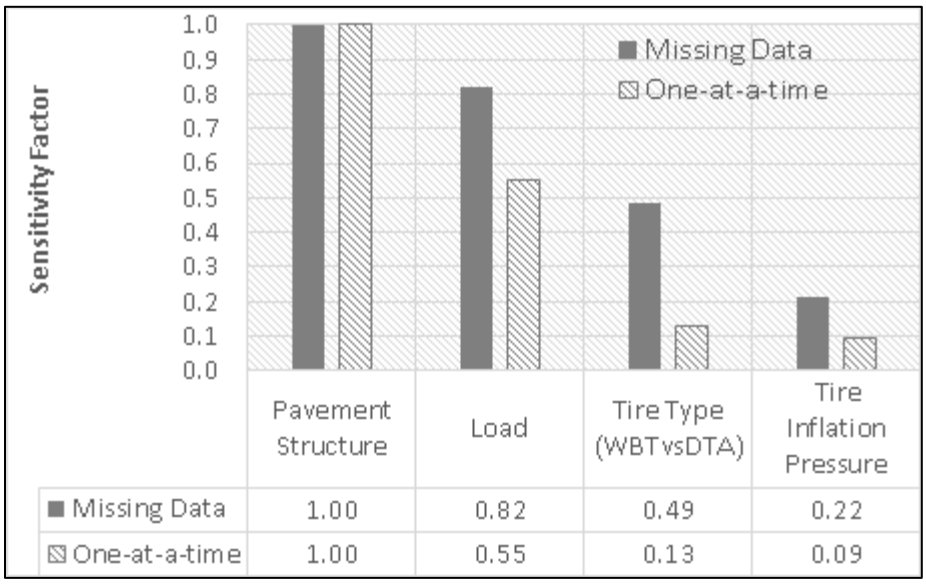

Figure 94. Graph. Sensitivity factor averaged over all models.

SUMMARY

A nonlinear mathematical model, ANN, was developed to replace the more sophisticated numerical FE model. The test matrix developed for FE models was used as the database for ANN modeling. A total of 44 ANN models were developed for each response (11 responses in total), pavement structure (thin and thick), and input level (Levels 1 and 2). Pavement loading information as well as pavement structure and material information were used as model variables. A 12-fold cross-validation technique was used in developing the models. One loading case out of the 12 load cases was set aside as a test dataset and 11 load cases were used as training dataset.

The results showed the ability of ANN models to predict responses in agreement with FE model results. Two sensitivity analysis, the missing data problem and OAT, were conducted to evaluate the variable effect on responses. The results indicate the significance of tire type (wide-base versus dual) on the responses; it can cause up to 10% difference in response prediction and hence in pavement damage. This indicates the importance of the dual versus wide-base tire assumption.

CHAPTER 7. ADJUSTMENT FACTOR FOR AASHTOWARE

INTRODUCTION

All AASHTO pavement design guides issued between early 1960s and 1993 are based on empirical equations, which rely heavily on the results of the AASHO Road Test conducted in Ottawa, Illinois, in the late 1950s (AASHTO, 2008). In order for empirical design guides to deliver accurate performance prediction, design inputs for new pavement structure should be similar to the ones used in the AASHO Road Tests. However, tire type, truck type, axle load limits, and materials have significantly changed since over the past five decades.

The need to have a pavement design guide that incorporates changes in materials and loadings and considers direct climate effects on pavement performance was clearly recognized by researchers, engineers, and transportation institutions in 1986 (AASHTO, 2008). Consequently, NCHRP Project 1-37A was launched in 1998 under the sponsorship of the AASHTO, NCHRP and FHWA for the development of an advanced and comprehensive design guide. The MEPDG was released in 2004. Afterwards, MEPDG was reviewed and revised under NCHRP 1-40A, 1-40B and 1-40D, which resulted in the development of MEDPG design software in 2007 (later known as DARWin-ME) and MEPDG - A Manual of Practice, Interim Edition in 2008. In August 2013, the current version, AASHTOWare Pavement ME Design software, was released.

In MEPDG (or AASHTOWare), the user assumes a pavement structure as a trial design and provides all other inputs to the software, such as traffic, material properties, and environmental conditions. Structural responses (strain, stress, and/or deflections) are then calculated within the pavement, which refers to the mechanistic part of the guide. By exploiting empirical models, these responses are linked to distress propagations over a design period and are consequently used for IRI assessment. Finally, the user checks design criteria against predicted ones. If design requirements are not satisfied, trial design should be modified and the steps should be repeated until design requirements are met. Figure 95 illustrates the MEPDG procedure.

Accurate prediction of the pavement responses is key for realistic simulation of distress propagation over time. Although MEDPG has a grounded methodology for pavement analysis, it has a number of limitations and unrealistic simplifications that result in inaccurate response predictions. On the other hand, and as indicated earlier, FE analysis simulates pavement responses more realistically in terms of loading conditions and material characterization. Therefore, a correction factor must be developed for structural pavement responses calculated by the MEPDG in accordance with FE results.

MECHANISTIC PART OF THE DESIGN GUIDE AND ITS LIMITATIONS

The mechanistic part of the Guide refers to pavement analysis conducted for obtaining critical responses. MEPDG exploits the multi-layered linear elastic theory (MLET) to compute pavement responses under tire loads. Several types of software implement MLET, such as MnLayer, KenLayer, BISAR, and JULEA; MEPDG uses the JULEA in its framework.

MEPDG indirectly considers AC as viscoelastic, its behavior depends on time, temperature, and frequency of loading. MEPDG incorporates the stiffening of AC layer with time through global aging model. On the other hand, temperature within the pavement is determined using the integrated climate model (ICM). Frequency of loading is calculated as a function of vehicle speed, axle type (single, tandem, or tridem) and pavement structure. In addition, the pavement is divided into sub-layers to account for temperature and frequency changes with respect to depth. Dynamic modulus, $|E^*|$, is computed at the mid-depth of each sublayer by considering aging, temperature and frequency and input into JULEA along with other inputs such as layer thicknesses, loads, and tire pressures.

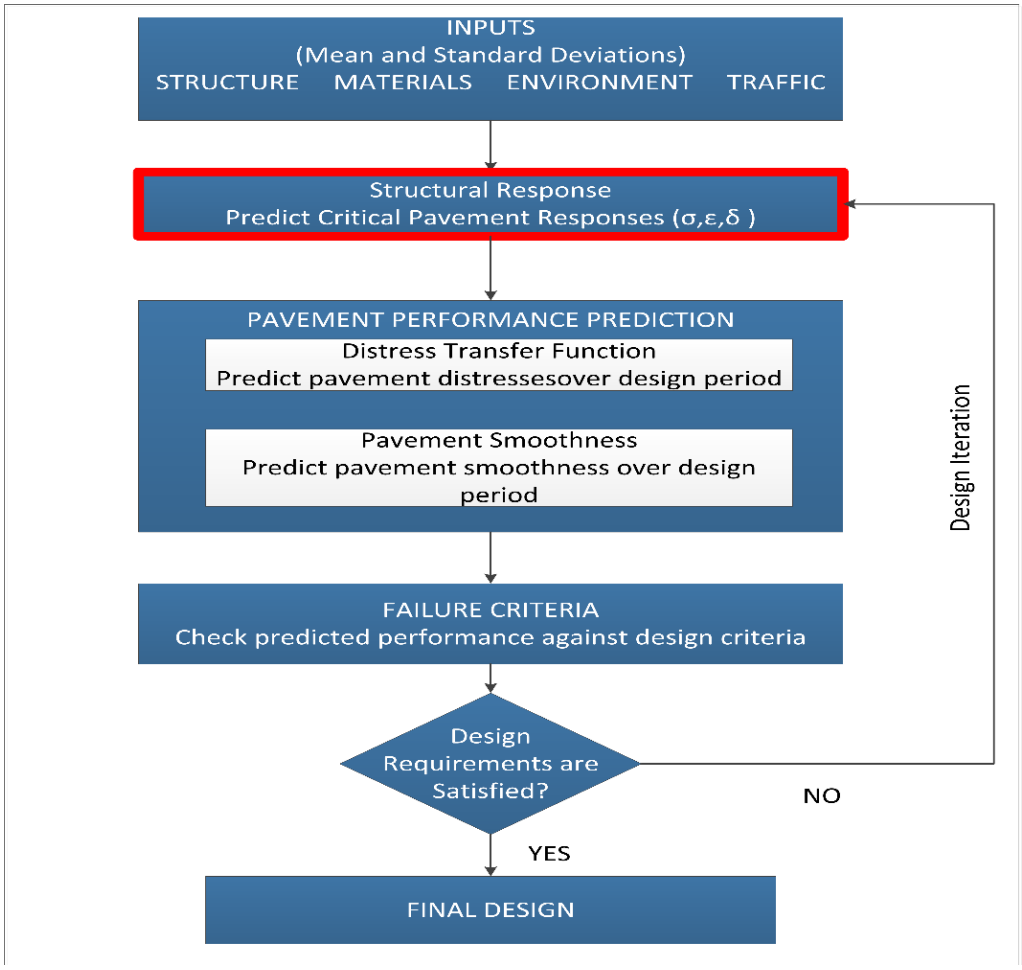

Figure 95. Illustration. MEPDG flowchart.

The mechanistic part of the Guide consists of a three-step procedure: i) subdivision of pavement structure; ii) calculation of modulus at the mid-depth of each sublayer considering aging, temperature and frequency of loading; and iii) running the JULEA with calculated dynamic modulus and other inputs such as layer thicknesses and load. Figure 96 shows MEDPG procedure for computing pavement responses.

Although the mechanistic part of the guide provides a theoretically sound procedure for computing critical pavement responses, it still has a number of limitations and simplifications, which may lead to unrealistic response prediction. These limitations and simplifications are mostly caused by the assumptions behind the MLET used in MEPDG's framework. On the other hand, FE method can simulate tire-pavement interaction more realistically by overcoming most of MEPDG's limitations.

Limitations of MEPDG Procedure for Loading Frequency Calculation

Table 31 demonstrates the limitations of MEPDG by comparing it with FEA. Tire-pavement interaction is simulated unrealistically because of the assumptions behind the MLET, such as uniform 2-D vertical tire pressure and circular contact area. In addition, Al-Qadi, Elseifi, et al. (2008) and Al-Qadi, Xie, et al., 2008b) proved that additional errors are introduced by MEPDG procedure for calculating loading frequency, which translates into inaccurate dynamic modulus calculation. The error in frequency calculation varies from 40% to 140% depending on vehicle speed and depth of calculation. There are two main sources of error in frequency calculation procedure: i) conversion from time domain to frequency domain, and ii) assuming stress distribution with 45° through the pavement's depth.

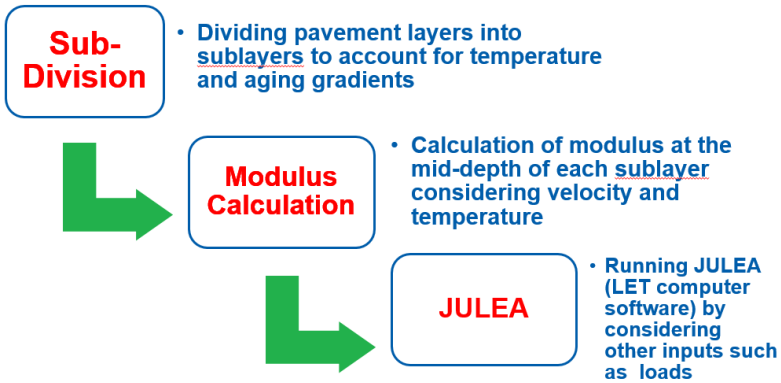

Figure 96. Illustration. MEPDG procedure.

MEPDG calculates loading frequency using the equation shown in Figure 97. Al-Qadi, Elseifi, et al. (2008) proved that this conversion does not realistically simulate loading frequency and is, thus, the first source of error. In the same study, a novel approach is suggested based on Fast Fourier Transformation and validated by FE simulations.

$$f = \frac{1}{t}$$

Figure 97. Equation. Loading frequency.

where: t = time of loading (s) and f= frequency of loading (Hz).
Time of loading in MEPDG is calculated as follows:

$$t = \frac{L_{eff}}{17.6\ v_s}$$

Figure 98. Equation. Time of loading.

where: v_s= vehicle speed, L_{eff} =Effective Length.

Table 31. Limitation of MEPDG Procedure Compared to FEA

	FEA	MEPDG Procedure
Analysis Type	Dynamic analysis, considering motion of tire and viscoelasticity of AC	Linear Elastic Analysis
Tire Type	Both WBT and DTA can be simulated	Only DTA can be considered
Contact Stress	Nonuniform realistic measured 3-D contact stresses	2-D uniform vertical pressure
Contact Area	True measured tire contact area	Circular contact area
Speed and Temperature	Directly considered in viscoelastic dynamic analysis	Implicitly considered in dynamic modulus calculations
Friction Between Layers	Elastic Stick Model, defined by τ_{max} and d_{max}	Distributed Spring Model
AC Layer Material Properties	Viscoelastic characterization using Prony Series	Dynamic modulus obtained from master curve (MEPDG procedure)**
Base Layer	Stress-dependent, nonlinear model for base – especially important for thin pavement	Linear elastic

To calculate effective length, all layer thicknesses are transformed into their equivalent thicknesses based on stiffness of the subgrade layer. This process is known as Odemark's method of thickness equivalency.

After transforming all layer thicknesses, the effective length (Figure 100) is computed by assuming that stress is distributed at 45° through the soil depth (Figure 101). This assumption is considered the second source of error in frequency calculation. The assumption especially fails to capture far-field effect of approaching-leaving rolling wheel (Al-Qadi, Elseifi, et al., 2008). The detailed procedure for calculating frequency of loading is found in NCHRP 2004 (NCHRP Appendix CC).

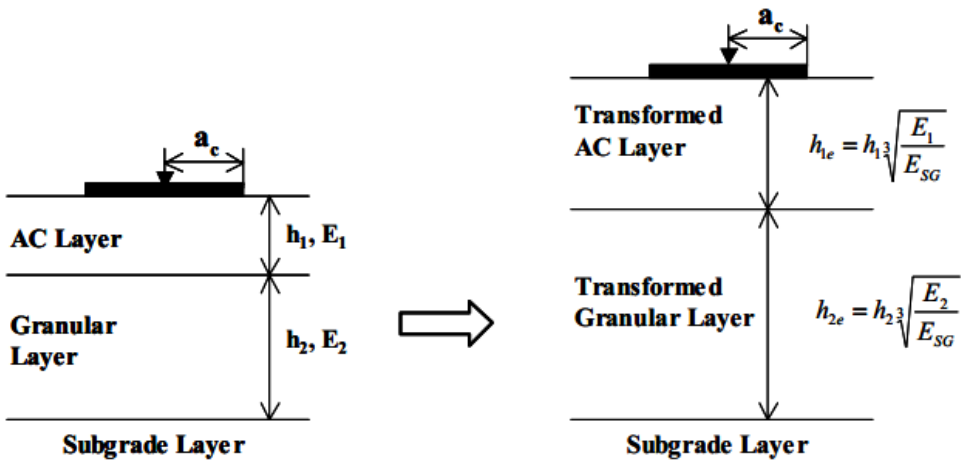

Figure 99. Illustration. Odemark's method of thickness equivalency.

$$L_{eff} = 2 * (a_c + Z_{eff})$$

Figure 100. Equation. Effective length.

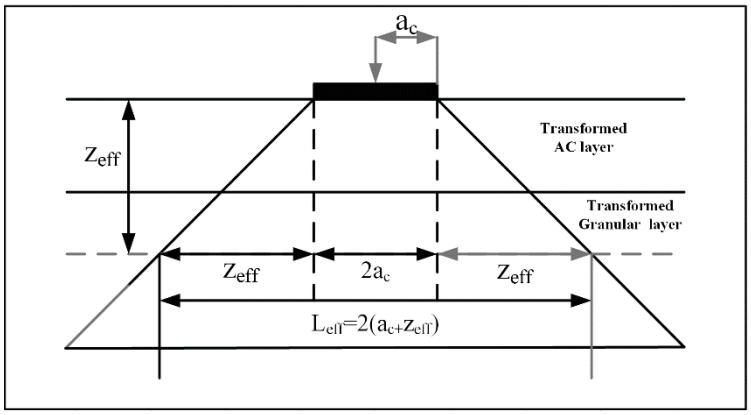

Figure 101. Illustration. Stress distribution through soil depth.

DEVELOPMENT OF THE ADJUSTMENT FACTORS

Pavement MEPDG procedure for computing pavement responses has a number of limitations, including the two-dimensional uniform vertical tire pressure with circular contact area, linear elastic analysis of AC layer, and static tire loading. In addition, the procedure is incapable of considering NG-WBT. Therefore, two adjustment factors are proposed: i) adjust to DTA based on FE results when using a wide-base tire; and ii) convert to MEPDG from FE results of DTA. The proposed method is summarized in Figure 102.

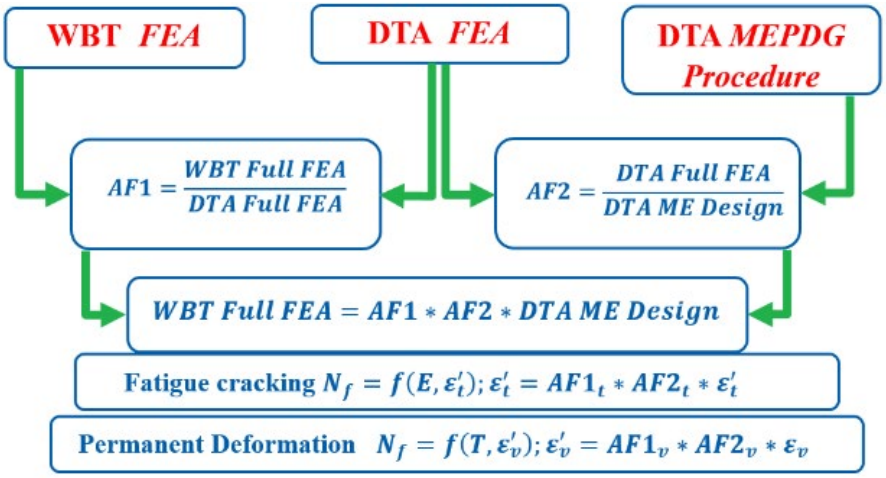

Figure 102. Illustration. Adjustment factor approach.

Adjustment Factor 1

Adjustment Factor 1 ($AF1$) was developed to convert the response resulting from DTA into NG-WBT. For $AF1$, only FE simulations were used because MLET is not capable of simulating the response NG-WBT properly. $AF1$ was developed using the ABAQUS, which runs considering the same material properties and pavement structures. The only difference was the contact stresses and contact areas which were measured under the same tire load for NG-WBT and DTA. $AF1$ is presented as linear function of the DTA response. Figure 103 through Figure 112 show the result for each pavement response. It should be noted that all plots have a line of equality ($y = x$) and a fitted straight line. The unity line is solid while the fitted line is dashed. The purpose of the equality line is to demonstrate the significance of applying an adjustment factor to each particular response.

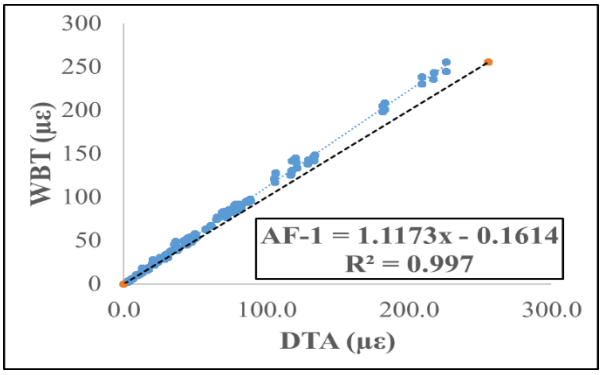

Figure 103. Graph. Maximum tensile strain along traffic direction at AC surface.

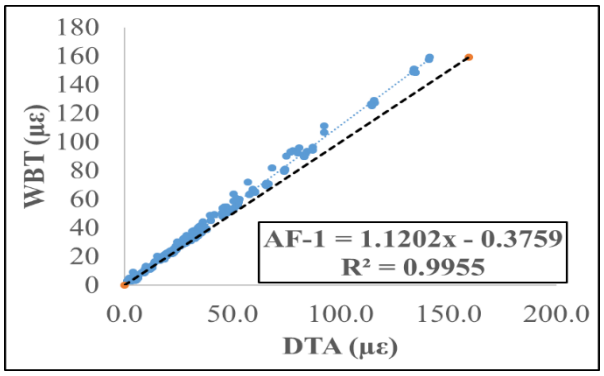

Figure 104. Graph. Maximum tensile strain along transverse direction at AC surface.

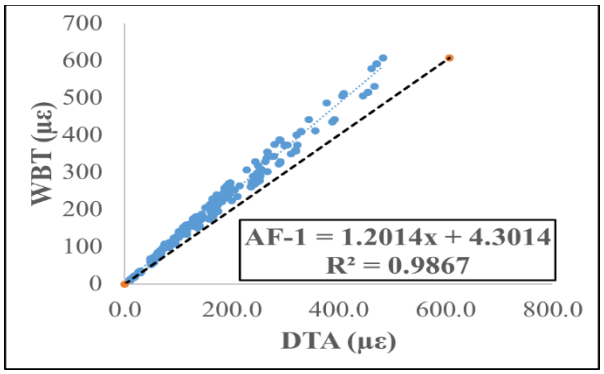

Figure 105. Graph. Maximum tensile strain along traffic direction at bottom of AC.

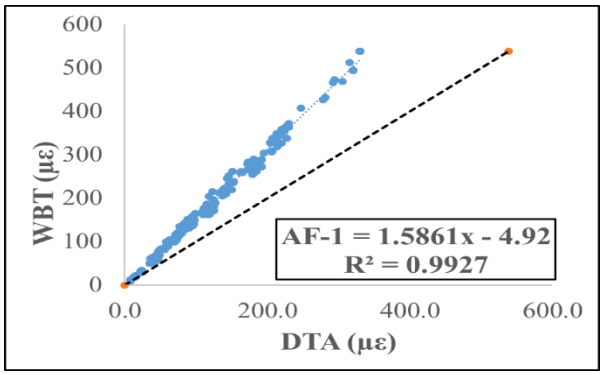

Figure 106. Graph. Maximum tensile strain along transverse direction at bottom of AC.

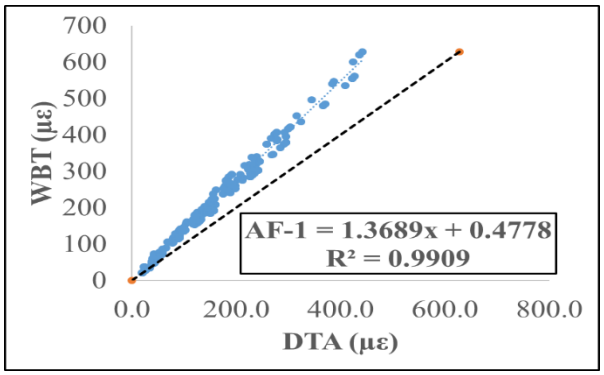

Figure 107. Graph. Maximum compressive strain within AC.

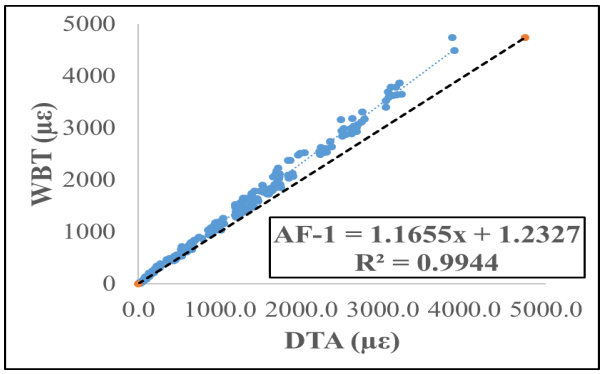

Figure 108. Graph. Maximum compressive strain within base.

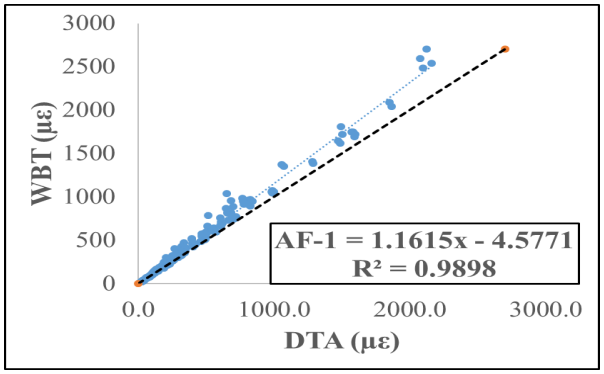

Figure 109. Graph. Maximum compressive strain within subgrade.

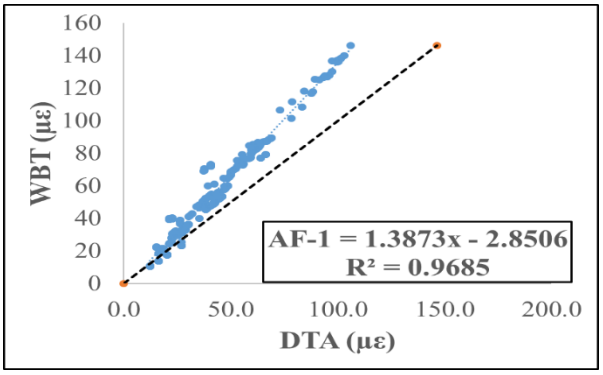

Figure 110. Graph. Maximum shear strain within AC.

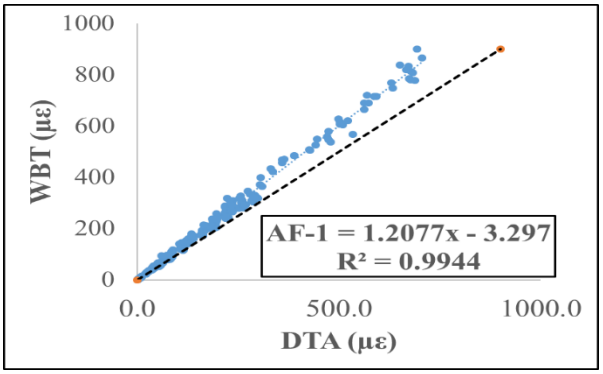

Figure 111. Graph. Maximum shear strain within base.

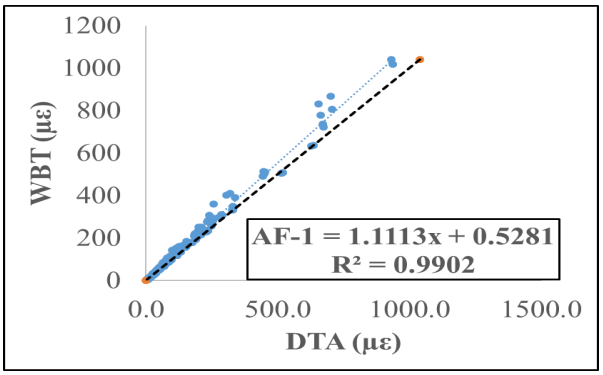

Figure 112. Graph. Maximum shear strain within subgrade.

Adjustment Factor 2

Adjustment factor 2 (*AF2*) was developed to modify the responses obtained from MEPDG procedure in accordance with FE analysis where tire-pavement interactions are simulated more accurately. The FE runs using DTA capturing extreme conditions (i.e., thick and thin pavement structures with strong and weak material properties) were used.

Initially, the AASHTOWare software was considered to obtain responses for the 336 cases. However, the implementation of MEPDG procedure as a separate numerical tool was needed for two reasons. First, it is time-consuming and cumbersome to run the AASHTOWare software for 336 cases, because the software uses a significant amount of inputs that makes comparison to FE results impossible. For instance, the software uses axle load spectra, and only one set of contact stresses belonging to the specific axle load/tire pressure combination is considered in each FE simulation. In addition, AASHTOWare has temperature-based models for material characterization of base and subgrade. Conversely, in FE analysis, the base and subgrade are characterized without taking temperature into account as it would take tremendous effort and time to adopt ICM into FE model. Second, the AASHTOWare software only gives critical pavement responses (e.g., tensile strain at the bottom AC or compressive strain within base layer); however, comparing shear strain within the pavement is of interest in this study; which is not provided as an output in the software. It is believed that shear strain in AC is relevant to near-surface and surface cracking.

Therefore, the MEPDG procedure was implemented by exploiting Matlab and AutoHotkey. The main steps of the MEPDG's procedure implementation are listed below:

1. Subdivision of pavement structure in sub-layers.
2. Calculation of dynamic modulus at mid-depth of each sublayer.
3. Creation of input file.
4. Running JULEA (Linear Elastic Computer Program used by MEPDG).
5. Post-processing to obtain pavement responses.

Pavement structures were sub-divided by applying the algorithm provided in MEPDG. Moreover, dynamic moduli were computed based on the frequency calculation guidance given previously.

Input Conversion from FE Model to MEPDG

It is critical to convert all inputs used in the FE analysis into the MEPDG procedure to be able to run comparable cases. Table 32 compares all inputs from FEA with the MEPDG's procedure.

The same load and tire inflation pressure, applied during experiments to measure contact stresses, were used as loading inputs for MEPDG. The contact area was calculated by dividing the load over tire pressure. While speed was used to calculate frequency of loading using the equation presented in Figure 98, the temperature was embedded into shift factor calculation. The same material parameters (e.g., elastic modulus and master curve) were given as input to both FE model and MEPDG.

The elastic stick model (ESM) was represented in MEPDG procedure. The ESM is an improved version of the well-known Coulomb friction model, is presented as follows:

$$\mu = \frac{\tau_{max}}{\sigma}$$

Figure 113. Equation. Friction coefficient.

where: μ: friction coefficient
τ_{max}= maximum shear stress
σ =normal stress at the interface

ESM allows tangential stress and a certain amount of elastic slip before the surfaces defining the interface start to slip. In Romanoschi and Metcalf (2001) τ_{max} and d_{max} are suggested as 205 psi and 0.063 in for pavement modeling based on direct shear test results. Conversely, MLET assumes uniformly distributed shear spring to connect the interfaces and allow relative horizontal movement between two layers. The spring works in radial direction and follows the relationship:

$$\tau_i = k_i \times (u_i - u_{i+1})$$

Figure 114. Equation. Radial shear stress at the interface between layers i and $i + 1$.

where: τ_i= = radial shear stress at the interface between layers i and i+1
$u_i - u_{i+1}$= relative radial displacement across the interface
k_i= interface spring stiffness

This law can be implemented in any layered elastic computer programs, including JULEA. To reduce numerical complications, JULEA converts the previous equation by using the variable l given in:

$$(1 - l_i) \cdot \tau_i = l_i \cdot (u_i - u_{i+1})$$

Figure 115. Equation. Variable l introduced by JULEA.

$$k_i = \frac{l_i}{1 - l_i}$$

Figure 116. Equation. Spring stiffness.

The variable l is computed using user-defined parameter m:

$$l = \begin{cases} 0 & \text{for } m \geq 100{,}000 \\ 10^{-m/E_2} & \text{for } m < 100{,}000 \end{cases}$$

Figure 117. Equation. Defining the variable l.

where, E_2= modulus of layer 2 (below the surface layer).

The spring stiffness is basically the slope of τ/d (Figure 118), i.e., ratio of τ_{max} and d_{max}. After computing spring stiffness, the user parameter m is calculated using the equation presented in Figure 117

Table 32. FEA and MEPDG Input Comparison

	FE (Reference)	**MEPDG Procedure**
Axle Load (P)	Known	Known
Contact Stress (p)	Nonuniform, 3-D stresses (pressure + traction) – measured for each axle load-known	2D uniform vertical stresses – applied inflation pressure
Contact Area (A)	True contact area – measured for each axle load	Circular (P/p)
Motion of Tire (Speed)	Tire is moved of a given velocity	Implicitly considered in dynamic modulus calculations
Temperature	Directly considered in viscoelastic analysis	Considered in dynamic modulus calculations
Friction Between Layers	Elastic Stick Model, defined by τ_{max} and d_{max}	Friction coefficient (user input)
AC Layer Material Properties	Viscoelastic	Dynamic modulus obtained from master curve
Base Layer	Thick = Linear elastic	Linear elastic
	Thin = Stress-dependent nonlinear model	
Subgrade	Linear elastic	Linear elastic

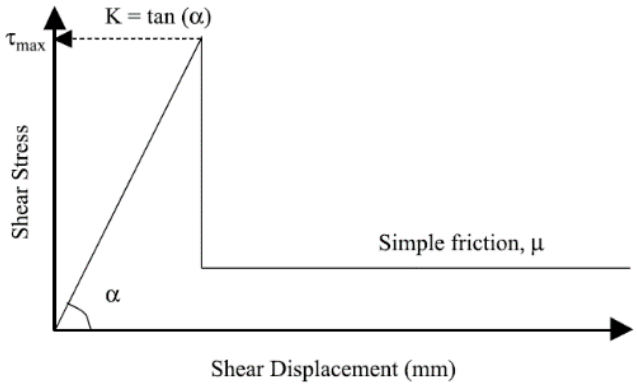

Figure 118. Graph. Elastic stick model.

Results of AF2

Differences in loading conditions between FE and MEPDG (three-dimensionality and non-uniformity of the contact stresses), material characterization, and layer interaction, introduce serious challenges that complicate the development of *AF2*. To obtain statistically good correlation for *AF2*, the cases were divided into thick pavement, thin pavement with strong base material, and thin pavement with weak base material. The reasoning behind this division is discussed in the following section.

AF2 for thick pavement

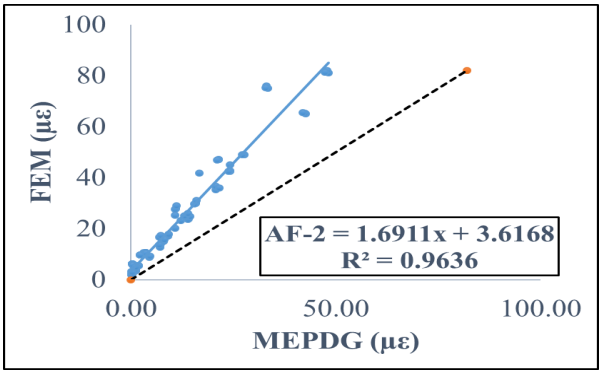

Figure 119. Graph. Maximum tensile strain along traffic direction at AC surface.

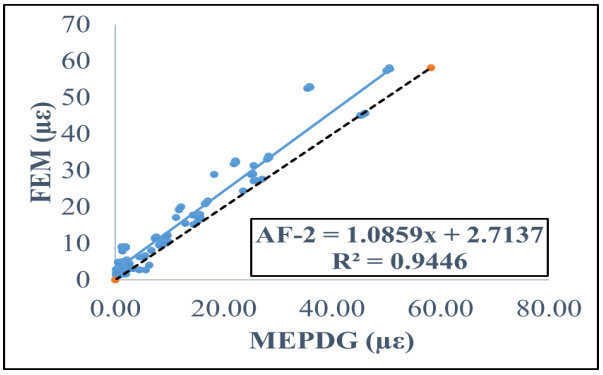

Figure 120. Graph. Maximum tensile strain along transverse direction at AC surface.

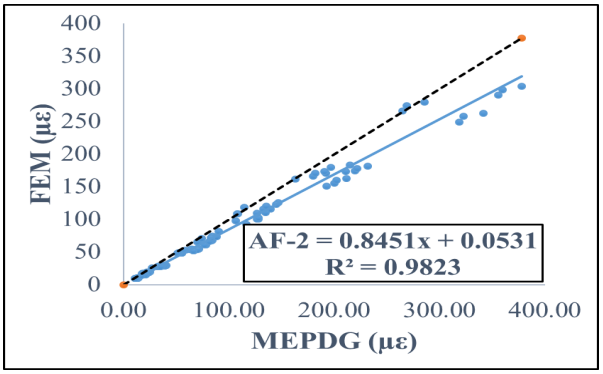

Figure 121. Graph. Maximum tensile strain along traffic direction at bottom of AC layer.

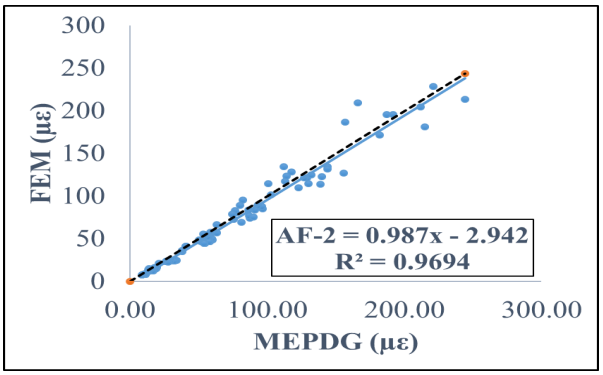

Figure 122. Graph. Maximum tensile strain along transverse direction at bottom of AC layer.

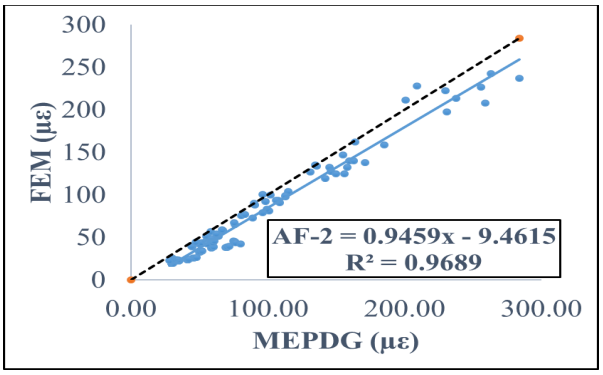

Figure 123. Graph. Maximum compressive strain within AC.

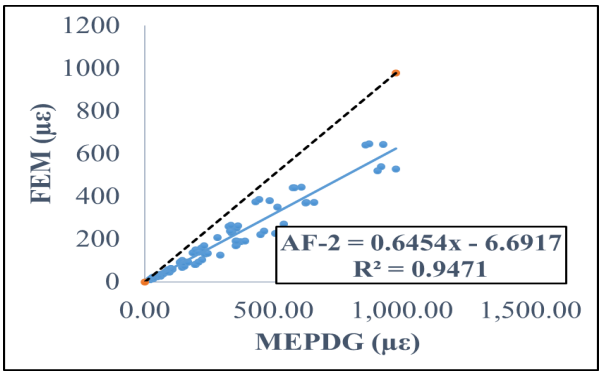

Figure 124. Graph. Maximum compressive strain within base.

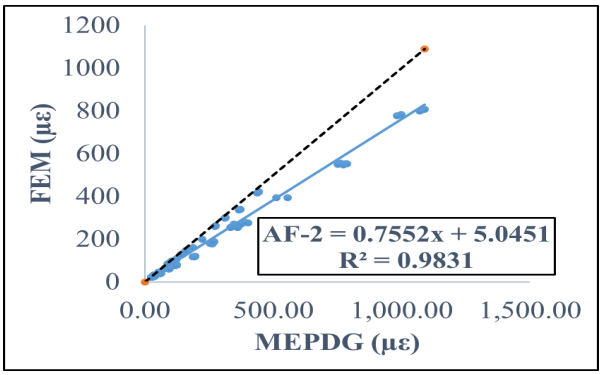

Figure 125. Graph. Maximum compressive strain within subgrade.

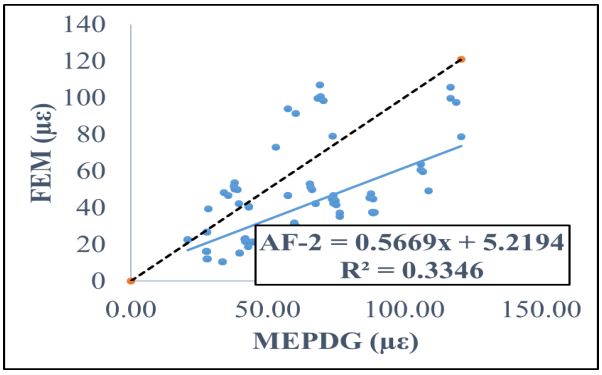

Figure 126. Graph. Maximum shear strain within AC.

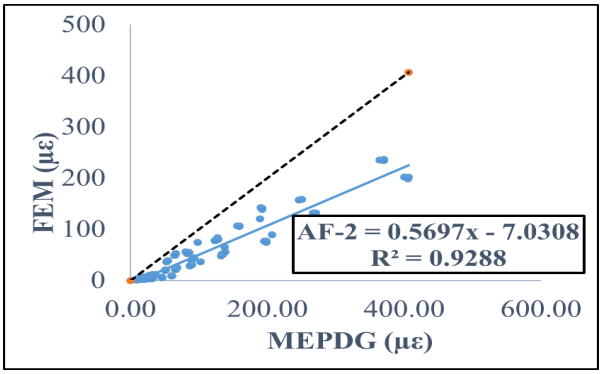

Figure 127. Graph. Maximum shear strain within base.

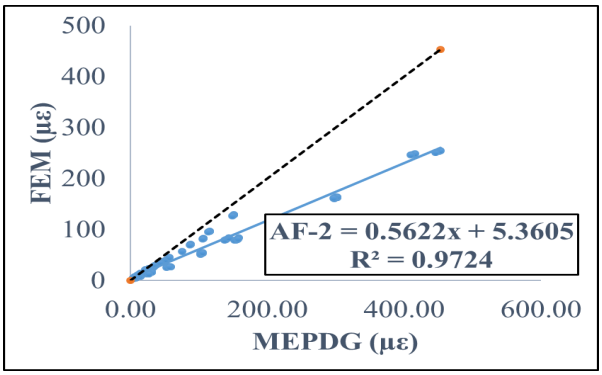

Figure 128. Graph. Maximum shear strain within subgrade.

***AF2* for thin pavement: weak and strong base**

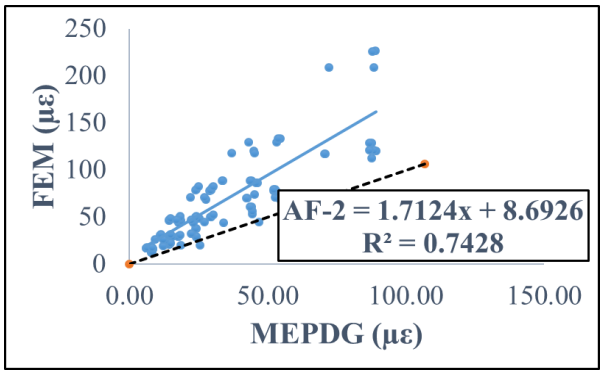

Figure 129. Graph. Maximum tensile strain in traffic direction at AC surface for weak base layers.

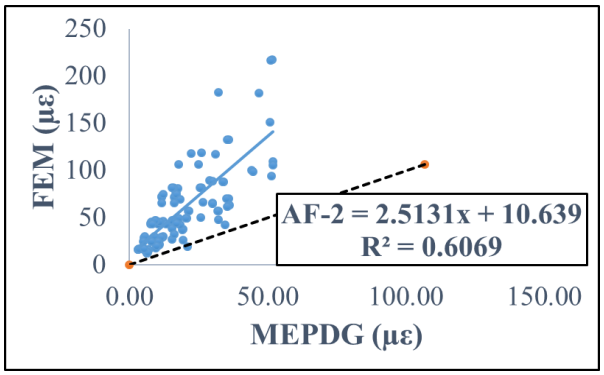

Figure 130. Graph. Maximum tensile strain in traffic direction at AC surface strong base layers.

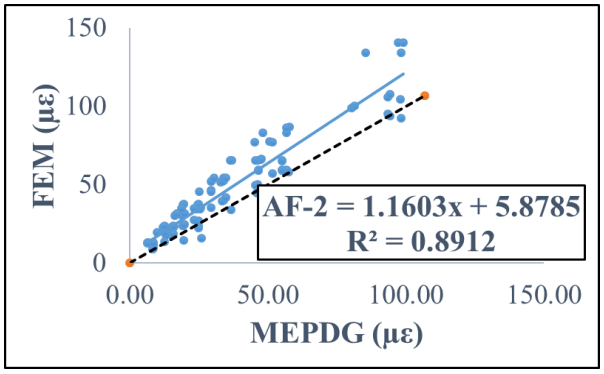

Figure 131. Graph. Maximum tensile strain in transverse direction at AC surface for weak base layers.

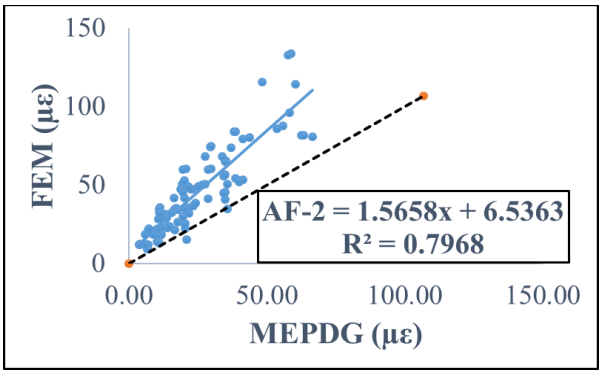

Figure 132. Graph. Maximum tensile strain in transverse direction at AC surface for strong base layers.

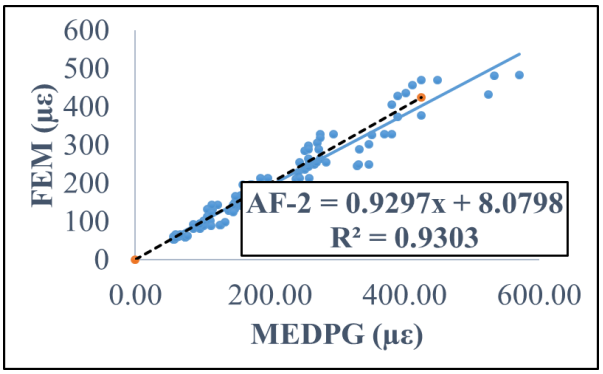

Figure 133. Graph. Maximum tensile strain in traffic direction at bottom of AC layer for weak base layers.

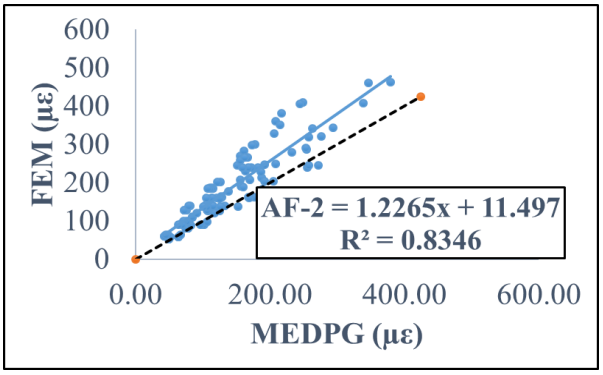

Figure 134. Graph. Maximum tensile strain in traffic direction at bottom of AC layer for strong base layers.

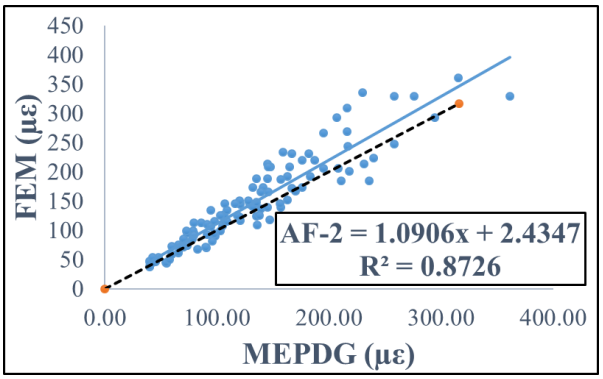

Figure 135. Graph. Maximum tensile strain in transverse direction at bottom of AC layer for weak base layers.

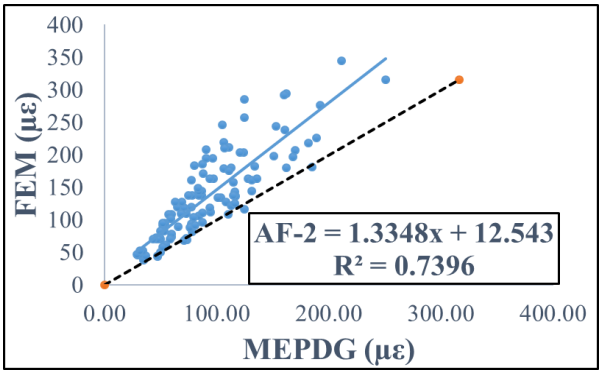

Figure 136. Graph. Maximum tensile strain in transverse direction at bottom of AC layer for strong base layers.

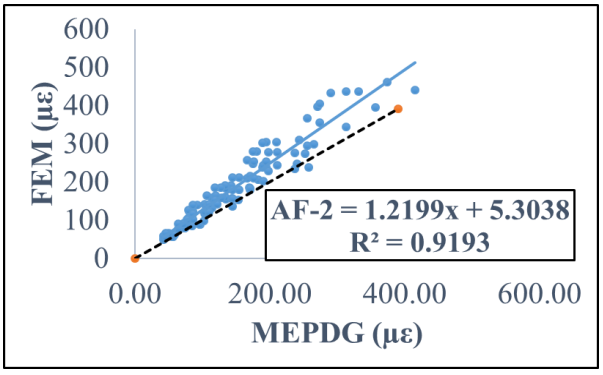

Figure 137. Graph. Maximum compressive strain within AC layer for weak base layers.

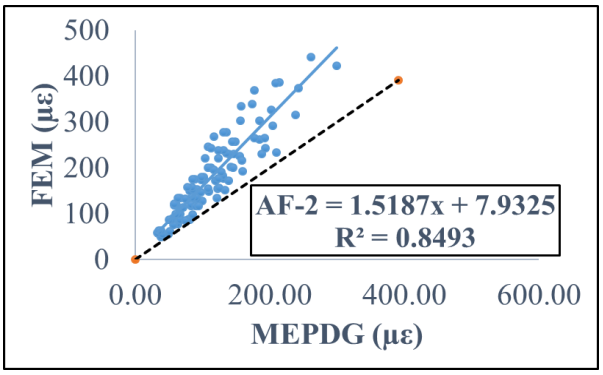

Figure 138. Graph. Maximum compressive strain within AC layer for strong base layers.

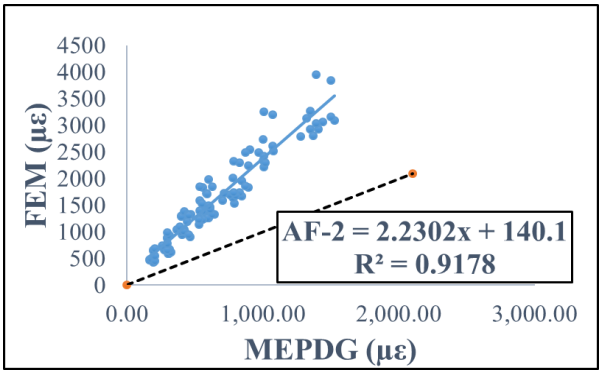

Figure 139. Graph. Maximum compressive strain within base for strong base layers.

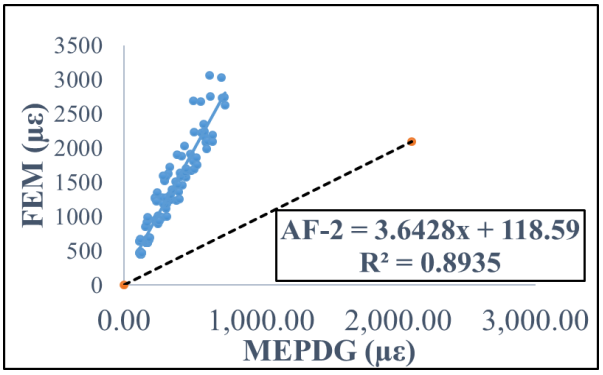

Figure 140. Graph. Maximum compressive strain within base for strong base layers.

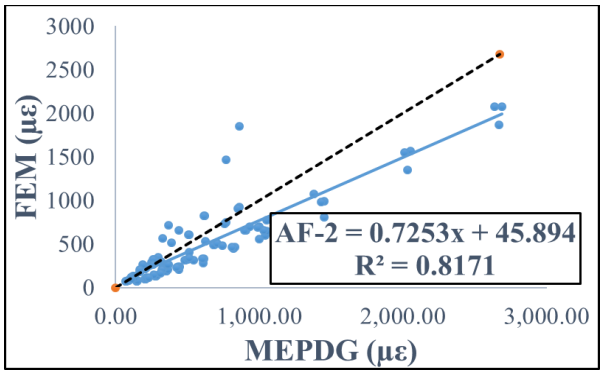

Figure 141. Graph. Maximum compressive strain within subgrade for weak base layers.

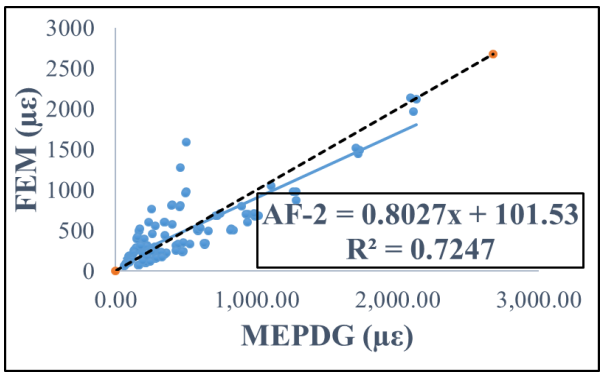

Figure 142. Graph. Maximum compressive strain within subgrade for strong base layers.

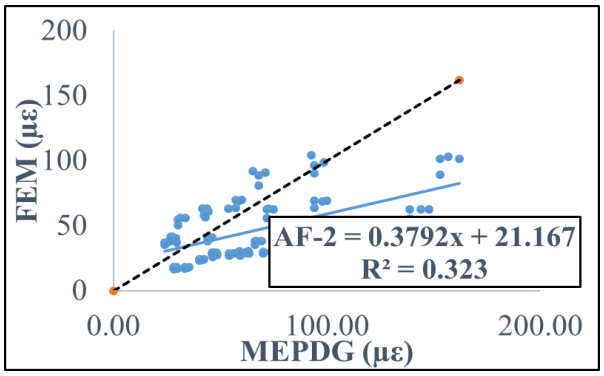

Figure 143. Graph. Maximum shear strain within AC layer for weak base layers.

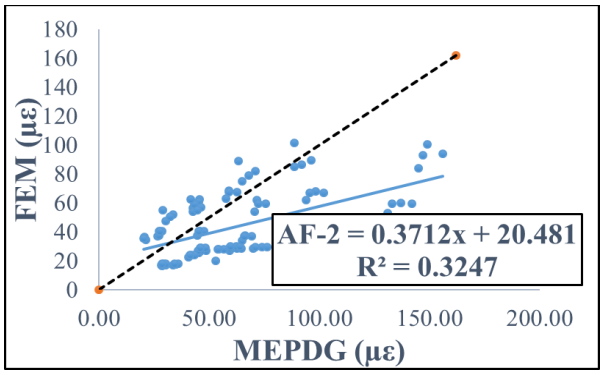

Figure 144. Graph. Maximum shear strain within AC layer for strong base layers.

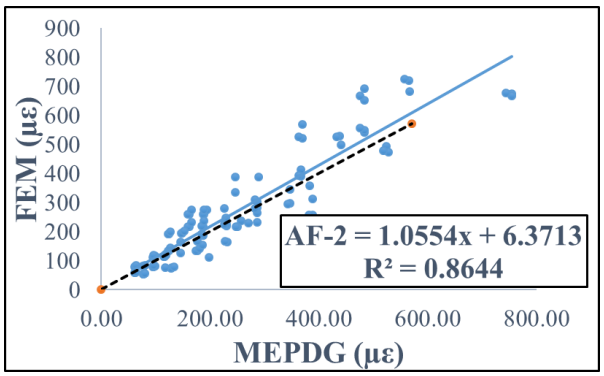

Figure 145. Graph. Maximum shear strain within base layer for weak base layers.

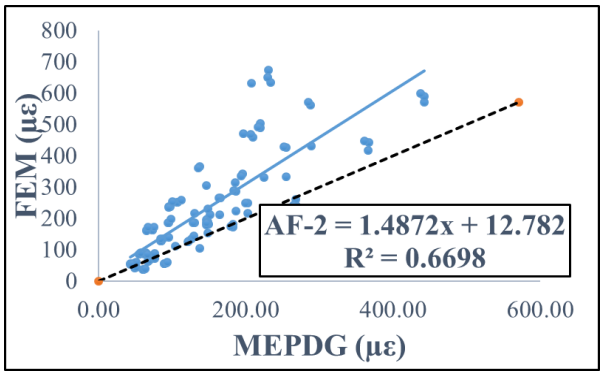

Figure 146. Graph. Maximum shear strain within base layer for strong base layers.

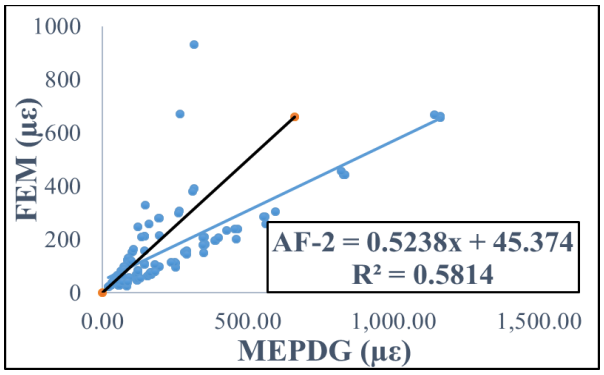

Figure 147. Graph. Maximum shear strain within subgrade for weak base layers.

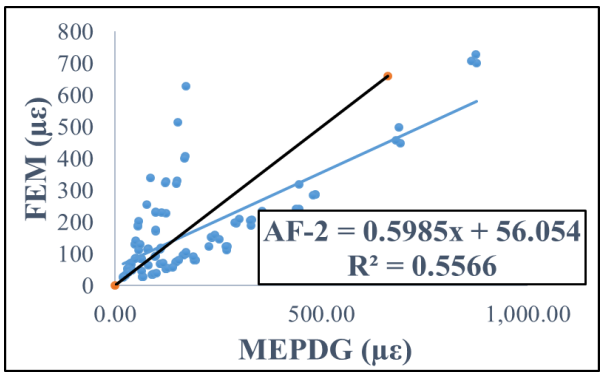

Figure 148. Graph. Maximum shear strain within subgrade for weak base layers.

DISCUSSION OF RESULTS

Importance of Using Advanced Analysis

As discussed earlier, FE and MEPDG procedures have significant differences regarding tire-pavement interaction. Among many others, 3-D nonuniform contact stress and nonlinear material characterization for base layer (in the case of thin pavement) seem to result in the highest differences in pavement responses between the two methods. Observations and comments on *AF2* results are presented as follows:

- After performing analyses on all cases (MEPDG versus FE analysis), two different trends were clearly observed based on AC layer thickness (thick or thin pavement). The effect of contact stresses diminishes as depth increases. Similar observations were reported by Al-Qadi and Yoo (2007). Therefore, the thick pavement cases were separated from the thin pavement cases when developing *AF2*.
- Thin pavement was separated into two different groups depending on its base material characterization (i.e., strong or weak) because of its nonlinear stress-dependent behavior.
- Higher R^2-values were obtained for thick pavement than for thin pavement because thick pavement responses were less affected by nonuniform contact stresses. Besides, stress-

dependent, nonlinear characterization complicates the comparison between FE and MEPDG for thin pavement.

- The coefficients of the independent variable in the fitted equations for thick pavement is smaller than 1 for all the responses except tensile strain at the surface. Consequently, it can be said that MEPDG overestimates the other pavement responses.
- There is no regular trend for thin pavement in terms of the coefficients of independent variable in the fitted equations. While MEPDG procedure yielded higher values for maximum compressive strain within subgrade, FE resulted in higher values for other type of responses such as tensile strain at the bottom of AC and compressive strain within AC and base layers.
- FE provided higher compressive strain within base than MEPDG's procedure for thin pavement. This observation emphasizes the importance of considering stress-dependent, nonlinear characterization for base material.
- The maximum shear strain within AC occurs at shallow depths (around 1 in below the AC surface), so it is governed by the nonuniform, 3-D contact stresses, which are not considered in the MEPDG procedure. Hence, as shown in Figure 126 and Figure 143low R^2 (between 0.2 and 0.3) was obtained for maximum shear within the AC.
- Maximum tensile strains at AC surface occurred far away from the loaded area, where the axle load was the dominant factor on pavement responses. Therefore, the R^2 value is generally high for maximum tensile strain at the surface.
- MEPDG procedure underestimates the maximum tensile strain at the AC surface for both thin and thick cases, which conforms to the literature.

Effect of Wide-Base Tire

AF1 was developed to convert responses from DTA to NG-WBT. Only FEA simulations were used for *AF1* because MLET cannot properly simulate WBT loading. Below are significant observations regarding *AF1*:

- *AF1* was developed for a total of ten different pavement responses. Responses obtained from MEPDG and FE analysis showed a strong correlation, as indicated by the fact that the coefficient of correlation is close to one for all cases.
- The coefficient of the independent variable in the equation for *AF1* is always higher than 1 for all responses. This indicates that NG-WBT causes higher responses than DTA for the same axle load and tire inflation pressure, which might result in greater pavement damage.
- *AF1* was developed for all cases without dividing the cases into subgroups. In other words, *AF1* can be applied to DTA responses for predicting NG-WBT response regardless of the material property and pavement structure used in MEPDG.

DEMOSTRATION OF ADJUSTMENT FACTORS APPLICATION

Numerical Example

Table 33 presents the numerical example of how adjustment factors can be applied to responses obtained from MEPDG.

Table 33. Numerical Example of Adjustment Factor Application

Response	MEPDG	With *AF1*	With *AF2*	With *AF1 x AF2*
$\varepsilon_{22,subg}$ (μ)	557.0	670.1	403.9	482.4

$\varepsilon_{22,subg}$, the maximum strain at the top of subgrade, is used as an example. MEPDG computes this response as 557.0 μ for 10 kip axle load, 110 psi tire inflation pressure, 5 in AC thickness and 6 in base layer thickness. This response increased to 670.1 με after applying *AF1* (*AF1 = 1.2258 x MEPDG – 12.681)*. It means that $\varepsilon_{22,subg}$ would increase to 670.1 με from 557.0 με if NG-WBT was used instead of DTA for same axle load and tire inflation pressure. On the other hand, the same response decreased to 403.9 με when *AF2* (*AF2=0.7443 x MEPDG – 10.163)* was applied. In other words, $\varepsilon_{22,subg}$ would drop to 430.9 με from 557.0 με if pavement were analyzed considering realistic loading conditions and material characterization. Finally, the last column shows the combined effect of *AF1* and *AF2*. It indicates that $\varepsilon_{22,subg}$ would decrease to 482.4 from 557.0 με if the tire were wide-base and the pavement were analyzed considering realistic conditions.

Pavement ME Design

Idea of implementing adjustment factor on AASHTOWare is demonstrated in Figure 149. There are two tick boxes suggested: one for considering wide-base tire effect during analysis, and one for considering model complexity effect such as three dimensional contact stress, non-linear base characterization, etc. User can activate either of them or both of them at the same time.

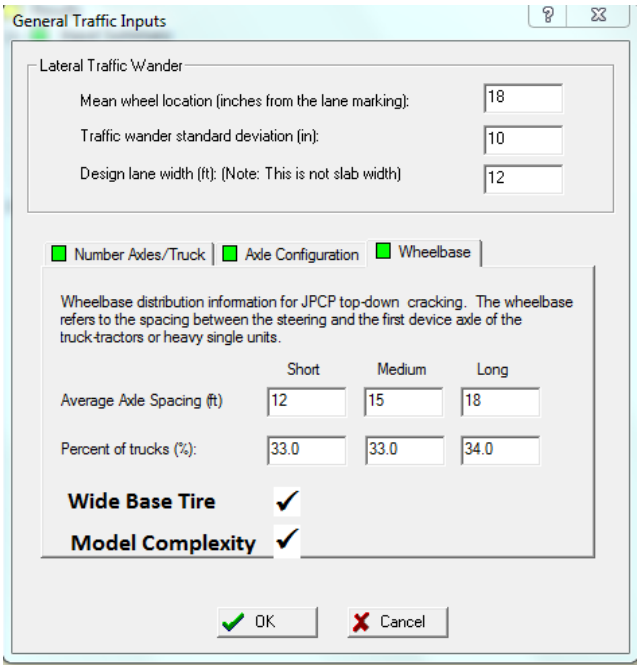

Figure 149. Illustration. Demonstration of adjustment factors implementation to pavement ME design software.

Implementation of *AF2* on the software is straight forward since it does not require any additional input parameters. In case of model complexity tick box activated by the user, the default strain value calculated by the software will be multiplied by *AF2* to account for advance simulation effects on the response. The new modified strain will be used in transfer functions to predict pavement performance.

By contrast, implementation of *AF1* requires additional information such as NG-WBT penetration in traffic. This additional input may complicate the implementation of *AF1* on the software. However, this can be implemented in the distress models. In case of fatigue crack prediction, it is recommended to account for NG-WBT penetration after calculating allowable number of axle-load applications (*Nf*) for each tire. Then, use modified *Nf* to predict fatigue crack propagation. For example, *Nf*(*WBT*) and *Nf(DTA)* are calculated as 1 million and 2 million, respectively. Note that *Nf*(*WBT*) stands for allowable number of axle-load repetition that is calculated using adjusted pavement response by *AF1*. Assuming 10% NG-WBT penetration, *Nf(combined)* should be calculated as such 0.9 x *Nf(DTA)* + 0.1 x *Nf(WBT)* = 1.9 million. Finally, this modified *Nf(combined)* should be used in Miner's rule equation to predict fatigue cracking.

Implementation of *AF1* for permanent deformation is relatively simpler as compared to fatigue cracking. Because transfer function used for predicting permanent deformation has linear relation with calculated response. Hence suggested approach is to calculate permanent deformation (*PD*) for two tire types and combine them considering NG-WBT penetration. For example, *PD(DTA)* and *PD(WBT)* are predicted as 0.15 and 0.20 in. Note that *PD(WBT)* is calculated using adjusted strain by *AF1*. Then *PD(combined)* should be reported as 0.9 x *P(DTA)* + 0.1 x P(WBT)=0.155 in.

SUMMARY

This chapter presents the theoretical background and results of adjustment factors, which may be applied to the ME pavement design software. Two different adjustment factors were developed to correct responses resulting from MEPDG. The first one converts DTA to WBT responses, which are always greater than that of DTA. This adjustment, *AF1*, was developed with high coefficient of determination. The second factor, *AF2*, accounts for the model complexities such as 3-D contact stresses, stress-dependent, nonlinear base material and accurate material and interface models. Although *AF2* showed high R^2-value for thick pavement, it was slightly lower for thin pavement. Stress-dependent, nonlinear base and the higher influence of nonuniform, 3-D contact stress caused lower coefficient of determination in thin pavements.

CHAPTER 8. EXPERIMENTAL PAVEMENT SECTIONS

TEST SECTIONS AT FLORIDA DOT

The pavement structure and instrumentation of the typical pavement section built in Florida are presented in Figure 150 through Figure 153. The sections were built at two locations: test pit and test track. Instrumentation was installed on top of the subgrade in the test pit section. Two pressure cells were placed on top of the subgrade and H-type strain gauges were placed at the bottom of the AC layers (three in each direction).

Three pavement structures were built at the test track. The AC layer of one section had a thickness of less than 1 in (SP-12.5 PG 67-22). No material characterization is available for the existing layer. A new AC layer (SP-12.5) was placed in two lifts, 1.5 in each with PG 76-22 binder. Each lift had various combinations of polymer and rubber to meet PG 76-22 binder. No instrumentation was installed in this section. Out of the two other sections, only one was instrumented with pressure cells. Each section had an existing 1.5-in AC (SP 12.5 PG 67-22). Two lifts of AC were placed, the first was 1.5-in SP-12.5 PG 67-22, and the second one, the surface lift, was either 12.5-, 9.5-, or 1-in of 0.187 in mix with PG 67-22 binder. One section was instrumented at the bottom of the new AC layers using three strain gauges in both directions. Similar instrumentation was applied at 1 in from the surface. Dynatest H-type strain gauges and pressure cells were used as pavement responses instrumentation. In addition, surface instrumentation, foil gauges, were installed at various offsets, as presented in Figures 147 and 148. Six sets of foil gauges, three in each traffic direction, were installed on the surface. Each set had four foil gauges at 3-in intervals from tire edge. The load and tire inflation pressure used during the APT is shown in Table 34; the speed during testing was 5 mph. More details regarding the testing facility, construction, instrumentation and testing are presented in Appendix E.

Table 34. Test Matrix for APT at Florida DOT

Tire Type	Tire Inflation Pressure (psi)	Tire Loading (kN)	Tire Loading (kN)	Tire Loading (kN)	Tire Loading (kN)	Tire Loading (kN)
WBT and DTA	80	6.0	8.0	10.0	14.0	18.0
WBT and DTA	100	6.0	8.0	10.0	14.0	18.0
WBT and DTA	110	6.0	8.0	10.0	14.0	18.0
WBT and DTA	125	6.0	8.0	10.0	14.0	18.0
DTA Only	60/110*	6.0	8.0	10.0	14.0	18.0
DTA Only	80/110*	6.0	8.0	10.0	14.0	18.0

**Differential tire inflation pressure*

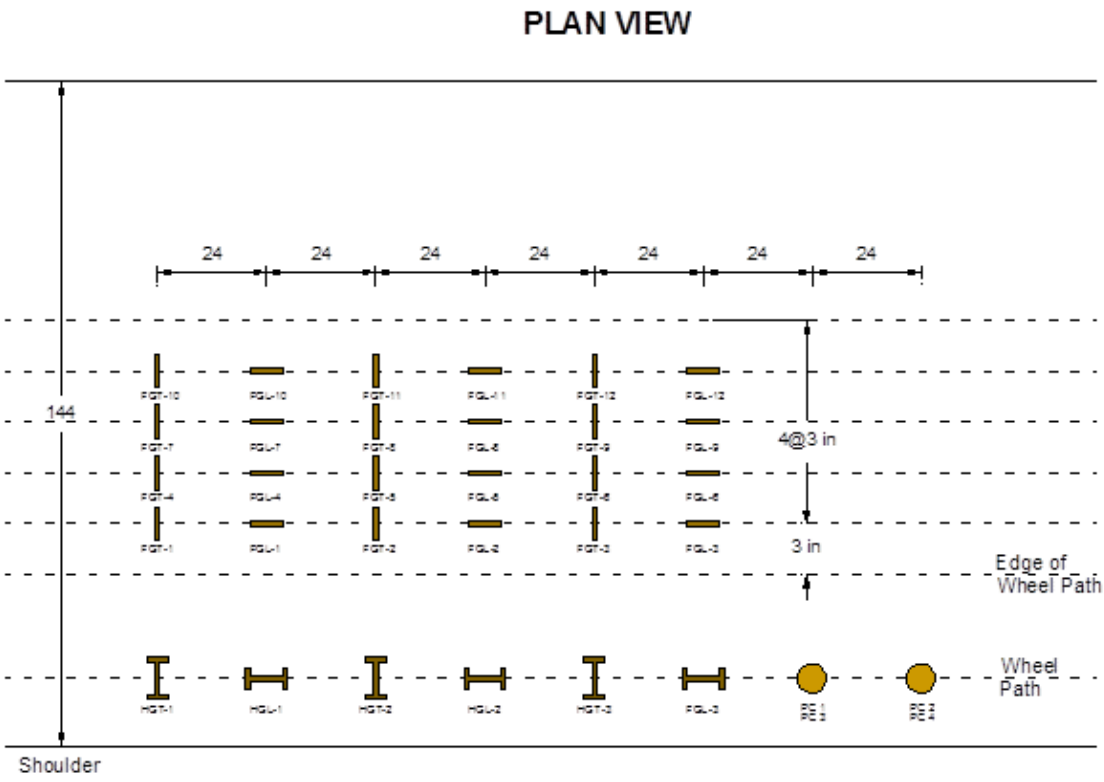

Figure 150. Illustration. Plan view of pavement structure and instrumentation for the test pit section.

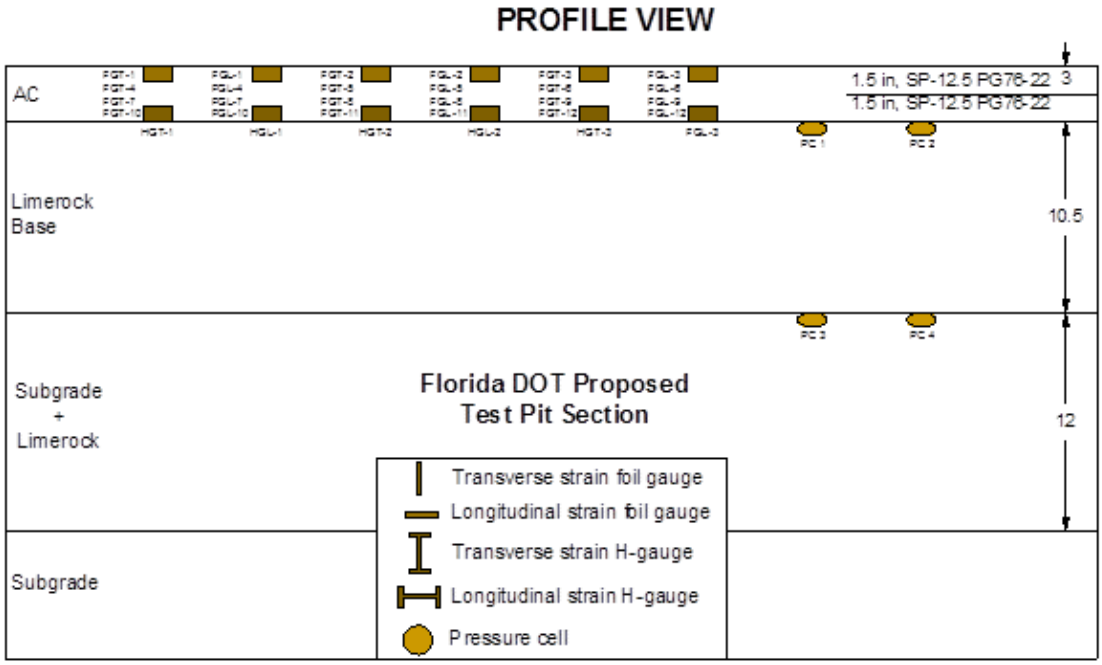

Figure 151. Illustration. Profile view of pavement structure and instrumentation for the test pit section.

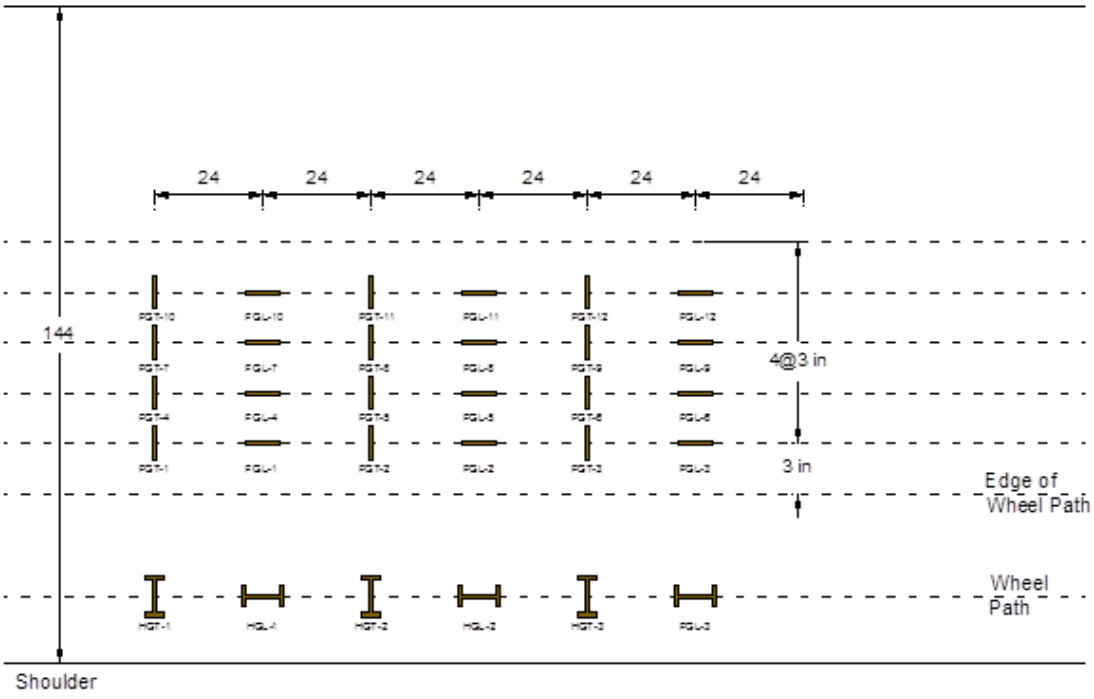

Figure 152. Illustration. Plan view of pavement structure and instrumentation for the test track section.

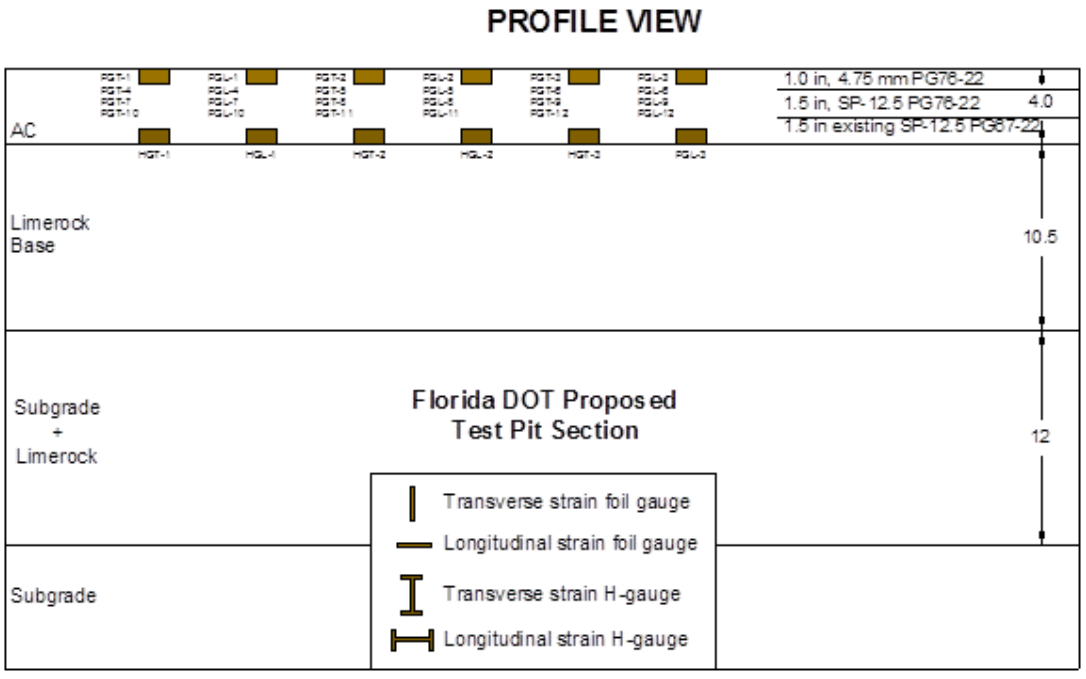

Figure 153. Illustration. Profile view of pavement structure and instrumentation for the test track section.

TEST SECTIONS AT UC-DAVIS

Figures 149 and 150 graphically describe the typical pavement structures built at UC-Davis. The two test sections are approximately 157.5 ft long and 13.1 ft wide with 10.6 in granular base layer on top of clayey subgrade. In addition, 10 in of granular recycled AC layer was placed on top of the base layer and 4.7 in wearing surface. The wearing surface of each section was 15% and 50% AC reclaimed asphalt pavement (RAP). The base was full-depth reclamation with no stabilizer (FDR-NS) for both sections. The instrumentation included strain gauges (Tokyo Sokki KM-100HAS) in both directions under each lift of the AC layer (2.4 in thick), and they were located at the middle of the wheel path. Each section had eight strain gauges, four under each lift of the surface layer. In addition, two pressure cells were installed at the bottom of the recycled granular layer and two at the bottom of the AC wearing surface in the section with 15% RAP. To measure deflection at different depths in the pavement structure, multi-depth deflectometers were used to complement the instrumentation response measurements.

The load and tire inflation pressure used during the APT is given in Table 34; the speed during testing was 5 mph, 100 cycles each. The temperature was set at a depth of 0.8 in from the surface as used by the Strategic Highway Research Program (SHRP). The traffic load was applied bi-directionally (back and forth) and was performed from low to high load and from low to high temperature to avoid pavement damage. Furthermore, a test was performed at different offsets for NG-WBT and DTA for a specific value of temperature, tire inflation pressure, and load (temperature=122 °F, tire inflation pressure=80 and 125 psi, and load=10 kips). The offset, or the distance from sensor line to tire center, was 7 and 12 in for both tires.

TEST SECTIONS AT DELAWARE, OHIO

The pavement structure and instrumentation of the three sections built in Ohio are presented in Figure 160 and Figure 167. The total thicknesses of the AC layer for the sections are 13 in for Sections A and B, and 15 in for Section C. For Sections A and B, the thickness of the asphalt treated base (ATB) is 6 in, while for Section C is 8 in. H-type strain gauges were installed at three different depths: the bottom of the fatigue resistant layer (FRL), the bottom of the ATB, and the bottom of upper lift of the surface layer. In addition, six longitudinal sensors were placed at the bottom of the FRL; six at the bottom of the ATB (3 longitudinal and 3 transverse); and four close to the surface (2 longitudinal and 2 transverse).

Instrumentation of these sections also included LVDTs, pressure cells, and strain gauge rosettes (SGR) as shown in Figure 164 and Figure 166. In addition to the pressure cells on top of the subgrade, another two pressure cells were installed at the bottom of the FRL. A total of 16 SGR were installed in Section A, two holes, and eight rosettes in each hole at four depths. One of the two holes was circular and the other rectangular. Section B had the same number of SGR and distribution as Section A.

During construction and instrumentation of the perpetual pavement sections in Ohio, samples of AC pavement were collected to perform laboratory test and further analysis of the pavement sections

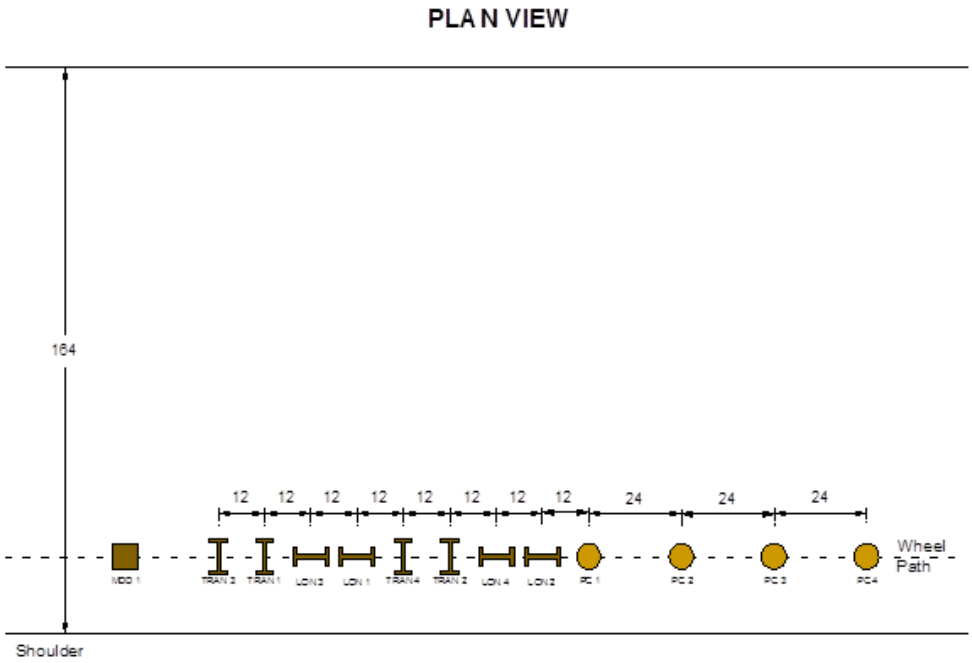

Figure 154. Illustration. Plan view of pavement structure and instrumentation for the 15%-RAP-AC test section at UC-Davis.

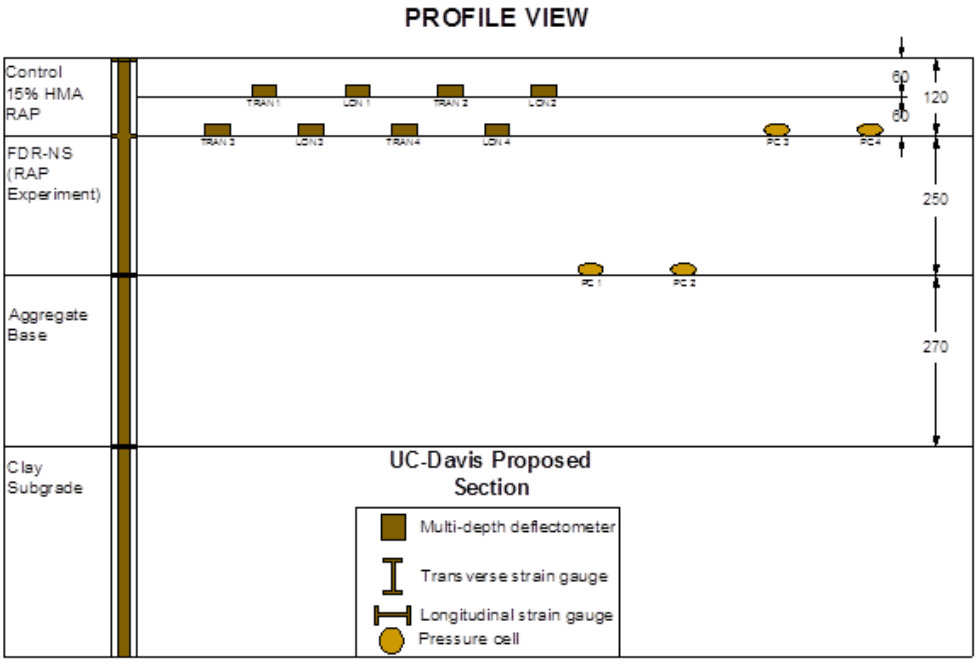

Figure 155. Illustration. Profile view of pavement structure and instrumentation for the 15%-RAP-AC test section at UC-Davis.

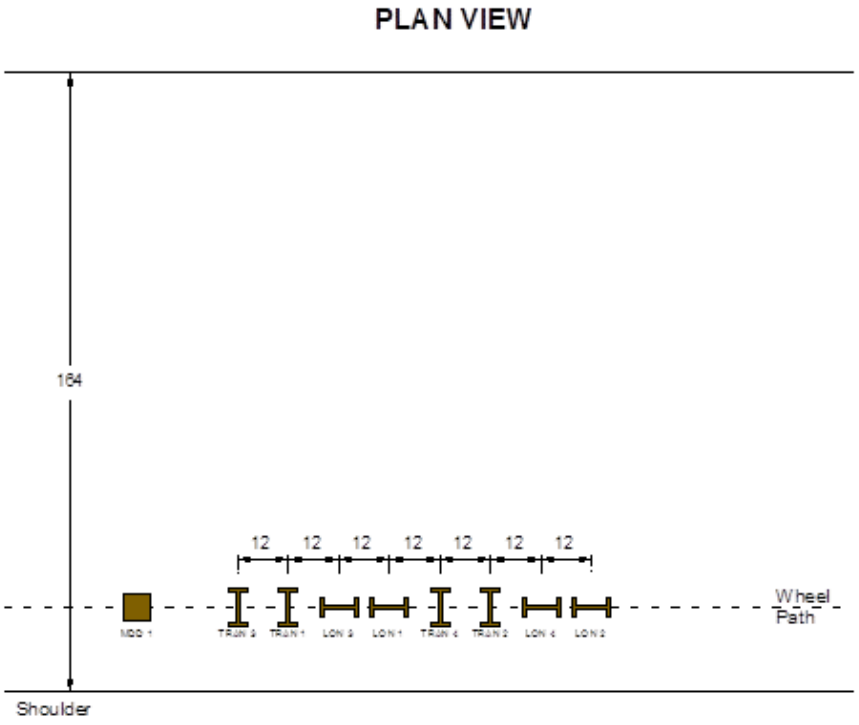

Figure 156. Illustration. Plan view of pavement structure and instrumentation for the 50%-RAP-AC test section at UC-Davis.

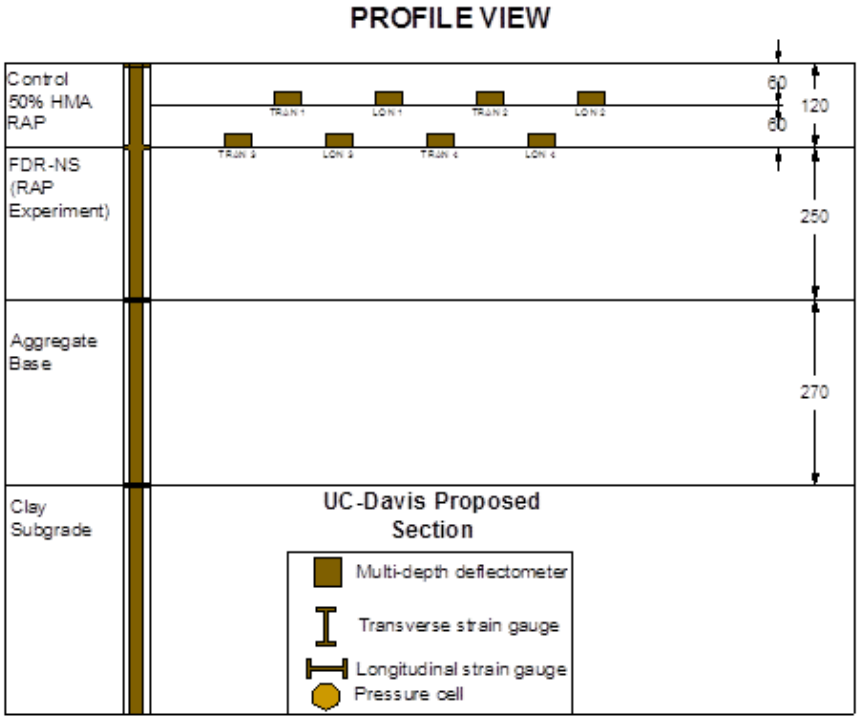

Figure 157. Illustration. Profile view of pavement structure and instrumentation for the 50%-RAP-AC test section at UC-Davis.

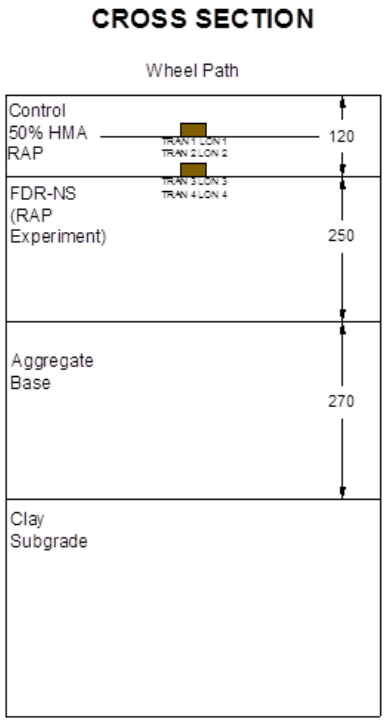

Figure 158. Illustration. Cross section of pavement structures and instrumentation for the 50%-RAP test section at UC-Davis (Multi-depth deflectometer not shown for clarity).

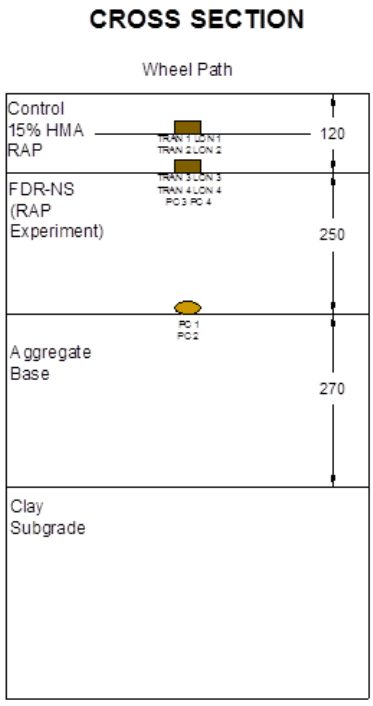

Figure 159. Illustration. Cross section of pavement structures and instrumentation for the 15%-RAP test section at UC-Davis (Multi-depth deflectometer not shown for clarity).

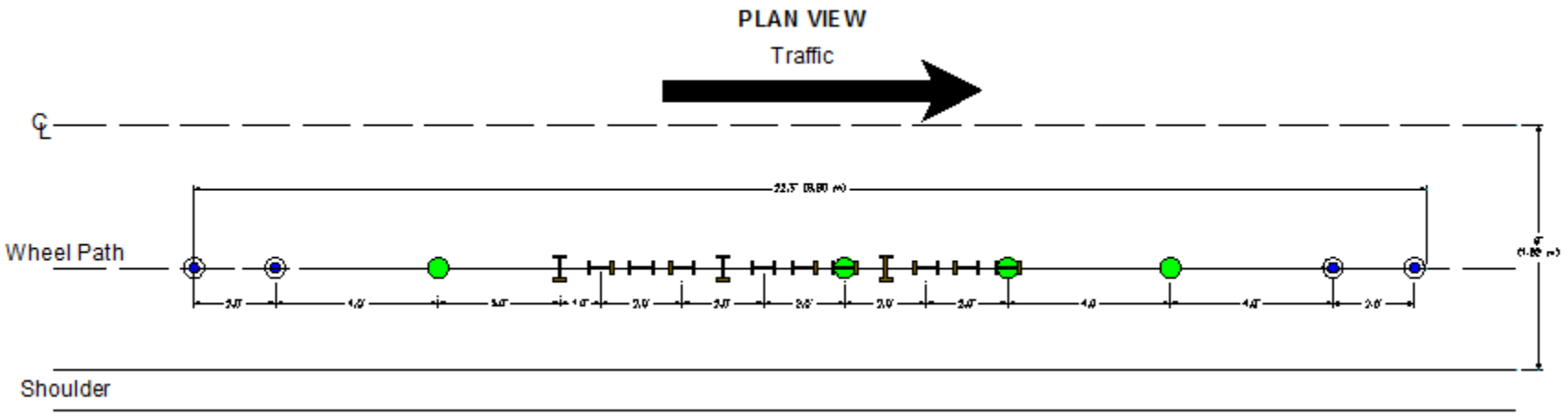

Figure 160. Illustration. Plan view of pavement structure and instrumentation of Sections A and B (13-in-thick).

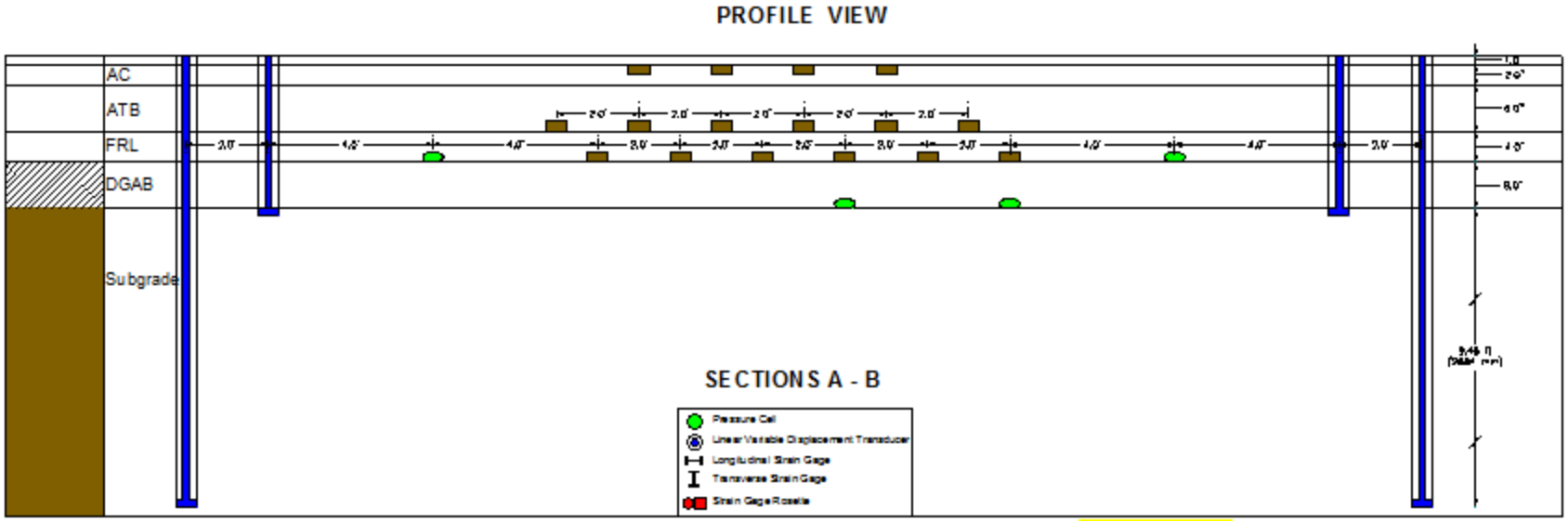

Figure 161. Illustration. Profile view of pavement structure and instrumentation of Sections A and B (13-in-thick).

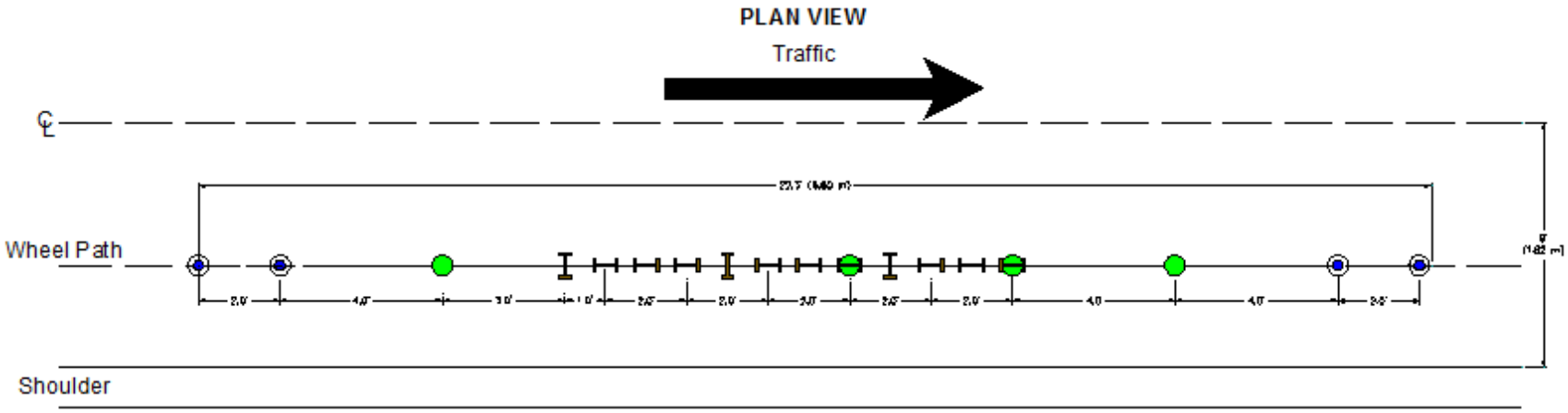

Figure 162. Illustration. Plan view of pavement structure and instrumentation of Section C (15-in-thick).

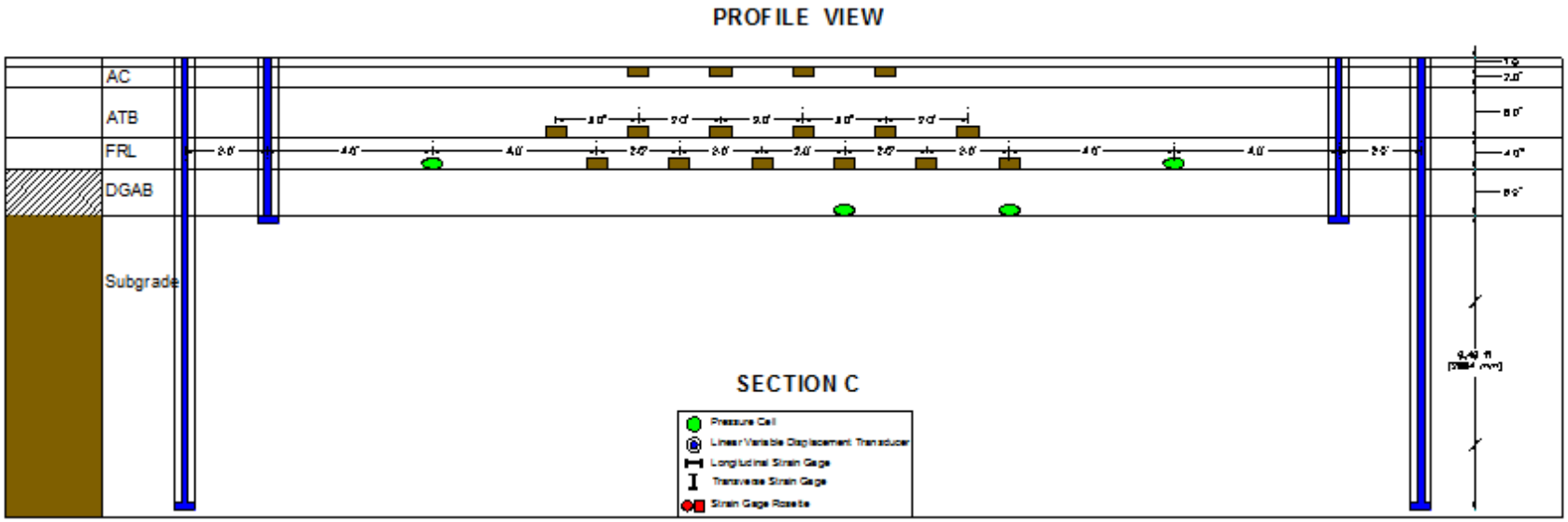

Figure 163. Illustration. Profile view of pavement structure and instrumentation of Section C (15-in-thick).

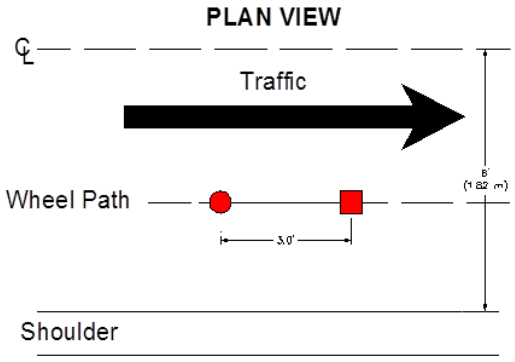

Figure 164. Illustration. Plan view detail of rosettes instrumentation for Sections A and B.

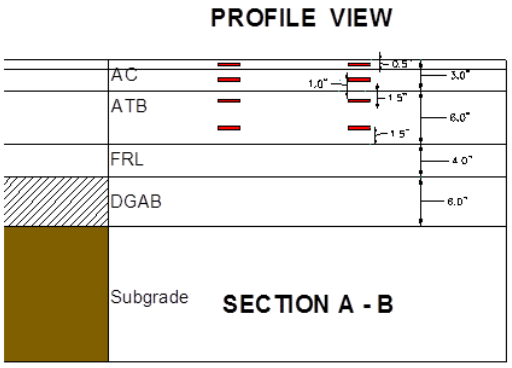

Figure 165. Illustration. Profile view detail of rosettes instrumentation for Sections A and B.

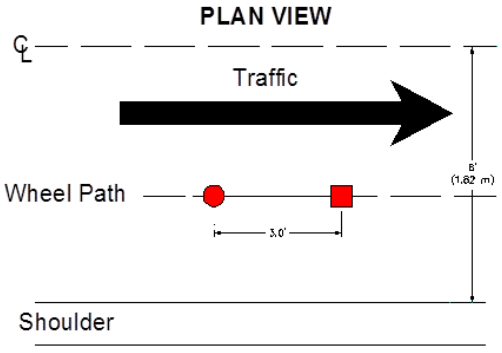

Figure 166. Illustration. Plan view detail of rosettes instrumentation for Section C.

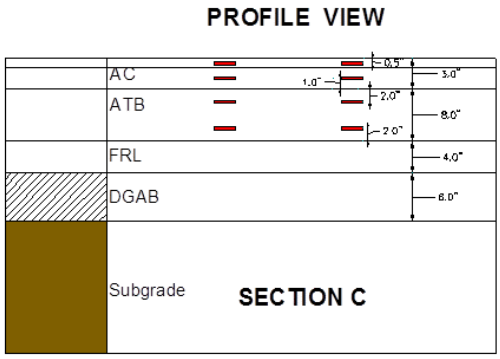

Figure 167. Illustration. Profile view detail of rosettes instrumentation for Section C.

DATABASE MANAGEMENT

An online database was developed to organize data and make the most use of both new and existing data from pavements that used WBT as part of their testing program. Database management procedure includes pre-processing data, filtering and smoothing, max/min response extraction, post-processing and summary, and online application design. Details of max/min response extraction with an example code and step-by-step database management is provided in Appendices G and H, respectively.

SUMMARY

Three new test sites were built and instrumented in Florida, California, and Ohio as part of this study. Strain, stress, and temperature were measured at various locations in the pavement structures. In addition, the research team gathered pavement responses from previous project that used WBT. Existing and new data were compiled and organized in an online database that could be available to the public.

CHAPTER 9. QUANTIFICATION OF PAVEMENT DAMAGE

Transfer functions are used to bridge the gap between mechanistic strain responses to pavement damage, as recommended by the mechanistic-empirical design guide. Five distresses are considered for evaluating pavement damage: three fatigue cracking (including bottom-up, near-surface due to shear, and near-surface due to tensile), AC rutting, and subgrade rutting, wherein each distress is related to a critical pavement response.

FATIGUE CRACKING

As traffic traverses over a pavement, it generates stresses and strains that induce cracking at the bottom of the AC that propagates to the surface after being loaded repeatedly – a phenomenon called bottom-up cracking. On the other hand, near-surface fatigue cracking originates at near-surface of the pavement and propagates downwards. Two mechanisms are believed to cause near-surface cracking: load-associated tensile strains and stresses at the pavement surface, shear stresses close to the tire edge, and aging of the AC. The authors believe near-surface cracking usually occurs close to the surface due the high shear in AC near surface and is frequently mistakenly referred to as top-down cracking.

The transfer function recommended by MEPDG for evaluating the number of repetitions related to fatigue cracking is the following:

$$N_f = k_{f1}(C)(C_H)\beta_{f1}(\varepsilon_t)^{k_{f2}\beta_{f2}}(E_{HMA})^{k_{f3}\beta_{f3}}$$
$$C = 10^M$$
$$M = 4.84\left(\frac{V_{be}}{V_a + V_{be}} - 0.69\right)$$

Figure 168. Equation. Fatigue transfer function.

where:

N_f= allowable number of axle load applications for a flexible pavement and AC overlays
ε_t= tensile or shear strain at critical locations calculated by the structural response model, in/in
E_{HMA}= dynamic modulus of AC measured in compression, psi
K_{f1}, K_{f2}, k_{f3}= global field calibration parameters (from NCHRP 1-40D recalibration, k_{f1} = 0.007566, k_{f2} = -3.9492, k_{f3} = -1.281, from Asphalt Institute, k_{f1} = 0.0796, k_{f2} = -3.291, k_{f3} = -0.854)
β_{f1}, β_{f2}, β_{f3}= local or mixture specific field calibration constants, for global calibration effort, these constants were set to 1.0
V_{be}= effective asphalt content by volume, %
V_a= percent air voids in the AC mixture
C_H= thickness correction term, dependent on cracking type

The equation presented in Figure 169 and Figure 170 pertain to bottom-up and near-surface cracking, respectively.

$$C_H = \frac{1}{0.000398 + \frac{0.003602}{1 + e^{(11.02 - 3.49 H_{HMA})}}}$$

Figure 169. Equation. Thickness correction for bottom-up cracking.

$$C_H = \frac{1}{0.01 + \frac{12.00}{1 + e^{(15.676 - 2.816 H_{HMA})}}}$$

Figure 170. Equation. Thickness correction for near-surface cracking.

where: H_{HMA}= total AC thickness, in

AC RUTTING

Another damage parameter is the permanent deformation or rutting within the AC layer, which results from densification, compression, or lateral movement of AC. The following expression is used to evaluate the number of repetitions to failure, by setting a threshold of $\Delta_{p(HMA)}$=0.5 in for the AC layer deformation.

$$\Delta_{p(HMA)} = \varepsilon_{p(HMA)} h_{HMA} = \beta_{1r} k_z \varepsilon_{r(HMA)} 10^{k_{1r}} n^{k_{2r}\beta_{2r}} T^{k_{3r}\beta_{3r}}$$
$$k_z = (C_1 + C_2 D) 0.328196^D$$
$$C_1 = -0.1039 (h_{HMA})^2 + 2.4868 h_{HMA} - 17.342$$
$$C_2 = 0.0172 (h_{HMA})^2 - 1.7331 h_{HMA} + 27.428$$

Figure 171. Equation. Transfer function and parameters related to AC rutting.

where:

$\Delta_{p(HMA)}$= accumulated permanent deformation in the AC layer/sublayer, in
$\varepsilon_{p(HMA)}$ = accumulated permanent axial strain in the AC layer/sublayer, in/in
$\varepsilon_{r(HMA)}$ = resilient strain calculated by the structural response model at mid-depth of each AC sublayer, in/in
h_{HMA}= AC layer thickness, in
n= number of axle load repetitions
T= pavement temperature, °F
K_z= depth confinement factor
k_{1r}, k_{2r}, k_{3r}= global field calibration parameters (from NCHRP 1-40D recalibration, k_{1r} = -3.35412, k_{2r} = 0.4791, k_{3r} = 1.5606), and

β_{1r}, β_{2r}, β_{3r} = local or mixture specific field calibration constants, for global calibration effort, these constants were set to 1.0
D= depth below the surface, in

SUBGRADE RUTTING

The last type of pavement distress deals with exceeding the elastic limit of the subgrade and is associated with repetitive shear strain in the subgrade. Using the following equation, subgrade rutting is evaluated.

$$N_f = 1.365 * 10^{-9} \varepsilon_v^{-4.477}$$

Figure 172. Equation. Transfer function related to subgrade rutting.

where:

N_f = allowable number of axle load applications for subgrade rutting failure
ε_v = maximum vertical strain on top of subgrade

COMBINED NG-WBT TO DTA RATIO

Each of the five distresses mentioned above results in a ratio of responses between the NG-WBT and DTA, defined as the quotient between the number of repetitions to failure, which corresponds to a reference load and the allowable number of repetition of the load case in question:

$$DW = \frac{N_{ref}}{N}$$

Figure 173. Equation. Response ratio of wide-base tire to dual tire assembly.

where:

DW= ratio of number of repetitions to failure between DTA and NG-WBT
N_{ref}= allowable number of loading repetitions for a reference load
N= allowable number of loading repetitions for a specific load

In this study, for the same applied load and tire inflation pressure, N_{ref} and N correspond to the DTA and NG-WBT cases, respectively. DW>1 indicates that more number of repetitios to failure are needed if DTA is used.

All failure mechanisms considered are combined using a logarithmic weighting factor. This is especially beneficial as the variables to be integrated spread over several orders of magnitude. The combined damage ratio is then calculated as follows:

$$CDW = a_1 DW_{BU} + a_2 DW_{TDS} + a_3 DW_{TDT} + a_4 DW_{RS} + a_5 DW_{RH}$$

$$a_i = \frac{\frac{1}{\log(N_i)}}{\sum_{j=1}^{n} \frac{1}{\log(N_j)}}$$

Figure 174. Equation. Cumulative damage ratio and logarithmic weighting factor.

where:
CDW= combined *WD* ratio
DW_{BU}= *WD* ratio for bottom-up fatigue cracking
DW_{TDS} = *WD* ratio for near-surface cracking caused by shear strain
DW_{TDT} = *WD* ratio for near-surface cracking caused by tensile strain
DW_{RS} = *WD* ratio for subgrade rutting
DW_{RH} = *WD* ratio for AC rutting
n= total number of failure mechanisms considered

For a direct comparison between NG-WBT and DTA, the *CDW* ratio was calculated for the same value of load and tire inflation pressure, taking DTA as reference. For instance, for a load and tire inflation pressure of *P* =10 kip and *S*=110 psi, the corresponding loading cases in Table 24 are *L11* and *L12* for NG-WBT and DTA, respectively. As a consequence, the *CWD* ratio was calculated for *L11* taking *L12*as reference.

THIN PAVEMENT STRUCTURES

Fatigue Cracking (Bottom-up and Near-surface)

Figure 175 through Figure 177 show the average fatigue damage ratio caused by the tensile strain at the bottom of the AC (or bottom up) DW_{BU}, and near-surface caused by shear strain DW_{TDS} and surface tensile strain DW_{TDH}. Each group of bars corresponds to the same load and tire inflation pressure applied to both tires. For instance, *L6:L2* compares NG-WBT and DTA subjected to *P*=6 kip and *S*=125 psi.

Lower damage for DW_{TDT} than the other fatigue cases was noted; the average damage ratio for near-surface fatigue cracking caused by surface tensile strain was 1.28, while for bottom-up and near-surface caused by shear 2.13 and 2.34, respectively. For bottom-up fatigue cracking, DW_{BU} decreased as the magnitude of the applied load increased, and it was less sensitive to layer thickness when the load was high. On the other hand, DW_{TDS} increased as the load increased. In the case if thin pavement, if *AC*=5 in, average DW_{TDT} was not affected by base thickness, applied load, or tire inflation pressure.

AC Rutting

The average damage ratio for AC rutting at different materials is presented in Figure 178. An interesting observation is the small effect of base thickness on the average difference between DW_{RH} of NG-WBT and DTA. A more relevant role of tire inflation pressure was also observed for AC rutting when compared to fatigue cracking if the applied load was low and the AC thickness was 5 in. On the other hand, the tire inflation pressure increased DW_{RH} when the applied load was high regardless of the layer thicknesses.

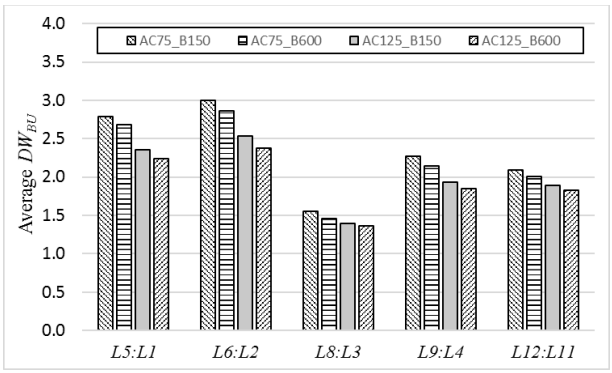

Figure 175. Graph. *DW* for bottom up fatigue cracking in thin pavements.

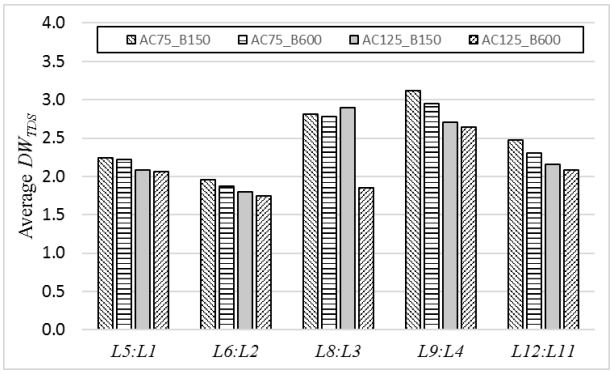

Figure 176. Graph. *DW* for top down fatigue cracking caused by shear strain in thin pavements.

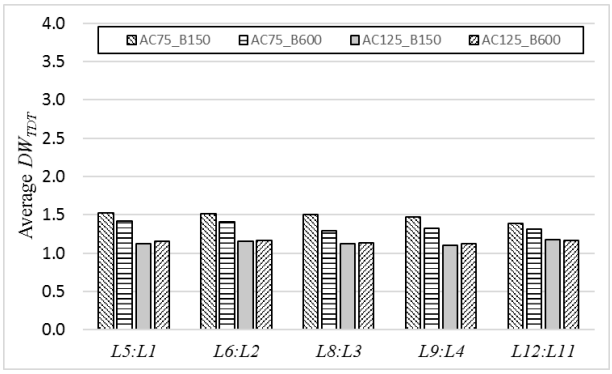

Figure 177. Graph. *DW* for top down fatigue cracking caused by surface strain in thin pavements.

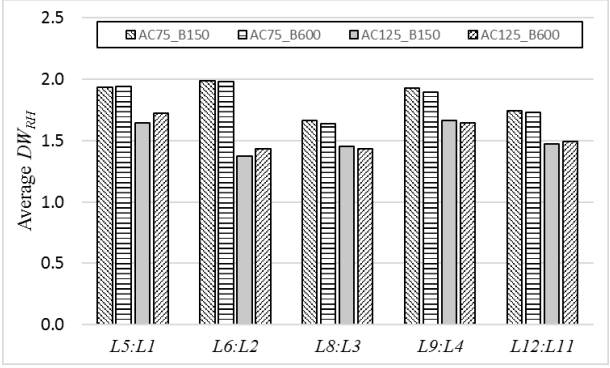

Figure 178. Graph. *DW* for AC rutting in thin pavements.

Subgrade Rutting

Figure 179 shows the average damage ratio for subgrade rutting, which depends on the vertical strain on top of the subgrade. If *AC*=5 in, the effect of base thickness was less significant than for *AC*=3 in because the magnitude of vertical strain in the base layer is smaller for the thick *AC* layer. Also, the effect of tire inflation pressure is more relevant if *AC*=3 in due to the proximity of the subgrade to the loaded area. It should be noted that the average damage ratios for subgrade rutting is low compared to the other distresses. This agrees with previous observation regarding the reduction in difference between NG-WBT and DTA at high pavement depths.

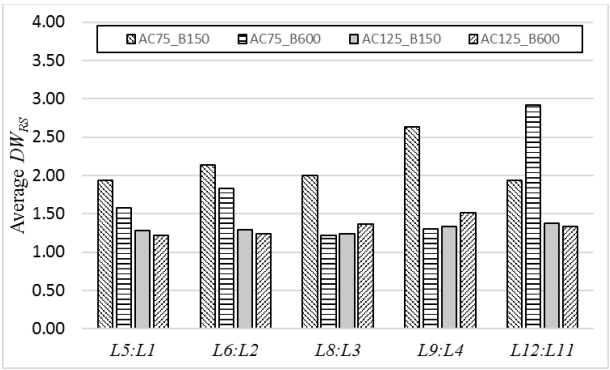

Figure 179. Graph. *DW* for subgrade rutting in thin pavements.

Combined *DW* Ratio

The average CDW ratio for the loading conditions studied is presented in Figure 180. The highest average ratio was 2.4 for *P*=6 kip, *S*=125 psi, *AC*=3 in, and *B*=6 in. The average value in Figure 180 is 1.8, with the highest values generally corresponding to pavement structures with thinnest AC. Even though, as shown in Chapter 5, tire inflation pressure did not greatly affect the magnitude of critical pavement responses, it did affect the combined damage ratios. This could be due the effect of combined factors.

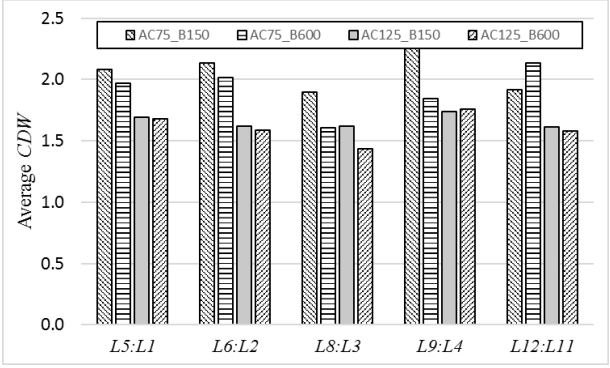

Figure 180. Graph. Combined damage ratio for thin pavements.

Damage ratio was also calculated to compare *DTA* with differential tire inflation pressure (*L7* and *L10*), and present the average *CDW* for these cases taking *L7* as reference. It is observed that the damage ratios are extremely high compared to other loading cases, indicating that applied load has a significant effect if the tire inflation pressure in both tires is not equal.

Table 35. Average *CDW* for DTA with Differential Tire Inflation Pressure

	AC75_B150	AC75_B600	AC125_B150	AC125_B600
L10:L7	72.9	18.42	69.17	90.44

THICK PAVEMENT STRUCTURES

By normalizing the DTA to the NG-WBT cases, the following ratios were obtained for each pavement distress considered. The effect of differential DTA is also presented wherein the high load case (*L10*) is normalized to low load case (*L7*) for comparison purposes. These values are not presented in the figures to focus on evaluating the impact of NG-WBT on pavement damage.

Fatigue Cracking (Bottom-up and Near-surface)

Based on Figure 181, the bottom-up fatigue *DW* ratio could be 1.2 to 3.2 times greater for NG-WBT cases. In addition, given the AC thickness of 5 in, NG-WBT induced higher damage than the ones with a 16-in-thick (given the high DW_{BU} ratios, which implies that the allowable number of repetitions of the DTA case is greater than that of the NG-WBT). High reduction in the DW_{BU} ratio between the NG-WBT and DTA is influenced by AC thickness when compared to granular base layer. One could observe that the relative difference between the two tire types diminishes with a 16 in thick AC layer, regardless of the loading condition as the resulting DW_{BU} ratios become 1.0. In other words, the DW_{BU} ratio between NG-WBT and DTA diminishes for an interstate highway system. It is noteworthy that the nomenclature of the horizontal axis (e.g., *L1: L5*) in Figure 176 signifies the case comparing the NG-WBT to DTA.

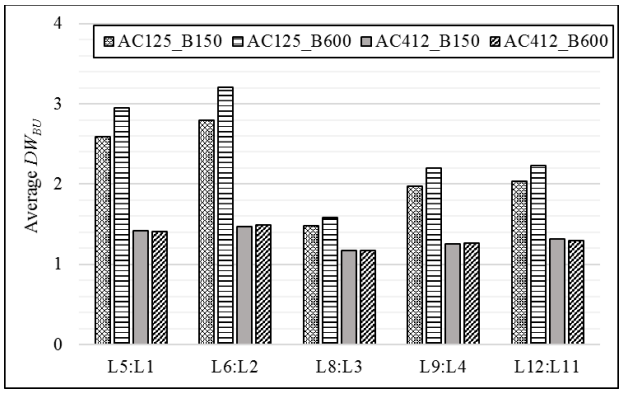

Figure 181. Graph. Average pavement response ratio for bottom-up cracking for thick pavements.

On the other hand, in regard to the near-surface cracking caused by shear strain, the ratios range from 0.5 to 10.8, implying the extent of additional number of repetitions a DTA can induce before reaching the same damage level of NG-WBT (Figure 182). It is worth noting that for this distress, when the AC thickness is considered to be 16 in and the applied load is 6 kip, the DW_{TDS} ratio tends to be below 1.0, which indicates that the number of repetitions from the DTA is much less than that of the NG-WBT.

As the applied load becomes greater than 6 kip, the DW_{TDS} ratio significantly increases. This increase is predominant when the AC layer is 16 in thick, wherein the DW_{TDS} ratio ranges from 8.7 to 10.8. One could infer that for thick pavements, the effect of the critical shear strain within the AC has a relatively high impact on "near-surface" fatigue damage, most especially under NG-WBT loading.

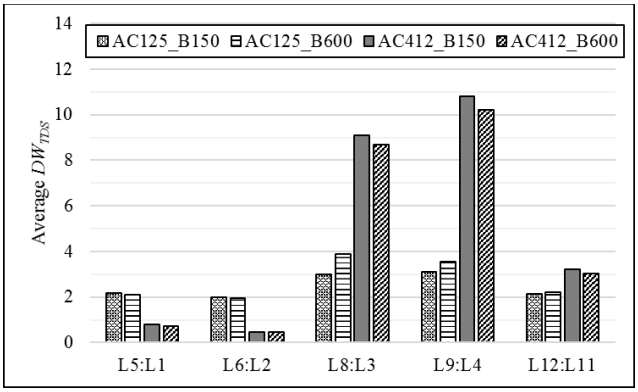

Figure 182. Graph. Average pavement response ratio for near-surface cracking caused by shear strain for thick pavements.

Conversely, when considering the near-surface cracking caused by the surface tensile strain, the DTA cases can impose 1.0 to 4.6 times more loading repetitions than that of the NG-WBT. Based on, cases with a 16 in thick AC layer were influenced more than the ones with 5 in. Although the maximum DW_{TDT} resulted from the case with AC of 5 in under an applied load of 6 kip, the cases with 16 in AC and loading condition of 18 kip and 80 psi resulted in consistently

high DW_{TDT} values. In addition, most DW_{TDT} values are illustrated to tend to 1.0, when the AC is 16 in thick (except for *L3:L8* comparison). This implies that the impact of NG-WBT tends to get closer to the DTA cases when the AC layer thickness increases – a similar trend that was previously presented in the analysis of strain responses. Lastly, varying the AC layer thickness has a greater influence than that of the granular base. It has to be noted that a load of half axle of 18 kips is extremely high and in practice is unrealistic. However, it was included in the analysis to cover a wide range of loading.

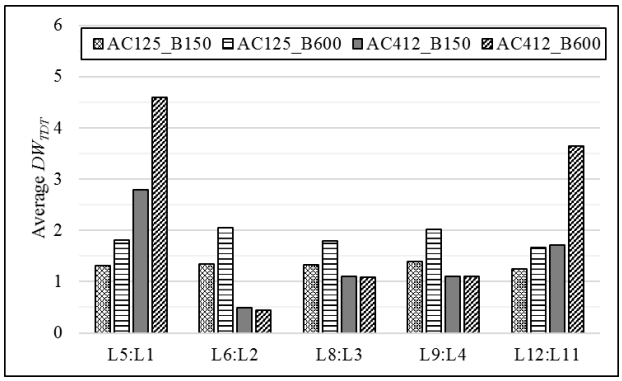

Figure 183. Graph. Average pavement response ratio for near-surface cracking caused by tensile strain for thick pavements.

AC Rutting

Another damage parameter is the permanent deformation within the AC layer. Based on Figure 184, the range of additional repetitions that the pavement can sustain under DTA loading is 1.2 to 2.4 more times than the NG-WBT. Given a 5 in thick AC layer, the ratios are around 1.0, which signifies that NG-WBT and DTA impact are similar. In contrast to these cases, the ones with 16 in AC layer produced significantly higher magnitudes than the cases for 5 in AC layer. One cause of the significant increase in DW_{RH} ratio magnitudes is the fact that the AC layer thickness is 16 in, wherein densification of thick AC layers can sustain a much greater amount of number of repetitions to the same failure level (recall threshold of 0.5 in). Moreover, the worst condition is observed when the AC is 16 in, applied load is very high (18 kip), and tire inflation pressure of 80 psi (*L3:L8*).

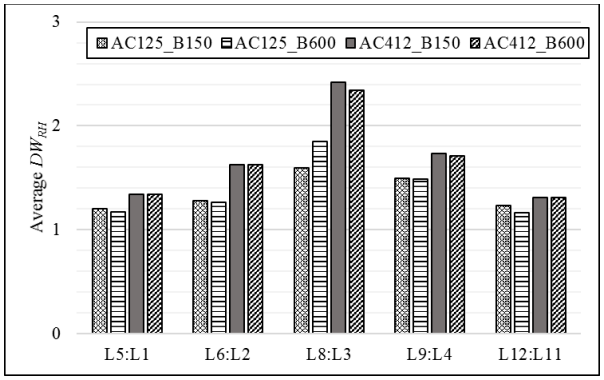

Figure 184. Graph. Average pavement response ratio for AC rutting for thick pavements.

Subgrade Rutting

The last pavement damage parameter considered is subgrade rutting. From Figure 185, DW_{RS} values range from 1.1 to 2.1, implying the increased number of repetitions to failure for DTA than the NG-WBT for the same resulting failure threshold. This is especially reflected for the cases with AC layer thickness of 5 in and base layer thickness of 6 in. On the other hand, considering a 5 in AC and 24 in granular base leads to similar DW_{RS} values of the cases with 16 in AC, implying the significant impact of a thick granular base on reducing subgrade rutting (only when AC layer is relatively thin).

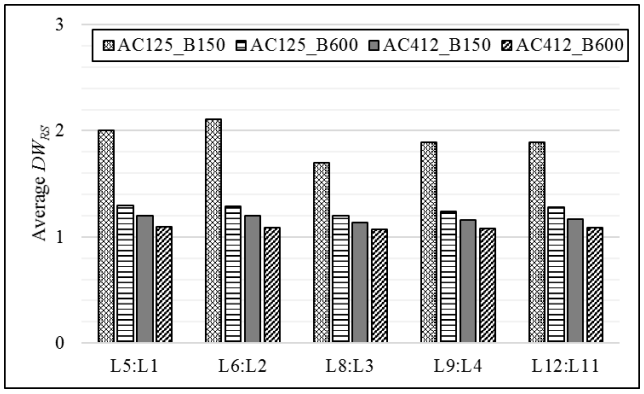

Figure 185. Graph. Average damage ratio for subgrade rutting for thick pavements.

Combined *DW* Ratio

Combining all the five distresses considered in this study, the Figure 186 presents the cumulative *DW* ratio (or *CDW* ratio), which vary from 1.0 to 3.8. One could observe that the majority of the *CDW* ratios remained under 2.0, indicating that the DTA could sustain twice the number of repetitions to failure than the NG-WBT (considering "cumulative" damage). Conversely, under an applied load of 18 kip and AC layer thickness of 16 in, the ratios significantly increased, which is governed by DW_{TDT} (Figure 183). In addition, the disparity between DTA and NG-WBT diminishes as the load level is decreased to 6 kip given a 16 in thick AC layer.

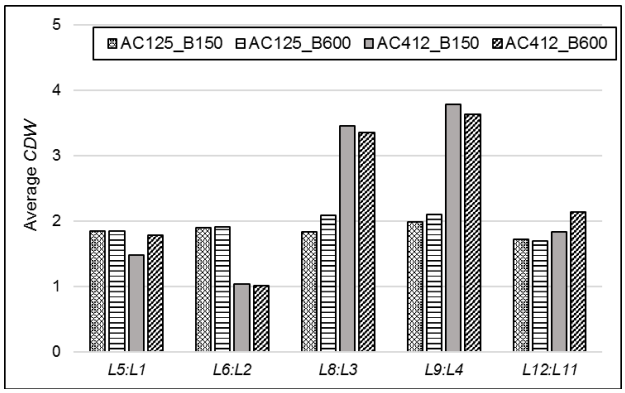

Figure 186. Graph. Combined damage ratio for thick pavements.

In contrast to the figures, which compare NG-WBT and DTA, Table 36 presents the *CDW* ratios of the differential DTA cases with an applied load of 6 and 18 kip for $L7$ and $L10$, respectively. The reference is taken as *L7* divided by the *L10* case, wherein the resulting ratios define the additional number of repetitions that the thick pavement could sustain. High values further support the significant influence of the applied load on the resulting number of repetitions to failure for all the five pavement distresses considered.

Table 36. Average CWD for DTA with Differential Tire Inflation Pressure on Thick Pavement.

	AC125_B150	AC125_B600	AC412_B150	AC412_B600
L10:L7	7.9	7.8	8.2	8.1

EFFECT OF WIDE-BASE TIRE MARKET PENETRATION

The effect of NG-WBT market penetration is studied using ICT-Wide tool. A typical pavement structure with 5 in AC and 6 in base is considered. The pavement materials are categorized as strong material according to previous discussions. In addition, a typical axle load of 10 kips and a tire pressure of 110 psi were used.

The pavement responses under DTA versus NG-WBT were determined. Figure 187 presents comparison between the critical pavement responses resulted from the two tires. In general, NG-WBT responses were 20% higher for the critical strain. This comparison is based on the assumption that either 100% DTA or NG-WBT are used. Figure 188 shows the percent increase in response for the two tires.

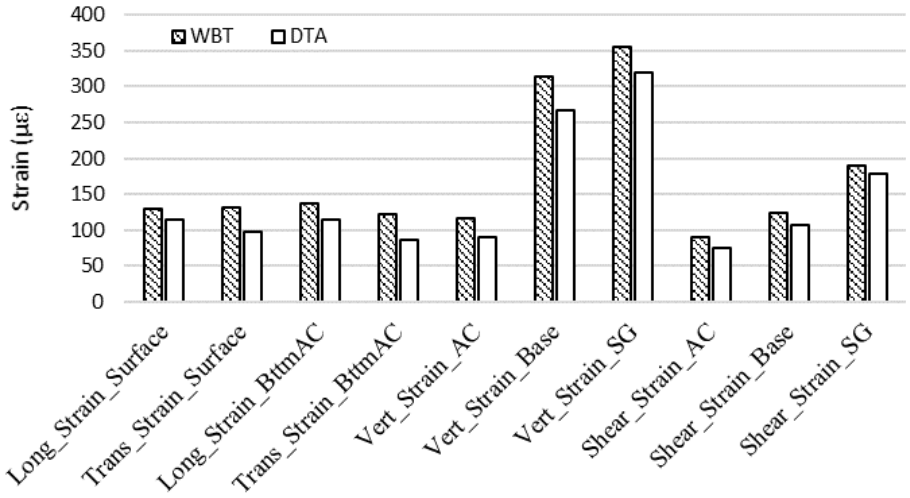

Figure 187. Graph. Pavement response under DTA and NG-WBT.

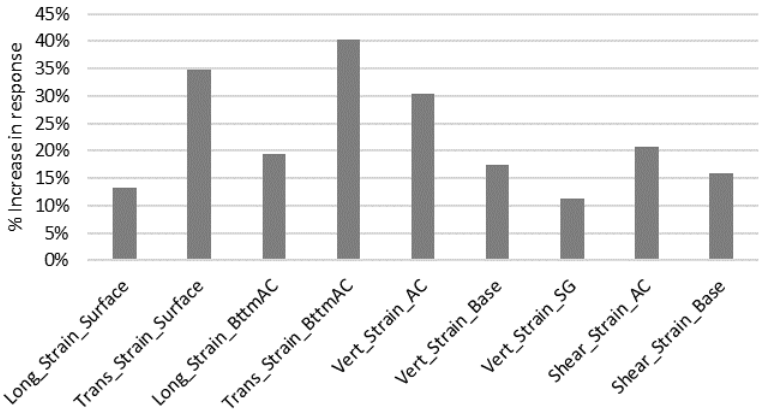

Figure 188. Graph. Percentage increased in critical strains due to NG-WBT.

Using ICT-Wide tool, the effect of the market penetration on CDW was studied. The following example illustrates the process. A pavement has a design life of 50 years and the average directional daily traffic for one lane is 40,000 with 20% trucks. The traffic growth rate of 1% is assumed. In addition, the market penetration of NG-WBT is studied at four levels: 0, 5, 10, 15 and 20%. Figure 189 shows the effect of NG-WBT market penetration on CDR calculated for five damage criteria. The damage ratio is normalized based on 0% NG-WBT market penetration (or 100% DTA). Changing the market penetration from 0 (100% DTA) to 25% increases the damage ration by almost 6%. This is not significant considering 20% of the traffic is composed of trucks; 50% of the axles in the 20% using NG-WBT.

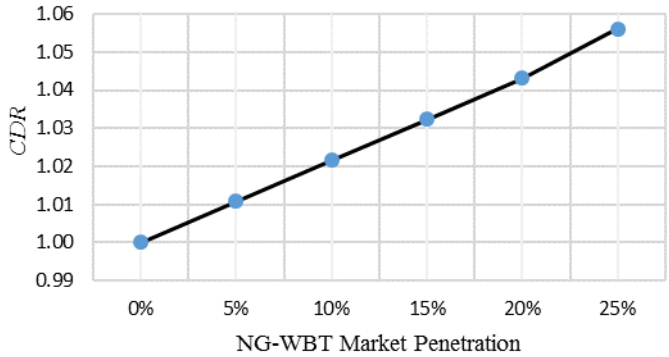

Figure 189. Graph. Effect of NG-WBT market penetration on normalized CDR.

PROPOSED ANALYSIS APPROACH USING THE STRESS/STRAIN DOMAIN

A series of drawbacks became apparent after implementing the transfer functions, for the comparison between NG-WBT and DTA:

- Transfer functions consider a point critical pavement response as input (e.g., compressive strain on top of subgrade for rutting prediction) and predict corresponding distress over time. Transfer functions are empirical equations developed based on laboratory experiments and are, therefore, very sensitive to small changes in strain. Hence, the validity

of prediction for the field performance strictly depends on effective calibration, which may increase the sensitivity of transfer functions to inputs, and expected to change with time and location,
- The scope of testing program for transfer function's regression coefficient does not cover our study's parametric ranges
- Calibration of transfer functions did not consider NG-WBT.

Although MEPDG provides transfer functions that directly link critical responses to damage, the locality of the point response inputs diminishes the significance of the multi-axial stress states. This behavior is especially important and predominantly influenced at the near-surface region, which is insufficiently quantified by transfer functions, and it is the region where the greatest difference between NG-WBT and DTA lies. Therefore, with the proposed approach, multi-axial stress states are adequately considered and quantified through a normalized scalar parameter.

Multi-Axial Stress and Strain States

In general, an element stress state can be represented by normal and tangential stresses. If a material element is rotated in a manner that leads to zero shear stresses, the element stress state can then be characterized using principal stresses, or the normal stresses acting on the element. Using the principal stresses, the hydrostatic stress, p_σ, and shear stress indicator, q_σ, can be defined using the following equations:

$$p_\sigma = \frac{1}{3}(\sigma_1 + \sigma_2 + \sigma_3)$$

Figure 190. Equation. Hydrostatic stress.

$$q_\sigma = \sqrt{\frac{1}{2}((\sigma_1 - \sigma_2)^2 + (\sigma_2 - \sigma_3)^2 + (\sigma_1 - \sigma_3)^2)}$$

Figure 191. Equation. Shear stress indicator.

where:

σ_1 = maximum principal stress
σ_2 = intermediate principal stress
σ_3 = minimum principal stress

Below, the same form of equations can represent the hydrostatic strain, p_ε, and shear strain indicator, q_ε.

$$p_\varepsilon = \frac{1}{3}(\varepsilon_1 + \varepsilon_2 + \varepsilon_3)$$

Figure 192. Equation. Hydrostatic strain.

$$q_\varepsilon = \sqrt{\frac{2}{9}[(\epsilon_1 - \varepsilon_2)^2 + (\varepsilon_2 - \varepsilon_3)^2 + (\varepsilon_1 - \varepsilon_3)^2]}$$

Figure 193. Equation. Shear strain indicator.

where:

ε_1 = maximum principal strain
ε_2 = intermediate principal strain
ε_3 = minimum principal strain

From the FEM, a subdomain was extracted that spans a cube with a side of 3.3 ft centered on the middle of the wheel path. As the stresses and strains tend to zero at the boundaries, the domain for the multi-axial stress state analysis could be limited to the selected subdomain. Furthermore, the critical loading step is selected when the tire is at the middle of the wheel path. Therefore, the domain of the analysis could be further reduced to a two-dimensional (2-D) plane (*y, z*) where *x* in the traffic direction is held constant.

Initially the plane was held at the mid-length of the pavement model; however, the variation of the given plane along the traffic direction indicated that the maximum stress and strain states occur behind the middle of the tire footprint. This observed behavior is alluded to the viscoelastic response of the AC layers. To ensure a fair comparison, the location of the maximum values was considered to be critical and was used in the proposed analysis approach.
Using the centroid of each finite element of the analysis domain, principal values were obtained and the hydrostatic stress and strain, and shear stress and strain indicators were calculated and plotted in the Cartesian plane. Figure 194 illustrates a sample *p - q* diagram in the stress domain.

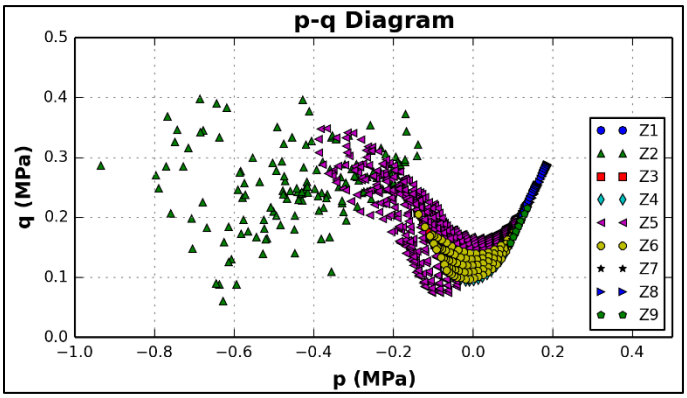

Note: 1 MPa = 145 psi

Figure 194. Graph. Multi-axial stress state of an AC layer.

In addition, each pavement layer was divided into nine regions, namely *Z1* through *Z9*, as presented in Figure 195. Using this zoning process, magnitudes throughout the layer depth could be easily differentiated, wherein the most critical regions included near-surface (*Z2*), tire edges (*Z1* and *Z3*), and mid-bottom of the layer (*Z8*). It is worth noting that the vertical boundaries were defined by the width of the tire footprint with an additional 2 in to the left and right of the

tire edges. The horizontal boundaries for the AC, base, and subgrade layers were 6, 2, and 2 in, respectively, from the top and bottom of each layer, to adequately capture the behavior at the near-surface and at the bottom.

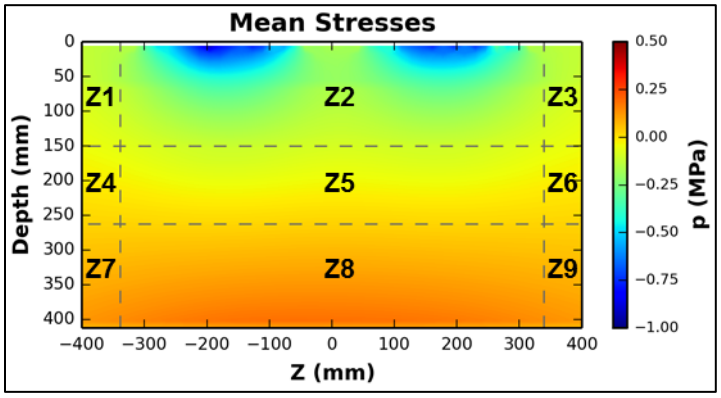

Note: 1 MPa = 145 psi

Figure 195. Graph. Nine zones are defined for each pavement layer to localize areas with high stress magnitudes.

Modified Drucker-Prager Cap Model

In the Modified Drucker-Prager Cap model, the yield surface consists of three parts: (1) the Drucker-Prager shear failure surface, (2) an elliptical cap limiting the hydrostatic pressure, and (3) a smooth transition zone between the failure surface and the cap (Figure 196).

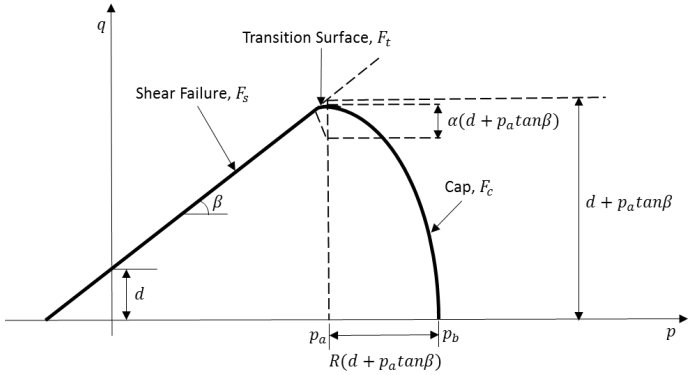

Figure 196. Graph. Modified Drucker-Prager Cap Model yield surfaces (Helwany, 2007).

The Drucker-Prager shear failure surface is defined by:

$$F_s = q - p\ tan\beta - d = 0$$

Figure 197. Equation. Drucker-Prager shear failure plane.

where:

β = angle of friction

d = cohesion

Moreover, the cap and transition yield surfaces are estimated by:

$$F_c = \sqrt{(p - p_a)^2 + \left[\frac{Rq}{(1 + \alpha + \alpha/cos\beta)}\right]^2} - R(d + p_a tan\beta) = 0$$

Figure 198. Equation. Cap surface.

$$F_t = \sqrt{(p - p_a)^2 + \left[q - \left(1 - \frac{\alpha}{cos\beta}\right)(d + p_a tan\beta)\right]^2} - R(d + p_a tan\beta) = 0$$

$$p_a = \frac{p_b - Rd}{1 + R\ tan\beta}$$

Figure 199. Equation. Transition yield surface

where:

R= material parameter that controls the shape of the cap

α = defines the smooth transition surface between the Drucker-Prager shear failure surface and the cap

p_b= mean effective yield stress and defines position of the cap

Polar Coordinate Transformation

To effectively relate the *p-q* diagram values to the failure envelope, the values in the Cartesian coordinate were transformed into polar coordinates. Two important parameters can be extracted from the *p-q* diagram in the Cartesian plane: i) the magnitude of the vector that forms from the point of origin to a specific *p-q* coordinate; and ii) the angle θ between the vector and the horizontal axis. The failure plane (red dashed line in Figure 200) was also transformed.

This transformation allowed the relative comparison of the cloud of stress and strain states to the failure plane. It was also realized that depending on the proximity of the point to the failure plane, the material may fail in compression and/or shear. Therefore, a weight factor was created to adequately penalize the stress/strain state point based on its location relative to the failure envelope. Common weight factors that are independent of the load case were defined by regionalizing the polar coordinate system into 30 sectors, which stemmed from defining six radii boundaries (0, 0.2, 0.4, 0.6, 0.8, and 1.0) and seven angle boundaries (0, π/6, π/3, π/2, 2π/3, 5π/6, π). The midpoint of each sector was estimated and the shortest distance from the centroid to the failure envelope was calculated.

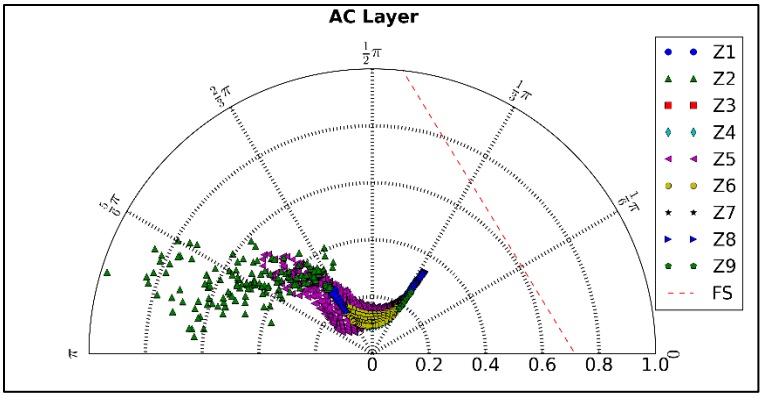

Figure 200. Illustration. Sample polar coordinate transformation.

Given the centroidal distances, the reciprocal is calculated by:

$$r = \frac{1}{d}$$

Figure 201. Equation. Reciprocal for the weight factor.

where:

r	= reciprocal
d	= shortest distance from sector centroid to failure envelope

Based on these reciprocals, the maximum reciprocal value indicated the shortest distance to the failure envelope and was quantified to be the highest value among the 30 sectors. For instance, from Figure 202, d1 < d2, therefore, r1> r2.

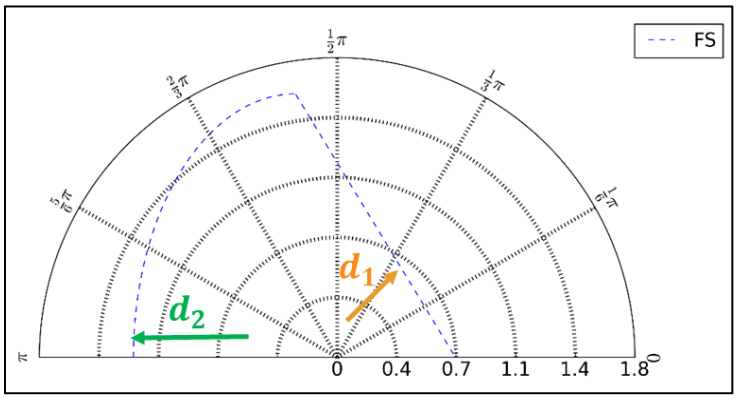

Figure 202. Illustration. Comparison of the sector centroids relative to the failure envelope.

The weight factors were then calculated by normalizing the reciprocals to the maximum reciprocal. This indicated a weight of value 1.0 was the closest sector to the failure envelope. Relating back to the example from Figure 202, w1 > w2. It is worth noting that this process was

only implemented in the regions within the failure envelope as absolute failure was assumed for the sectors beyond.

Using the vector magnitude and weight factors, the *p-q* point cloud can be combined into one cumulative scalar value, coined as the cumulative stress, C_σ , or cumulative strain, C_ε. However, a direct comparison between various loading cases was deemed to be relatively unfair given that their corresponding mesh geometries differ. For instance, the DTA load case would generate a higher number of points in the *p-q* diagram than the NG-WBT case. Therefore, a homogenizing factor was defined to take into account the geometric difference between load cases and to make an even comparison between load cases. The homogenizing factor, A_{elem}, was calculated by considering the elemental area relative to the total area covered by the specific zone.

$$A_{elem} = \frac{a_{jl}}{A_l}$$

Figure 203. Equation. Homogenizing factor.

where:

A_{elem} = is the homogenizing factor of a specific element
a_{jl} = area of element *j* within zone *l*
A_l = total area of zone *l*

This parameter accounted for area influenced by the principal stresses and strains, and was used to normalize the cases according to load-specific areas. In addition, recall the previously introduced load factor, which addresses the difference between the applied and resultant loads. Furthermore, to account for the three-dimensionality of the response, additional slices within the tire-pavement contact area were included in the analysis. Using the same analysis method, a volumetric comparison of the stress and strain states were conducted. The final scalar parameter that compared the cumulative stress/strain values is defined as the cumulative stress ratio or cumulative strain ratio, *CRS* or *CRE*, respectively. The ratio is calculated using the equation in Figure 205.

$$C\sigma, \varepsilon_{case} = \frac{\sum_{l=1}^{z}\sum_{j=1}^{e}\sum_{i=1}^{s}\left|(pq)_{\sigma,\varepsilon}\right|_{jl} a_{jl} * l_{elem} * w_i}{A_z * L_{sub}}$$

Figure 204. Equation. Cumulative stress/strain per load case.

$$CRS, E = \frac{C\sigma, \varepsilon_{case} * LF_{case}}{C\sigma, \varepsilon_{ref} * LF_{ref}}$$

Figure 205. Equation. Cumulative stress/strain ratio.

where:

$C\sigma, \varepsilon_{case}$ = cumulative stress/strain of the specific load case
$\left|(pq)_{\sigma,\varepsilon}\right|_{jl}$ = vector magnitude of the element *j* for a total of *e* elements within the zone *l* for a total of *z* zones
l_{elem} = element length along the travel direction
w_i = weight of the specific sector *i* for a total of *s* sectors
L_{sub} = total length of the subdomain
CRS, E = cumulative stress/strain ratio (unitless)
$C\sigma, \varepsilon_{ref}$ = cumulative stress/strain of the reference load case
LF_{case} = load factor of the specific load case
LF_{ref} = load factor of the reference load case

The same domain analysis was performed for each pavement layer and for the entire pavement data set to provide a comprehensive understanding of the sensitivity of the cumulative ratio parameter to the variables considered in the numerical matrix.

Preliminary Testing

In lieu of using the transfer functions, the aforementioned domain analysis approach was implemented to several cases considering typical loading conditions on a thick pavement with AC thickness of 16.2 in and granular base thickness of 6 in, wherein both layers were characterized with strong material properties. The typical trailer tire loading condition considered an applied load of 10 kip with a uniform tire inflation pressure of 110 psi (NG-WBT and reference DTA, aforementioned as cases *L11* and *L12*) and differential DTA inflation pressure of 80 and 110 psi. In addition, the loading condition for a steer tire was also evaluated, given the applied load of 7 kip and tire inflation pressure of 100 psi. It is worth noting that the steer and differentially inflated tire cases are denoted as *L13* and *L14*. In total, four cases were considered.

The following figures illustrate the cumulative ratio variation in the stress and strain domains for the individual pavement layer (AC, base, and subgrade), the entire pavement data set, and tire edges – all corresponding to the critical 3-D subdomain. For the individual pavement layers, critical zones were related to important pavement distresses:

- AC layer: zones 2 and 8 correspond to near-surface and bottom-up fatigue cracking regions, respectively; and
- Base and subgrade layers: zone 2 corresponds to permanent deformation or rutting region.

The vertical axis of the following figures indicates the cumulative ratio normalized to the reference DTA under a typical loading condition, whereas the horizontal axis enumerates the four cases considered. Based on Figure 206, NG-WBT has higher cumulative stress states in the middle-top zone (or zone 2) and middle-bottom zone (or zone 8) of the AC layer. However, for the steer tire, the middle-top zone was slightly greater than the DTA reference by 5.09%, and middle-bottom zone of the AC layer was lower, which could be due to the reduced applied load. On the other hand, for the case considering differential tire inflation pressure, the resulting volumetric ratio within the middle-bottom zone of the AC layer was slightly lower than the reference DTA by 8.5%, which can be attributed to the volumetric averaging method.

NG-WBT invoked the highest stress state followed by the steer tire within the AC layer. However, as pavement depth increases, the disparity between NG-WBT and DTA diminishes, as for higher depths the governing factor is the load. Therefore, given the same applied load, the ratio between the two tends to 1.0. On the other hand, as the steer tire is carrying a lower load, then one can observe that the ratio with respect to the DTA reference is less than 1.0. Moreover, for the bulk 3-D stress state, the NG-WBT indicated the highest ratio. This bulk behavior was predominantly due to the high ratios within the AC layer. It is noteworthy that the cumulative stress ratio for the entire pavement subdomain was not a simple addition of the ratios of the individual pavement layers but the addition of the cumulative stresses normalized to the uniformly inflated DTA case.

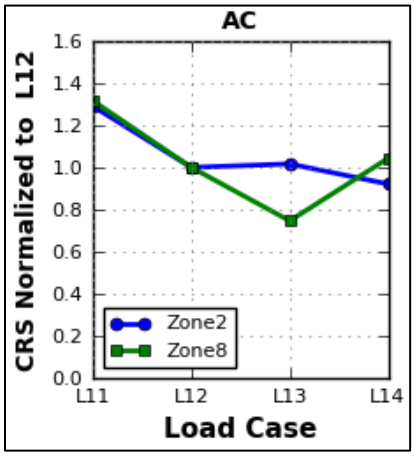

Note: 4.45 kN = 1 kip; 6.89 kPa = 1 psi

Figure 206. Graph. Cumulative ratio variation in the stress domain normalized to L12 - AC.

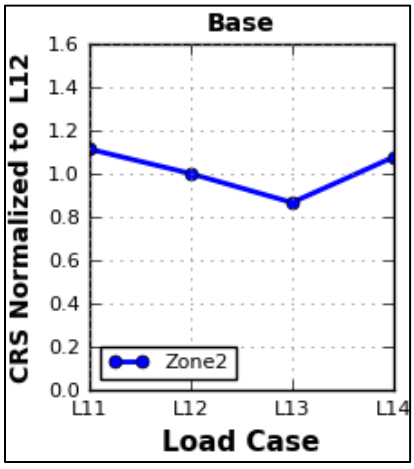

Figure 207. Graph. Cumulative ratio variation in the stress domain normalized to L12 - base.

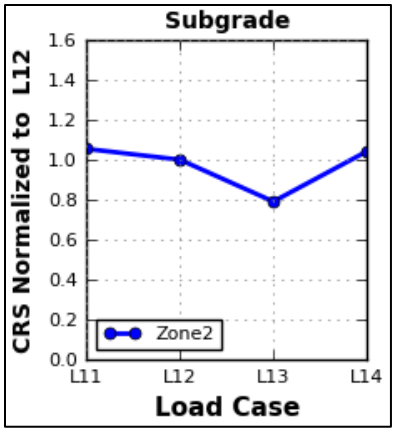

Figure 208. Graph. Cumulative ratio variation in the stress domain normalized to L12 - subgrade.

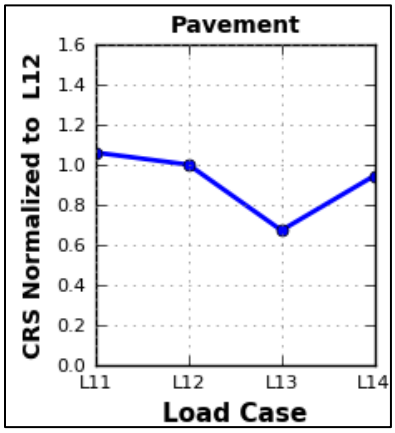

Figure 209. Graph. Cumulative ratio variation in the stress domain normalized to L12 - pavement.

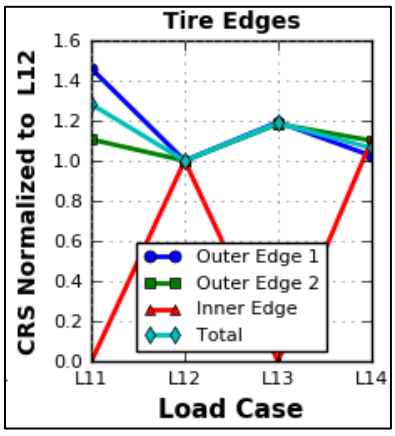

Figure 210. Graph. Cumulative ratio variation in the stress domain normalized to L12 – tire edges.

Due to the inherent observation of similar stress states for the DTA cases considering uniform (L12) and differential tire inflation pressures (L14), within zone 2, the analysis domain was further localized to tire edges only. Recall that the tire footprint width was extended by 2 in from the tire edges, three local zones within zone 2 were generated by removing the area directly underneath the tire(s). The zones governed by tire edges only included two outer edges (named "Outer Edge 1" and "Outer Edge 2"), and the spacing between the DTA (coined as "Inner Edge").

Figure 206 through Figure 210 illustrate that the stress state at one of the outer edges of the NG-WBT was greater than the other, which could be alluded to the high level of non-uniformity of the stresses at near-surface. Although for the remaining three cases, the stress states at all tire edges for DTA were relatively uniform and indicated much lower ratios than the NG-WBT. Please note that single tires (e.g. NG-WBT and steer tire) do not have inner tire edges..

As stress is analogous to excitation, strains, on the other hand, correspond to the resulting pavement response. Using the strain domain, a holistic evaluation of the pavement behavior with both stresses and strains is provided. In comparison to the stress domain, similar trends were observed for the resulting ratios of the four cases. However, in contrast to the stress ratio values of the DTA tire with differential inflation pressure, the strain ratios in the base and subgrade layers increased to 1.14 and 1.17, respectively. In addition, the cumulative ratio increased from the AC layer towards the subgrade layer for the DTA tire with differential inflation pressure. For the DTA with differential tire inflation pressure, the tire with the higher inflation pressure resulted in an increase in strain magnitudes as the AC layer depth increased. Lastly, the steer tire, with an inflation pressure of 100 psi, and the DTA with uniform tire inflation pressure resulted in a similar cumulative ratio for zone 2 within the AC layer.

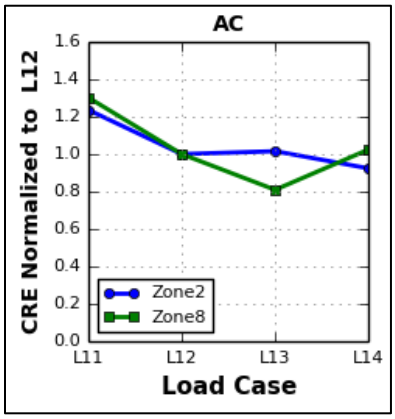

Note: 4.45 kN = 1 kip; 6.89 kPa = 1 psi

Figure 211. Graph. Cumulative ratio variation in the strain domain normalized to L12 - AC.

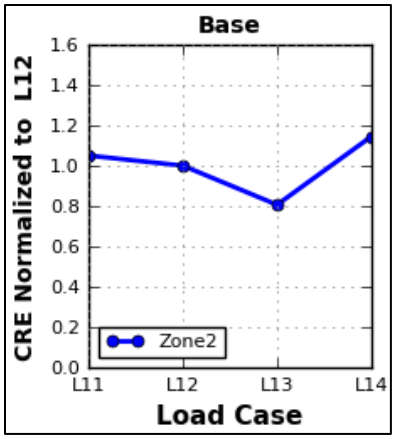

Figure 212. Graph. Cumulative ratio variation in the strain domain normalized to L12 - base.

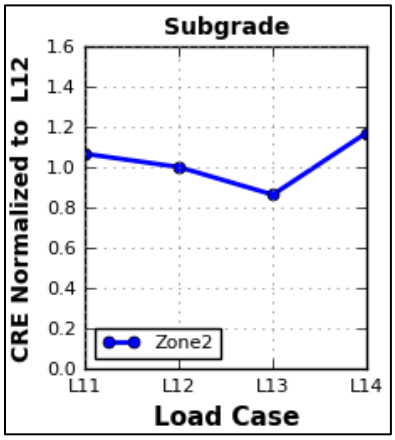

Figure 213. Graph. Cumulative ratio variation in the strain domain normalized to L12 - subgrade.

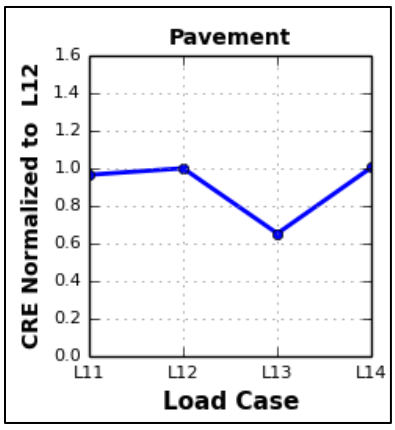

Figure 214. Graph. Cumulative ratio variation in the strain domain normalized to L12 - pavement.

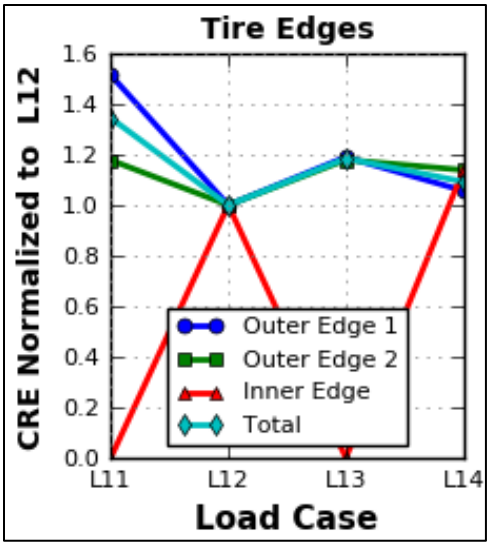

Figure 215. Graph. Cumulative ratio variation in the strain domain normalized to L12 – tire edges.

For a bulk single value indicator for the entire pavement data set, a clear disparity between the two DTA cases was not captured (see Figure 214). Due to this unexpected behavior, a more in-depth study of its causes was completed. As seen in Figure 216 and Figure 217, there was a highly uneven distribution of loads for the reference DTA with uniform inflation pressure. From the given load input of *L12*, the applied and the total resultant loads differed by 13.2%, where one tire carried 4.10 and the other 4.73 kip. Similar to the point responses, generally the load difference is used as a linear factor to normalize the responses. However, due to increasing the resulting stress and strain states by the aforementioned percent difference, the anticipated disparity between the uniformly and differentially inflated DTA was not observed.

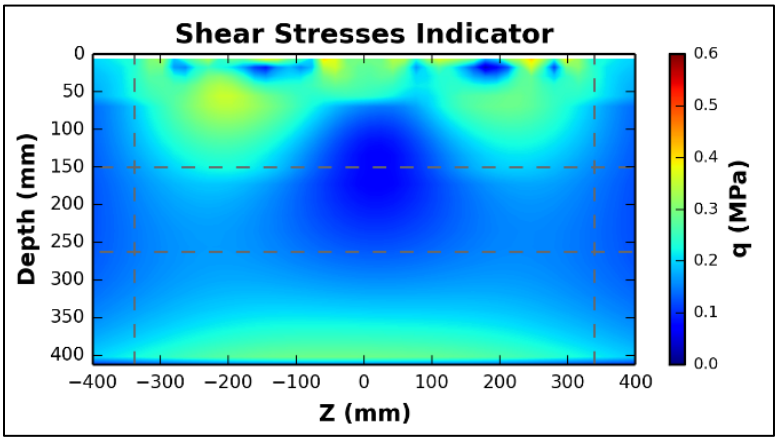

Note: Conversion factor (25.4 mm = 1 in)

Figure 216. Graph. Shear stress indicator of L12.

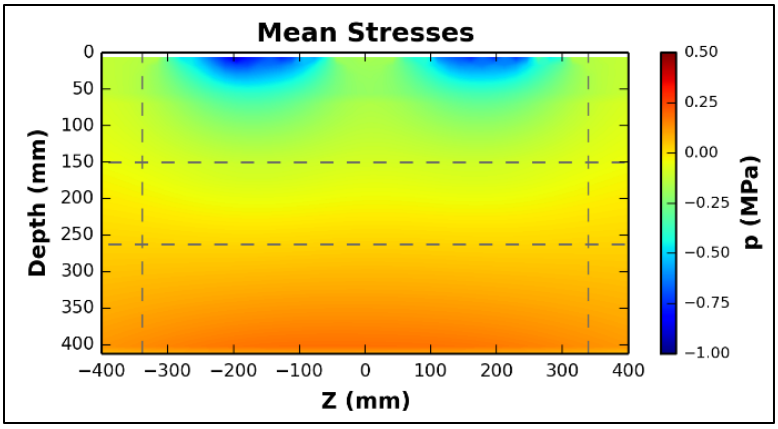

Figure 217. Graph. Mean stress indicator of L12.

Measured contact stress data for *L12* (DTA with uniform inflation pressure) showed a 15.2% difference between the resultant load on each tire. In order to fairly compare the DTA cases with uniform and differential inflation pressures, a new case, L12B, was generated. This case mirrored one of the L12 tires with a resultant load of 4.73 kip, which reduced the difference between the total applied and total resultant forces to 5.3%. Figure 218 through Figure 227 illustrate the cumulative ratio variation in the stress and strain domains, normalized to the new case, L12B. For the individual pavement layers and entire 3-D pavement subdomain, similar trends were observed (in comparison to L12). However, the disparity between zones 2 and 8 within the AC layer decreased and the tire edges showed a higher difference. This observation supports the highly nonlinear and localized behavior at near-surface of the pavement.

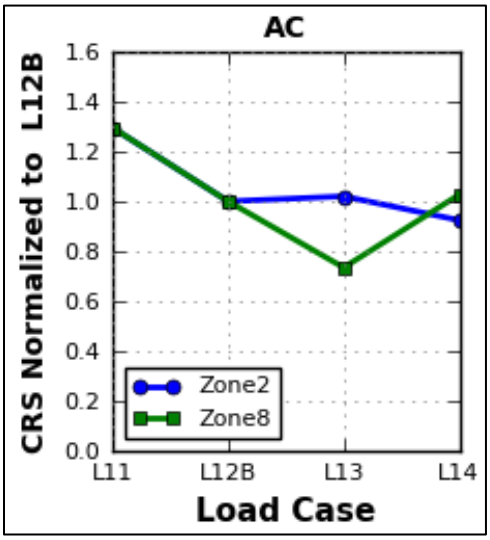

Note: 4.45 kN = 1 kip; 6.89 kPa = 1 psi

Figure 218. Graph. Cumulative ratio variation in the stress domain normalized to L12B.

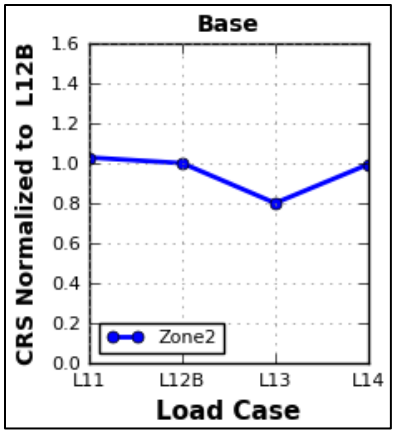

Figure 219. Graph. Cumulative ratio variation in the stress domain normalized to L12B.

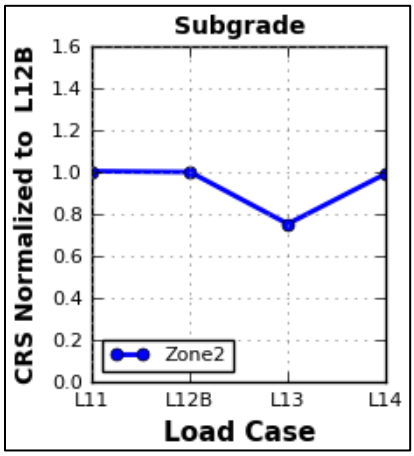

Figure 220. Graph. Cumulative ratio variation in the stress domain normalized to L12B.

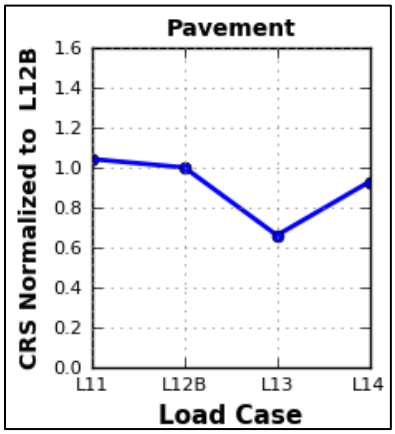

Figure 221. Graph. Cumulative ratio variation in the stress domain normalized to L12B.

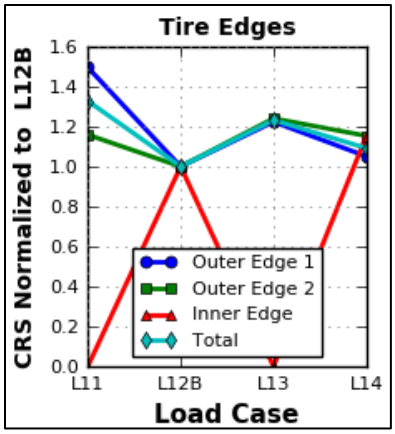

Figure 222. Graph. Cumulative ratio variation in the stress domain normalized to L12B.

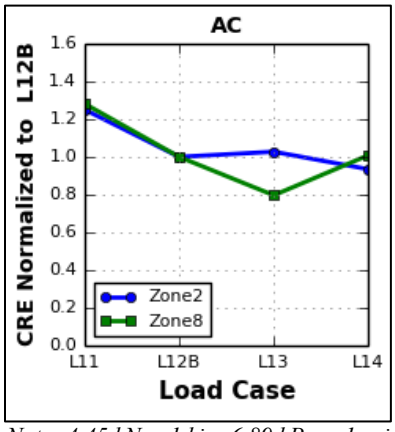

Note: 4.45 kN = 1 kip; 6.89 kPa = 1 psi

Figure 223. Graph. Cumulative ratio variation in the strain domain normalized to L12B.

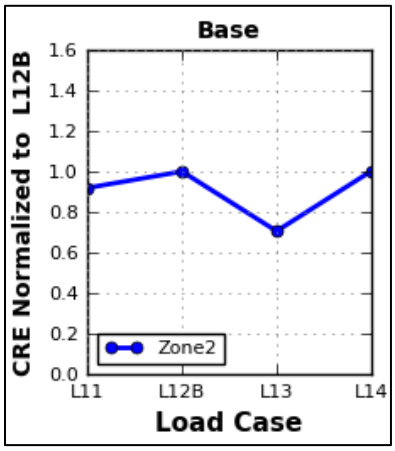

Figure 224. Graph. Cumulative ratio variation in the strain domain normalized to L12B.

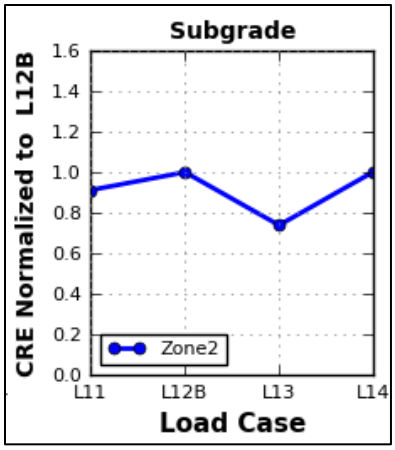

Figure 225. Graph. Cumulative ratio variation in the strain domain normalized to L12B.

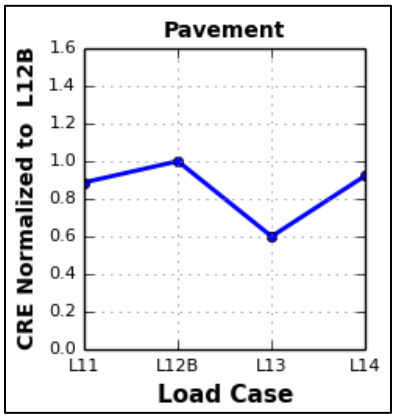

Figure 226. Graph. Cumulative ratio variation in the strain domain normalized to L12B.

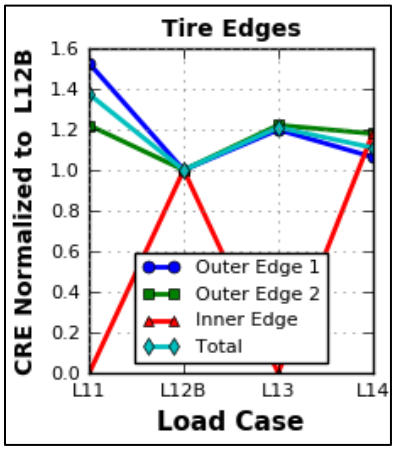

Figure 227. Graph. Cumulative ratio variation in the strain domain normalized to L12B.

However, the given near-surface zone did not fully capture the impact of the differential tire inflation pressure where the tendency of one tire to carry a higher load than the other could be clearly observed (Figure 228).

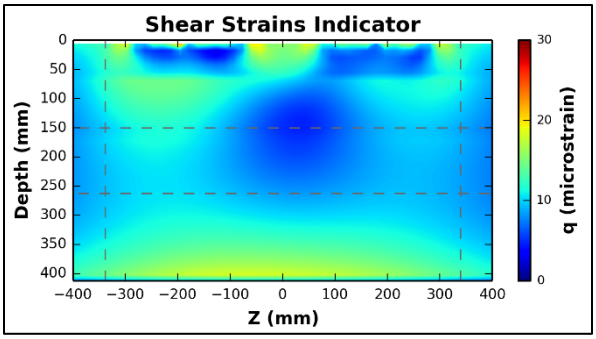

Note: 25.4 mm = 1 in

Figure 228. Graph. Shear strain indicator of L14.

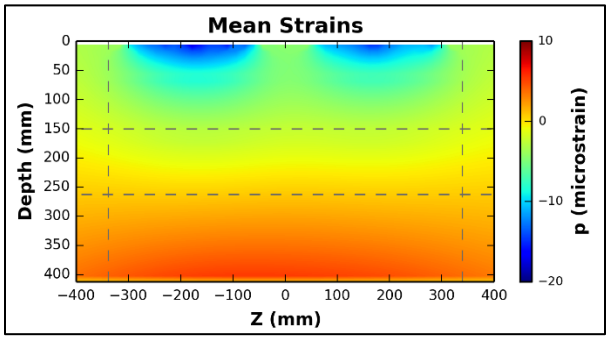

Figure 229. Graph. Mean strain indicator of L14.

The nine zones were then modified by introducing another partition within zones 2 and 5. Two cases were considered: i) vertically cut zones 2 and 5 along the middle of the tire width to isolate each of the DTA tires, and ii) maintain the aforementioned vertical cut and add another partition horizontally along the depth at 3 in. The second case is introduced to focus the resolution of the ratios within the top and bottom sections of zone 2. For the first case, the cumulative ratios considered the combination of zones 2 and 5 for each tire, wherein one tire has a higher tire inflation pressure than the other. The resulting cumulative strain ratios for each zone combination were 1.093 and 0.913. In particular, the higher cumulative ratio of 1.172 belonged to the tire with a higher tire inflation pressure. This suggest an increase damage potential of 9.3%.

The new zones were further discretized, as noted in the second case, by adding a horizontal cut along 3 in. Recall that the intent was to further isolate the near-surface behavior within the top section of zone 2 from the bottom. Therefore, the resulting ratios included three new zones: top and bottom sections within zone 2, and zone 5.

The resulting cumulative ratios revealed a slight difference of up to 1% for both tires. This was anticipated as within each of the nine zones, the proposed method effectively magnifies the areas with greater shear impact using the polar sector weights (recall that the closer the stress/strain state to the failure plane, the more it is penalized). Further discretization of the nine zones may not change the cumulative ratios significantly. In addition, combining zones 2 and 5 (along with

isolating each of the tires) not only provided an effective way to isolate the impact of the differential tire inflation pressures, but also captured the impact of the higher tire inflation pressure at a greater depth.

Therefore, with the proposed domain analysis method, the followings were noted:

- The three-dimensional pavement stress and strain states were effectively quantified using a scalar parameter,
- Load cases could be conveniently compared using the scalar parameter in both stress and strain domains,
- The nine zones could be effectively related to regions of critical pavement distresses, and
- Modifications to the zones could capture the influence of differential tire inflation pressures.

SUMMARY

MEPDG transfer functions were used to determine the damage caused by each tire on thin and thick pavements. The distresses considered were bottom-up fatigue cracking, near-surface cracking caused by shear strain and tensile surface strain, and permanent deformation in the AC and subgrade. These distresses were combined using logarithmic weighting factor to create a combined dual-to-wide ratio. For thin pavement, it was found that for 10-kip load applied and 110 psi tire inflation pressure, the pavement can withstand twice as many repetitions if it is loaded only with DTA compared to NG-WBT. The same comparison for near-surface cracking and subgrade rutting was 1.26 and 1.89, respectively. For the thick pavement and same loading condition, the average *DW* ratios for near-surface fatigue cracking caused by tensile and shear strain, and AC rutting are 2.2, 2.6, and 1.3, respectively. The average combined dual-to-wide ratio for P=10 kip and S=110 psi was 1.8 and 1.9 for thin and thick pavement, respectively.

It is worth to note that the previous values are calculated assuming the pavement is loaded by one type of tire only; hence, this could be misleading. To consider the effect of NG-WBT's market penetration, ICT-Wide tool was used to compute *CDW* on a typical pavement structure. It was found that the average percentage difference between the critical pavement responses was 20%, and *CDW* for a 10% market penetration of NG-WBT was 2.1% greater than when the pavement was subjected to DTA only.

In order to overcome some of the limitations of the MEPDG to calculate pavement damage, a novel procedure was proposed. The new methodology considers the three-dimensional stress and strain states in each layer and divides the pavement structure into critical zones typically associated with the various distresses. In addition, the proposed domain analysis approach allows to successfully capture the three-dimensional state of the pavement into a single value indicator, with the ability of isolating tensile and shear components. The domain analysis shows that if a pavement is loaded at 10 kip with DTA having differential tire inflation pressure at 80 and 110 psi, the damage potential would be 9.3% greater when the DTA loading is the same and the inflated tire pressure of both tires is 80 psi.

CHAPTER 10. LIFE-CYCLE ASSESSMENT AND COST ANALYSIS

The life-cycle assessment (LCA) and life-cycle cost analysis (LCCA) approaches have been used to provide a preliminary evaluation of the environmental and economic effects of NG-WBT. The two approaches are considered to satisfy the following objectives:

- Evaluate life-cycle energy consumption, greenhouse gas emissions (GHG), and cost from pavement when using NG-WBT, while focusing on interactions between the impacts of NG-WBT on the pavement design life and on improvement in fuel economy as a result of vehicle operation during the pavement use stage.
- Produce initial case studies using the approaches developed, examine how NG-WBT can affect the life-cycle impacts of pavement, and use these initial case studies to provide a preliminary indication of the net effects on greenhouse gas emissions, energy use, and cost of changes in the market penetration of NG-WBT, considering the entire life cycle of a preservation treatment as defined by the framework, including material production, construction, and vehicle use.

The University of Illinois at Urbana-Champaign (UIUC) pavement LCA tool was used to evaluate the life-cycle energy consumption, GHG emissions in the material and construction stages based on pavement maintenance and rehabilitation (M&R) strategies affected by implementing NG-WBT. A pavement LCA model based on the guideline presented by Harvey et al. [(70)] was initially developed to evaluate total energy use and greenhouse gas (GHG) emissions from pavement M&R strategies. The use stage model developed by UIUC and UC-Davis was used to evaluate roughness-induced energy consumption, GHG emissions, and cost during the use stage. The cost in the material and construction stages was also calculated using the tool.

In this study, international roughness index (IRI) and mean profile depth (MPD) progression models were used to calculate the extra energy consumption from variations in the pavement surface profile (Tseng, 2012; Lu et al., 2009). This study evaluated energy consumption, GHG emissions, and cost for two different pavements, which are derived from the APT tests (at UC-Davis) and exposed to two levels of truck traffic. In addition, three scenarios, representing three possible pavement design lives with different performances, were analyzed along with five different levels of market penetration of NG-WBT.

EXISTING STUDIES

Santero et al. (2010, 2011), Kendall (2007), Zhang et al. (2009), Mukherjee and Cass (2012), and Wang (2013) and others evaluated existing pavement LCA studies and models. Based on those studies and models, Wang et al. (2012) developed an approach for considering pavement surface characteristics, vehicle type, traffic conditions, and their impact on rolling resistance, vehicle energy consumption, and GHG emissions in the use stage of pavement LCA.

Heavy trucks are responsible for nearly 20% of the total on-road GHG emissions (U.S. Department of Energy, 2009) so it is important to improve fuel efficiency of trucks. One of possible techniques to improve fuel economy of heavy trucks is to use NG-WBT.

A few studies evaluated the vehicle fuel consumption of NG-WBT, including the GENIVAR Consulting Group (now rebranded WSP Global) of Montreal, Quebec, which performed an economic study to evaluate the cost and benefits of adopting NG-WBT on heavy duty vehicles in 2005. This study focused on the market for heavy-duty vehicles and road networks in the Quebec area using variables such as number of trips, average distance per trip, and road networks used by heavy duty trucks. The study also included calculations of the benefits and costs to the trucking industry (such as reduced fuel costs and vehicle maintenance costs), increased agency costs (such as increased road damage costs), and increased benefits to society (such as reduced CO_2 emissions and reduced tire disposal costs).

For the fuel consumption reduction of these economic impacts, the Quebec study first cited a result previously obtained, which found that NG-WBT can reduce a vehicle's rolling resistance by about 12% and thus reduce its fuel consumption by about 4%. The study then reported that according to a survey conducted among Quebec trucking firms that used NG-WBT, six of the seven firms stated that the fuel economy improvement ranged from 3.5 to 12%. [Note: The final fuel economy improvements adopted in this current study were 1.5%] per axle equipped with NG-WBT].

The GENIVAR study did not include any mechanistic components of pavement-vehicle interaction, i.e., the impact from pavement and NG-WBT on rolling resistance and fuel consumption, when analyzing the fuel consumption and GHG emissions. The fuel economy improvement was directly applied to calculate the reduced fuel consumption and GHG emissions.

Franzese et al. (2010) installed instantaneous fuel consumption monitors on six Class 8 trucks to collect real-world performance data on normal freight operations. The study focused on the configuration of truck-trailer tires (combining DTA and NG-WBT) and on load level (tractor only, light, medium, and heavy). The results showed that fuel economy always improved when NG-WBT were included in the truck-trailer tire configuration compared with the basic scenario (standard dual tires on both tractor and trailer) and that the fuel economy improvement increased as the number of NG-WBT increased. When either the truck or the trailer was equipped with NG-WBT, the improvement was around 6%, and when both were equipped with NG-WBT, the improvement reached 9%. In addition, the study showed that these improvements were more significant as load levels increased; the specific values varied with load level. Thus the study—which included a mix of highway driving conditions and stop-and-go driving conditions—confirmed that NG-WBT can improve fuel economy in real-world situations. However, as with the Quebec study, this study did not include any mechanistic components of pavement-vehicle interaction, and therefore the only direct relationship derived was the one between NG-WBT and changes to fuel consumption.

Bachman et al. (2005) tested the fuel economy and nitrogen oxide (NO_x) emissions of two similar Class 8 trucks to evaluate the benefits of a variety of technologies, including the NG-WBT. The study found that: i) NG-WBT can increase fuel economy and reduce NO_x emissions for both highway conditions (at both 55 mph and 65 mph) and suburban stop-and-go traffic conditions; and ii) that there appeared to be no significant difference between the improvements

for the two drive cycles. But, as with the other studies cited here, this one made no effort to tie rolling resistance to the NG-WBT or to pavement surface characteristics.

The aforementioned studies only focused on the direct fuel consumption savings from using the NG-WBT, without considering any mechanistic approach to evaluate the vehicle fuel consumption of the pavement use stage through analysis of pavement-vehicle interaction. Therefore, in this study's analysis of the fuel economy of pavement, the use stage models developed by UIUC and UC-Davis were only used to evaluate standard dual tires; the fuel consumption of NG-WBT was assessed by applying a direct fuel economy improvement factor based on results derived from the literature for standard dual tires. In addition to UIUC's use stage model, the life cycle energy consumption and GHG emissions associated with the material and construction stages were calculated using the UIUC pavement LCA tool. To evaluate the life cycle cost of pavement M&R strategies affected by different levels of market penetration of NG-WBT, the same tool was used.

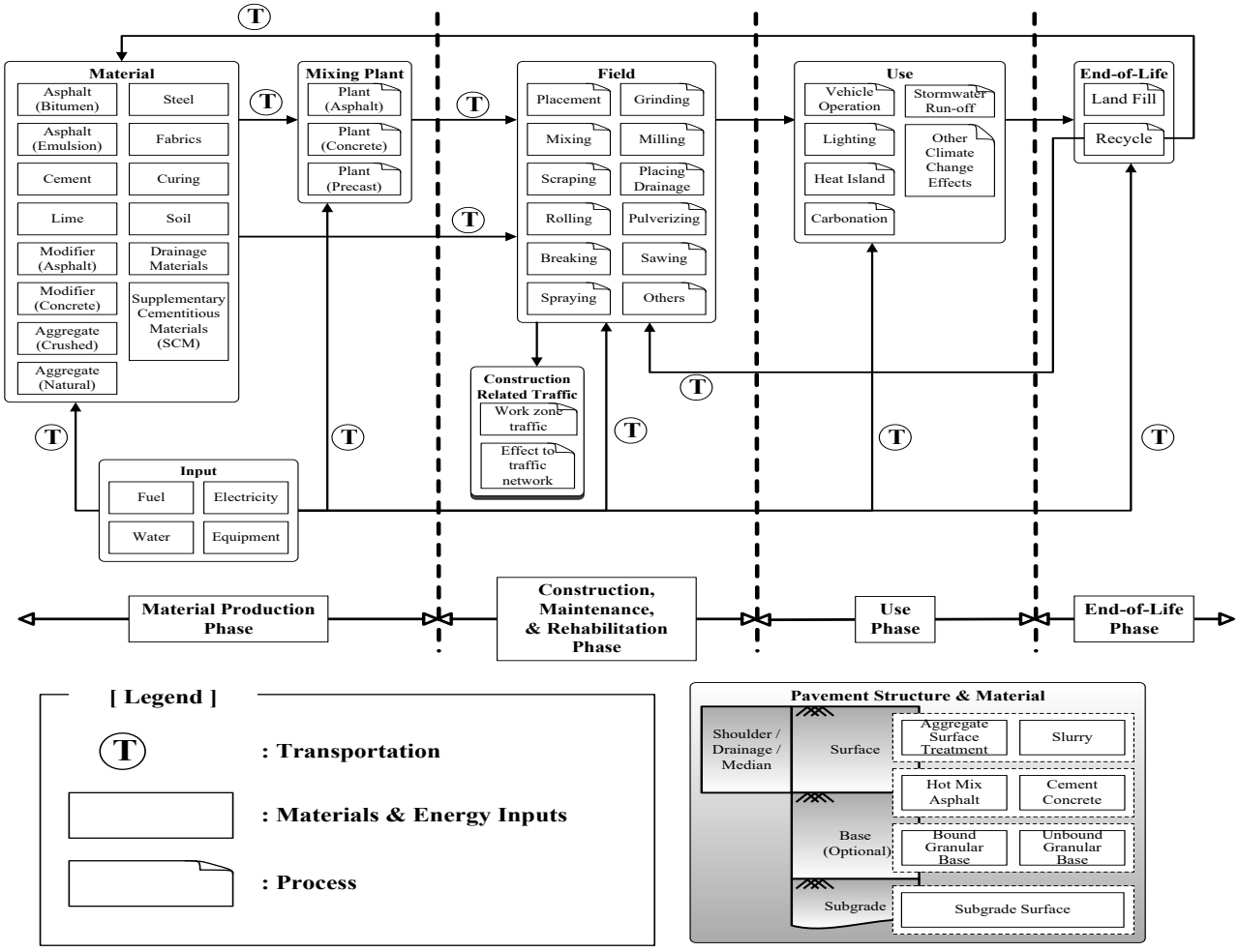

Figure 230. Illustration. A generic life cycle of a pavement system (Wang, Lee, et al., 2012) (Note: The lists in this figure are not intended to be comprehensive or exhaustive).

METHODOLOGIES

Basic Approach

Any thorough evaluation of the effects of NG-WBT on the environment would have to consider the numerous complex conditions present on a highway network at any given time. Therefore, for a preliminary study such as this one, it would be inaccurate to create an "average" scenario to capture conditions on the entire network. Instead, the following approach was taken:

- The highway network was divided into categories based on factorial variables similar to those in the UCPRC Pavement LCA study (Wang, Lee, et al., 2012).
- Case studies were performed for each category based on the settings of the factorials. Each case study included all life cycle stages of a pavement segment, and the life cycle impacts from the different tire technologies (i.e., standard DTA and NG-WBT) associated with that segment. The impacts were based on vehicle miles traveled.
- Results from the categorical case studies were applied to the network with additional sensitivity analyses, including different types of tires and traffic levels and congestion.

As a first demonstration of the approach developed for this study, only a few selected variables are considered in the example case studies included in this report. Among the selected variables are two asphalt pavement structures, with two levels of the truck traffic, and five levels of market penetration of NG-WBT.

Scope and System Boundary

This study focuses on pavement damage caused by the introduction of NG-WBT and the resultant changes in energy consumption, GHG emissions, and cost. Theoretically, in a study of this kind the environmental impacts that occur over the tire life cycle would also be included. They are not included herein, however, because a life-cycle inventory of tire manufacturing is currently unavailable. Even if it was, the contribution from tires to the results of this evaluation would likely be very small since only a very small portion of a tire's life would be allocated to the pavement segment analyzed.

The life cycle of a generic pavement system includes the material production, construction, use, M&R, and end-of-life (EOL) stages. The modeling in this study considers the material production, construction, and use stages. Because the M&R and EOL stages were assumed to be the same for the selected pavement types, they were not considered.

Only asphalt pavement was included in the current analysis because only that type of pavement was performance-tested under NG-WBT with the APT. This study focused on asphalt mill and overlay treatments.

Selection of an analysis period for the study was problematic as the scenarios for different structures, traffic levels, and tire types each led to a different pavement design life. Theoretically, the analysis period for a pavement LCA study should be based on the design life of the longest-lived pavement in the study (i.e., with design life defined as the time period between the end of

construction and when the failure criteria for the performance model are reached). Two options for selecting an analysis period were proposed for this study: i) using a common analysis period for all scenarios and including at least one M&R event in each scenario; and ii) annualizing the total environmental impacts in each scenario within the design life of that scenario, and assuming that the M&R treatment is repeated in the future. Under the first option, it is expected that multiple M&R treatments are performed in some of the scenarios. Therefore, the environmental impacts from the material production and construction stages in the pavement life cycle of the last M&R treatment need to be annualized, and only those within the analysis period should be included to ensure a fair comparison among the different scenarios. In the second option, the total life cycle impacts within the design life of the pavement of each scenario are first calculated and then annualized so that comparisons can be made among the different scenarios. In this study, a range of possible market penetrations of NG-WBT were analyzed, which inevitably led to a range of possible design lives. With the first method, this created the problem of arbitrarily selecting an analysis period to cover all possible service lives and increases the complexity. The second option was used in this study to avoid this problem, with the assumption that these treatments are repeated when they reach their design life. In addition, the design life was determined when the pavement fails due to bottom-up fatigue cracking or rutting, or when pavement roughness reached its threshold value (170 in/mi).

In terms of environmental impacts, a decision was made to limit this study to energy consumption, measured in mega-joules (MJ), and to GHG emissions, measured in CO_2-equivalents (CO_2-e), the most common indicator used when discussing global warming. This was decided because the study's scope was limited to evaluating potential contributions from pavements to global warming and was supported by a broad interest in the fossil-energy dependence of on-road transportation systems. CO_2-e is a midpoint indicator (as opposed to endpoint indicator, such as damage to the economy due to sea level rise or damage to ecosystems) and its use is supported by various scientific studies. The GHG emissions assessed in the study include carbon dioxide (CO_2), methane (CH_4), and nitrous oxide (N_2O). The quantities of the emissions were normalized into CO_2-e using their 100-year global warming potentials (GWPs) (IPPC, 2007). In terms of economic impacts, the present worth dollar was used as the monetary indicator.

Overall Procedure

This study examined the difference in GHG emissions, energy consumption, and cost between two tire technologies: standard DTA and NG-WBT. The life-cycle energy consumption, GHG emissions, and cost from the selected pavement segments were calculated using the following:

- A pavement performance model based on standard DTA and NG-WBT
- Life-cycle inventories (LCIs) of the material production and construction stages
- Vehicle emissions factors based on standard DTA and NG-WBT in the pavement use stage
- Unit cost information for pavement materials and equipment operation activities

The characteristics of both tires are given in Table 37, and the procedure followed is shown in Figure 231 and described in detail below.

For the scenario DTA (i.e., 0 percent market penetration of NG-WBT), GHG emissions and energy consumption for the pavement life cycle were calculated using standard DTA, and this was treated as the baseline case. LCIs and costs of unit processes for each pavement life cycle stage were taken from the UIUC's database. The calculated pavement design life was based on different pavement damage scenarios, which are discussed in detail below. For the NG-WBT scenarios, a series of market penetration levels of those tires were evaluated. Calculations for these were similar to those used for standard DTA, but the vehicle fuel economy values in the use stage were higher for NG-WBT.

Table 37. Characteristics Used to Describe the Two Tire Types

	Standard Dual-Tire (Baseline)	Wide-Base Tire
NG-WBT market penetration	0%	5%, 10%, 50%, 100%
Design life	Calculated based on different damage scenario using Miner's rule	Calculated based on different damage scenario using Miner's rule
LCIs of material production and construction stages	UIUC LCI database	UIUC LCI database
Use stage vehicle fuel economy improvement	0	1.5% improvement per axle compared with baseline

Pavement Life Cycle Modeling

Material Production

The material production stage of pavement included a detailed investigation of aggregates, asphalt binder, and asphalt mix production. Multiple data sources for each material were reviewed, data sources were disaggregated to the process level, processes were compared with respect to related technologies, and then the data sources were recalculated based on the local condition and redefined system boundary. The results from this stage were considered to represent the LCI up to the time when materials left the "factory gate"; transportation of the processed materials to and from the construction site was considered part of the construction stage.

The spatial scale of materials used in pavement construction ranges from local to global. In this case, aggregates and asphalt are usually produced locally or regionally. LCI data are usually collected through field surveys and laboratory experiments. However, in the absence of such data, data from published LCI data sources and other LCA reports were used. Because each selected data source represents different local conditions, technologies, and system boundaries, they were customized before being used. For example, some were truncated or expanded to make the system boundary the same.

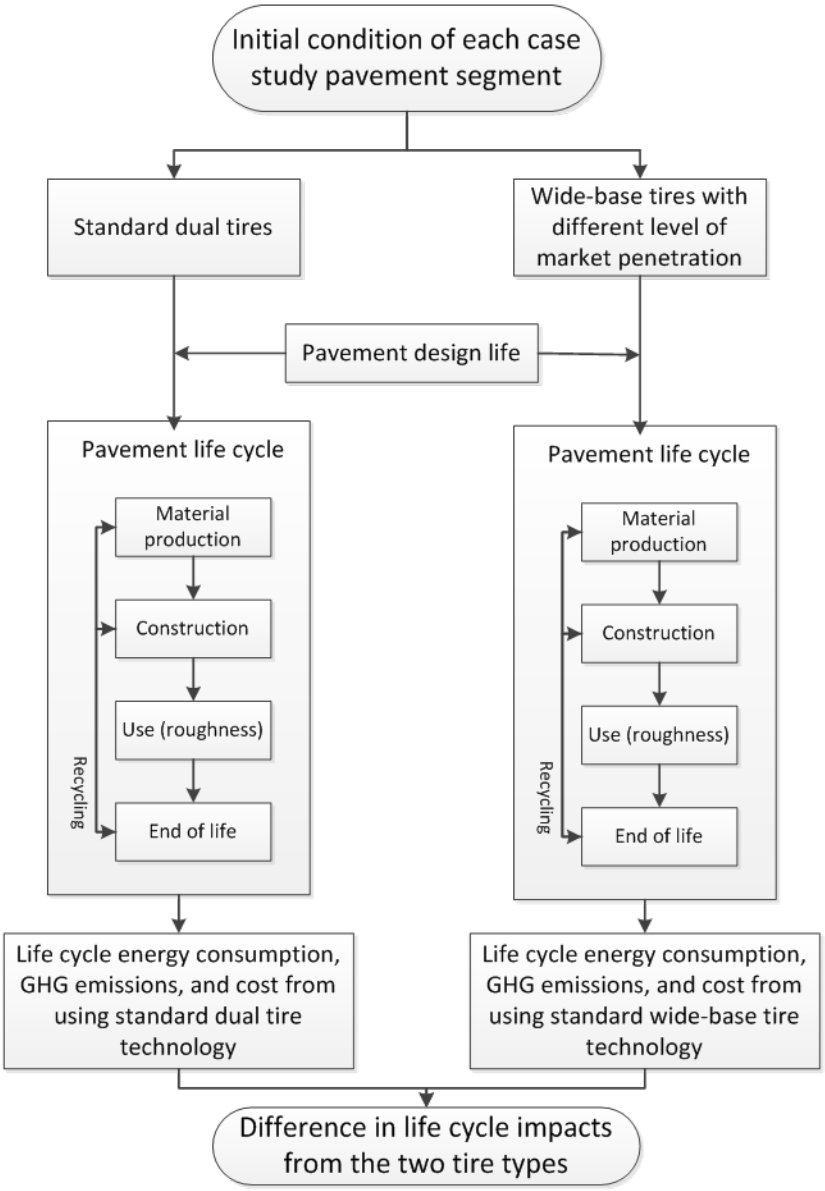

Figure 231. Illustration. Overall procedure for the LCA and cost analysis.

In the LCI database developed by UIUC, multiple data sources such as commercial LCI database (Ecoinvent) and survey questionnaires were considered for each material. A number of data sources for the primary energy consumption of major materials are shown in Table 38 for comparison purposes. Data sources for this benchmark include the pavement LCI produced by Stripple et al. in Sweden (Stripple, 1998), asphalt inventory produced by the Athena Institute in Canada (2006), Ecoinvent (Swiss Centre for Life Cycle Inventories, 2011), and the U.S. Life Cycle Inventory (U.S. LCI) produced by the National Renewable Energy Laboratory (NCHRP, (2004). Default US-Ecoinvent 2.2 unit processes were used for production of binder, aggregate, and electricity, and material hauling in this study to reflect general conditions of North America. For regional inventory database development, Emissions and Generation Resources Integrated Database (eGRID) (2012), Greenhouse Gases, Regulated Emissions, and Energy Use in

Transportation (GREET) (2013), and data from the U.S. Energy Information Administration (2014) were used for the electricity, fuel, asphalt binder production models, respectively. For the asphalt mixing plant, data from survey questionnaires were used, but modified with default US-EI electricity model.

As shown in Figure 240 and Figure 241, UIUC's pavement LCA tool was used to evaluate the economic saving in the material stage from implementing different M&R strategies affected by using NG-WBT. The results of economic savings were annualized in present value with a discount rate of 3%.

Table 38. Primary Energy Consumption per Mass of Each Material or Process (MJ/kg) (Lee, 2013)

	Stripple	Athena	EcoInvent	U.S. LCI
Crushed aggregate	0.0786	0.0576	0.14	0.056
Natural aggregate	0.00767	0.0360	0.059	0.0397
Asphalt: Feedstock	40.2	40.2	40.2	40.2
Asphalt: Manufacturing	2.89	5.32	9.0	10.5
Asphalt mixing plant: Hot-mix asphalt (with reclaimed asphalt pavement)	0.551	0.531	--	--

Construction

Because pavement may have different performances under standard DTA and NG-WBT, the construction activities triggered by pavement performance were different with different levels of NG-WBT traffic.

The environmental impacts that occur in the pavement construction stage include fuel use and the emissions contributed by both construction equipment and construction-related traffic. An example of the construction stage data flow is shown in Figure 232. It was assumed that construction occurs during nine-hour nighttime closures, so there would be minimal impact from construction-related traffic.

A list of construction tasks was obtained from historic construction data. Information on the productivity and fuel consumption of construction equipment from the National Cooperative Highway Research Program (NCHRP) Report 744 (2013), PaLATE pavement LCA tool (Horvath, 2007), ROADEO road emission optimization tool (ASTAE, 2011), and the Athena Institute's Impact Estimator software (2013) were used to calculate inventories of construction activities. EPA's NONROAD (2008) was used to obtain the fuel use and emission factors of construction equipment and environmental impacts associated with diesel combustion was obtained from SimaPro (PRe Constultants, 2013).

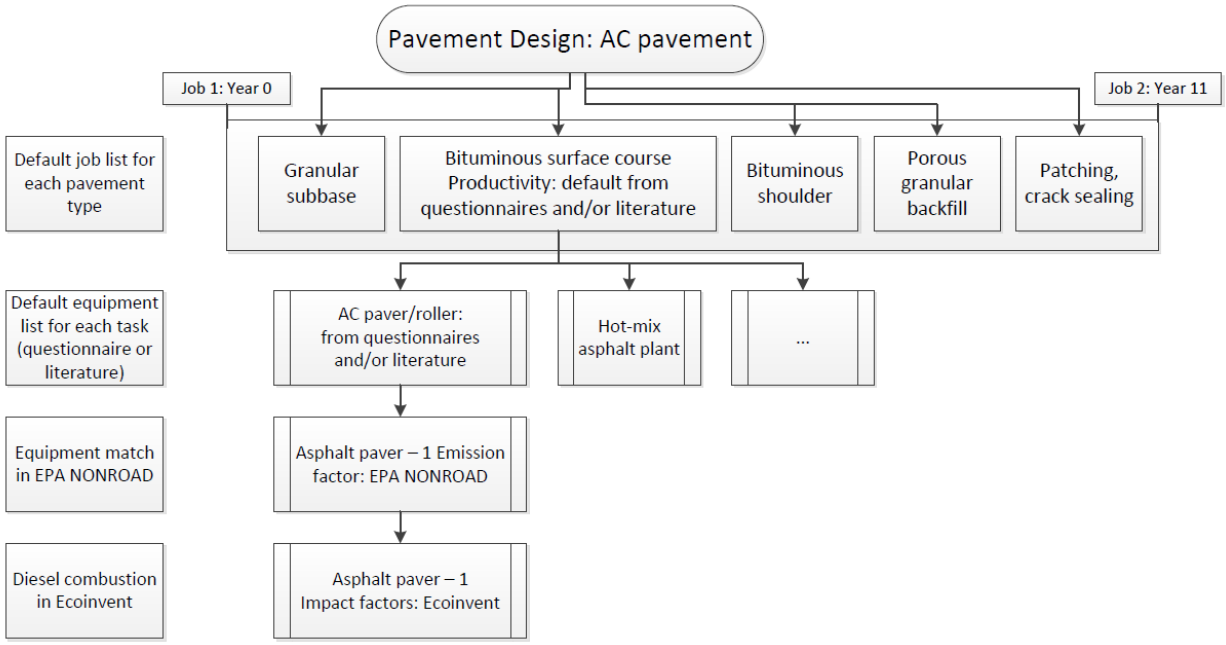

Figure 232. Illustration. An example construction stage data flow for JPCP.

As seen in Figure 232, construction data flow begins with the design. The design pavement structure is related to a given set of construction, maintenance, and rehabilitation tasks grouped together based on the construction plan. Each task has a productivity rate indicating how fast the task can be done and a set of default equipment is assigned to each task. The task productivity is related to the individual equipment fuel consumption to calculate the fuel usage for the task. Based on the fuel used by each piece of equipment, the emissions and environmental impacts are then computed. Construction tasks used in the study include pavement milling, removal, paving, and hauling. Cost information associated with these tasks was obtained from an estimator and compared various sources (Caltrans, 2011; Brock & Richmond, 2006; U.S. Energy Information Administration, 2014).

Based on the pavement structures presented in Figure 240 and Figure 241, UIUC's pavement LCA tool was used to evaluate changes in economic performance in the construction stage from implementing different M&R strategies affected by using NG-WBT.

Use

According to the UCPRC Pavement LCA Guideline (Harvey et al., 2010), the pavement use stage includes additional vehicle operation resulting from deterioration of the pavement (including increases in fuel consumption, pollutant emissions, damage to vehicles, damage to freight, tire wear), the heat island effect from the pavement, non-GHG-related climate change effects from the pavement albedo, roadway lighting effects from pavement albedo, and water pollution from leachate and runoff. But when these case studies were conducted, the only quantitatively reliable model available was the one that considered additional fuel consumption

and GHG emissions. As a result, this study only considers the effect of pavement on fuel economy during the use stage.

Figure 233 shows the modeling procedure. First, the time progression of pavement surface characteristics under standard DTA on a road segment was generated from a pavement condition survey or pavement performance model. At the same time, using different M&R strategies and percentages of NG-WBT, different scenarios were developed based on these surface characteristics under standard DTA. Using a rolling resistance model, rolling resistance values were calculated based on these surface characteristics, and the values were used to update the relevant parameters in a vehicle emissions model, which simulates an engine's running status. The vehicle emissions model selected had to be capable of analyzing emissions at the microscopic level to allow for updating the rolling resistance parameters. However, the updating procedure could vary among different vehicle emissions models.

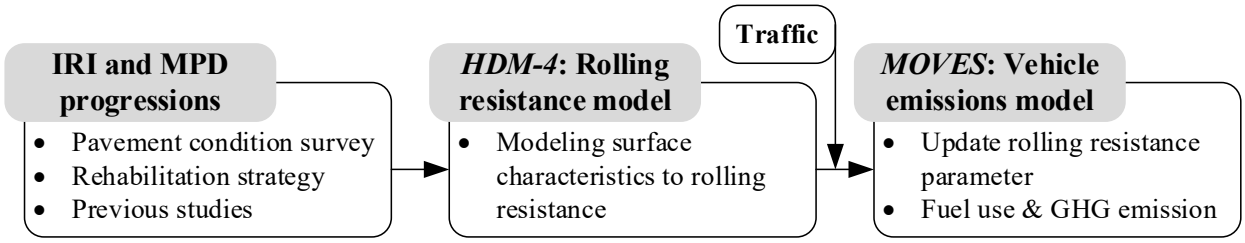

Figure 233. Illustration. Procedure to address additional fuel consumption and GHG emission.

Next, traffic data for this road segment were extracted from a traffic database. Once this was done and the rolling resistance parameter was updated, fuel consumption and emissions could be modeled through the vehicle emissions model, and the net difference between different M&R strategies could be evaluated.

In the UIUC approach, the HDM-4 by PIARC (World Road Association) and MOVES (Motor Vehicle Emission Simulator) by the U.S. Environmental Protection Agency (2014) were adopted as the rolling resistance model and the vehicle emissions model, respectively. HDM-4 has a rolling resistance model that simulates rolling resistance based on IRI and an engine model that considers rolling resistance as it addresses vehicle fuel consumption. Based on the vehicle fuel consumption, emissions factors were supplemented from MOVES simulations. Similarly, the UC-Davis approach was adopted for the rolling resistance model due to MPD.

Because no model of IRI performance has been developed based on NG-WBT, three scenarios were developed for evaluating the potential impacts from NG-WBT on pavement IRI. Further, because the relationships among pavement surface characteristics, rolling resistance, and vehicle fuel consumption for vehicles equipped with NG-WBT have not been fully developed to date either, this study adopted an average reduction in vehicle fuel consumption from NG-WBT of 1.5% per axle, a typical range of fuel saving from NG-WBT in literature, derived from various data sources. The fuel consumption and GHG emissions resulting from use of standard DTA were calculated by applying the existing UIUC and UC-Davis use stage models. The results obtained were then lowered by 1.5% (per axle) for NG-WBT.

The economic saving from fuel economy improvement of 1.5% (per axle) was calculated by converting the energy savings to the amount of fuel using a higher heating value of diesel. The upstream energy associated with diesel production was not included. The amount of fuel saved was then multiplied by the unit price of diesel to compute the monetary value saving in the use stage. The discount rate of 3% was applied in cost calculations.

Pavement Performance Model

MPD and IRI

To assess energy consumption and GHG emissions reduction in the use stage, it is necessary to evaluate IRI and MPD performance with and without pavement treatment activities. Because of the lack of sufficient performance data on pavement surface characteristics under NG-WBT, some of the scenarios in this study assume that IRI and MPD have the same progression model under standard DTA and NG-WBT.

The IRI progression model for medium thickness asphalt overlays is obtained from a study by Tseng at UCPRC (Tseng, 2012). This model uses the number of ESALs, IRI value before the overlay, overlay type, and climate region as inputs. Equations in Figure 234 and Figure 235 show the models for initial IRI after construction and IRI progression, respectively.

$$IRI_{initial} = a \times IRI_{previous} + b$$

Figure 234. Equation. Initial IRI after construction.

$$IRI_t = IRI_{initial} + c \times Age^d$$

Figure 235. Equation. IRI progression.

where:

$IRI_{initial}$= IRI immediately after construction of the overlay, in in/mi
$IRI_{previous}$= IRI value before the overlay, in in/mi
a and b= coefficients in the overlay progression model, which are different for each type of overlay defined in the pavement management system
IRI_t= IRI value at Age t years, in units of in/mi
Age= age of the pavement section after last treatment, years
c and d= coefficients in the progression model, which are different for each type of treatment, ESAL level (as defined by the model), and climate region group

Table 39. Coefficients of IRI Model for Asphalt Overlay

Overlay Type[1]	ESAL Level[2]	Climate Region Group[3]	*a*	*b*	*c*	*d*
Medium Overlay (0.1 to 0.25 ft)	A	Severe	0.40	42.23	6.175	1.44
Medium Overlay (0.1 to 0.25 ft)	A	Mild	0.40	42.23	5.89	1.35
Medium Overlay (0.1 to 0.25 ft)	B	Severe	0.40	42.23	6.5	1.44
Medium Overlay (0.1 to 0.25 ft)	B	Mild	0.40	42.23	6.2	1.35
Medium Overlay (0.1 to 0.25 ft)	C	Severe	0.40	42.23	6.825	1.44
Medium Overlay (0.1 to 0.25 ft)	C	Mild	0.40	42.23	6.51	1.35
Thick Overlay (> 0.25 ft)	A	Severe	0.62	12.18	0.76	2.07
Thick Overlay (> 0.25 ft)	A	Mild	0.62	12.18	0.76	1.98
Thick Overlay (> 0.25 ft)	B	Severe	0.62	12.18	0.8	2.16
Thick Overlay (> 0.25 ft)	B	Mild	0.62	12.18	0.8	1.98
Thick Overlay (> 0.25 ft)	C	Severe	0.62	12.18	0.84	2.16
Thick Overlay (> 0.25 ft)	C	Mild	0.62	12.18	0.84	1.98

Note:
1: These treatments are defined in the pavement management system based on the thickness of the overlay. Because this study used two pavement designs with different thicknesses, the corresponding type of overlay was selected in the modeling process.
2. Annual ESAL level is defined in accordance with the pavement management system:
A: Annual ESAL ≤ 100,000;
B: 100,000 < Annual ESAL ≤ 500,000; and
C: Annual ESAL > 500,000.
3. Climate region group is defined as:
Severe climate: Central Coast, Desert, Inland Valley, South Mountain;
Mild climate: High Desert, High Mountain, Low Mountain, North Coast, South Coast.
The climate regions are defined by Caltrans to show the impact of temperature, precipitation, freezing/thawing, and solar radiation on pavement (*2013*). The climate region group is defined by Tseng (2012).

The progression of MPD over time for AC surfaces was taken from a previous study performed by the UCPRC (Lu et al., 2009). The model of MPD progression for an AC overlay is shown in Figure 236.

$$MPD(micron) = -93.7089 - 4.2910 \times AirVoid(\%) + 47.8933 \times Age(year) + 28.2136 \times FinenessModulus - 9.9487 \times NMAS(mm) - 5.4209 \times Thickness(mm) - 0.7087 \times NumberOfDays > 30C - 0.0402 \times AADTTinLane$$

Figure 236. Equation. Progression of mean profile depth with time.

where *NMAS* is the nominal maximum aggregate size, and others variables are indicated by their names.

Fatigue Cracking

Because a range of market penetration levels of NG-WBT was assessed, which would lead to a range of service lives of pavement, the performance model for fatigue and rutting was also used in this study.

The Asphalt Institute fatigue equations were used to determine cracking life. MEPDG was not used because it provided unreasonable results. The equations are shown in Figure 237 and Figure 238, where N_f is the maximum allowed repetition; C is the correction factor; V_a is the volume of asphalt in the mix; V_b is the volume of air in the mix; ε_t is the tensile strain; and $|E^*|$ is the dynamic modulus in units of psi, which is the stiffness of the asphalt. To account for the difference between laboratory and field conditions, a factor of 18.4 was included as follows:

$$N_f = 0.0795 \times C\varepsilon_t^{-3.291}|E^*|^{-0.854}$$

Figure 237. Equation. Maximum allowed repetition.

$$C = 10^{4.84\left(\frac{V_b}{V_a+V_b}-0.69\right)}$$

Figure 238. Equation. Correction factor.

Subgrade Rutting

The Asphalt Institute rutting model was used to determine rutting performance because, as in the case of fatigue cracking, MEPDG transfer functions provided unreasonable results for rutting. The maximum number of axle load repetitions to reach 0.5 in rut depth (N_d) is:

$$N_d = 1.365 \times 10^{-9}\varepsilon_c^{-4.447}$$

Figure 239. Equation. Number of repetitions to rutting failure.

where ε_c is the vertical compressive strain on top of the subgrade.

CASE STUDIES

Two case studies that focused on asphalt pavements were performed using the described LCA approach. The case studies were undertaken to obtain a preliminary indication of the net effects on GHG emissions, cost, and energy use of NG-WBT and different truck traffic levels.

Functional Unit and System Boundary

Both case studies considered an asphalt overlay treatment. In this type of treatment, an old asphalt layer is milled and a new asphalt overlay is applied. The LCA stage considered in the modeling included material production, construction, and use. The routine maintenance and EOL stages were assumed to be the same for each pavement type, so they were not considered. Transportation of materials removed during the treatments in the EOL stage was considered in the material production and construction stages. Annualized impacts were used from the pavement life cycle to avoid inconsistent pavement design lives among the different scenarios, assuming that these treatments will be repeated when the pavements reach the end of their design lives.

The two case studies were based on the following two structure designs used in the APT experiments (see Table 40 for a detailed description and Figure 240 for cross section of the pavement structures):

- A segment, case study 671HC, using a thick AC layer for a high truck traffic volume
- A segment, designated case study 670HC, using a thin AC layer for a low truck traffic volume

Two criteria were used for selecting the segments: i) the truck traffic level on the segment would lead to a reasonable design life; and ii) the roughness level on the segment was high enough (170 in/mi) to trigger an M&R treatment. The designs were applied to two segments in the highway network that met these criteria. The design for case 671HC was applied on a segment of westbound Interstate 80 (I-80) in Nevada County in California with two lanes per direction. The segment is a two-mile rural highway with an IRI value of about 102.5 in/mi. The one-way AADT on this segment was 13,500 with 19% truck percentage. The design for case 670HC was applied to a two-mile segment of southbound State Route 213 in Los Angeles County, California with two lanes per direction. The IRI before the treatment was 113.6 in/mi. The one-way AADT on this segment was 15,750 with 2% trucks.

Each case study considered an AC overlay treatment carried out in 2012 with the same thickness as the AC layer in the original pavement. Each case also modeled standard DTA as the baseline (i.e., where a 0% market penetration of NG-WBT is in place), and four levels of market penetration of NG-WBT (5%, 10%, 50%, and 100%). These market penetrations were assumed to be constant throughout the analysis period. The differences in energy consumption and GHG emissions were evaluated between the NG-WBT and standard DTA. Because roughness was not included in the APT tests and because of the unavailability of an IRI performance model for NG-WBT, the following three scenarios were designed for and analyzed in this study to assess the potential impacts from NG-WBT.

Table 40. Summary of the Two Case Studies

Case Study	671HC (Thick Asphalt)	670HC (Thin Asphalt)
County	Nevada	Los Angeles
Route	I-80 Westbound	SR-213 Westbound
Surface	Asphalt concrete	Asphalt concrete
Section length	3,129 mi (2 miles)	3,129 mi (2 miles)
Number of lanes in each direction	2	2
Lane width	3.66 mi	3.66 mi
AADT (one-way)	13,500	15,750
Truck percentage	19%	2%
Construction type	Mill and asphalt overlay	Mill and asphalt overlay
AC layer thickness	4.9 in	3.0 in
Tire types analyzed	Standard DTA and four levels of market penetration of NG-WBT	Standard DTA and four levels of market penetration of NG-WBT

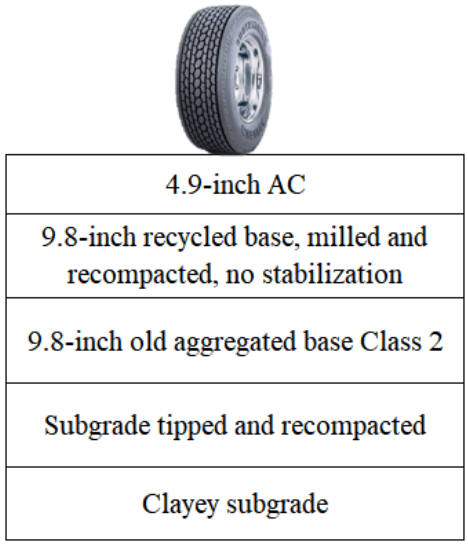

Figure 240. Illustration. Cross-sections of the 671HC section (thick AC).

3.0-inch AC
9.8-inch recycled base, milled and recompacted, no stabilization
9.8-inch old aggregated base Class 2
Subgrade tipped and recompacted
Clayey subgrade

Figure 241. Illustration. Cross-sections of the 670HC section (thin AC).

- Scenario I: standard DTA and NG-WBT have the same impact on the pavement's fatigue cracking and roughness (indicated by IRI) performance. In this scenario, any level of market penetration of NG-WBT results in the same level of damage to the pavement, and therefore the pavement has the same design life, which is calculated based on the fatigue cracking performance under standard DTA. The only difference expected from the different levels of NG-WBT market penetration would be the fuel economy improvement gained from their use.
- Scenario II: standard DTA and NG-WBT have different impacts on pavement's cracking performance and the same impacts on the pavement's roughness performance. The pavement design life is determined by the maximum allowed repetitions calculated from the fatigue cracking model. In this scenario, different levels of market penetration of NG-WBT lead to different design lives of pavement, calculated using Miner's rule. Annualized life cycle inventory was used in this study, i.e., the annualized GHG emissions from the material production and construction stages and the annualized GHG emissions reduction from the use stage, therefore avoiding the problem of adopting an analysis period that covers the different design lives resulting from different use levels of NG-WBT.
- Scenario III: standard DTA and NG-WBT have the same impacts on pavement's fatigue cracking performance, but different impacts on the pavement's roughness performance. The rutting performance model was used as an approximate indicator for roughness performance. The difference in IRI performance between standard DTA and NG-WBT was considered proportionate to the difference in their respective rutting life. The annual IRI value under NG-WBT was calculated using Equation (10.7).

$$\Delta \mathrm{IRI}_{NGWBT\ between\ year\ j\ and\ 1} = \Delta IRI_{DTA\ between\ year\ j\ and\ 1} \times \frac{Rutting\ life_{DTA}}{Rutting\ life_{NGWBT}}$$

Figure 242. Equation. Evolution of IRI value under NG-WBT.

where:

$\Delta IRI_{NGWBT\ between\ year\ j\ and\ 1}$	= increase of IRI value between Year j and Year 1 under NG-WBT
$\Delta IRI_{DTA\ between\ year\ j\ and\ 1}$	= increase of IRI value between Year j and Year 1 under DTA
$Rutting\ life_{DTA}$	= pavement design life in years under standard DTA calculated based on the rutting model shown by the equation in Figure 239
$Rutting\ life_{NGWBT}$	= pavement design life in years under NG-WBT calculated based on the rutting model given by the equation in Figure 239

Material Production Stage

The material production stage includes the extraction and initial processing of aggregates, asphalt, and the AC mixing process at the mixing plant. Processes in this stage include raw material acquisition, transport of raw materials to and from the plant, and material manufacturing. The transport of AC to and from the site was attributed to the construction stage.

Construction Stage

LCIs of the construction stage of each pavement segment were calculated on a prorated basis depending on the size of each construction event. Calculation was based on the total amount of AC material needed. Hauling of AC materials from plants to the construction site was considered. Based on the number of hours of equipment operation for each construction task, the amount of fuel used was calculated and the corresponding impacts were computed.

Use Stage

As noted in the discussion of the system boundary, this study focused on assessing life-cycle energy consumption, GHG emissions, and cost under three scenarios. The greatest difference between these three scenarios occurred in the pavement performance of the use stage.

In the use stage, case studies focused on the effects of pavement surface characteristics, IRI and MPD, on fuel economy. In order to simplify the study, some assumptions and adjustments were made for items that were common to all the scenarios:

- Use of NG-WBT instead of standard DTA resulted in an average improvement in vehicle fuel economy of 1.5% per axle when all other conditions are kept constant.
- Routine maintenance activities in the use stage were assumed to be equal and were therefore ignored.
- Traffic volume and fleet composition were the same during weekdays and weekends.
- Hourly traffic distribution was the same for all types of vehicles.
- Alternative fuel vehicles were not considered.

For each scenario, it was necessary to determine the pavement design life and roughness performance in order to calculate the annualized emissions based on the market penetration of NG-WBT. The following steps were used to calculate the design life under each situation:

- The maximum repetitions allowed were calculated using either the maximum tensile strain at the bottom of the AC layer or the maximum compressive strain on top of the subgrade (depending on whether it is fatigue cracking or rutting, respectively) using the results obtained from the UIUC ICT-Wide tool, based on the specific performance equation.
- The number of repetitions that the pavement receives each year was calculated based on the ESAL count, and that result was divided by the maximum allowed repetitions (as shown in Table 41) to calculate the annual damage to the pavement.
- Using Miner's Law, the design life was calculated by counting how many years it would take the cumulative damage to reach a value of 1. Because a series of market penetrations of NG-WBT were assessed, the damage from standard DTA and NG-WBT were calculated separately and then summed when Miner's rule was applied.

The time for pavement roughness to reach the IRI threshold value (170 in/mi) was used as the design life if this happens before the failure due to fatigue cracking or rutting.

The UIUC's ICT-Wide tool was used to predict the maximum tensile strain and maximum compressive strain in cases 670HC and 671HC (Table 41). Maximum tensile strain values were obtained under 18-kip axle load, temperature of 68 °F, and 100 psi tire pressure. The maximum allowed repetitions and the design life for each scenario are shown in Table 42 through 44, respectively.

Figure 243 and Figure 244show the *IRI* progression over five years for cases 671HC and 670HC for Scenarios I and II (these two scenarios have the same IRI performance), using the pavement performance previously discussed. Figure 245 and Figure 246 show the IRI progression over five years for Scenario III of cases 671HC and 670HC, using rutting performance to predict IRI performance under NG-WBT. Figure 247 and Figure 248 show the MPD progression over five years under all tires.

Table 41. Maximum Tensile and Compressive Strain in Cases 670HC and 671HC

Tire Type	Distress Type	Location and Type of Strain	Case 670HC (Thin AC)	Case 671HC (Thick AC)
Standard DTA	Fatigue cracking	Maximum tensile strain on the bottom of AC (με)	282.29	178.38
Standard DTA	Fatigue cracking	Maximum allowed repetitions	617,891	4,572,714
Standard DTA	Rutting	Maximum compressive strain on the top of subgrade (με)	529.53	339.34
Standard DTA	Rutting	Maximum allowed repetitions	634,271	4,650,284
NG-WBT	Fatigue cracking	Maximum tensile strain on the bottom of AC (με)	355.52	211.38
NG-WBT	Fatigue cracking	Maximum allowed repetitions	289,239	2,615,586
NG-WBT	Rutting	Maximum compressive strain on the top of subgrade (με)	615.86	375.61
NG-WBT	Rutting	Maximum allowed repetitions	322,568	2,951,443

Table 42. Annual Damage and Design Life: Scenario I under Different WBT Market Penetrations

Case	Market Penetration of NG-WBT	Annual Damage	Design Life (Years)	Time to IRI Threshold (Years)
671HC (thick AC)	0% (standard DTA, i.e., baseline)	0.125	12	11
671HC (thick AC)	5%	0.125	12	11
671HC (thick AC)	10%	0.125	12	11
671HC (thick AC)	50%	0.125	12	11
671HC (thick AC)	100%	0.125	12	11
670HC (thin AC)	0% (standard DTA, i.e., baseline)	0.269	11	7
670HC (thin AC)	5%	0.269	11	7
670HC (thin AC)	10%	0.269	11	7
670HC (thin AC)	50%	0.269	11	7
670HC (thin AC)	100%	0.269	11	7

Table 43. Annual Damage and Design Life: Scenario II under Different WBT Market Penetrations

Case	Market Penetration of NG-WBT	Annual Damage	Design Life (Years)	Time to IRI Threshold (Years)
671HC (thick AC)	0% (standard DTA, i.e., baseline)	0.125	12	11
671HC (thick AC)	5%	0.129	11	11
671HC (thick AC)	10%	0.134	11	11
671HC (thick AC)	50%	0.170	9	11
671HC (thick AC)	100%	0.215	7	11
670HC (thin AC)	0% (standard DTA, i.e., baseline)	0.268	11	7
670HC (thin AC)	5%	0.273	11	7
670HC (thin AC)	10%	0.278	10	7
670HC (thin AC)	50%	0.319	7	7
670HC (thin AC)	100%	0.370	6	7

Table 44. Annual Damage and Design Life: Scenario III under Different WBT Market Penetrations

Case	Market Penetration of Wide-Base Tires	Annual Damage	Design Life (Years)	Time to IRI Threshold (Years)
671HC (thick AC)	0% (standard DTA, i.e., baseline)	0.243	12	11
671HC (thick AC)	5%	0.248	11	11
671HC (thick AC)	10%	0.254	11	11
671HC (thick AC)	50%	0.296	9	10
671HC (thick AC)	100%	0.350	8	9
670HC (thin AC)	0% (standard DTA, i.e., baseline)	0.171	12	7
670HC (thin AC)	5%	0.176	11	7
670HC (thin AC)	10%	0.180	11	7
670HC (thin AC)	50%	0.218	8	5
670HC (thin AC)	100%	0.264	6	5

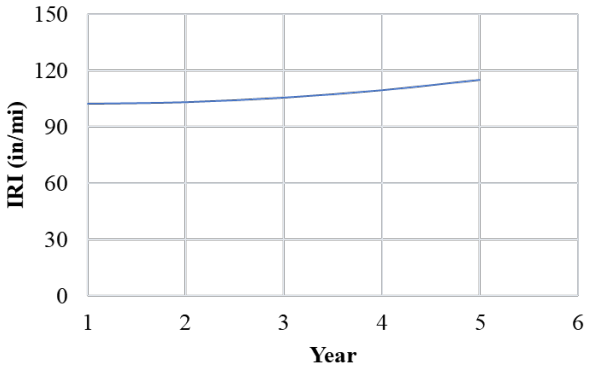

Figure 243. Graph. Scenario I and Scenario II IRI progression for case 671HC (thick AC).

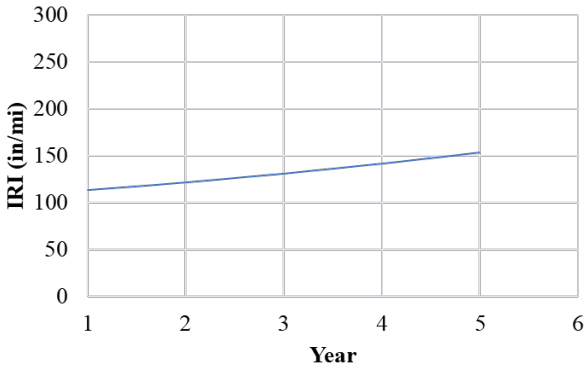

Figure 244. Graph. Scenario I and Scenario II IRI progression for case 670HC (thin AC).

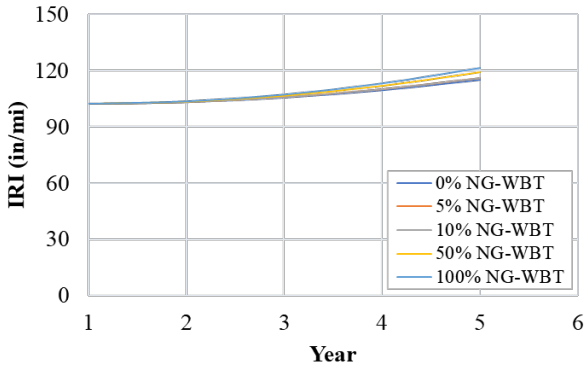

Figure 245. Graph. Scenario III IRI progression for case 671HC (thick AC).

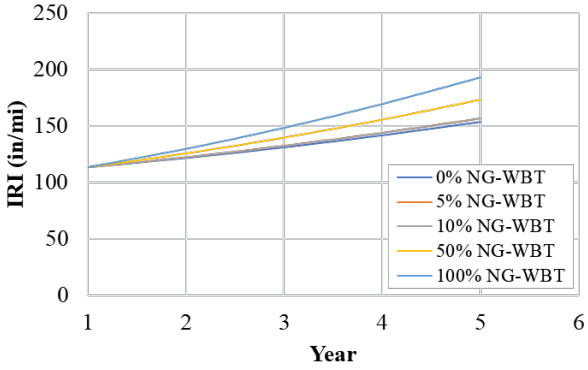

Figure 246. Graph. Scenario III IRI progression for case 670HC (thin AC).

In case 671HC (thick AC), 0% NG-WBT (standard dual-tire), 5% NG-WBT, 10% NG-WBT, 50% NG-WBT, and 100% NG-WBT showed nearly the same IRI progression on each lane. Initial IRI values are different because the two lanes carried different initial IRI values. In addition, in case 670HC (thin AC), 0% NG-WBT (standard dual-tire), 5% NG-WBT, and 10% NG-WBT showed the same IRI progression on each lane. The 50% NG-WBT tire and 100%

NG-WBT showed the same IRI progression on each lane. Finally, initial IRI values are different because the two lanes carried different initial IRI values.

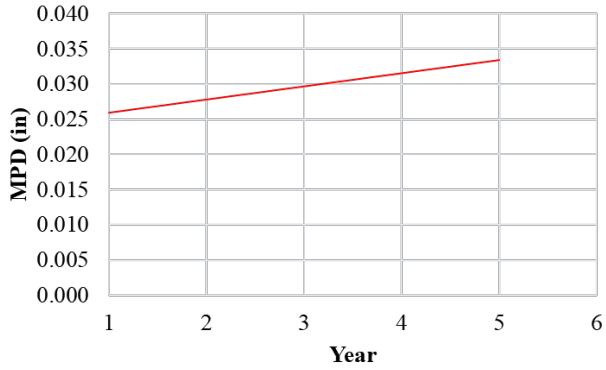

Figure 247. Graph. MPD progression in all scenarios for case 671HC (thick asphalt).

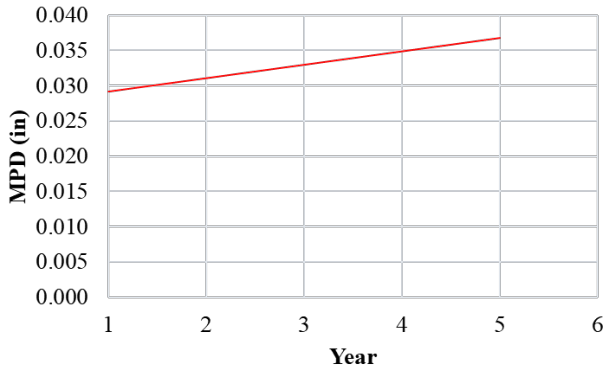

Figure 248. Graph. MPD progression in all scenarios for case 670HC (thin asphalt).

Results and Discussion

Scenario I: Same Fatigue and IRI Performance between Two Tires

In this scenario, the pavement performed the same under the standard DTA and NG-WBT. Therefore, the only difference in the results is the improved fuel economy due to use of the NG-WBT. Table 45 and 46 show the results for cases 671HC and 670HC, respectively, and Figure 249 and Figure 250 shows the GHG emissions reduction for each case.

The results are intuitive: since no other impacts on the pavement from use of NG-WBT were included, the only benefits were improved fuel economy and an expected reduction in GHG emissions (due to less fuel consumed) for both cases. Also, because only trucks were equipped with NG-WBT, the higher the truck traffic volume and the greater the market penetration of NG-WBT, the greater the fuel savings (both environmentally and economically) and the greater the anticipated emissions reduction.

Table 45. Scenario I Results for Case 671HC (Thick AC): Energy Savings and GHG Emissions Reductions Compared with the Baseline (DTA) per year

	Market Penetration of Wide-Base Tires	Use Stage	Life Cycle Result
Energy saving compared with the baseline (MJ)	5%	53,077	53,077
Energy saving compared with the baseline (MJ)	10%	106,153	106,153
Energy saving compared with the baseline (MJ)	50%	530,767	530,767
Energy saving compared with the baseline (MJ)	100%	1,061,534	1,061,534
GHG reduction compared with the baseline (kg CO_2-e)	5%	0	0
GHG reduction compared with the baseline (kg CO_2-e)	10%	3,999	3,999
GHG reduction compared with the baseline (kg CO_2-e)	50%	7,998	7,998
GHG reduction compared with the baseline (kg CO_2-e)	100%	39,988	39,988
Economic saving compared with the baseline ($ Present)	5%	924	924
Economic saving compared with the baseline ($ Present)	10%	1,847	1,847
Economic saving compared with the baseline ($ Present)	50%	9,237	9,237
Economic saving compared with the baseline ($ Present)	100%	18,474	18,474

Scenario II: Fatigue Performance Determines the Design Life

In this scenario, the pavement life is determined by fatigue cracking performance. Because the NG-WBT introduced a higher tensile strain at the bottom of the AC layer, which increased the expected amount of fatigue cracking and shortened pavement life, as market penetration of NG-WBT increases, the pavement design life decreases. As noted, this study annualized the energy consumption and GHG emissions were annualized from the material production and construction stages to avoid having different pavement design lives. Therefore, as the market penetration of NG-WBT increases, the annualized energy consumption and GHG emissions from the material production and construction stages increase. At the same time, the pavement's IRI performance was the same for NG-WBT and the DTA. Table 46 and Table 47 show the results for cases 671HC and 670HC, respectively, and Figure 251 and Figure 252 show the GHG emissions reduction for each case.

The results show that the damage to pavement from NG-WBT imposed a very significant impact on the material production and construction stages. When this impact was included in the analysis, various consequences were observed for the thin and thick sections. For the 671HC section, net savings in energy consumption and GHG were positive for all market penetration of NG-WBT. However, the net economic saving at 50 and 100% market penetration was negative

as the ratio of calorific or energy value and unit cost of fuel is very high compared with that of pavement materials. Similarly, for the 670HC section, net savings in energy consumption and GHG were positive for all market penetration but economic savings were negative at 100% market penetration because of a reduced pavement service life and a low truck percent.

Table 46. Scenario I Results for Case 670HC (Thin AC): Energy Savings and GHG Emissions Reductions Compared with the Baseline (DTA) per year

	Market Penetration of Wide-Base Tires	Use Stage	Life Cycle Result
Energy saving compared with the baseline (MJ)	5%	6,981	6,981
Energy saving compared with the baseline (MJ)	10%	13,961	13,961
Energy saving compared with the baseline (MJ)	50%	69,806	69,806
Energy saving compared with the baseline (MJ)	100%	139,612	139,612
GHG reduction compared with the baseline (kg CO_2-e)	5%	0	0
GHG reduction compared with the baseline (kg CO_2-e)	10%	526	526
GHG reduction compared with the baseline (kg CO_2-e)	50%	1,052	1,052
GHG reduction compared with the baseline (kg CO_2-e)	100%	5,259	5,259
Economic saving compared with the baseline ($ Present)	5%	129	129
Economic saving compared with the baseline ($ Present)	10%	257	257
Economic saving compared with the baseline ($ Present)	50%	1,285	1,285
Economic saving compared with the baseline ($ Present)	100%	2,571	2,571

It should be noted that this conclusion is heavily dependent on the pavement design life calculated from the performance model. If the pavement has the same design life for both DTA and NG-WBT, the difference in the material production and construction stages between the baseline and the other scenarios will be zero, and the benefit from the use stage will dominate the results. Further, not only is the tensile strain introduced by NG-WBT larger than that from DTA, the NG-WBT also has larger traffic wander. Therefore, when the damage from NG-WBT was calculated, the cumulative damage might have been overestimated, thus resulting in a shortened pavement design life.

Table 47. Scenario II Results for Case 671HC (Thick AC): Energy Savings and GHG Emissions Reductions Compared with the Baseline (DTA) per year

	Market Penetration of Wide-Base Tires	Material Production Stage	Construction Stage	Use Stage	Life Cycle Result
Energy saving compared with the baseline (MJ)	5%	0	0	0	0
Energy saving compared with the baseline (MJ)	10%	0	0	53,077	53,077
Energy saving compared with the baseline (MJ)	50%	-105,407	-19,333	106,153	106,153
Energy saving compared with the baseline (MJ)	100%	-271,048	-49,713	637,187	512,447
GHG reduction compared with the baseline (kg CO_2-e)	5%	0	0	3,999	3,999
GHG reduction compared with the baseline (kg CO_2-e)	10%	0	0	7,998	7,998
GHG reduction compared with the baseline (kg CO_2-e)	50%	-6,388	-1,483	48,114	40,242
GHG reduction compared with the baseline (kg CO_2-e)	100%	-16,428	-3,814	92,864	72,622
	Market Penetration of Wide-Base Tires	**Material Production and Construction Stages**	**n/a**	**Use Stage**	**Life Cycle Result**
Economic saving compared with the baseline ($ Present)	5%	0	0	924	924
Economic saving compared with the baseline ($ Present)	10%	0	0	1,847	1,847
Economic saving compared with the baseline ($ Present)	50%	-23,465	0	10,923	-12,541
Economic saving compared with the baseline ($ Present)	100%	-60,338	0	21,670	-38,668

Table 48. Scenario II Results for Case 670HC (Thin AC): Energy Savings and GHG Emissions Reductions Compared with the Baseline (DTA) per year

	Market Penetration of Wide-Base Tires	Material Production Stage	Construction Stage	Use Stage	Life Cycle Result
Energy saving compared with the baseline (MJ)	5%	0	0	6,981	6,981
Energy saving compared with the baseline (MJ)	10%	0	0	13,961	13,961
Energy saving compared with the baseline (MJ)	50%	0	0	69,806	69,806
Energy saving compared with the baseline (MJ)	100%	-74,538	-13,814	212,779	124,428
GHG reduction compared with the baseline (kg CO_2-e)	5%	0	0	526	526
GHG reduction compared with the baseline (kg CO_2-e)	10%	0	0	1,052	1,052
GHG reduction compared with the baseline (kg CO_2-e)	50%	0	0	5,259	5,259
GHG reduction compared with the baseline (kg CO_2-e)	100%	-4,518	-1,060	16,125	10,548
	Market Penetration of Wide-Base Tires	**Material Production and Construction Stages**	**n/a**	**Use Stage**	**Life Cycle Result**
Economic saving compared with the baseline ($ Present)	5%	0	0	129	129
Economic saving compared with the baseline ($ Present)	10%	0	0	257	257
Economic saving compared with the baseline ($ Present)	50%	0	0	1,285	1,285
Economic saving compared with the baseline ($ Present)	100%	-17,408	0	3,700	-13,708

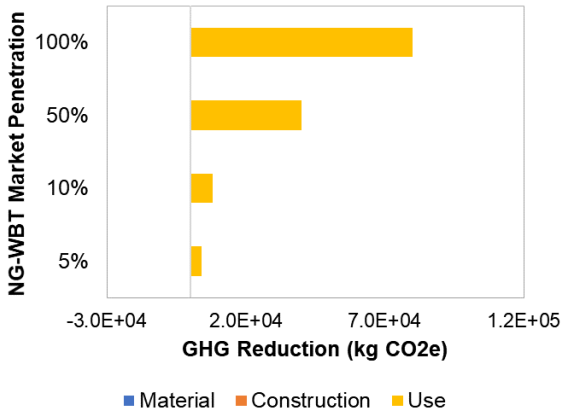

Figure 249. Graph. Scenario I GHG emissions reduction compared with the baseline (standard dual tires): case 671HC (thick AC).

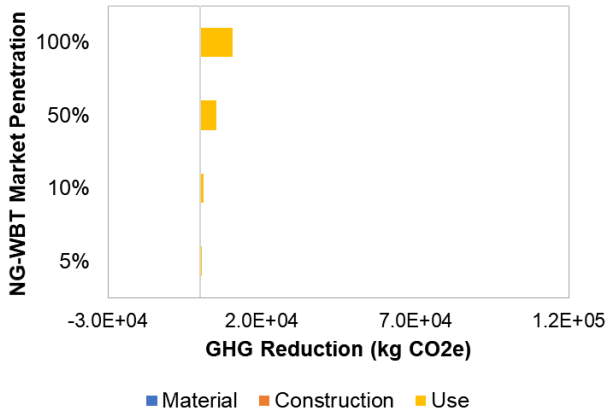

Figure 250. Graph. Scenario I GHG emissions reduction compared with the baseline (standard dual tires): case 670HC (thin AC).

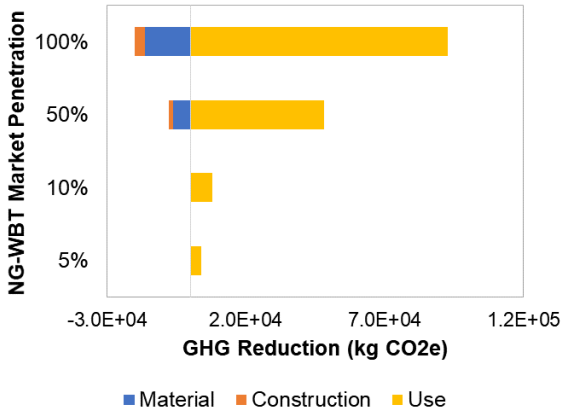

Figure 251. Graph. Scenario II GHG emissions reduction compared with the baseline (standard dual tires): case 671HC (thick AC).

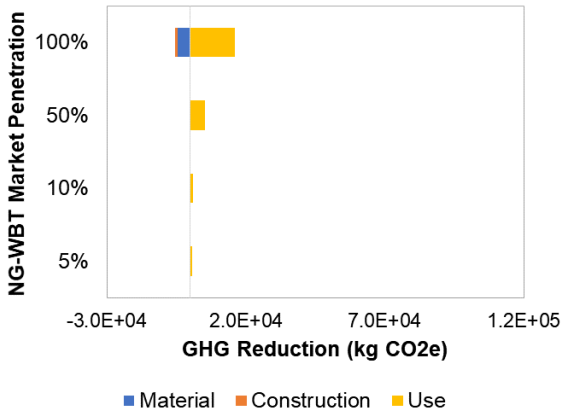

Figure 252. Graph. Scenario II GHG emissions reduction compared with the baseline (standard dual tires): case 670HC (thin AC).

Scenario III: IRI Performance Determines Design Life

In this scenario, the pavements have the same fatigue cracking performance for DTA and NG-WBT, and IRI performance is the determining factor for design life. This part of the study used rutting life to estimate the IRI performance under NG-WBT. Table 49 and 50 show the results for cases 671HC and 670HC, respectively, and Figure 253 and Figure 254 show the GHG emissions reduction for each case.

The use stage results of scenario III for cases 671HC and 670HC were contrasting. For the 671HC case, savings in energy and GHG from fuel economy improvement were greater than roughness-induced burdens so net savings in energy and GHG in the use stage were positive at all market penetration. At certain market penetrations (50 and 100%), net economic savings were negative because the ratio of calorific or energy value and unit cost of fuel is very high compared with that of pavement materials. The 670HC case experienced minimal or net savings in energy, GHG, and cost in the use stage because roughness-induced burdens were greater than savings from fuel economy improvement at lower market penetration (5 and 10%). At higher market penetration (50 and 100%), fuel economy saving from NG-WBT slightly exceeded the roughness-induced burdens. For both cases, reduced overlay service lives resulted in additional burdens in the material and construction stages.

Table 49. Scenario III Results for Case 671HC (Thick AC): Energy Savings and GHG Emissions Reductions Compared with the Baseline (DTA) per year

	Market Penetration of NG-WBT	Material Production Stage	Construction Stage	Use Stage	Life Cycle Result
Energy saving compared with the baseline (MJ)	5%	0	0	53,108	53,108
Energy saving compared with the baseline (MJ)	10%	0	0	106,216	106,216
Energy saving compared with the baseline (MJ)	50%	-105,407	-19,333	634,798	510,058
Energy saving compared with the baseline (MJ)	100%	-177,875	-32,624	1,319,576	1,109,077
GHG reduction compared with the baseline (kg CO_2-e)	5%	0	0	4,001	4,001
GHG reduction compared with the baseline (kg CO_2-e)	10%	0	0	8,002	8,002
GHG reduction compared with the baseline (kg CO_2-e)	50%	-6,388	-1,483	47,934	40,062
GHG reduction compared with the baseline (kg CO_2-e)	100%	-10,781	-3,814	99,678	85,083
	Market Penetration of Wide-Base Tires	**Material Production and Construction Stages**	**n/a**	**Use Stage**	**Life Cycle Result**
Economic saving compared with the baseline ($ Present)	5%	0	0	924	924
Economic saving compared with the baseline ($ Present)	10%	0	0	1,848	1,848
Economic saving compared with the baseline ($ Present)	50%	-23,465	0	10,881	-12,584
Economic saving compared with the baseline ($ Present)	100%	-39,597	0	23,226	-16,370

Table 50. Scenario III Results for Case 670HC (Thin AC): Energy Savings and GHG Emissions Reductions Compared with the Baseline (DTA) per year

	Market Penetration of NG-WBT	Material Production Stage	Construction Stage	Use Stage	Life Cycle Result
Energy reduction compared with the baseline (MJ)	5%	0	0	-27,418	-27,418
Energy reduction compared with the baseline (MJ)	10%	0	0	-20,619	-20,619
Energy reduction compared with the baseline (MJ)	50%	-178,891	-33,153	90,778	-121,266
Energy reduction compared with the baseline (MJ)	100%	-178,891	-33,153	44,477	-167,567
GHG reduction compared with the baseline (kg CO_2-e)	5%	0	0	-2,109	-2,109
GHG reduction compared with the baseline (kg CO_2-e)	10%	0	0	-1,596	-1,596
GHG reduction compared with the baseline (kg CO_2-e)	50%	-10,842	-2,544	6,874	-6,512
GHG reduction compared with the baseline (kg CO_2-e)	100%	-10,842	-2,544	3,243	-10,143
	Market Penetration of Wide-Base Tires	**Material Production and Construction Stages**	**n/a**	**Use Stage**	**Life Cycle Result**
Economic saving compared with the baseline ($ Present)	5%	0	0	-505	-505
Economic saving compared with the baseline ($ Present)	10%	0	0	-380	-380
Economic saving compared with the baseline ($ Present)	50%	-41,780	0	1,166	-40,613
Economic saving compared with the baseline ($ Present)	100%	-41,780	0	289	-41,491

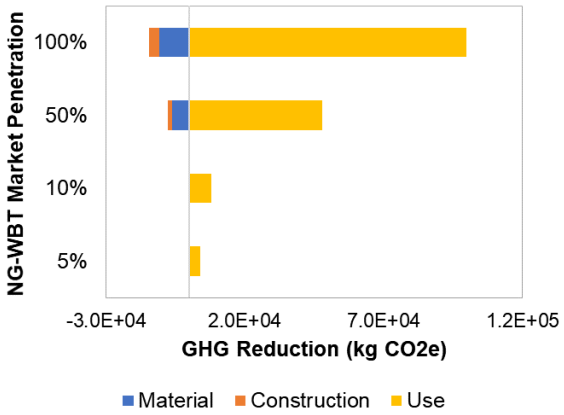

Figure 253. Graph. Scenario III GHG emissions reduction compared with the baseline (DTA): case 671HC (thick asphalt).

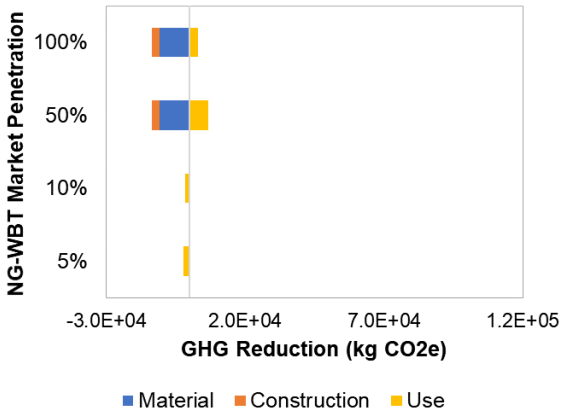

Figure 254. Graph. Scenario III GHG emissions reduction compared with the baseline (DTA): case 670HC (thin asphalt).

In summary, the results indicated the following:

- Scenario I resulted in significant cost and fuel consumption savings and GHG emissions reductions when NG-WBT is used. The higher the NG-WBT market penetration, the greater the cost and environmental impact.
- Scenario II showed that 670HC and 671HC experienced an overall saving in energy consumption and GHG emissions when NG-WBT was used. The savings from the use stage were greater than the burdens in the material and construction stages due to the possible increase in damage. The net savings increased by 77% when the NG-WBT market penetration changed from 50% to 100%. For the case 670HC, there was no savings or burden in the material and construction stages except for market penetration of 100% because the design life remained the same.
- Scenario III resulted in NG-WBT having lower life cycle energy consumption and GHG emissions but higher cost compared with the baseline for 671HC, while energy, GHG, and cost were higher for 670HC. For the case 671HC, net savings increased by 100% when NG-WBT market penetration increased from 5% to 10%. For the case 670HC, the overlay design life was

the same as the baseline when the NG-WBT market penetration is 5 or10%. Hence, no saving or burden in the material and construction stages was observed. However, at higher market penetration, due to additional fuel consumption from faster roughness progression and reduced overlay design life, case 670HC experienced greater burdens in energy and GHG. Therefore, the net savings were negative.

It is evident that NG-WBT can result in significant savings in life cycle energy consumption and cost, and GHG emissions; however, these benefits are sensitive to the method used to determine pavement performance; especially that a small change in pavement strain may result in significant changes in pavement life.

SUMMARY

To assess the environmental and economic impacts of adopting NG-WBT, an approach was developed to evaluate the life-cycle energy consumption and cost, and GHG emissions from their use. The life cycle stages analyzed in this study include pavement material production, pavement construction, and pavement use stages. The life cycle of tires was not included due to unavailability of data, and the contribution of tires to the results would be very limited since only a very small portion of a tire's life would be allocated to the pavement segments analyzed in the study. The impacts from pavement roughness and macrotexture on vehicle fuel consumption, as well as the fuel economy improvement from using NG-WBT, are included in the pavement use stage. In general, the use of NG-WBT may result in significant savings in life cycle energy consumption and cost, and reduction in GHG emissions. However, this depends on pavement structure and design life, traffic, truck percentage and NG-WBT market penetration.

CHAPTER 11. CONCLUSIONS AND RECOMMENDATIONS

The main objective of this study was to compare the impact of NG-WBT and DTA on road infrastructure. Contact stresses of the NG-WBT and DTA were measured. A numerical model was developed to simulate realistic pavement structures, materials, and applied loading conditions. The model was validated with various field test sections across the United States. Good agreement was noted between FE analysis results and pavement field instrument responses when using proper material characterization parameters, especially for vertical pressure and tensile strain at the bottom of AC in transverse direction. The FE model is capable of realistically simulating tire-pavement interaction in the field when accurate data are used

It was evident that NG-WBT responses were generally greater than DTA for thin and thick pavements. The difference decreased with depth, and a few cases showed higher responses for DTA (e.g., shear strain in the subgrade in thin pavement). A small change in pavement responses resulted in enormous changes in pavement performance or life when using transfer functions, and therefore the impact of pavement response was presented in stresses and strain changes. The following conclusions summarize the findings of this study:

1) Elastic theory and empirical transfer function may not be accurate for predicting the impact of NG-WBT on flexible pavement. Hence, realistic models should be used to quantify the impact of NG-WBT including 3-D FEM, proper material characterization (e.g., viscoelastic AC properties and anisotropic unbound materials for thin pavements, etc.), and moving nonuniform three-dimensional tire loading.
2) DTA with differential tire inflation pressure produces higher damage than DTA with the same tire inflation pressure when compared to the tire with the highest tire inflation pressure.
3) For local roads, subgrade rutting is the controlling distress of the pavement life; the difference between the two tires impact on subgrade failure is not significant. Building pavements with strong granular base layer may diminish changes in potential subgrade rutting. The impact of NG-WBT is greater than that of DTA on interstate highways where the controlling distress in AC for perpetual pavement is top-down or near-surface cracking and possible AC rutting. Durable, high-performance wearing surface materials (e.g., SMA), usually implemented in the interstate system, can control this damage. For typical (non-perpetual) pavement, the impact of NG-WBT is still greater than DTA but to a lesser degree.
4) MEPDG may not be used directly for predicting responses of NG-WBT. Therefore, two adjustment factors were developed to modify the pavement responses obtained from MEPDG to FE: i) adjustment of MEPDG results to FE results; and ii) adjustment of MEPDG DTA FE results to NG-WBT FE.
5) To simplify the process of using NG-WBT and allow for implementation by agencies, an ANN tool was developed to predict the pavement response without running FE. The tool results rendered by the ANN surrogate models were highly accurate with average prediction error less than 5% and R-square values higher than 0.95. The ANN tool can be incorporated in mechanistic design methods, such as the AASHTOWare.
6) Although NG-WBT may cause greater pavement repsonse than DTA for some roads, NG-WBT demonstrates significant improvement compared with the first generation of wide-base tires.

7) Based on the life cycle assessment (LCA) models developed and applied and the NG-WBT market penetration percentages considered, NG-WBT can save energy and reduce GHG and emissions, depending on corresponding pavement performance.
8) Based on the results of the study and using the developed tools, for a NG-WBT market penetration of 10%, it is expected that the pavement damage increase is less than 5% compared to the scenario where only DTA is used. However, this additional pavement damage could be outweighed by the environmental benefits as well as cost.

APPENDIX A. THREE-DIMENSIONAL CONTACT STRESSES

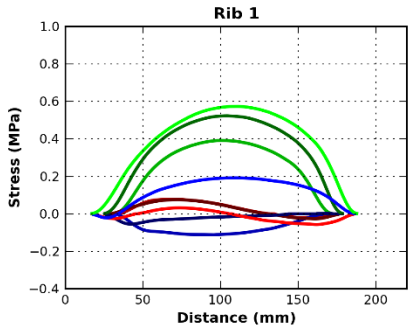

Note: 1 MPa = 145 psi

Figure 255. Graph. Three-dimensional contact stresses when *P*=6 kip and *S*=80 psi for NG-WBT – Rib 1.

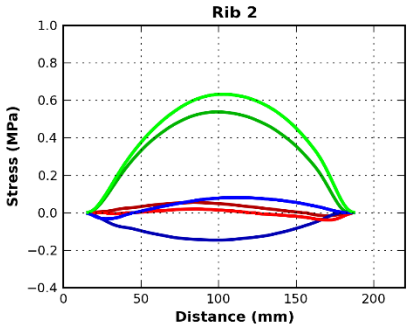

Figure 256. Graph. Three-dimensional contact stresses when *P*=6 kip and *S*=80 psi for NG-WBT – Rib 2.

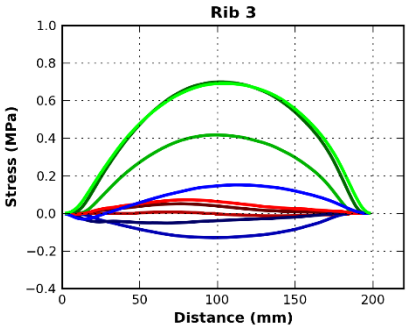

Figure 257. Graph. Three-dimensional contact stresses when *P*=6 kip and *S*=80 psi for NG-WBT – Rib 3.

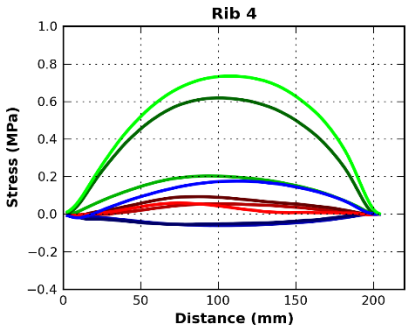

Figure 258. Graph. Three-dimensional contact stresses when *P*=6 kip and *S*=80 psi for NG-WBT – Rib 4.

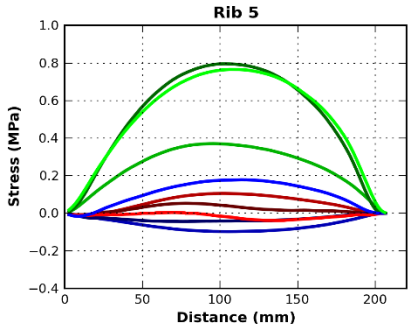

Figure 259. Graph. Three-dimensional contact stresses when *P*=6 kip and *S*=80 psi for NG-WBT – Rib 5.

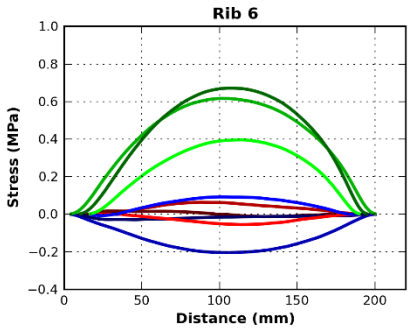

Figure 260. Graph. Three-dimensional contact stresses when *P*=6 kip and *S*=80 psi for NG-WBT – Rib 6.

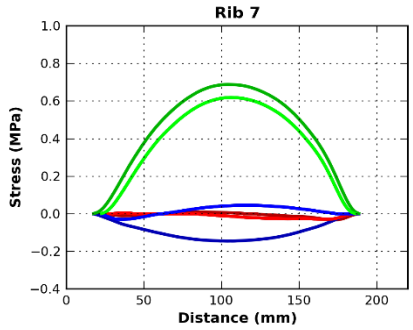

Figure 261. Graph. Three-dimensional contact stresses when *P*=6 kip and *S*=80 psi for NG-WBT – Rib 7.

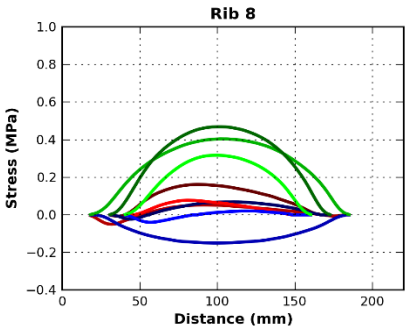

Figure 262. Graph. Three-dimensional contact stresses when *P*=6 kip and *S*=80 psi for NG-WBT – Rib 8.

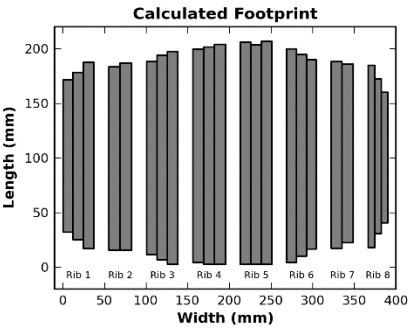

Figure 263. Graph. Three-dimensional contact stresses when *P*=6 kip and *S*=80 psi for NG-WBT – calculated footprint.

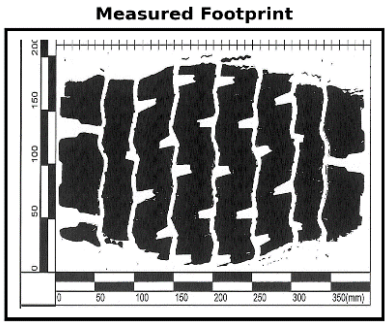

Figure 264. Graph. Three-dimensional contact stresses when *P*=6 kip and *S*=80 psi for NG-WBT – measured footprint.

APPENDIX B. MODELING RESULTS THIN PAVEMENT

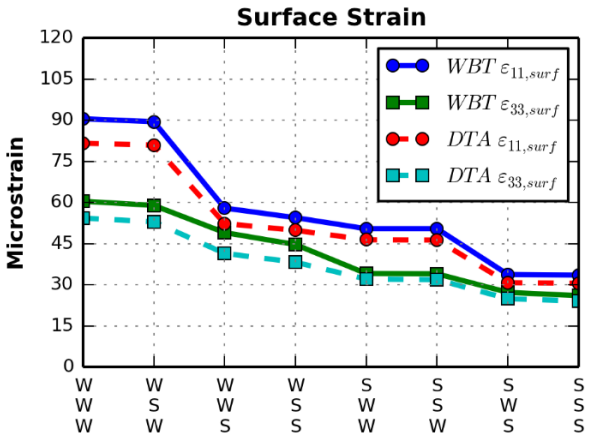

Note: 1 MPa = 145 psi

Figure 265. Graph. Surface strain for AC=3 in, B=6 in, *P* =6 kip, and *S* =80 psi.

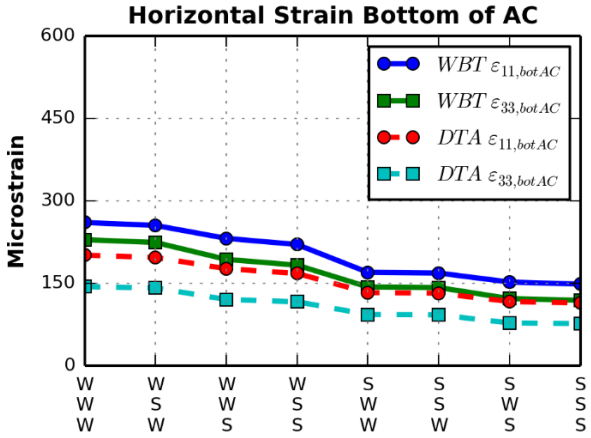

Figure 266. Graph. Horizontal strain at the bottom of the AC for AC=3 in, B=6 in, *P*=6 kip, and *S*=80 psi.

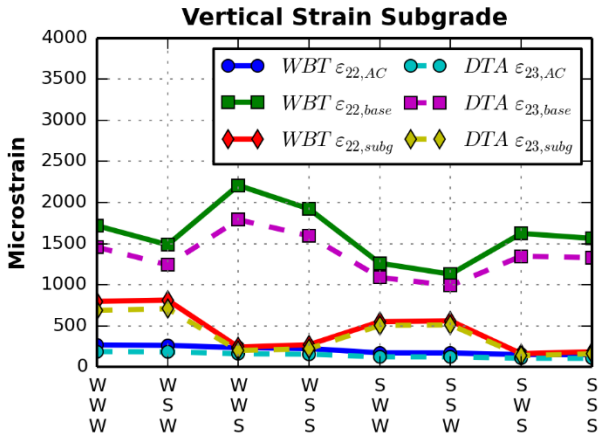

Figure 267. Graph. Vertical strain for AC=3 in, B=6 in, *P*=6 kip, and *S*=80 psi.

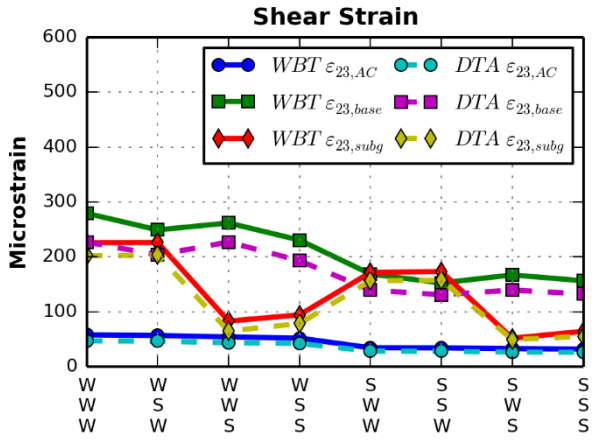

Figure 268. Graph. Shear strain for AC=3 in, B=6 in, *P*=6 kip, and *S*=80 psi.

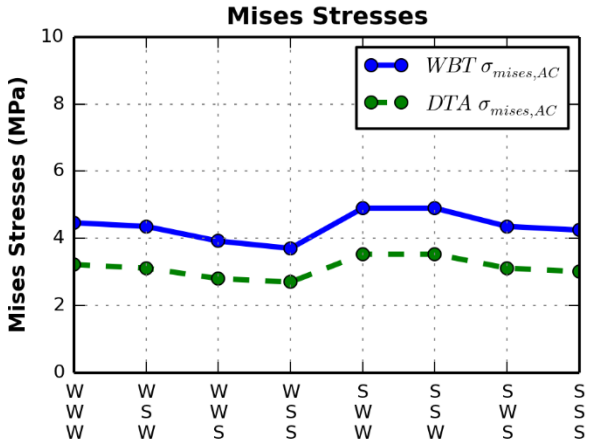

Figure 269. Graph. Mises stresses for AC=3 in, B=6 in, *P*=6 kip, and *S*=80 psi.

APPENDIX C. MODELING RESULTS THICK PAVEMENT

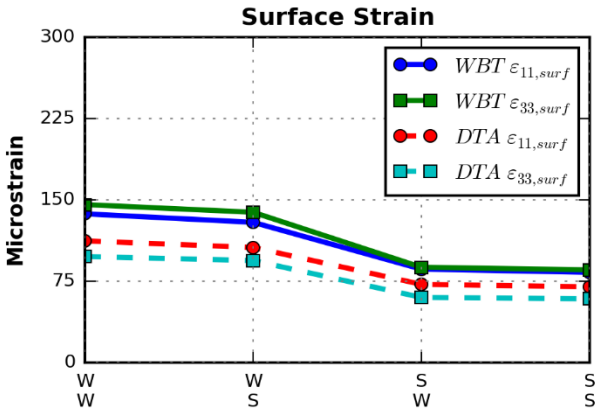

Note: 1 MPa = 145 psi

Figure 270. Graph. Surface strain for AC=5 in., B=6 in., *P*=6 kip, and *S*=80 psi.

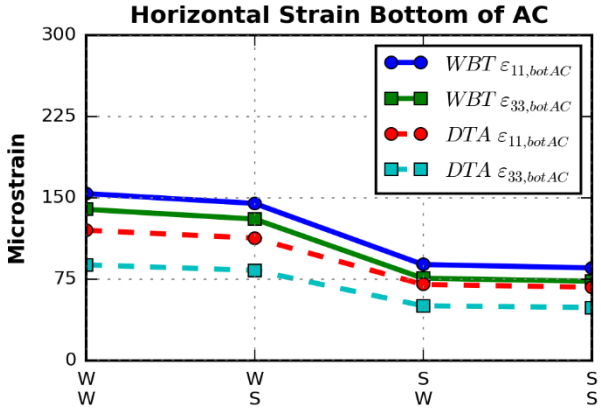

Figure 271. Graph. Horizontal strain at the bottom of the AC for AC=5 in., B=6 in., *P*=6 kip, and *S*=80 psi.

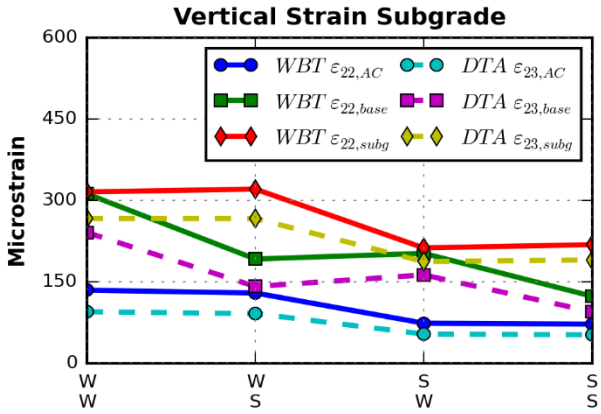

Figure 272. Graph. Vertical strain for AC=5 in., B=6 in., *P*=6 kip, and *S*=80 psi.

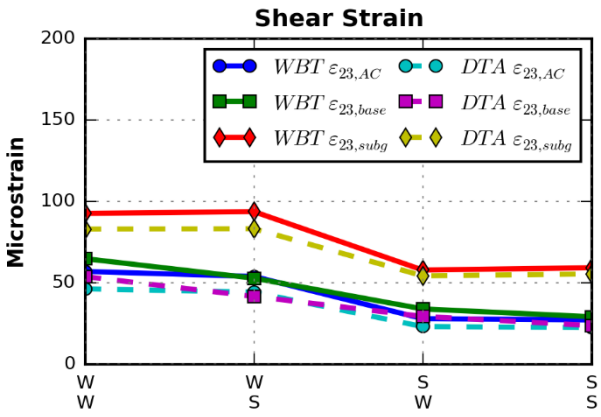

Figure 273. Graph. Shear strain for AC=5 in., B=6 in., *P*=6 kip, and *S*=80 psi.

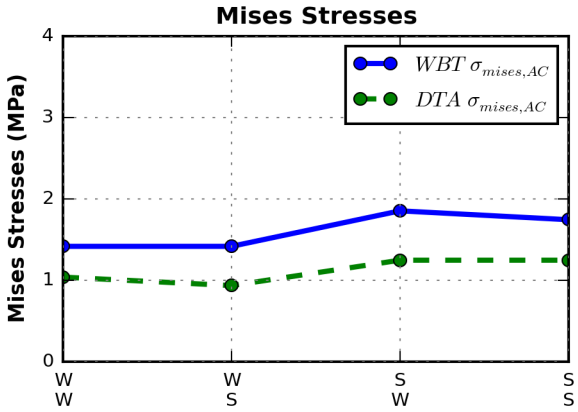

Figure 274. Graph. Mises stresses for AC=5 in., B=6 in., *P*=6 kip, and *S*=80 psi.

APPENDIX D. ICT-WIDE TOOL

Installation guide: the software package includes the following files:

- Application file 'ICT-Wide102.exe
- MyAppInstaller_mcr.exe
- MyAppInstaller_web.exe
- splash.png and
- readme.txt file

First, install the file 'MyAppInstaller_mcr'. In case of error, the updated version can be found on the internet by searching the key word 'mcr Matlab R2015a'. After installing mcr file, run the application ICT-Wide to use the tool.

Figure 275 to Figure 278 show a few snapshots of the tool. There are two main input modules; the output module is located at the bottom. The user provides inputs in the load and structure modules and specifies one of the two options; response prediction or damage calculation. There are two options for inputting structure information: low-volume (thin) or interstate (thick) structures. Accordingly, two levels of inputs, Level 1 and Level 2, are provided to enter material properties. Upon selecting input level, details can be entered by pressing "open" (Figure 272).

In response prediction user is prompt to specify the responses of interest. After completing inputs, the tool will generate the selected responses. Three possible windows can be seen as a result. If the model runs successfully, a window will appear requesting a destination folder to save the results. If any of the inputs is entered incorrectly, a window will appear asking for correcting possible mistakes. Finally, if the user enters invalid or out-of-range inputs, which might lead to unrealistic output, a window will appear warning the user. The output will be saved as a csv file including the inputs specified by user and predicated responses. Different cases can be appended to the same file.

In the damage calculation additional information will be needed. These include traffic information and NG-WBT market penetration information. Figure 273 shows the required inputs. Upon running the tool user will be asked to choose a method (MEPDG or AI) to calculate damage. These methods are explained in Chapter 9. Upon successful running and checking for input errors a new window will appear showing the damage calculation results. Figure 278 shows an example output for damage calculation.

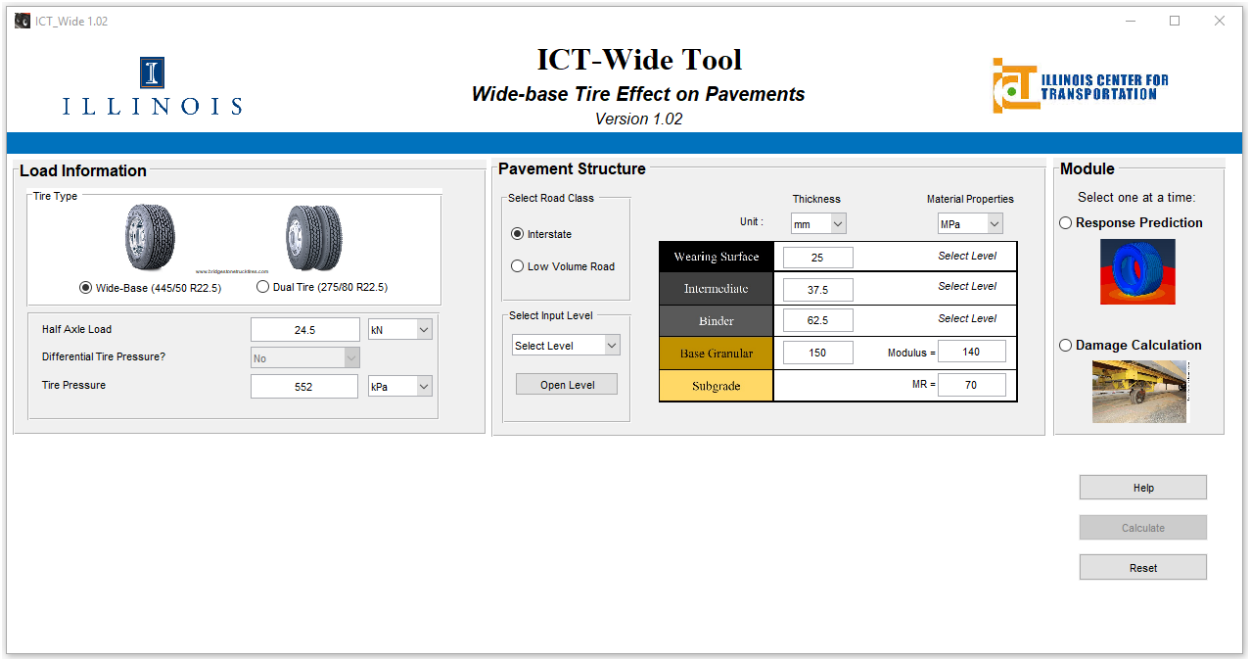

Figure 275. Main page of ICT-Wide tool.

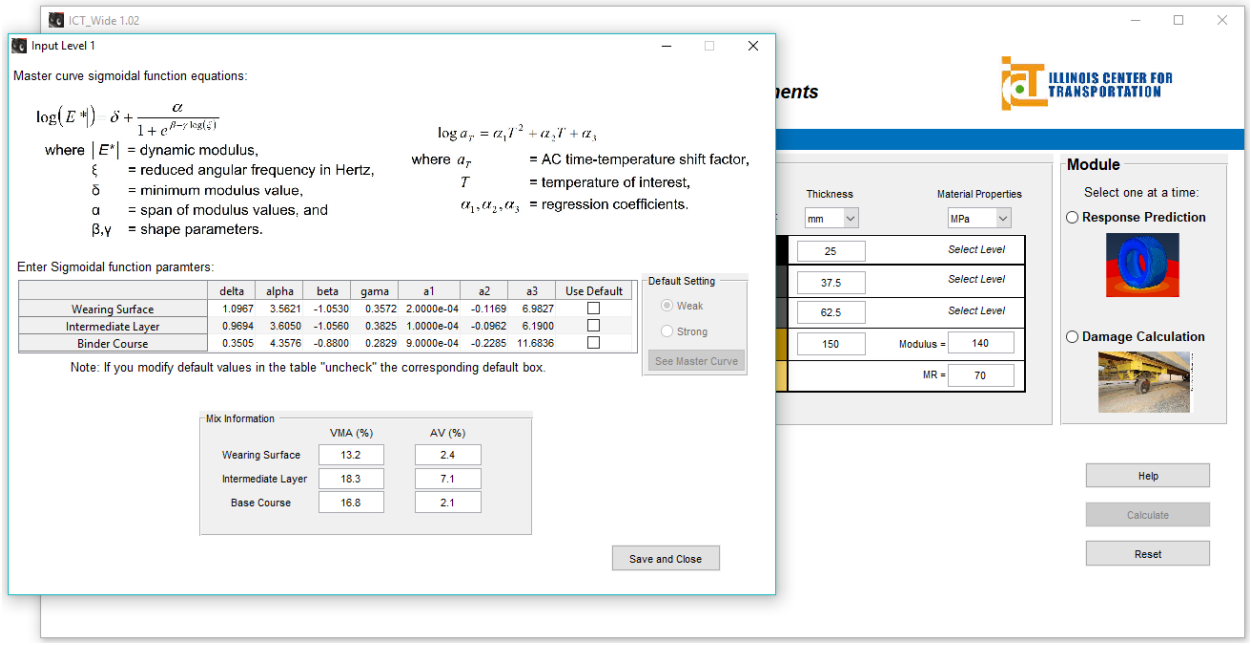

Figure 276. Illustration. Prompt for Level 1 input.

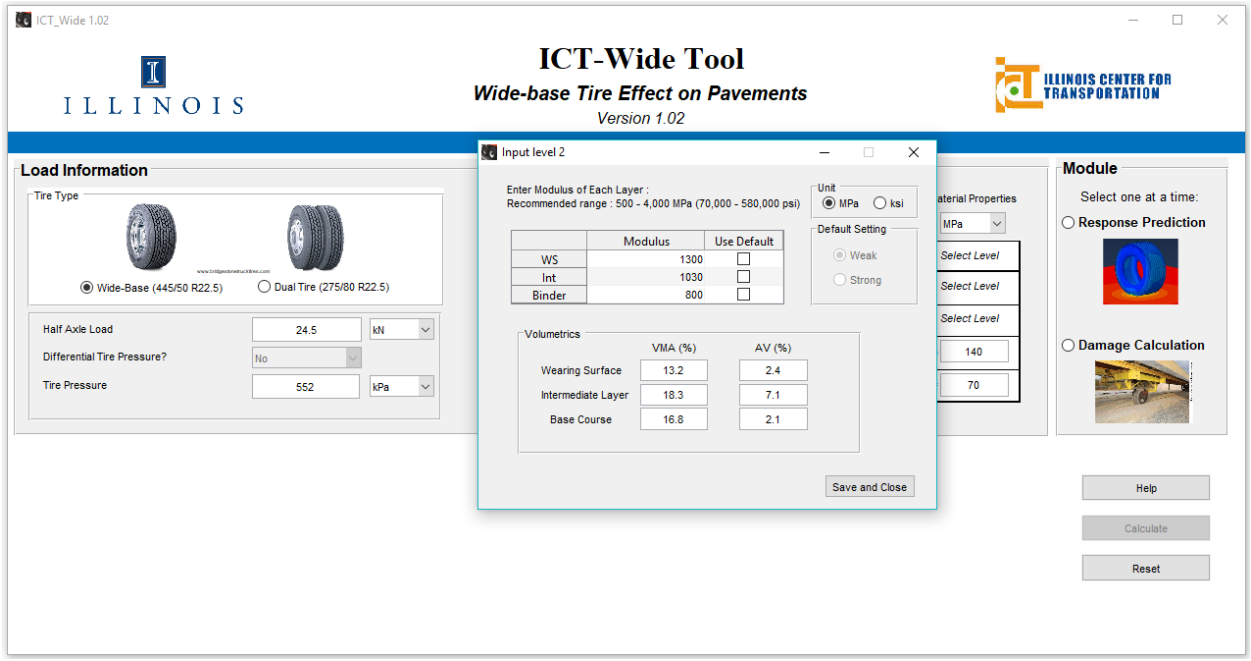

Figure 277. Illustration. Prompt for Level 2 input.

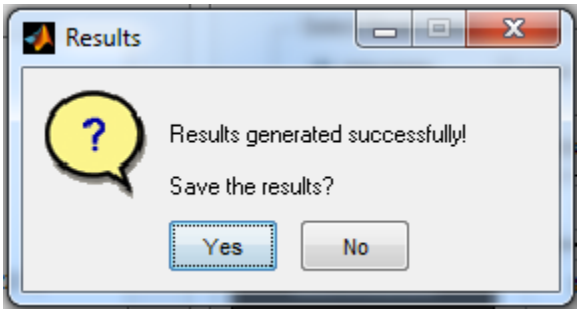

Figure 278. Illustration. Three possible windows to appear after running tool: results.

Figure 279. Illustration. Three possible windows to appear after running tool: error.

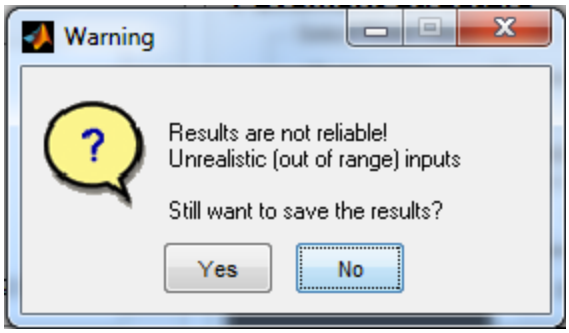

Figure 280. Illustration. Three possible windows to appear after running tool: warning.

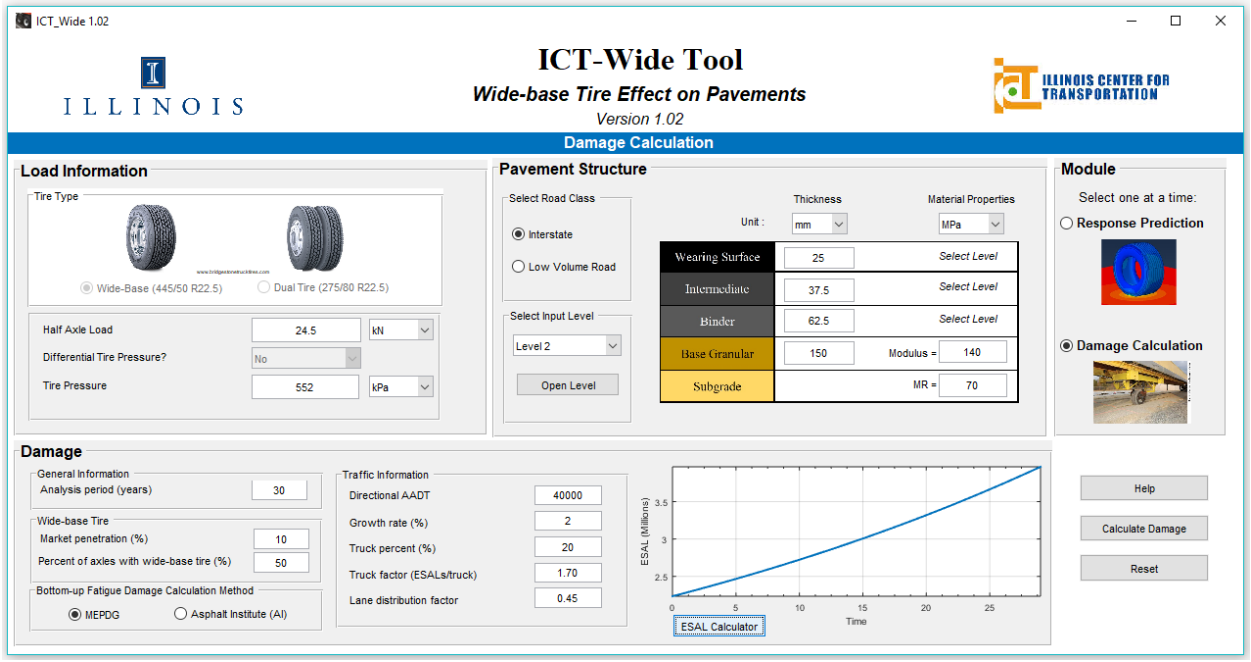

Figure 281. Illustration. Damage calculation module.

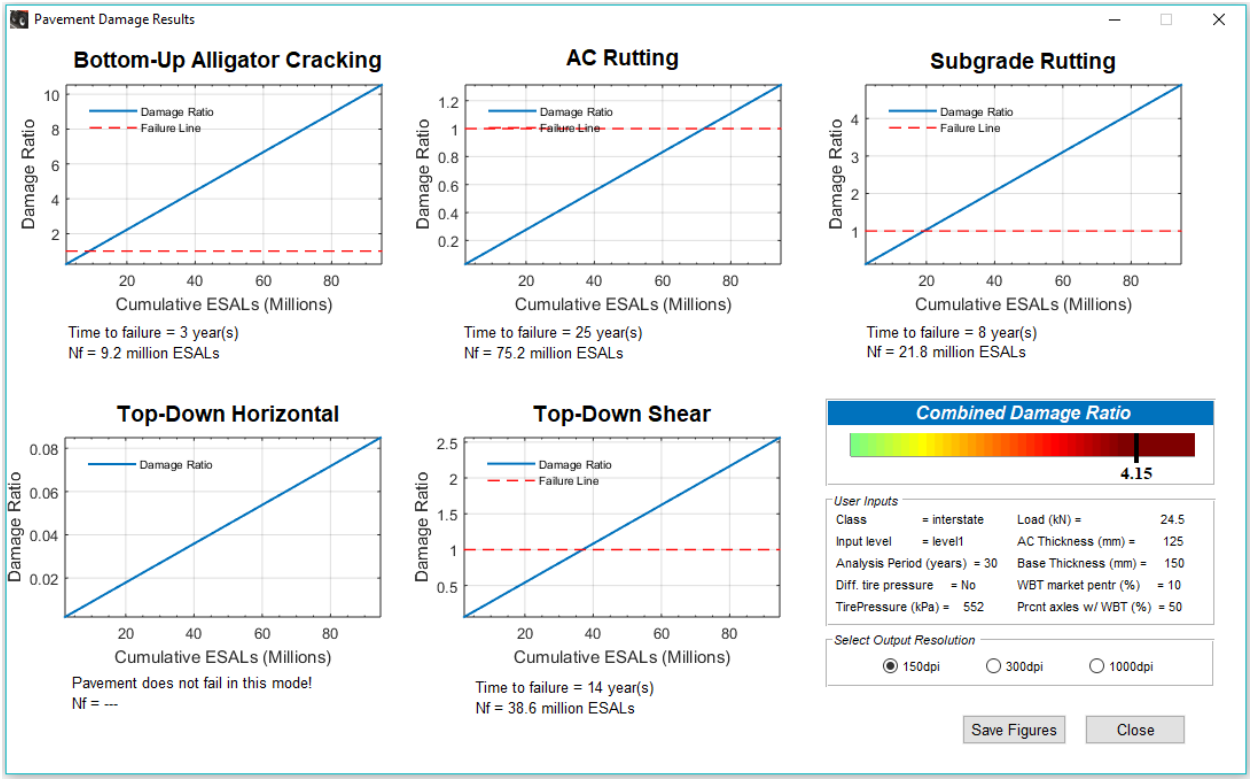

Figure 282. Illustration. Pavement damage calculation results.

APPENDIX E. FLORIDA DOT PAVEMENT SECTIONS

As part of this study, the Florida Department of Transportation (FDOT) constructed and instrumented two test sections to measure pavement response. The effort made to construct, instrument, and test these sections are documented.

FDOT ACCELERATED PAVEMENT TESTING FACILITY

Florida's APT facility is housed within the State Materials Research Park in Gainesville. The original test lanes measured 150 ft. long and 12 ft. wide. A recent expansion of the test track extended each lane an additional 300 ft. The supporting soil layers consist of a 10.5 in limerock base over a 12 in mixture of limerock and native A-3 soil. Two additional 50 ft. long test tracks (referred to as the test pits) are enclosed by a sump with an interconnecting channel system for controlling the water table. A photograph of the original test tracks and empty test pits are shown in Figure 283 and Figure 284.

Figure 283. Photo. HVS test tracks.

Figure 284. Photo. HVS test pits.

Accelerated loading was performed using a heavy vehicle simulator (HVS), Mark IV model. The HVS can apply wheel loads between 7 and 45 kips at speeds of 2 mph to 8 mph along a 30 ft test strip. The effective test segment within this span is approximately 20 ft. The remaining 5 ft, at either end of the test strip, allows the load wheel to reach programmed parameters controlling load and speed levels. Wheel wander of up to 30 in can be induced. A heater system and insulated panels, shown in Figure 285, maintain a constant testing temperature within the test section area.

Figure 285. Photo. Insulated panels on HVS.

CONSTRUCTION

Test Section Construction

Two test sections were constructed in October, 2012. One section was built on the east test pit while the second was constructed on Lane 7 of the test track extension. The test pit pavement consisted of two similar 1.5 in Superpave (SP-12.5) layers with a PG 67-22 asphalt binder. The test track consisted of a 1.5 in SP-12.5 layer with a PG 67-22 asphalt binder, a 1.5 in SP-12.5 layer with a PG 76-22, and a 1.0 in., 0.187 in mixture with a PG 76-22. The pavement sections were constructed in accordance with FDOT specifications and standards. The pavement structures for these sections are shown in Figure 286 and Figure 287.

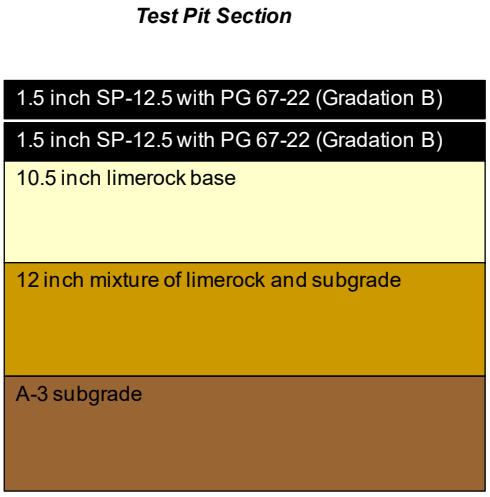

Figure 286. Illustration. Pavement structure of test pit section.

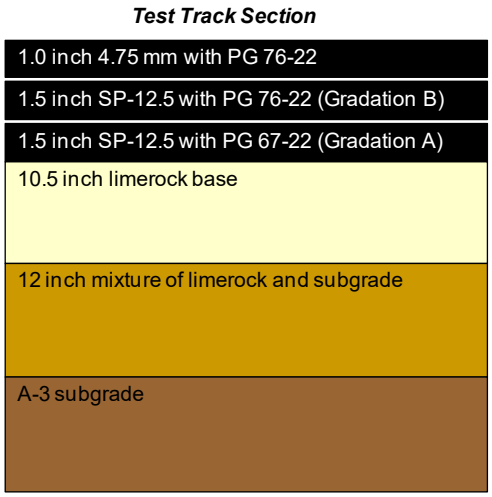

Figure 287. Illustration. Pavement structure of test track section.

Material Sampling

Both test sections had similar supporting granular layers as indicated in Figure 286. A summary of laboratory test results is included in Table 51. The resilient modulus values listed in this table were obtained using the relationship developed from each individual test (resilient modulus versus bulk stress- with bulk stress, θ, defined as $\theta = \sigma_1 + \sigma_2 + \sigma_3)$. The resilient modulus values are an average of two individual tests from each sample location. The resilient modulus samples were compacted to within 1 pound per cubic foot (pcf) of the maximum density and 0.5 percent of the optimum moisture content as determined by AASHTO T99 for the embankment and AASHTO T180 for the subgrade and base. The bulk stresses typically used to represent in-situ stresses of embankment, subgrade, and base layers are 11 psi, 16 to 18 psi, and 20 to 30 psi, respectively. The resilient modulus is determined by $M_r = k_1\theta^{k_2}$:

Table 51. Granular Layer Properties AASHTO T99 or AASHTO T180

AASHTO T99 or AASHTO T180	AASHTO T99 or AASHTO T180	AASHTO T99 or AASHTO T180	AASHTO T99 or AASHTO T180	AASHTO T99 or AASHTO T180
Material	Max Density (pcf)	Opt. Moist. (%)	Actual Density (pcf)	Actual Moisture (%)
Limerock Base	114	12	112.5	10.3
Stabilized Subgrade	114	11	113.8	9.3
Embankment	115	11	113.3	9.3

Table 52. Granular Layer Properties AASHTO T307

Material	Bulk Stress 11 psi	Bulk Stress 18 psi	Bulk Stress 40 psi	Avg.	k_1	k_2
Limerock Base	13,083	17,365	27,482	27,482	3,297	0.5752
Stabilized Subgrade	14,332	18,553	28,197	18,553	4,079	0.5244
Embankment	12,806	16,538	25,035	12,806	3,687	0.5193

AC material was sampled from delivery trucks during construction (Figure 288) for mixture performance tests and three random cores were retrieved from each lane to verify in-situ density. In addition, 30 cores from each test section were extracted and shipped to the University of Illinois for further testing. Table 53 summarizes the gradations and volumetric properties of the asphalt mixtures.

Figure 288. Photo. Loose mixes sampled from trucks – in truck.

Figure 289. Photo. Loose mixes sampled from trucks - sample.

Table 53. Gradation and Volumetric Property Data

	Test Pit	Test Pit	Test Track	Test Track	Test Track	Test Track	Test Track	Test Track
Sieve	**SP-12.5 JMF, % Passing**	**SP-12.5 Plant Avg, % Passing**	**4.75 JMF, % Passing**	**4.75 Plant Avg, % Passing**	**SP-12.5 JMF, % Passing**	**SP-12.5 Plant Avg, % Passing**	**SP-12.5[1] JMF, % Passing**	**SP-12.5[1] Plant Avg, % Passing**
3/4"	100	100.0	100	100.0	100	100.0	100	99.9
1/2"	100	98.3	100	100.0	100	98.4	98	96.8
3/8"	87	86.0	100	100.0	87	87.5	88	85.0
#4	62	59.6	99	98.7	62	61.9	59	57.0
#8	41	39.7	77	78.2	41	42.4	40	38.8
#16	29	28.7	56	55.0	29	31.1	29	28.4
#30	22	22.2	39	40.0	22	24.0	22	21.7
#50	12	13.2	26	26.0	12	13.8	12	12.9
#100	4	5.3	15	15.6	4	5.2	4	4.9
#200	2	2.9	8.9	9.5	2	2.9	2	2.9

Table 54. Gradation and Volumetric Property Data – Binder Content

Binder Type	**PG 67-22 (un-mod.)**	**PG 67-22 (un-mod.)**	**PG 76-22 (mod.)**	**PG 76-22 (mod.)**	**PG 76-22 (mod.)**	**PG 76-22 (mod.)**	**PG 67-22 (un-mod.)**	**PG 67-22 (un-mod.)**
%AC	5.1	4.7	6.5	6.3	5.1	4.9	5.1	4.9
%AV	4.0	4.0	4 to 6	4.6	4.0	3.9	4.0	3.3

Table 55. Gradation and Volumetric Property Data – Core Density and Lift Thickness

Core Property		**SP-12.5**	**4.75**	**SP-12.5**	**SP-12.51**
% Density		94.2	11.5	94.8	94.6
Lift Thickness, Inch		1.5	0.9	1.6	1.4

Note: The SP-12.5 mixture placed on the test track was paved approximately 1 year prior to the mixture placed on the test pit.

The AMPT is a testing device designed to determine the asphalt mixture dynamic modulus for use in pavement structural design (e.g., the MEPDG) and the flow number for the evaluation of potential mixture performance. The AMPT test provides a dynamic modulus master curve that indicates the modulus of asphalt mixture for any combinations of temperature and load frequency. AASHTO PP 61 standardizes the construction of dynamic modulus master curve using the AMPT. In addition, the flow number measured from the AMPT enables the evaluation of rutting resistance of asphalt mixtures.

Dynamic modulus and flow number tests were conducted in accordance with AASHTO TP 79. The plant mix sampled during construction was compacted using the Superpave Gyratory Compactor (SGC). Three replicates were made for dynamic modulus tests and one replicate was prepared for the flow number test according to AASHTO PP 60. The AMPT test setup is shown in Figure 290. The dynamic modulus master curves generated for the three different mixtures and flow number results are also presented in the same figure.

Superpave IDT tests were conducted on mixtures to determine key mixture fracture properties. The standard Superpave IDT tests, including resilient modulus, creep compliance and strength test, were performed at 50 ºF. A complete description of test procedures and data analysis are presented by Roque et al. (1997). The plant mixes sampled from truck were compacted using the SGC. Three replicates per mixture type were prepared and tested. Table 56 summarizes the information of three cut specimens for testing and Figure 293 shows the configuration of Superpave IDT test setup.

Figure 290. Picture. AMPT test setup.

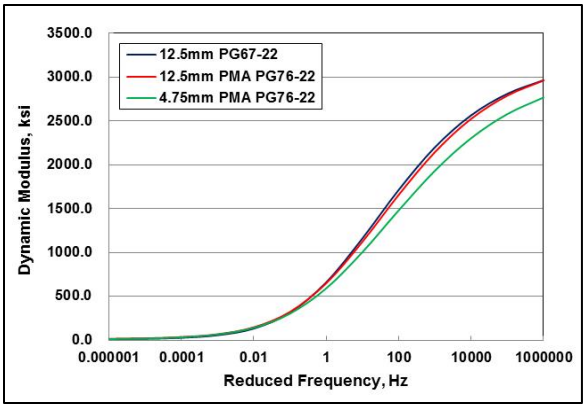

Figure 291. Graph. Dynamic modulus master curve.

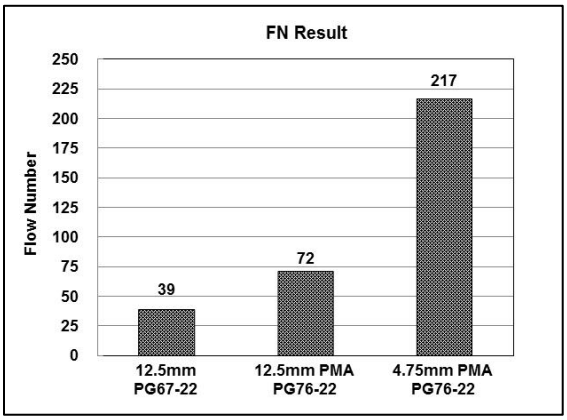

Figure 292. Graph. Flow number results.

Table 56. Information of Cut Specimens for Superpave IDT Tests

Mixture Types	Specimen Number	Air Voids (%)	Average Diameter (inch)	Average Thickness (inch)
12.5mm PG67-22	1	6.9	5.93	1.53
12.5mm PG67-22	2	6.8	5.92	1.57
12.5mm PG67-22	3	6.5	5.92	1.51
12.5mm PMA PG76-22	1	7.0	5.93	1.49
12.5mm PMA PG76-22	2	6.7	5.92	1.51
12.5mm PMA PG76-22	3	6.9	5.92	1.48
4.75mm PMA PG76-22	1	7.3	5.92	1.51
4.75mm PMA PG76-22	2	6.7	5.92	1.50
4.75mm PMA PG76-22	3	6.9	5.92	1.54

Figure 293. Photo. Superpave IDT test setup.

Table 57 summarizes the results of Superpave IDT tests and Figure 294 presents three key mixture fracture properties most strongly related to cracking performance of asphalt pavements. Generally, a higher *ER* value is associated with a higher *FE* and a lower creep rate. The aforementioned trend is consistent with the results shown in Figure 294. In particular, it was found that 0.187 in mixture with polymer-modified PG 76-22 binder had a relatively higher *FE*, lower creep rate, and higher entities and relationships (ER) values that may result in better fracture resistance than the 0.5 in mixtures.

Table 57 Superpave IDT Test Results

Mixture Types	Temp. (°F)	m-value	D_1 (1/psi)	Creep Compl. (1/GPa)	S_t (MPa)	M_R (GPa)	ε_f (10^{-6})	FE (KJ/m^3)	$DCSE_f$ (KJ/m^3)	Creep Rate (1/psi·sec)	ER
12.5mm PG67-22	50	0.46	3.55E-07	1.281	2.44	13.97	1300.23	2.30	2.09	3.83E-09	2.81
12.5mm PMA PG76-22	50	0.41	4.17E-07	1.058	2.54	13.16	1533.00	2.80	2.55	2.77E-09	4.16
4.75mm PMA PG76-22	50	0.35	3.84E-07	0.658	2.90	14.21	2050.62	4.40	4.10	1.47E-09	10.93

Note: 1 MPa=145 psi.

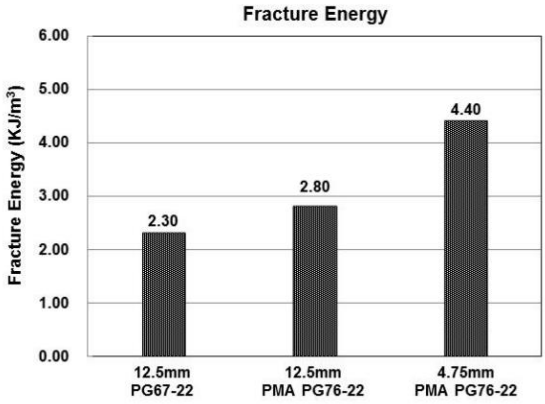

Figure 294. Graph. Key mixture fracture properties determined from Superpave IDT tests: Fracture energy.

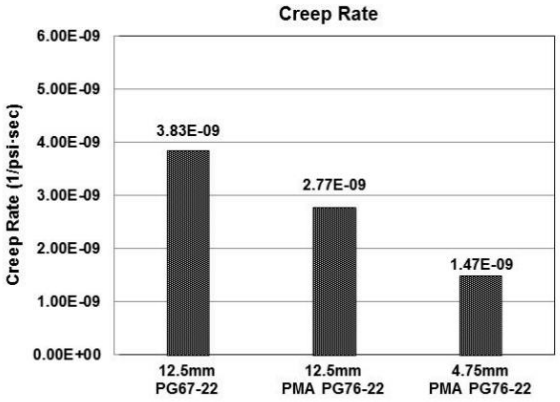

Figure 295. Graph. Key mixture fracture properties determined from Superpave IDT tests: creep rate.

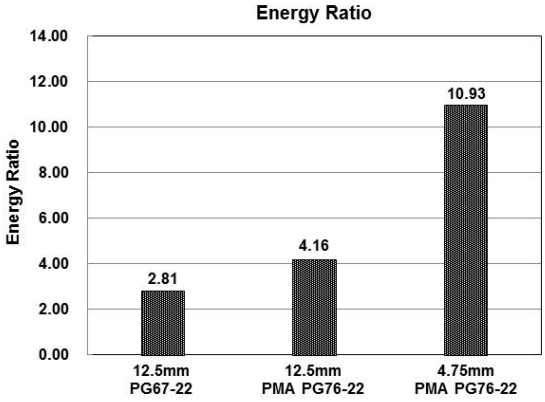

Figure 296. Graph. Key mixture fracture properties determined from Superpave IDT tests: energy ratio.

Instrumentation

Each test section was instrumented to measure pavement response resulting from wheel loading. Prior to construction, each embedded sensor was placed in the appropriate location, labeled, and checked for adequate response. Immediately after construction, the response was again checked to make sure each embedded sensor survived the compaction and heat associated with the placement of AC. Standard sensor installation methods used by FDOT can be found on the State Materials Office website. Table 58 summarizes the types and locations of sensors. Diagrams of the exact sensor locations are shown in Figure 298 and Figure 300. Instrumentation data were collected with a mobile National Instruments data acquisition (DAQ) system (Figure 301) at 200 Hz for the surface gauges and pressure cells and at 100 Hz for the embedded H-gauges.

Table 58. Sensor Types and Locations

Sensor Type	Number of Sensors per Test Section	Model	Vertical Location	Offset from Wheel Path
Surface strain gauge	24	Tokyo Sokki PFL-30-11-5L	AC surface	Transverse and longitudinal orientations at various offsets from wheel path edge
Asphalt strain gauge	6	Tokyo Sokki KM-100HAS	Bottom of new AC	Transverse and longitudinal orientations below tire center
Pressure cell	2	RST Instruments LPTPC09-S	Bottom of new AC	Below tire center
Pressure cell (Test Pit only)	2	Geokon 3500	Bottom of base	Below tire center

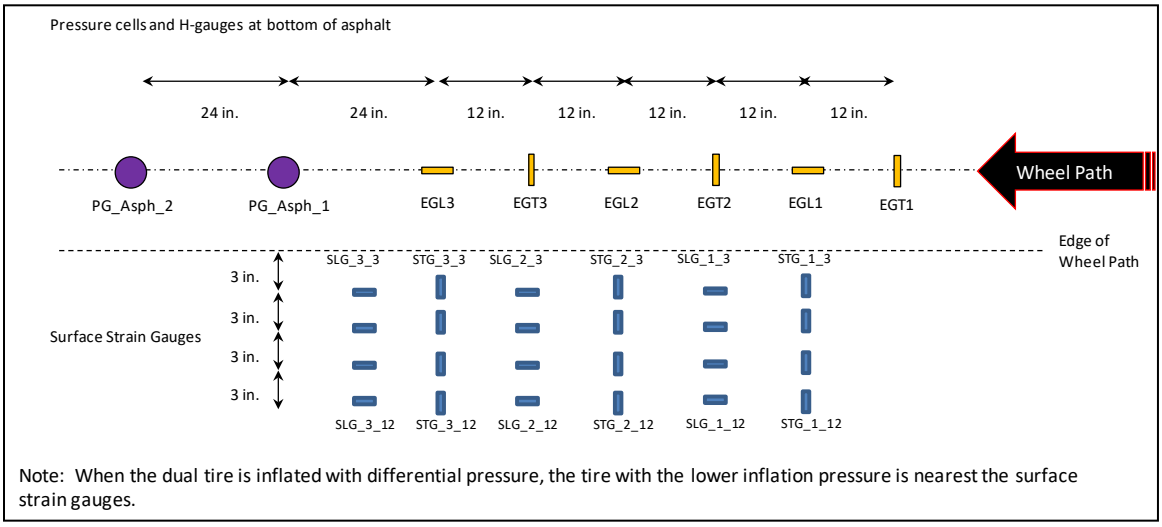

Figure 297. Illustration. Plan view of test pit instrumentation layout.

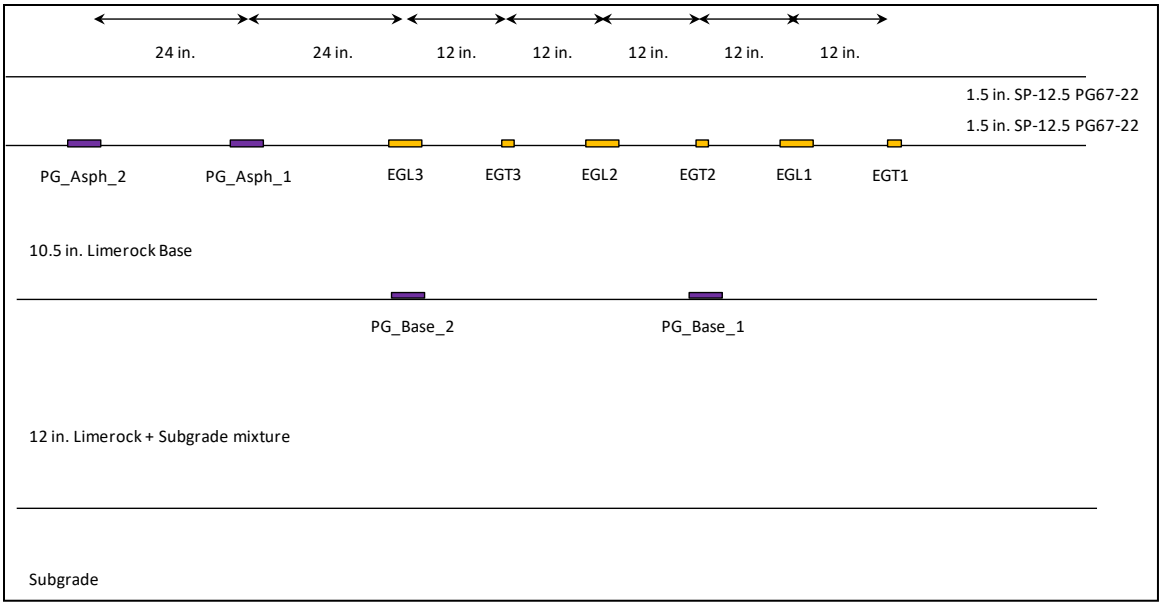

Figure 298. Illustration. Profile view test pit instrumentation layout.

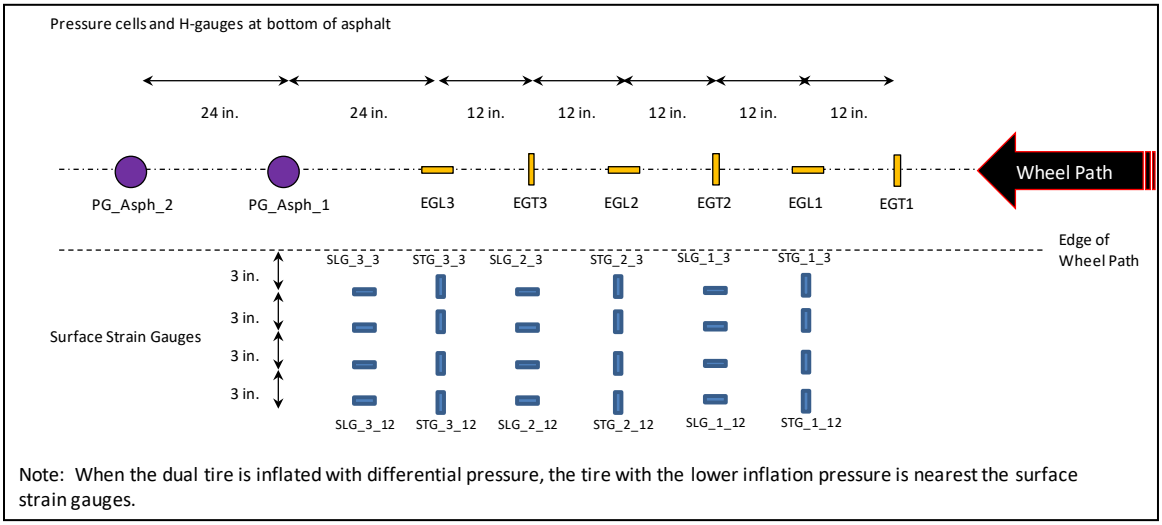

Note: When the dual tire is inflated with differential pressure, the tire with the lower inflation pressure is nearest the surface strain gauges.

Figure 299. Illustration. Plan view test track instrumentation.

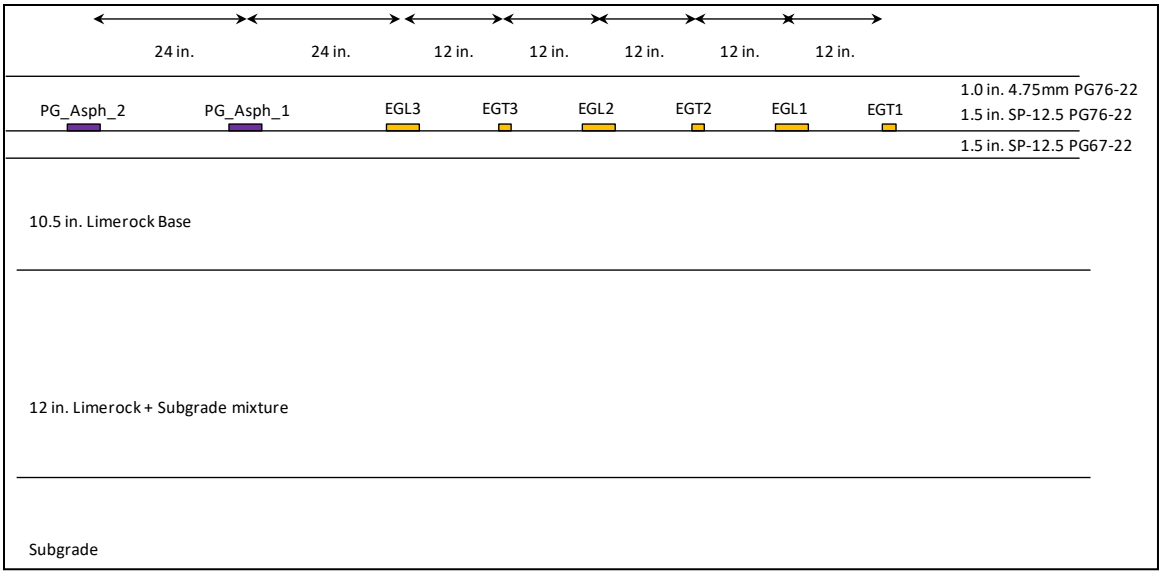

Figure 300. Illustration. Profile view test track instrumentation.

Figure 301. Photo. Mobile DAQ system - box.

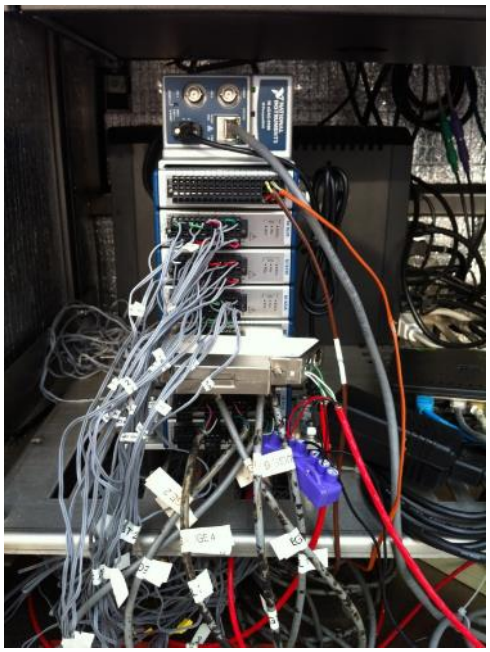

Figure 302. Photo. Mobile DAQ system - wires.

HVS Loading

Several combinations of inflation pressure, tire load, and pavement temperature were used for each tire type, as shown in Table 59. HVS loading was initiated on January 24 on the test pit using the dual-tire and was completed on February 12. HVS loading on the test track started on February 20 using the 445 mm wide base tire and was completed on April 10. A main motor failure during loading of the test track delayed testing for more than two weeks. Table 59 shows the load and temperature combinations that were used.

Table 59. HVS Test Matrix

Tire Type	Inflation Pressure (psi)	Tire Load (kips)	Tire Load (kips)	Tire Load (kips)	Tire Load (kips)	Tire Load (kips)
NG-WBT & Dual	80	6	8	10	14	18
NG-WBT & Dual	100	6	8	10	14	18
NG-WBT & Dual	110	6	8	10	14	18
NG-WBT & Dual	125	6	8	10	14	18
Dual Only	60/110	6	8	10	14	18
Dual Only	60/110	6	8	10	14	18

Each loading combination was conducted at 25°C, 40°C, and 55°C

APPENDIX F. UC-DAVIS PAVEMENT SECTIONS

TEST TRACK LOCATION, DESIGN, AND CONSTRUCTION

Experiment Location

The NG-WBT experiment is located on the North Test Track at the University of California Pavement Research Center facility in Davis, California. An aerial view of the site is shown in Figure 303. This was the second test undertaken on this test track and the original pavement was reconstructed for this study.

Figure 303. Photo. Aerial view of the UCPRC research facility.

Test Track Layout

The North Test Track is 361 ft. (110 m) long and 49.2 ft. (15 m) wide. It has a two percent crossfall in the north-south direction. The track was first constructed as part of the third phase of a Caltrans/UCPRC warm-mix asphalt study, and it was used to investigate and compare differences in the performance of seven different warm-mix asphalt technologies in gap-graded rubberized asphalt mixes against that of two gap-graded rubberized hot-mix asphalt control sections.

The test track was recycled in place to investigate four different full-depth reclamation strategies (no stabilizer [FDR-NS], foamed asphalt with cement [FDR-FA], engineered emulsion [FDR-EE], and Portland cement [FDR-PC]). The track was divided into four lanes for this study. The

track layout is shown in Figure 304 (The two test sections for the NG-WBT study are situated in Cells #1 and #2, respectively). All test track measurements and locations discussed in this technical memorandum are based on this layout.

The NG-WBT study was undertaken on Lane #1 with FDR-NS. Two sections were selected for testing, one within Cell #1 and one within Cell #2.

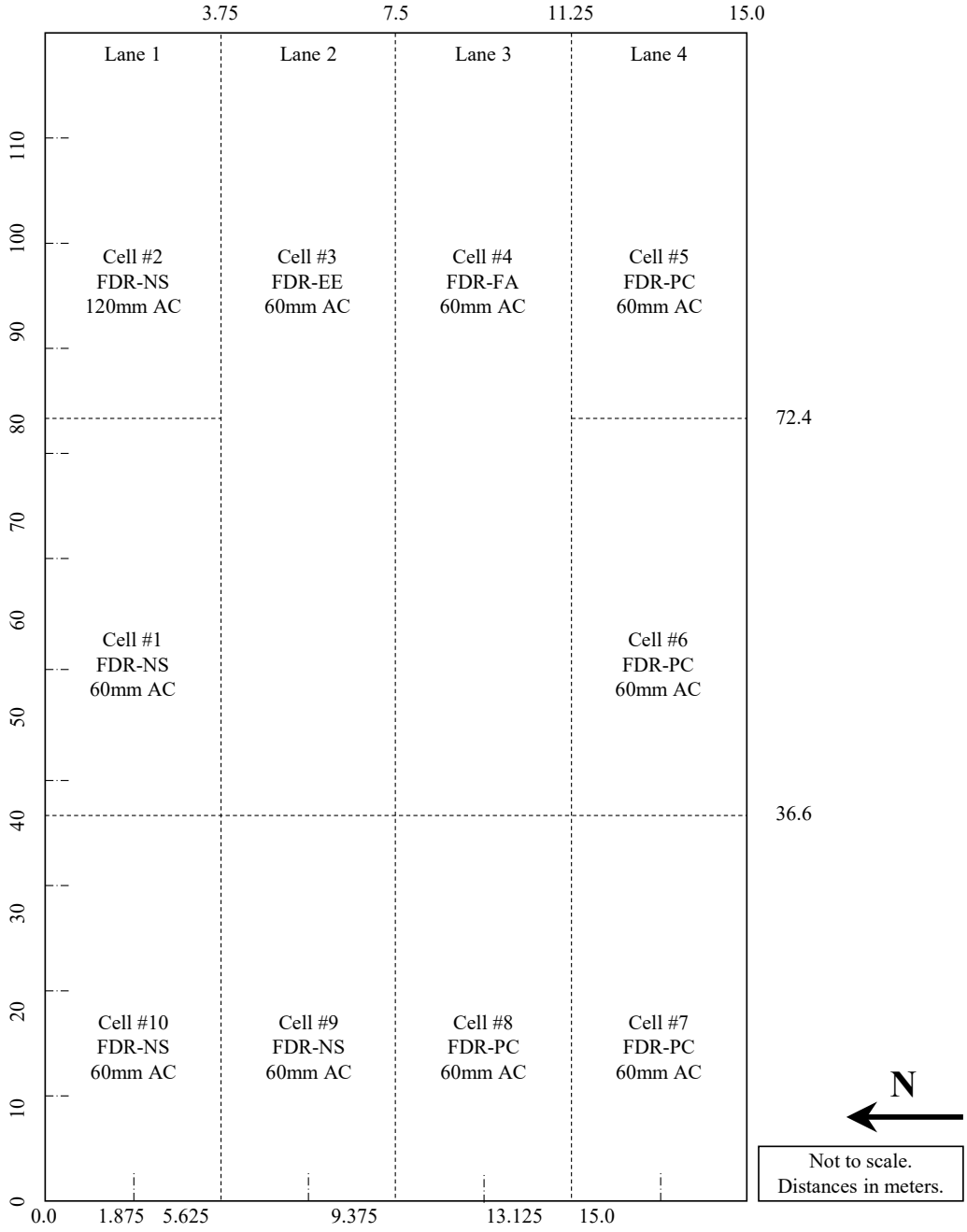

Figure 304. Graph. Test track layout.

Pavement Design

Pavement design for the FDR study was based on typical Caltrans practice. Recycle depth was set at 0.83 ft. (250 mm), resulting in a new recycled base layer consisting of 0.4 ft. (120 mm) of recycled AC and 0.43 ft. (130 mm) of the existing base. Given that the study was dedicated to understanding the behavior and performance of the recycled base, a relatively thin (0.2 ft. [60 mm]) AC surfacing was used in the design. Part of the FDR-NS lane was surfaced with 0.4 ft. (120 mm) of AC to compare performance of FDR-NS with two surfacing thicknesses. The pavement designs for the original and recycled test track are shown in Figure 305 and Figure 306. Details for the subgrade and original base material are provided below.

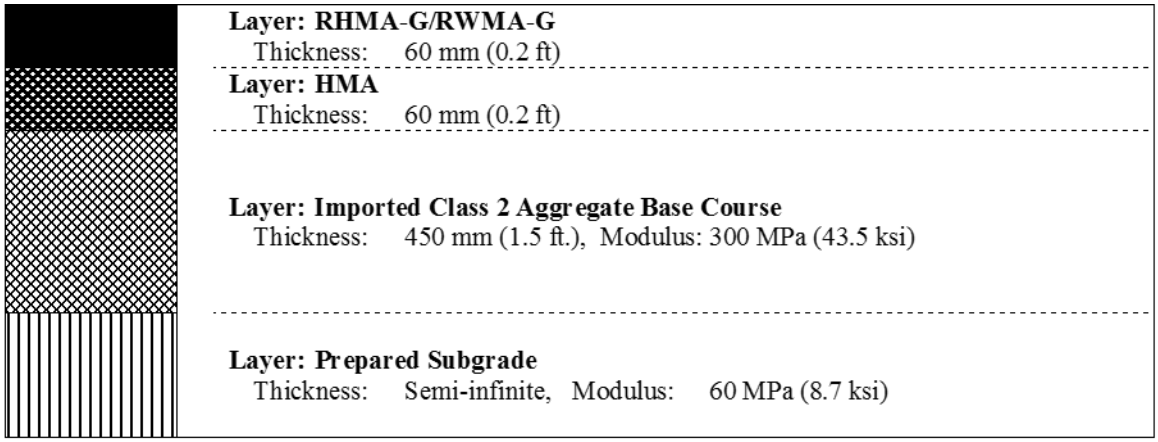

Figure 305. Illustration. Original pavement structure for rubberized warm-mix asphalt test sections.

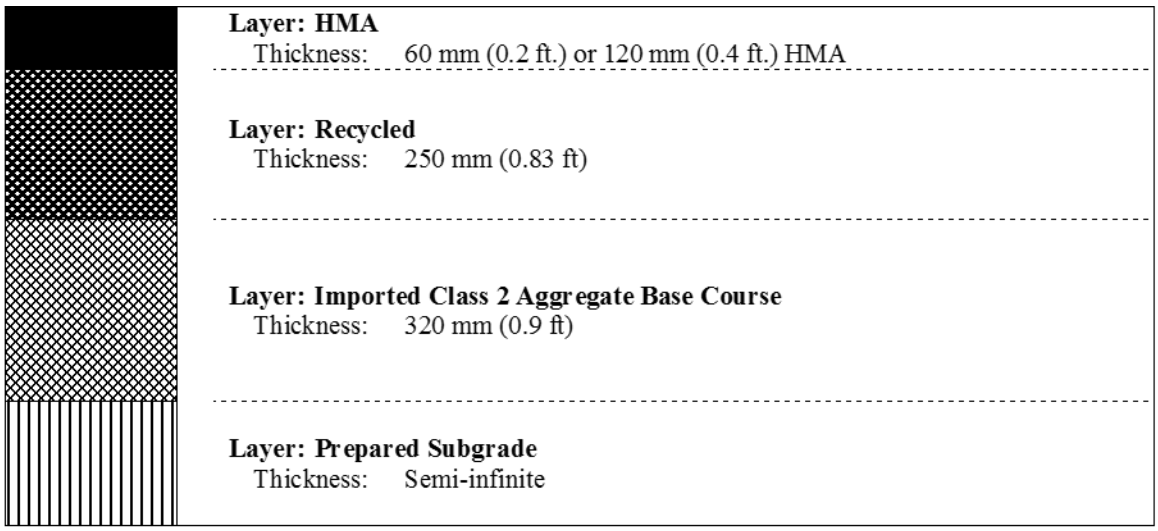

Figure 306. Illustration. Pavement structure for FDR and wide-base tire study test sections.

Subgrade and Base Course Properties (Original Pavement)

Dynamic cone penetrometer (DCP) tests were performed along the center lines of each the three lanes over the length and width of the test track prior to construction to obtain an indication of the in-situ subgrade strength. Results are summarized in Table 60. Penetration rates varied between 0.43 in per blow and 1.2 in per blow, with the weakest areas in the middle of the track. Variation was attributed to the degree of soil mixing, to temporary stockpiling of lime-treated soils used during adjacent building pad construction (lime treatment was used to dry the soil in some areas of the site), to compaction from equipment during construction of the adjacent facility, and to varying subgrade moisture contents.

Table 60. Summary of DCP Survey on Subgrade Material

Test Location[1] (m)	mm/blow Lane #1	mm/blow Lane #2	mm/blow Lane #3	CBR[2] Lane #1	CBR Lane #2	CBR Lane #3	Stiff.[2] (MPa) Lane #1	Stiff. (MPa) Lane #2	Stiff. (MPa) Lane #3
10	17	21	19	11	9	9	56	41	44
20	16	18	15	12	10	13	60	46	63
30	14	16	13	14	12	15	66	60	71
40	13	22	16	15	8	12	71	40	60
50	13	26	15	15	6	13	71	36	63
60	12	25	16	17	6	12	77	37	60
70	15	30	15	13	5	13	63	30	63
80	14	28	15	14	5	13	66	34	63
90	12	26	14	17	6	14	77	36	66
100	11	20	15	19	9	13	85	42	63

[1] Measured from southwest corner of the track.
[2] Estimated from DCP software tool.
1 MPa = 145 psi, 1 m = 3.3 ft

Subgrade Preparation for the Original Pavement

Subgrade preparation included vegetation removal, preliminary leveling, ripping, watering and mixing, compaction, and final leveling to include a two percent north-south crossfall as follows:

- Removing vegetation with a grader, windrowing of the deleterious material towards the center of the track, collecting this material with a scraper and dumping it in a temporary stockpile for removal
- Preliminary leveling with a grader followed by watering
- Ripping to a depth of 12 in (300 mm)
- Watering and mixing using both the scraper and grader. Pockets of high clay content soils were observed during this process, which required additional working with the grader and scraper to break up the clods
- Initial compaction with a padfoot roller. Despite extensive mixing, some clay pockets were still observed after completion of the initial compaction, with padfoot impressions clearly visible. Clay pockets appeared to predominate on the eastern half of the track
- Final compaction with a vibrating smooth drum roller
- Final leveling with a grader
- Density checks on the finished surface with a nuclear density gauge

Quality control of the subgrade preparation was limited to density checks with a nuclear gauge following California Test 231 (CT 231) and comparison of the results against a laboratory maximum density of 134.2 lb/ft^3 (2,150 kg/m^3) determined according to California Test 216 (CT 216). Nuclear gauge measurements were taken at ten different locations selected according to a nonbiased plan. Samples for laboratory density determination were taken at the first three locations. The results summarized in Table 61 indicate that the subgrade density was generally consistent across the test track. Relative compaction varied between 95.4 percent and 99.2 percent with an average of 97.0 percent, two percent above the Caltrans-specified minimum density of 95 percent for subgrade compaction. No location had a relative compaction lower than this minimum.

Table 61. Summary of Subgrade Density Measurements

Location	Wet Density (lb/ft^3)	Wet Density (kg/m^3)	Moisture Content (%)	Dry Density (lb/ft^3)	Dry Density (kg/m^3)	Relative Compaction (%)
1	130.5	2,091	15.6	112.6	1,804	97.3
2	132.6	2,124	17.3	113.1	1,811	98.8
3	131.3	2,103	16.8	112.4	1,801	97.8
4	130.2	2,086	16.2	112.1	1,796	97.0
5	133.2	2,133	15.2	115.6	1,852	99.2
6	128.9	2,065	17.8	109.5	1,754	96.0
7	132.2	2,117	17.9	112.1	1,795	98.5
8	128.1	2,052	18.7	107.9	1,728	95.4
9	132.3	2,120	16.5	113.6	1,820	98.6
10	128.7	2,062	15.0	111.9	1,793	95.9
Average	130.8	2,095	17.0	112.1	1,795	97.0
Std. Dev.	1.8	29	1.2	2.1	34	1.3

Base Course Construction for the Original Pavement

Base course aggregates were sourced from the Teichert Cache Creek quarry near Woodland, California. Key material properties are summarized in Table 62. The material met Caltrans specifications, except for the percent passing the #200 sieve, which exceeded the specification operating range by 3.0 percent, and just met the contract compliance limits.

The warm-mix asphalt test track base course was constructed two days after the subgrade preparation. The construction process included aggregate spreading, watering, compaction, and final leveling to include a two percent north-south crossfall as follows:

- Transporting crushed base course material (alluvial) that complied with Caltrans Class 2 aggregate base course specifications from the Teichert Cache Creek aggregate source to the test track with a fleet of bottom-dump trucks and trailers
- Dumping the aggregate in windrows
- Spreading the aggregate with a grader to a thickness of approximately 4.0 in (100 mm)
- Adding water to bring the aggregate to the optimum moisture content and re-mixing with the grader to ensure even distribution of the moisture throughout the material
- Initial compaction of the spread material with a vibrating steel wheel roller
- Repeating the process until the design thickness of 1.5 ft. (450 mm) was achieved

- Applying a generous application of water followed by compaction to pump fines to the surface to provide good aggregate interlock (slushing)
- Final leveling with a grader. Final levels were checked with a total station to ensure that a consistent base course thickness had been achieved
- Removal of excess material with a scraper followed by final compaction
- Density checks on the finished surface with a nuclear density gauge

Table 62. Base Course Material Properties

Property			Result	Operating Range	Contract Compliance
Grading:	1"	(25 mm)	100	100	100
	3/4"	(19 mm)	99.1	90 – 100	87 – 100
	1/2"	(12.5 mm)	90.1	–	–
	3/8"	(9.5 mm)	83.5	–	–
	#4	(4.75 mm)	63.3	35 – 60	30 – 65
	#8	(2.36 mm)	48.8	–	–
	#16	(1.18 mm)	39.2	–	–
	#30	(600 µm)	30.8	10 – 30	5 – 35
	#50	(300 µm)	21.6	–	–
	#100	(150 µm)	15.6	–	–
	#200	(75 µm)	12.3	2 – 9	0 – 12
Liquid Limit			Non-plastic	–	–
Plastic Limit				–	–
Plasticity Index				–	–
Maximum Dry Density			140.6 (2,252)	–	–
(lb/ft^3)(kg/m^3)			6.0	–	–
Optimum Moisture Content					
R-Value			79	–	>78
Sand equivalent			30	25	>22
Durability index – course			78	–	>35
Durability index – fine			52	–	>35

Quality control of the base course construction was limited to density checks with a nuclear gauge following CT 231 and comparison of the results against a laboratory maximum wet density of 150.5 lb/ft^3 (2,410 kg/m^3) determined according to CT 216. Nuclear gauge measurements were taken at ten different locations selected according to a nonbiased plan. A sample for laboratory density determination was taken at the first location. Results are summarized in Table 63 and indicate that the base course density properties were generally consistent across the test track, but that the material was relatively wet compared with the laboratory-determined optimum moisture content. Relative compaction varied between 96.7 percent and 99.4 percent with an average of 98.0 percent, three percent above the Caltrans-specified minimum density of 95 percent for base compaction. No location had a relative compaction lower than this minimum.

Table 63. Summary of Nuclear Gauge Density Measurements on Base Course Layer

Location	Wet Density (lb/ft^3)	Wet Density (kg/m^3)	Moisture Content (%)	Dry Density (lb/ft^3)	Dry Density (kg/m^3)	Relative Compaction (%)
1	146.5	2,346	6.6	137.4	2,201	97.3
2	148.5	2,379	7.0	138.8	2,223	98.7
3	148.0	2,371	8.0	137.0	2,195	98.4
4	147.1	2,356	7.8	136.5	2,186	97.8
5	148.7	2,382	6.3	139.9	2,241	98.8
6	145.5	2,330	6.8	136.2	2,182	96.7
7	149.0	2,387	8.2	137.7	2,206	99.0
8	145.6	2,332	7.7	135.2	2,165	96.8
9	149.5	2,395	6.9	139.8	2,240	99.4
10	145.7	2,334	7.8	135.2	2,165	96.8
Average	147.4	2,361	7.3	137.3	2,200	98.0
Std. Dev.	1.5	25	0.7	1.7	27.6	1.0

Follow-up DCP measurements were also undertaken on the base at the same locations as the original subgrade DCP survey. The results are summarized in Table 64 and indicate that although average penetration rates (mm/blow) were consistent across the track, there was considerable difference in the average calculated stiffness of the base from the redefined layers based on actual penetration. Consequently, the contractor was requested to re-compact the track with a static steel drum roller prior to priming to consolidate the base layer and accelerate movement of any infiltrated water to the surface. A significant improvement in subgrade stiffness attributed to the subgrade preparation and confinement by the base was also noted.

Table 64. Summary of DCP Survey on Base and Subgrade Material – Penetration Rate (mm/blow)

Test Location (m)[1]	Base Lane #1	Base Lane #2	Base Lane #3	Subgrade Lane #1	Subgrade Lane #2	Subgrade Lane #3
10	3	-	-	9	-	-
20	-	3	-	-	8	-
30	-	-	3	-	-	7
40	4	-	-	9	-	-
50	-	4	-	-	9	-
60	-	-	4	-	-	9
70	4	-	-	10	-	-
80	-	4	-	-	10	-
90	-	-	4	-	-	7
100	4	-	-	11	-	-

[1] Measured from southwest corner of the track. (1 m = 3.3 ft)

Table 65. Summary of DCP Survey on Base and Subgrade Material – Stiffness (MPa [ksi])[2]

Test Location (m)[1]	Base Stiff. Lane #1	Base Stiff. Lane #2	Base Stiff. Lane #3	Subgrade Stiff. Lane #1	Subgrade Stiff. Lane #2	Subgrade Stiff. Lane #3
10	430 (62)	-	-	111 (16)	-	-
20	-	395 (57)	-	-	119 (17)	-
30	-	-	320 (46)	-	-	139 (20)
40	332 (48)	-	-	114 (17)	-	-
50	-	299 (43)	-	-	107 (16)	-
60	-	-	279 (41)	-	-	137 (20)
70	255 (37)	-	-	99 (14)	-	-
80	-	260 (38)	-	-	105 (15)	-
90	-	-	273 (40)	-	-	148 (22)
100	259 (38)	-	-	116 (17)	-	-

[2] Estimated from DCP software tool.

Full-Depth Reclamation

Conventional FDR construction procedures were followed on the FDR-NS lane (304). The recycler and connected water tanker made a single pass to pulverize and mix the material to optimum moisture content for compaction. Initial rolling was completed with a pad foot roller, followed by vibrating smooth drum and rubber-tired rollers. Final levels were achieved with a grader after initial rolling. Compaction was measured with a nuclear gauge. Material properties and nuclear gauge compaction results are provided in Table 66 and Table 67, respectively.

Figure 307. Photo. Test track recycling - 1.

Figure 308. Photo. Test track recycling - 2.

Table 66. Recycled Layer Material Properties

Property			Result	Operating Range	Contract Compliance
Grading:	1"	(25 mm)	100	100	100
	3/4"	(19 mm)	99	90 – 100	87 – 100
	1/2"	(12.5 mm)	91	–	–
	3/8"	(9.5 mm)	82	–	–
	#4	(4.75 mm)	66	35 – 60	30 – 65
	#8	(2.36 mm)	46	–	–
	#16	(1.18 mm)	31	–	–
	#30	(600 µm)	21	10 – 30	5 – 35
	#40	(425 µm	14	–	–
	#50	(300 µm)	11	–	–
	#100	(150 µm)	8	–	–
	#200	(75 µm)	5	2 – 9	0 – 12
Liquid Limit			Non-plastic	–	–
Plastic Limit				–	–
Plasticity Index				–	–
Maximum Dry Density (lb/ft^3) (kg/m^3)			135.5 (2,171)	–	–
Optimum Moisture Content			4.8	–	–

Table 67. Summary of Nuclear Gauge Density Measurements on Recycled Layer

Location	Wet Density (lb/ft^3)	Wet Density (kg/m^3)	Moisture Content (%)	Dry Density (lb/ft^3)	Dry Density (kg/m^3)	Relative Compaction (%)
1	135.6	2,172	8.0	125.4	2,008	100.3
2	130.1	2,083	9.3	120.8	1,935	96.7
3	144.3	2,311	11.7	132.6	2,124	106.1
4	139.1	2,229	9.8	126.8	2,030	101.4
5	140.2	2,246	8.7	129.0	2,066	103.2
6	127.8	2,046	7.3	119.0	1,906	95.2
7	141.6	2,268	9.6	129.3	2,071	103.4
8	140.3	2,247	8.9	128.8	2,063	103.0
9	131.0	2,098	7.0	122.4	1,960	97.9
Average	136.6	2,189	8.9	126.0	2,018	100.8
Std. Dev.	5.8	93	1.4	4.5	72	3.6

Material Properties of AC during Construction

Dense-graded AC was sourced from the Teichert Perkins Asphalt Plant in Sacramento, California. Key material design parameters are summarized in Table 68. The material met Caltrans specifications for Type-A AC with three-quarter inch aggregate gradation and contained 15 percent RAP.

Table 68. Key AC Mix Design Parameters

Parameter			Wearing Course Actual	Wearing Course Compliance
Grading:	1"	(25 mm)	100	100
	3/4"	(19 mm)	99	94 – 100
	1/2"	(12.5 mm)	85	94 – 100
	#4	(4.75 mm)	49	44 – 58
	#8	(2.36 mm)	32	31 – 41
	#30	(600 µm)	18	16 – 24
	#200	(75 µm)	4	3 – 7
Asphalt binder grade			PG 64-16	–
Asphalt binder content (% by aggregate mass)			4.8	–
Hveem stability at optimum bitumen content			37.0	>37
Air void content (%)			4.9	2 – 6
Voids in mineral aggregate (LP-2) (%)			13.8	>13
Voids filled with asphalt (LP-3) (%)			64.9	65 – 75
Sand equivalent (%)			72.0	>47
Specific gravity (compacted, Gmb)			2.451	–
Specific gravity (Max, Gmm)			2.576	–

Prime Coat Application

Prior to prime coat application, the surface was broomed to remove all loose material (Figure 309). An SS-1H asphalt emulsion prime coat was applied to the surface at a rate of 0.15 gal/yd2 (0.68 L/m2). Although a consistent application was achieved (Figure 306), some differential penetration, which was attributed to patches of near-surface moisture, was observed.

Figure 309. Photo. Broomed surface.

Figure 310. Photo. Primed surface.

AC Placement

AC was placed on November 14, 2012. Construction started at approximately 8:30 a.m. ambient air temperature was 45 °F and the relative humidity was 86 percent. Construction was completed at approximately 11:00 a.m., when ambient temperature was 55 °F and the relative humidity was 70 percent.

The mix was transported using end-dump trucks. Paving started in Lane #1, followed by Lanes #2, #3, and #4. The second lift on Lane #1 was placed after completion of the first lift on the other lanes. Paving was carried out in a west-east direction and followed conventional procedures. A breakdown roller closely followed the paver applying about four passes. A single pass was made with an intermediate rubber-tired roller, followed by another four passes with a finish roller. Compaction of the lower lift appeared to be consistent and no problems were noted. On the short section with the second lift (see Cell #2 in Figure 304), the mix appeared tender and some shearing was noted in the vicinity of the instrumentation cables.

Construction Quality Control

Compaction was measured by the UCPRC using a nuclear gauge on the day of construction using the mix design specific gravity values. Measurements were taken at 60 ft. (18 m) intervals along the center line of each lane, with a focus on checking densities in the areas that would be used for HVS testing. A summary of the results is provided in Table 69. The results indicate that there was some variability in the measurements in the first lift, but that satisfactory compaction had been achieved. Density measurements were generally lower on the second lift and were attributed to tenderness in the mix and problems with shearing in the vicinity of the instrumentation cables.

Table 69. Summary of AC Density Measurements

Position	Lane #1 First Lift	Lane #1 First Lift	Lane #1 First Lift	Lane #1 Second Lift	Lane #1 Second Lift	Lane # Second Lift
	Gauge	Gauge	Relative	Gauge	Gauge	Relative
	lb/ft^3	kg/m^3	lb/ft^3	lb/ft^3	kg/m^3	(%)
1	146.0	2,339	92.8	141.6	2,269	90.0
2	145.3	2,328	92.4	142.5	2,283	91.0
3	147.8	2,367	93.9	142.3	2,280	90.5
4	143.0	2,290	90.9	–	–	–
5	146.1	2,341	92.9	–	–	–
6	146.5	2,346	93.1	–	–	–
Average	145.8	2,335	92.7	142.1	2,277	90.5
Std. Dev.	1.6	25.6	1.0	0.5	7.4	0.5
RICE	2.520					

Temperatures were systematically measured throughout the placement of the AC using infrared temperature guns, thermocouples, and an infrared camera. Mix temperature behind the paver screed was 297 °F. Temperatures at the start and completion of rolling were 295 °F and 141 °F, respectively. The thermal camera image (*FLIR Systems ThermaCAM PM290*) of the mat behind the paver, in Figure 311 clearly shows consistent temperature across the mat.

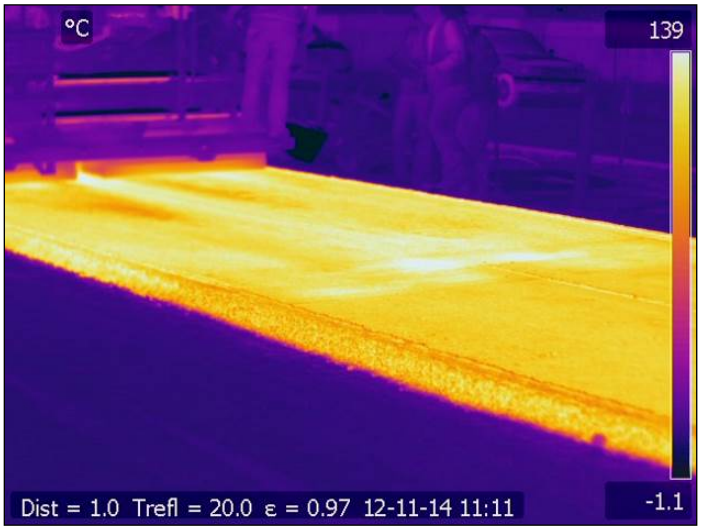

Figure 311. Illustration. Thermal images of test track during construction.

Thickness was monitored with probes by the paving crew throughout the construction process. The thickness of cores removed for laboratory testing after construction was measured for quality control purposes. Average thicknesses of the bottom and top lifts were 2.6 in (67 mm) and 2.5 in (64 mm), respectively.

TEST TRACK LAYOUT, INSTRUMENTATION, AND SAMPLING

Accelerated Pavement Testing was conducted on two test sections on the lane with full-depth reclaimed aggregate base with no stabilization (FDR-NS). One of the test sections had a single 0.2 ft. lift of AC and the second one had two 0.2 ft. lifts.

Protocols and Coordinate System

The HVS test section layout, test setup, trafficking, and measurements followed standard UCPRC protocols. A schematic in Figure 312 shows the HVS test section along with the stationing and coordinate system. The thermocouple tree locations and coordinate system are also presented; the z-axis points upward following the right-hand convention with zero at the pavement surface. Station numbers (0 to 16) refer to fixed points on the test section and are used for measurements and as a reference for discussing performance. Stations were placed at 1.6 ft (0.5 m) increments. The test section is 26.2 ft. (8.0 m) long and 3.3 ft (1.0 m) wide. A sensor installed at the center of the test section has an *x*-coordinate of 13.1 ft and a *y*-coordinate of 1.6 ft.

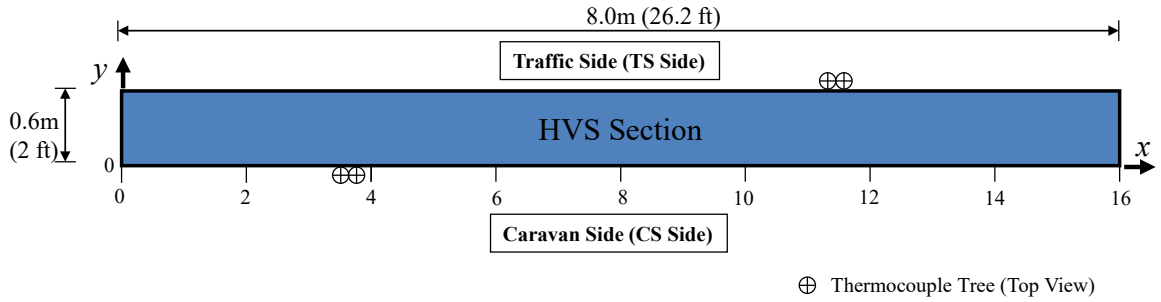

Figure 312. Graph. Schematic of an HVS test section and stations.

Test Track Layout

The FDR study test track layout is shown in Figure 313. Two HVS test sections were demarcated for the NG-WBT testing (Sections 670HC and 671HC). All test sections were situated at the center of the lane.

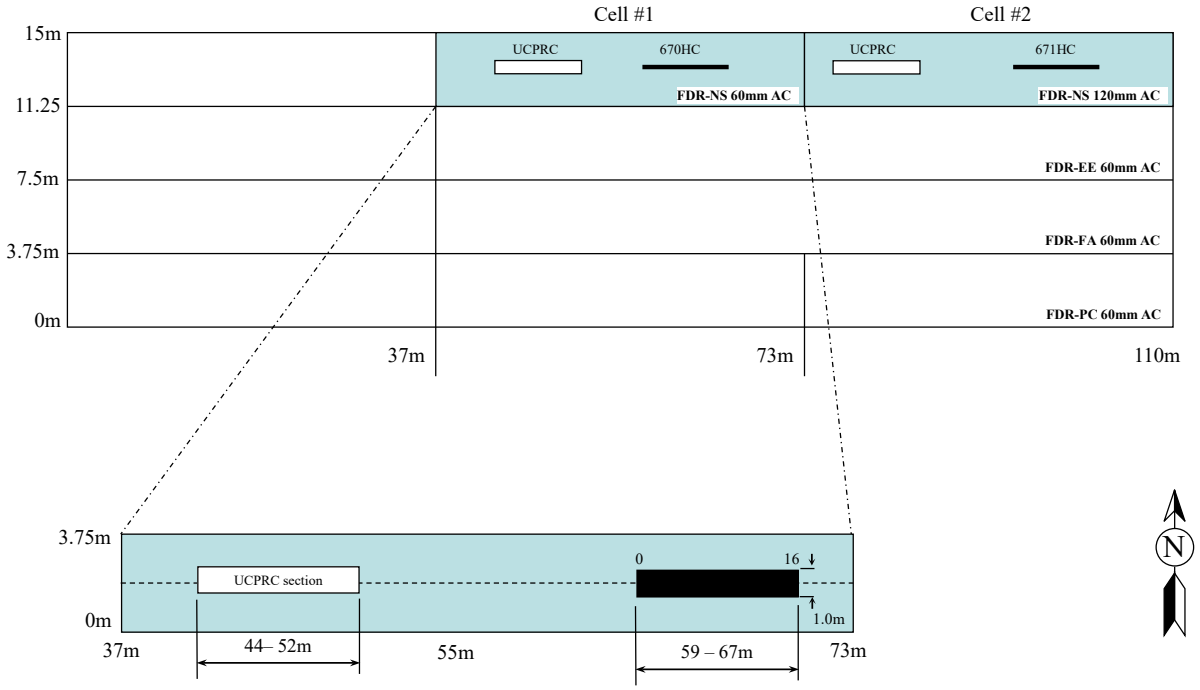

Figure 313. Illustration. Layout of test sections.

Instrumentation Layout

Measurements were taken with embedded instruments including a multi-depth deflectometer (MDD), strain gauges, a pressure cell, and thermocouple trees. The layout of the embedded instruments is shown in Figure 314 and Figure 315 respectively for the two test sections. Photographs of the layout of the strain gauges and pressure cells in Section 670HC and Section 671HC are shown in Figure 316 and Figure 317 respectively. The exact coordinates of the instruments are listed in Table 60 and Table 61.

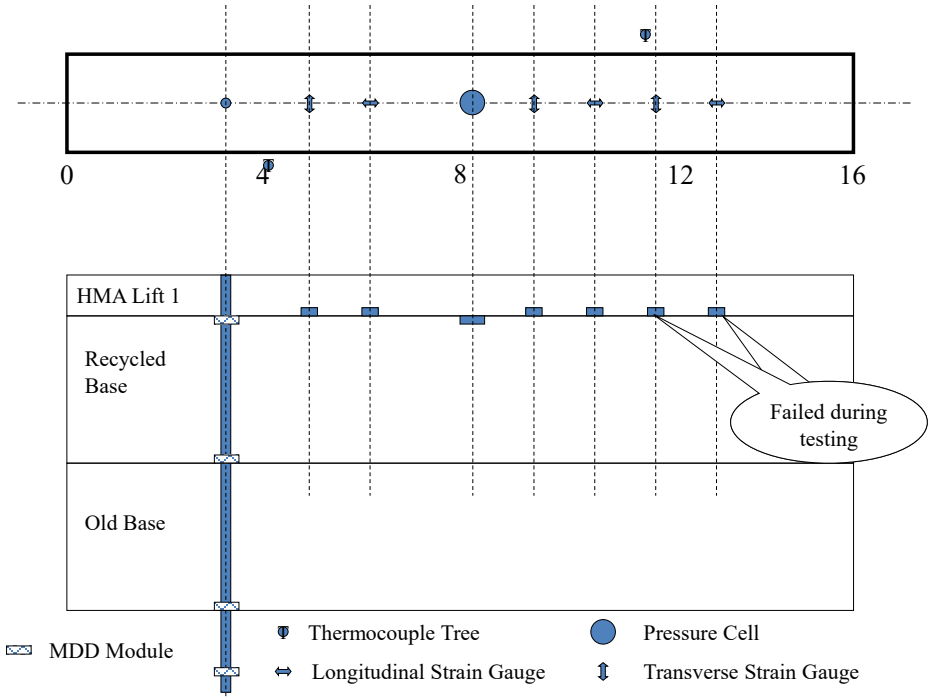

Figure 314. Illustration. Layout of embedded instruments for Section 670HC (one lift of AC).

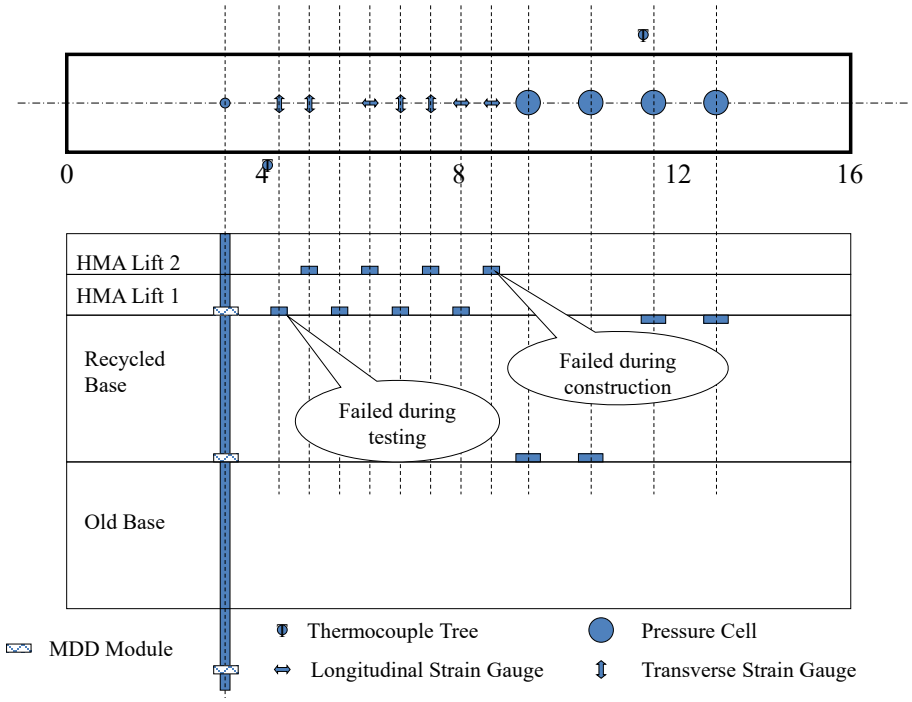

Figure 315. Illustration. Layout of embedded instruments for Section 671HC (two lifts of AC).

Figure 316. Photo. View of strain gauges and pressure cells installed on Section 670HC during construction.

Figure 317. Photo. View of strain gauges and pressure cells installed on Section 671HC during construction - instruments on top of the recycled base.

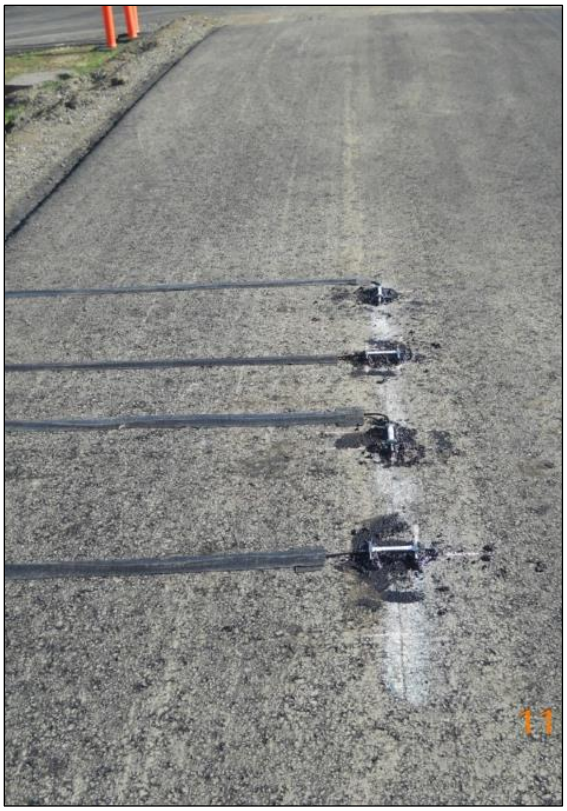

Figure 318. Photo. View of strain gauges and pressure cells installed on Section 671HC during construction - strain gauges on top of the bottom lift of AC.

Table 70. Coordinates of Embedded Instruments for Section 670HC

Section	Type	Name	PosX (mm)	PosY (mm)	PosZ (mm)	Orientation
670HC	MDD	MDD3-70	1,500	500	-70	Vertical
670HC	MDD	MDD3-310	1,500	500	-310	Vertical
670HC	MDD	MDD3-550	1,500	500	-550	Vertical
670HC	MDD	MDD3-850	1,500	500	-850	Vertical
670HC	Pressure Cell	PC8CL_RAB_T	4,000	500	-60*	Vertical
670HC	Strain Gauge	SG5CL_T_HMA_B	2,500	500	-50[x]	Transverse
670HC	Strain Gauge	SG6CL_L_HMA_B	3,000	500	-50 [x]	Longitudinal
670HC	Strain Gauge	SG9CL_T_HMA_B	4,610	500	-50 [x]	Transverse
670HC	Strain Gauge	SG10CL_L_HMA_B	5,219	500	-50 [x]	Longitudinal
670HC	Strain Gauge	SG12CL_T_HMA_B	5,829	500	-50 [x]	Transverse
670HC	Strain Gauge	SG13CL_L_HMA_B	6,438	500	-50 [x]	Longitudinal
670HC	Thermocouple	4CS-0	2,000	-100	0	N/A
670HC	Thermocouple	4CS-20	2,000	-100	-20	N/A
670HC	Thermocouple	4CS-50	2,000	-100	-50	N/A
670HC	Thermocouple	4CS-90	2,000	-100	-90	N/A

Section	Type	Name	PosX (mm)	PosY (mm)	PosZ (mm)	Orientation
670HC	Thermocouple	4CS-120	2,000	-100	-120	N/A
670HC	Thermocouple	12TS-0	6,000	1,100	0	N/A
670HC	Thermocouple	12TS-20	6,000	1,100	-20	N/A
670HC	Thermocouple	12TS-50	6,000	1,100	-50	N/A
670HC	Thermocouple	12TS-90	6,000	1,100	-90	N/A
670HC	Thermocouple	12TS-120	6,000	1,100	-120	N/A

*: installed flush with the top of the recycled base
x: installed on top of the recycled base
25.4 mm = 1 in

Table 71. Coordinates of Embedded Instruments for Section 671HC

Section	Type	Name	PosX (mm)	PosY (mm)	PosZ (mm)	Orientation
671HC	MDD	MDD3-100	1,500	500	-100	Vertical
671HC	MDD	MDD3-365	1,500	500	-365	Vertical
671HC	MDD	MDD3-1000	1,500	500	-1,000	Vertical
671HC	Pressure Cell	PC9CL_RAB_B	4,671	500	-365	Vertical
671HC	Pressure Cell	PC11CL_RAB_B	5,281	500	-365	Vertical
671HC	Pressure Cell	PC12CL_RAB_T	5,890	500	-135	Vertical
671HC	Pressure Cell	PC13CL_RAB_T	6,500	500	-135	Vertical
671HC	Strain Gauge	SG4CL_T_HMA_BL_B	2,233	500	-116	Transverse
671HC	Strain Gauge	SG5CL_T_HMA_TL_B	2,538	500	-65	Transverse
671HC	Strain Gauge	SG6CL_L_HMA_BL_B	2,842	500	-116	Longitudinal
671HC	Strain Gauge	SG6CL_L_HMA_TL_B	3,147	500	-65	Longitudinal
671HC	Strain Gauge	SG7CL_T_HMA_BL_B	3,452	500	-116	Transverse
671HC	Strain Gauge	SG8CL_T_HMA_TL_B	3,757	500	-65	Transverse
671HC	Strain Gauge	SG8CL_L_HMA_BL_B	4,062	500	-116	Longitudinal
671HC	Thermocouple	4CS-0	2,000	-100	0	N/A
671HC	Thermocouple	4CS-20	2,000	-100	-20	N/A
671HC	Thermocouple	4CS-50	2,000	-100	-50	N/A
671HC	Thermocouple	4CS-90	2,000	-100	-90	N/A
671HC	Thermocouple	4CS-120	2,000	-100	-120	N/A
671HC	Thermocouple	12TS-0	6,000	1,100	0	N/A
671HC	Thermocouple	12TS-20	6,000	1,100	-20	N/A
671HC	Thermocouple	12TS-50	6,000	1,100	-50	N/A
671HC	Thermocouple	12TS-90	6,000	1,100	-90	N/A
671HC	Thermocouple	12TS-120	6,000	1,100	-120	N/A

*: installed flush with the top of the recycled base
x: installed on top of the recycled base
25.4 mm = 1 in

Thermocouples

Type-K thermocouples were used to measure pavement and air temperatures (both inside and outside the temperature chamber). Five thermocouples were bundled together to form a "thermocouple tree" (Figure 319) for measuring pavement temperatures at multiple depths at each location.

Figure 319. Photo. Thermocouple tree with five Type-K thermocouples on a plastic dowel.

Laser Profilometer

A laser profilometer was used to the measure transverse surface profile of the test section at every station, (i.e., from Station 0 to Station 16). The difference between the surface profile after HVS trafficking and the initial surface profile is the permanent change in surface profile. Based on the change in surface profile, the maximum total rut was determined for each station, as illustrated in Figure 320.

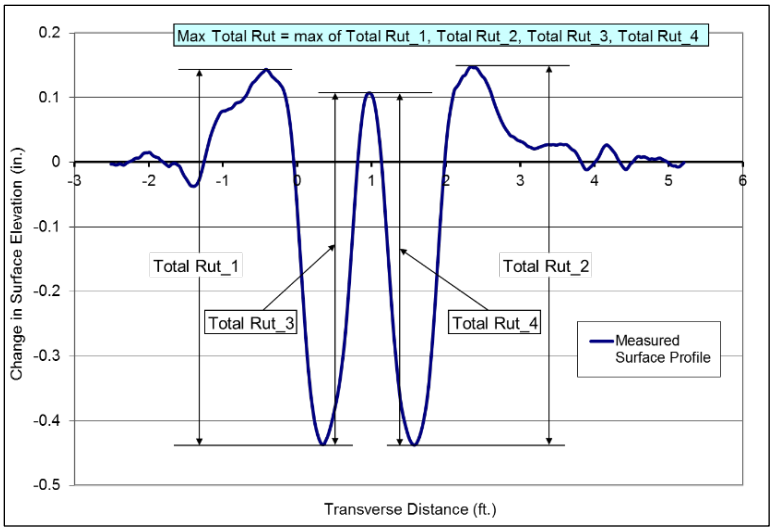

Figure 320. Illustration. Maximum rut depth for a leveled profile.

Strain Gauges

Tokyo Sokki Kenkyujo Inc. KM100-HAS 350 Ω full bridge strain gauges were used on both sections. Gauges were attached to the pavement surface using a paste prepared by mixing sand and asphalt emulsion. Installation of a strain gauge on top of the recycled base is shown in Figure 321.

Figure 321. Photo. Installation of *Tokyo Sokki KM100-HAS* strain gauge.

The strain gauges were connected to a *National Instruments NI cDAQ-9237* module. A virtual channel was created for each strain gauge using the *Measurement & Automation Explorer* (NI-MAX) software provided by *National Instruments*. The settings for the virtual channel are shown in Figure 322. Using these settings, the strain gauge virtual channel readings are determined as Strain = $-V_r/GF = -V_r/0.5 = -2V_r$; where *Strain* is the output of the virtual channel; *GF* is the gauge factor in the virtual channel setting; and V_r is the ratio between output and input voltages of the Wheatstone bridge inside the strain gauge.

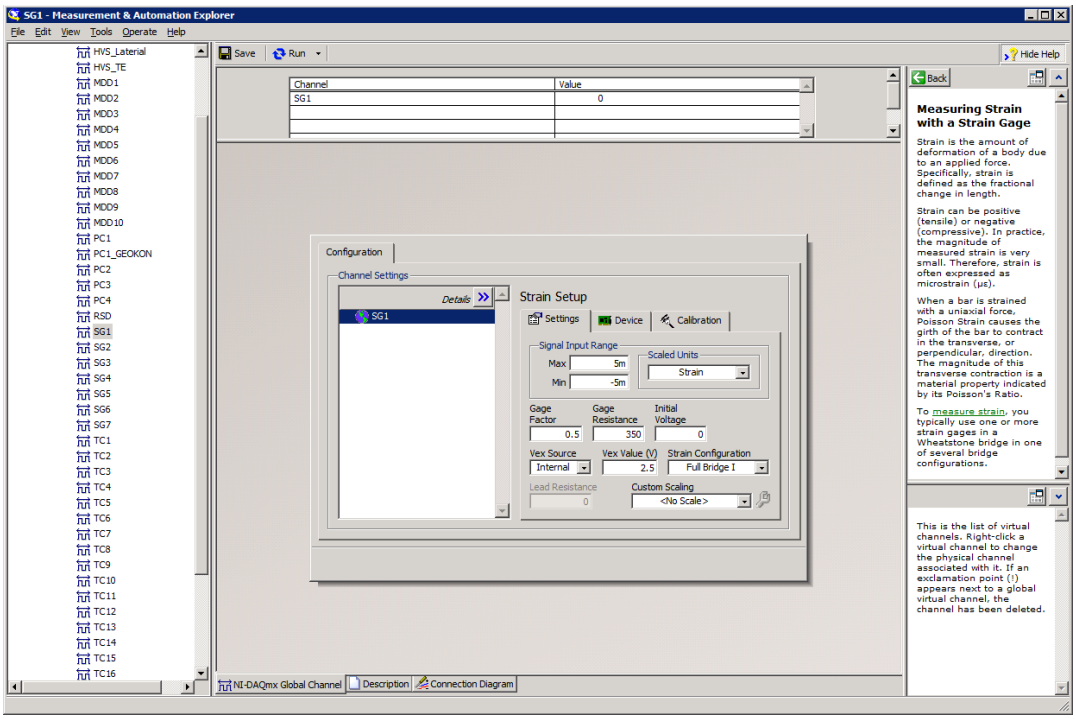

Figure 322. Illustration. Virtual channel settings for strain gauges used in this project.

A gauge factor (*GF*) of 0.5 was used to configure the virtual channel to accommodate the *Tokyo Sokki* calibration coefficient (C_ε) for each gauge based on the assumption that the voltage ratio (V_r) was multiplied by 2.0 when converting to strain. The data acquisition software then converted the virtual channel reading into microstrain by multiplying it by -0.830 x 10^6. The negative sign was necessary to ensure that tensile strain will increase the final readings. The value of 0.830 was the average calibration coefficient provided by *Tokyo Sokki*. Once the strain readings were recorded, they were loaded into a database where the actual calibration coefficients for each specific strain gauge were stored. When data were extracted from the database, the necessary minor rescaling was built into the query to ensure that the individual gauge factors were used in place of the average value of 0.830.

Example strain data recorded from one of the strain gauges is presented in Figure 323, which shows the variation of the strain gauge reading versus wheel position as the wheel travels from one end of the test section to the other. Several quantities are summarized based on the raw readings. Specifically, the reference value is the reading when the wheel is at the far end of the test section. The peak and valley are maximum and minimum values deviating from the reference value, respectively.

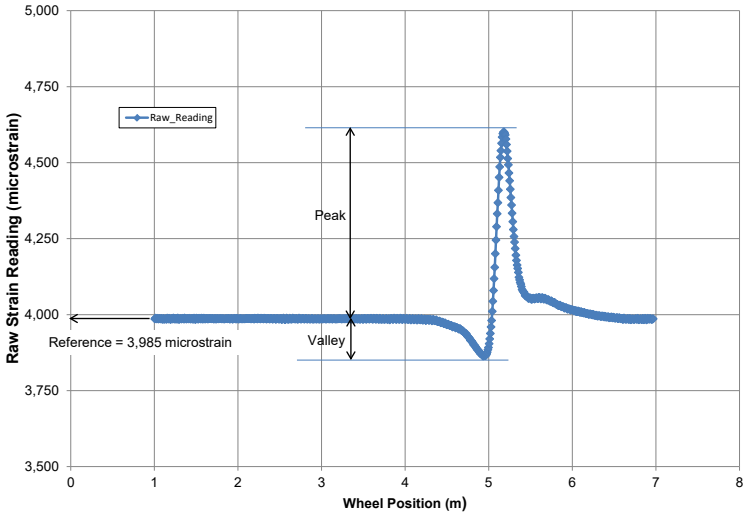

Figure 323. Illustration. Example strain reading and definitions of summary quantities.

Earth Pressure Cells

Two sets of earth pressure cells were used; one was installed in the thin AC section (Section 670HC) and the other in the thick section (Section 671HC). Installation of the pressure cells is shown in Figures 321 and 322.

Figure 324. Photo. Installation of earth pressure cells for the two test sections - pressure cell on 670HC.

Figure 325. Photo. Installation of earth pressure cells for the two test sections - pressure cells on 671HC.

Example data recorded from one of the pressure cells is shown in Figure 326, which presents variation of the pressure reading versus wheel position as the wheel travels from one end of the test section to the other. Several quantities are summarized based on the raw readings. Specifically, the reference value is the reading when the wheel is at the far end of the test section. The peak and valley are maximum and minimum values deviating from the reference value, respectively.

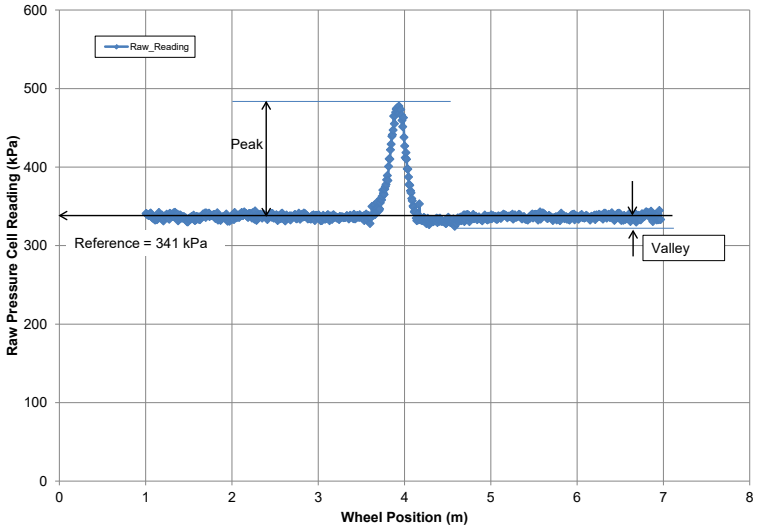

Figure 326. Illustration. Example pressure cell reading and definitions of summary quantities.

Multi-Depth Deflectometers

A multi-depth deflectometer is essentially a stack of linear variable differential transformer (LVDT) modules fixed at different depths in a single borehole. LVDT modules have nonspring-loaded core slugs linked into one long stick that is fixed at the bottom of a 10 ft. (3.3 m) borehole. The borehole was 1.5 in (38 mm) in diameter. A model MDD with five modules is shown in Figure 327. The LVDT modules were fixed to the pavement, which allowed permanent vertical deformations at various depths to be recorded in addition to measurement of the elastic deformation caused by the passage of HVS wheels.

An example set of MDD data are presented in Figure 328, which shows the variation of the elastic vertical deflections measured at different depths versus wheel position as the wheel travels from one end of the test section to the other. The elastic vertical deflection is the difference between total vertical deflection and the reference value, defined as the reading when the wheel is at the far end of the test section. The peak values are the maximum elastic vertical deflection for each individual module.

Figure 327. Photo. A model multi-depth deflectometer (MDD), showing five modules.

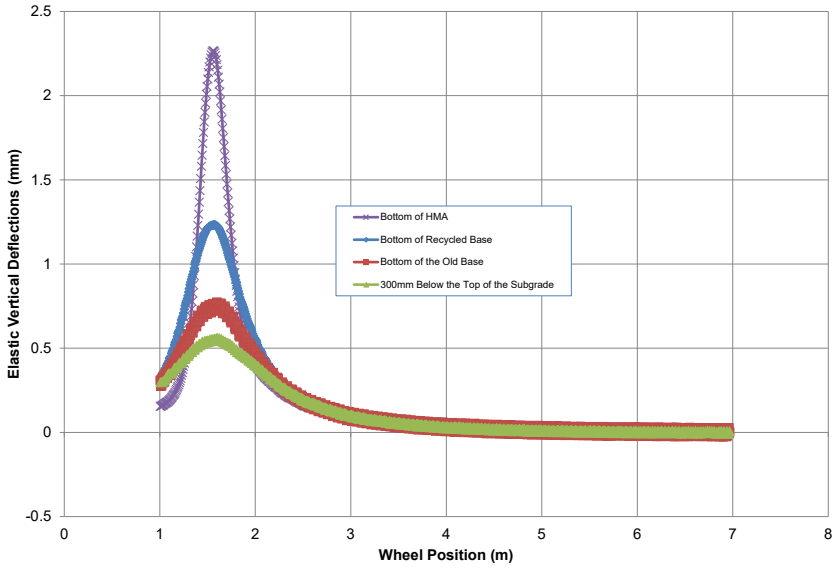

Note: 25.4 mm = 1 in; 1 m = 3.3 ft

Figure 328. Graph. Example elastic vertical deflection measured with MDD.

Material Sampling

Thirty-two cores were sampled from Section 670HC and 16 cores were sampled from Section 671HC (Figure 329). All cores were 6 in (150 mm) in diameter and were sampled from untrafficked areas approximately 20 in (0.5 m) away from the HVS test sections after testing was completed.

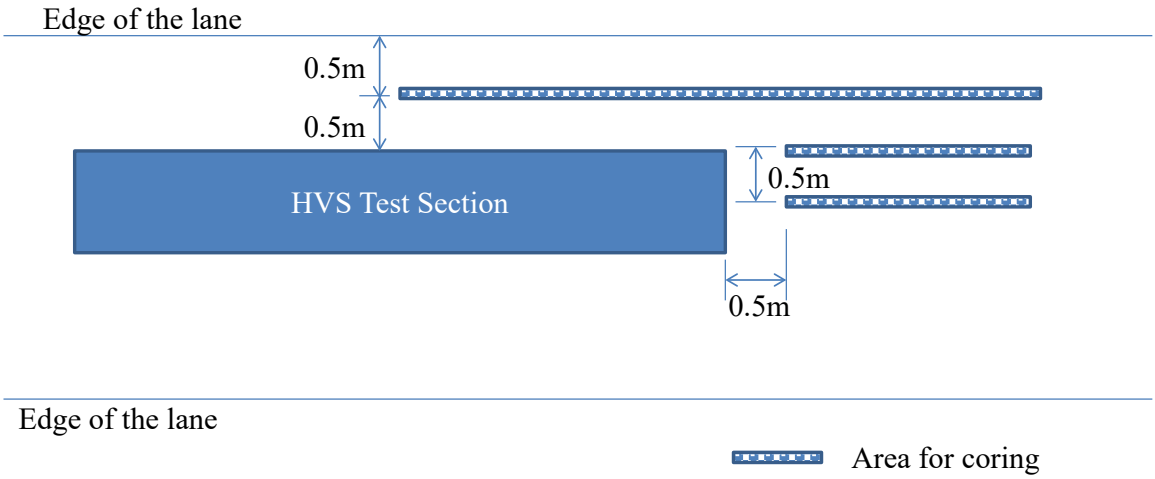

Note: 1 m = 3.3 ft

Figure 329. Illustration. Schematic of coring layout (overhead view).

As-Built Layer Thicknesses

As-built layer thicknesses were determined using different methods depending on the layer type. AC layer thicknesses were determined from cores taken near the test section, as described above, and from the cores taken while drilling the MDD boreholes. The as-built AC layer thicknesses for the two test sections are listed in Table 72.

Table 72. As-Built AC Layer Thicknesses

Layer	Method	670HC Average (in)	670HC Std. Dev.[1] (in)	671HC Average (in)	671HC Std. Dev. (in)
Bottom Lift	MDD hole	2.4		2.0	
Bottom Lift	6 in cores	2.6	0.2	3.0	0.1
Top Lift	MDD hole	N/A		2.6	
Top Lift	6 in cores	N/A		2.5	0.1

[1] Std. dev. = standard deviation

The recycled base and existing aggregate base thicknesses were determined from DCP measurements conducted for the nearby UCPRC test sections. For each DCP test, an 8 in (200 mm) diameter core was first drilled through the AC layer. DCP testing was then conducted inside the core hole. The penetration curves for the two cells where Sections 670HC and 671HC were located are shown in Figure 330 and Figure 331, respectively. Layer interfaces are indicated by the changes in penetration rate.

According to Figure 330, there was only one clear change in penetration rate at approximately 20 in (500 mm) below the bottom of the AC layer on Section 670HC. This indicates that the recycled base and old aggregate base layer had similar mechanical properties. Their combined as-built thicknesses were comparable to the 22.5 in (570 mm) design thickness. According to Figure 331, there were two clear changes in penetration rate for Section 671HC. The first was located approximately 10.2 in (260 mm) below the bottom of the AC layer, indicating the interface between the recycled base and the old aggregate base. The second was located between 20.5 in (520 mm) and 21.8 in (555 mm) below the bottom of the AC layer, corresponding to the interface between the old aggregate base and the subgrade.

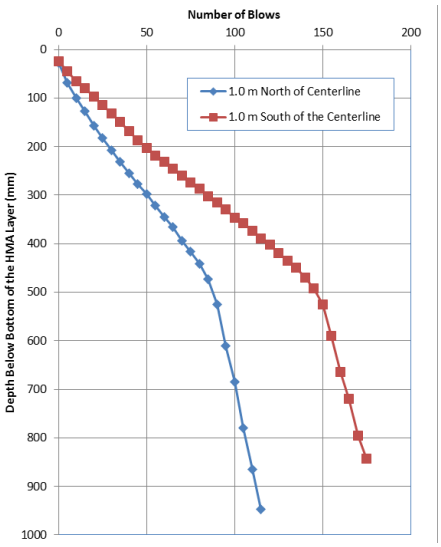

Note: 1 m = 3.3 ft

Figure 330. Graph. Unbound layer DCP penetration curves for Section 670HC.

Data Collection

The main objective of the APT study was to collect pavement response data during trafficking with different tires (NG-WBT versus DTA) under various loading conditions, including varied tire pressures, pavement temperatures, wheel loads, and lateral offsets. The APT was conducted using an MK VI HVS manufactured by *Dynatest Consulting Inc*. Photographs of the HVS are shown in Figure 332. The HVS is a linear loading machine with the following key features:

- Effective distance of travel of either 19.7 ft. (6 m) (as in this study) or 42.7 ft. (13 m) with an extension
- 26,000 bi-directional passes per day
- Half single axle load application
- Loading range of 5.6 to 22.5 kips (25 to 100 kN) using dual truck tires, and up to 45 kips (200 kN) using an aircraft tire
- Maximum speed of up to 12.4 mph (20 km/h) with a 42.7 ft. (13 m) travel distance
- Maximum of 2.9 ft. (0.9 m) transverse travel in increments of 1.0 to 3.0 in (25 to 75 mm)

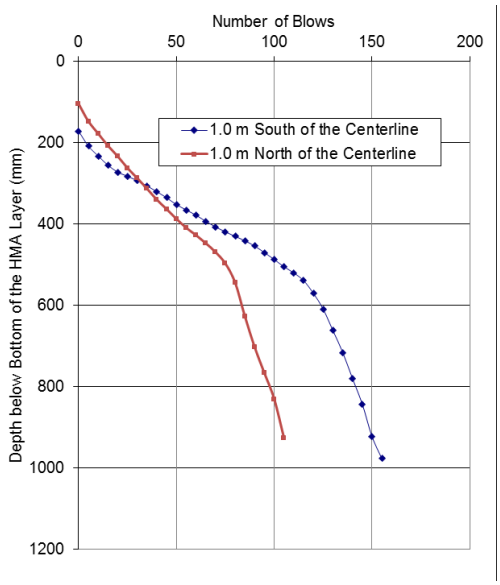

Note: 1 m = 3.3 ft

Figure 331. Graph. Unbound layer DCP penetration curves for Section 671HC.

Figure 332. Photo. Heavy Vehicle Simulator (HVS) – outside view.

Figure 333. Photo. Heavy Vehicle Simulator (HVS) – inside view.

Loading Program

The loading program for each HVS test section was designed to allow measurements of pavement responses under the different tires with the following loading combinations:

- A full factorial of pavement temperature, tire pressure, and half-axle load with the following levels:
  - Pavement temperatures: 68, 95, and 122°F
  - Tire pressures: 80, 100, 110, 125 psi for both DTA and the WBT, and 60/110, 80/110 psi for dual DTA with the two tires set to different tire pressures
  - Half-axle loads: 6, 8, 10, 14, 18 kips
- Distance between CLTA and centerline of the test section fixed at 0
- A smaller full factorial of tire pressure and lateral position of the centerline of the tire or tire assembly (CLTA) with the following levels:
  - Pavement temperature fixed at 122°F
  - Tire pressures: 80 and 125 psi
  - Half-axle load fixed at 10 kips
  - Distance between CLTA and centerline of the test section: 0, 7, and 12 in.

Once the above loading combinations were completed, a selected subset of loading combinations was repeated to evaluate changes in pavement condition caused by the testing. The selected subset included a full factorial of the following combinations:

- Pavement temperatures: 68, 95, and 122°F
- Tire pressures: 100 and 125 psi
- Half-axle load fixed at 10 kips

Unless specified otherwise, the CLTA was always aligned with the centerline of the HVS test section. The detailed planned testing sequence is shown in Table 73. Also, it should be noted that the actual testing sequence had some slight variations from the planned sequence due to operational constraints. (Table 74 lists the conversion values between the English and SI units for the quantities used in the loading program.) The actual loading sequence can be found in the "SectionHistory" table of the *MS Access* database delivered with this technical memorandum.

One hundred load repetitions were applied for each loading combination, and loading was applied in a channelized mode (i.e., no wander) in both directions.

Table 73. Planned HVS Loading Program

Sequence	Tire Type	Temperature (°F)	Tire Pressures (psi)	Half-Axle Load (kips)	Offset (inches)	Number of Cases
1	DTA	68	80, 100, 110, 125, 60/110, 80/110	6, 8, 10, 14	0	24
2	DTA	95	80, 100, 110, 125, 60/110, 80/110	6, 8, 10, 14	0	24
3	DTA	122	80, 100, 110, 125, 60/110, 80/110	6, 8, 10, 14	0	24
4	DTA	122	80, 125	10	0, 7, 12	6
5	NG-WBT	68	80, 100, 110, 125	6, 8, 10, 14	0	16
6	NG-WBT	95	80, 100, 110, 125	6, 8, 10, 14	0	16
7	NG-WBT	122	80, 100, 110, 125	6, 8, 10, 14	0	16
8	NG-WBT	122	80, 125	10	0, 7, 12	6
9	DTA	68	80, 100, 110, 125, 60/110, 80/110	18	0	6
10	DTA	95	80, 100, 110, 125, 60/110, 80/110	18	0	6
11	DTA	122	80, 100, 110, 125, 60/110, 80/110	18	0	6
12	NG-WBT	68	80, 100, 110, 125	18	0	4
13	NG-WBT	95	80, 100, 110, 125	18	0	4
14	NG-WBT	122	80, 100, 110, 125	18	0	4
15	NG-WBT	122	100, 125	10	0	2
16	NG-WBT	95	100, 125	10	0	2
17	NG-WBT	68	100, 125	10	0	2
18	DTA	68	100, 125	10	0	2
19	DTA	95	100, 125	10	0	2
20	DTA	122	100, 125	10	0	2
					Total	**174**

Table 74. Conversion Table for the Quantities Used in the Loading Combinations

Quantity	English Value	English Unit	SI Value	SI Unit
Tire Pressure	60	psi	419	kPa
Tire Pressure	80	psi	559	kPa
Tire Pressure	100	psi	698	kPa
Tire Pressure	110	psi	768	kPa
Tire Pressure	125	psi	873	kPa
Temperature	68	°F	20	°C
Temperature	95	°F	35	°C
Temperature	122	°F	50	°C
Distance	0	inch	0	mm
Distance	7	inch	178	mm
Distance	12	inch	305	mm
Load	6	kips	27	kN
Load	8	kips	36	kN
Load	10	kips	44	kN
Load	14	kips	62	kN
Load	18	kips	80	kN

Tire Assemblies

The model and overall tread width of the tires used in the tests are listed in Table 75. The tires were supplied by the tire manufacturer. A schematic of the geometry for the two tire assemblies is shown in Figure 334 and the tire footprints are illustrated in Figure 335 and Figure 336 for 9 kip half-axle load and 100 psi tire inflation pressure.

Table 75. Specifications for Tires Used in the Testing

Assembly Type	Model	Tread Width (in)
DTA	275/80 R22.5	9.45
NG-WBT	445/50R225 Radial	15.3

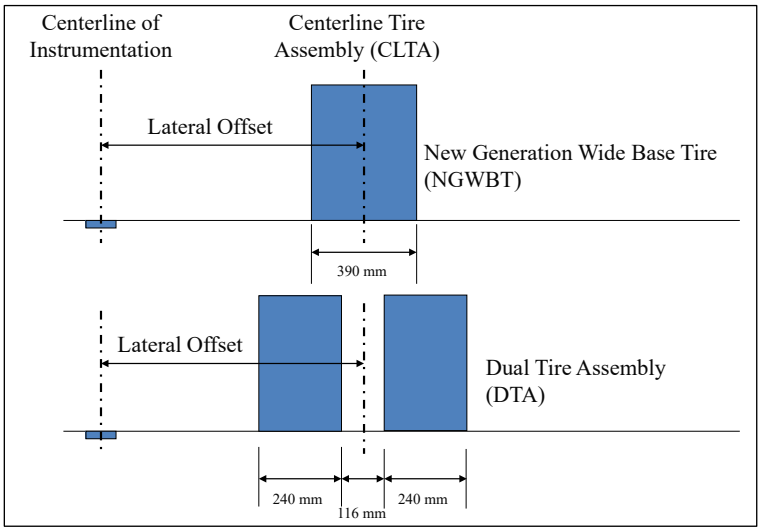

Figure 334. Illustration. Schematics of the tire assembly geometries.

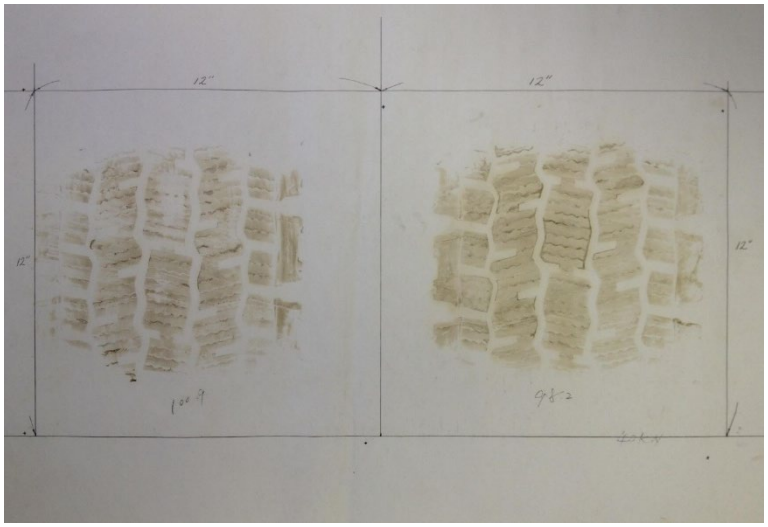

Figure 335. Illustration. DTA footprint.

Data Collection Schedule

Data collected during the testing can be grouped into two types: static data and dynamic data. Static data are obtained from measurements that do not vary with wheel position, such as pavement temperature and surface profile. Dynamic data are obtained from measurements that vary with wheel position and include strain, pressure, and elastic deflection. Static data collection was triggered by schedule, while dynamic data collection was triggered by wheel movement. Dynamic data are essentially influence lines that describe how different pavement responses change with wheel position.

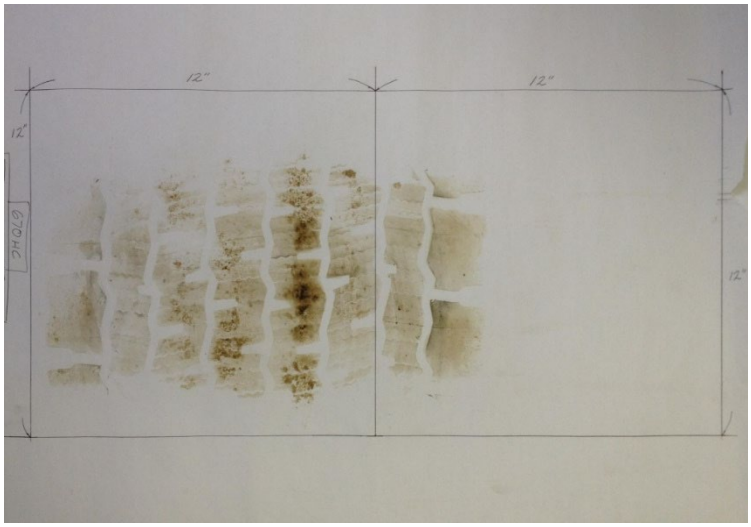

Figure 336. Illustration. New-generation wide-base tire footprint.

Pavement temperatures were recorded every five minutes and whenever dynamic data were collected. Surface profiles were measured at the beginning and end of testing and when the tire assembly was changed.

Dynamic data measured by the different sensors was collected using a shared sampling clock. All sensors were read simultaneously every time the wheel moved 0.3 in (7.4 mm). The wheel speeds were also recorded. Dynamic data were collected for every HVS load repetition.

Deflection Measurements

Deflection measurements were taken with a Dynatest falling weight deflectometer (FWD) along the centerline of each test section before and after testing. The drop locations are illustrated in Figure 337 and cover both trafficked and untrafficked areas. Two FWD test sessions were conducted, the first in the early morning when the pavement was still cold and the second in midafternoon when the pavement was warmer.

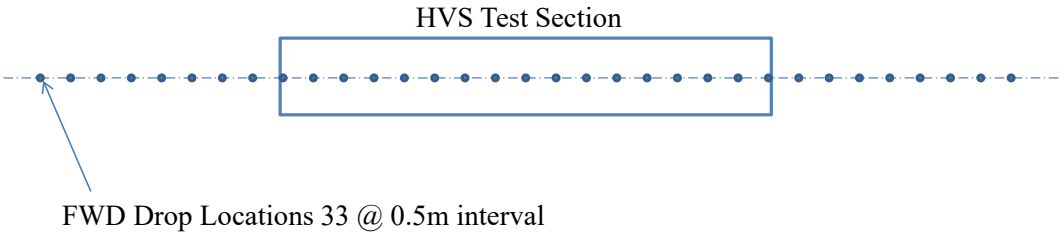

Figure 337. Illustration. Schematic of FWD drop locations.

APPENDIX G. DETAILED DATA SAMPLE, FILTERING, AND MAX/MIN SELECTION

Some of the filtered and extracted data plots are provided in the figures below.

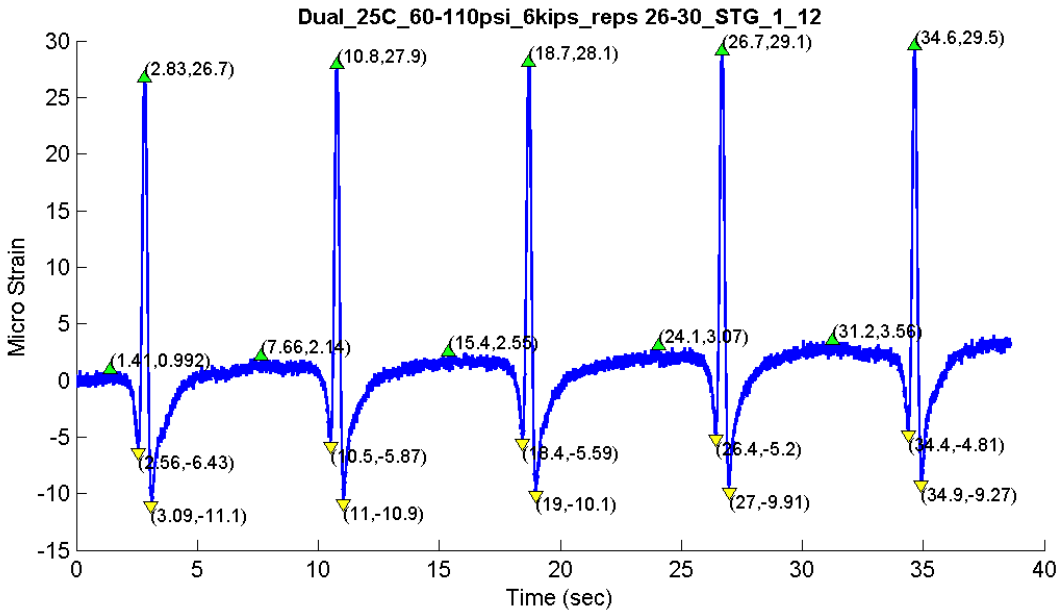

Figure 338. Graph. Florida, test pit section, surface transverse strain gauge 1_12 for dual-tire 25C, 60-110 psi tire pressure, 6 kips load.

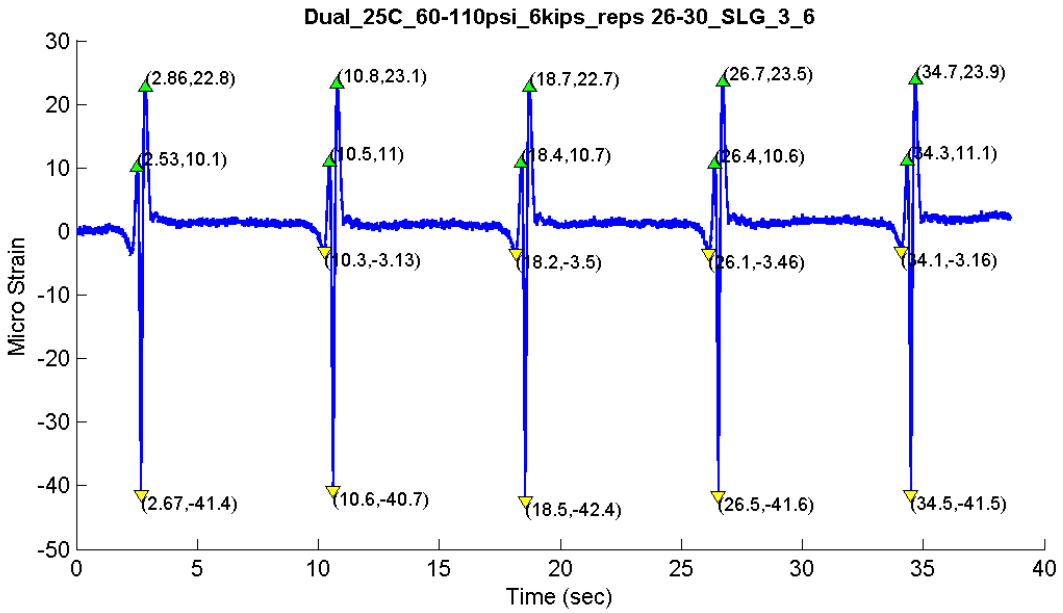

Figure 339. Graph. Florida, test pit section, surface longitudinal strain Gauge 3_6 for dual-tire 77 °F, 60-110 psi tire inflation pressure, 6 kips load.

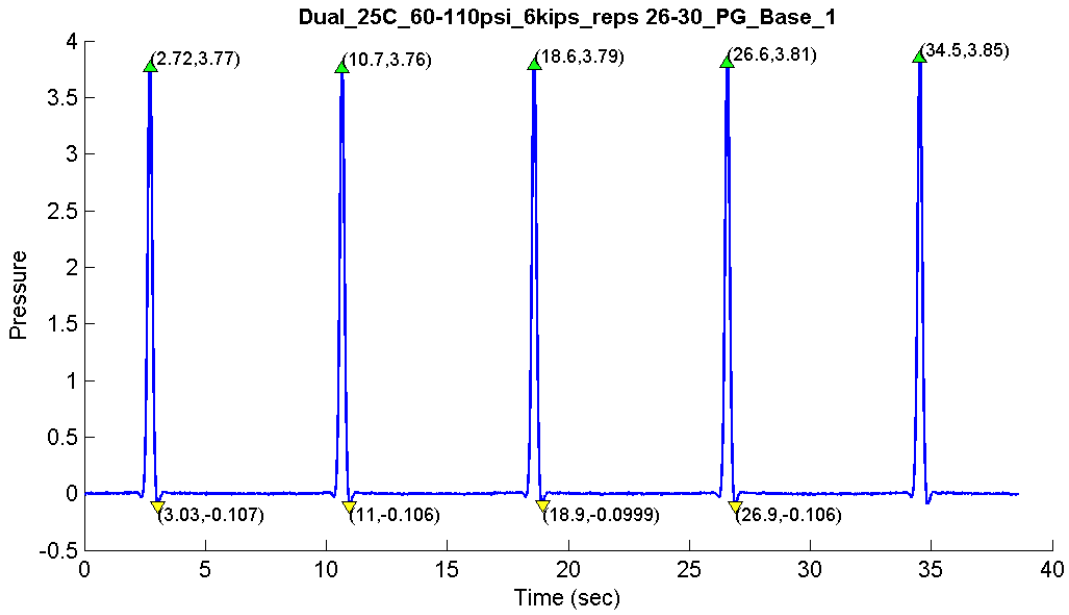

Figure 340. Graph. Florida, test pit section, pressure gauge at base sensor No. 1 for dual-tire 77 °F, 60-110 psi tire inflation pressure, 6 kips load.

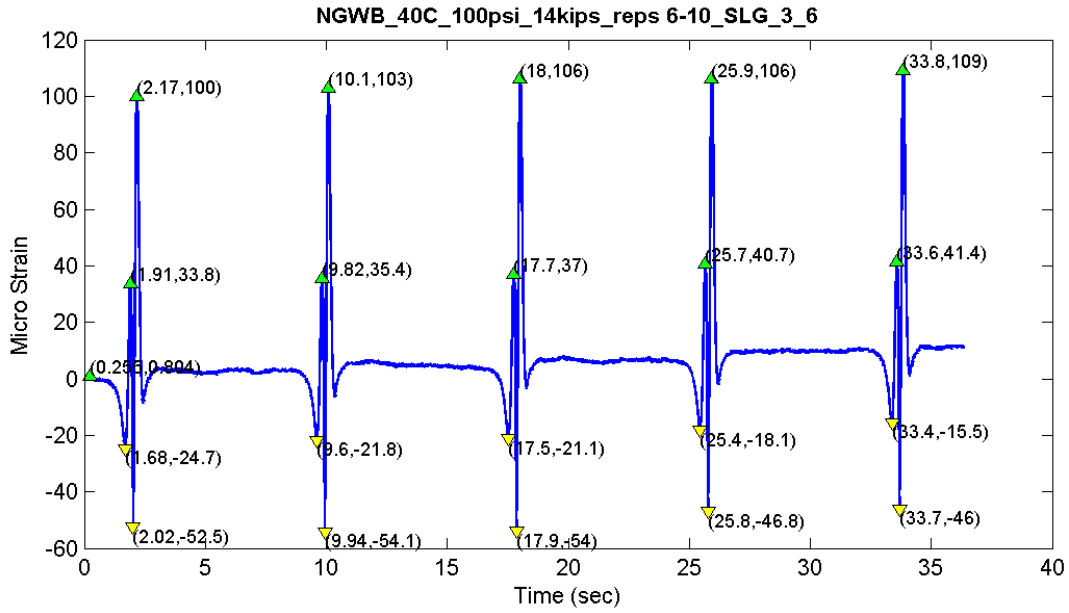

Figure 341. Graph. Florida, test pit section, surface longitudinal strain gauge sensor 3_6 for wide-base tire 104 °F, 100 Psi tire pressure, 14 kips load.

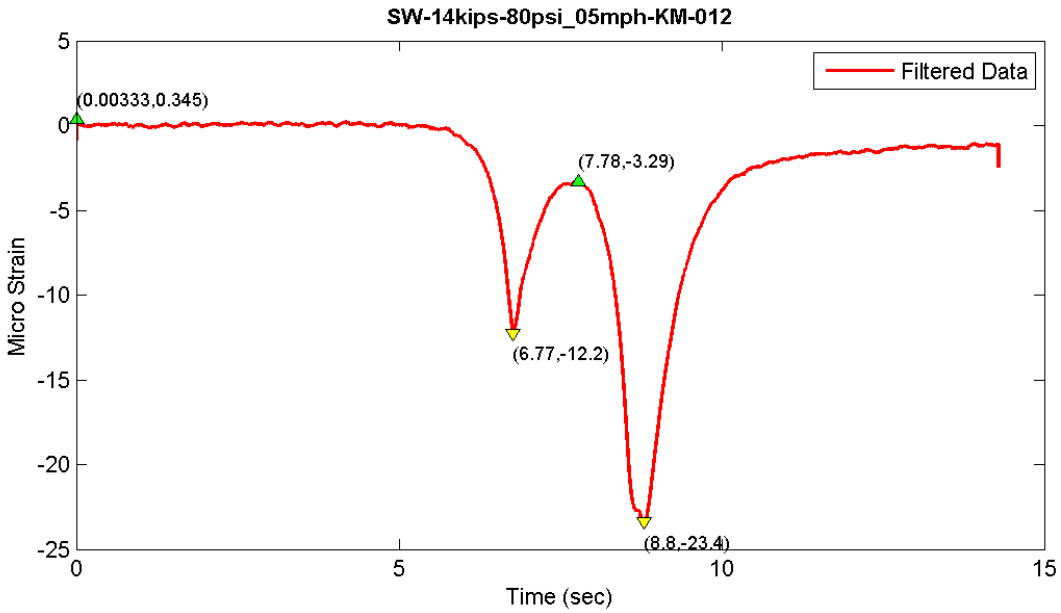

Figure 342. Graph. Ohio, driving section, strain gauge type KM sensor 12 for single wide-base tire run No. 26.

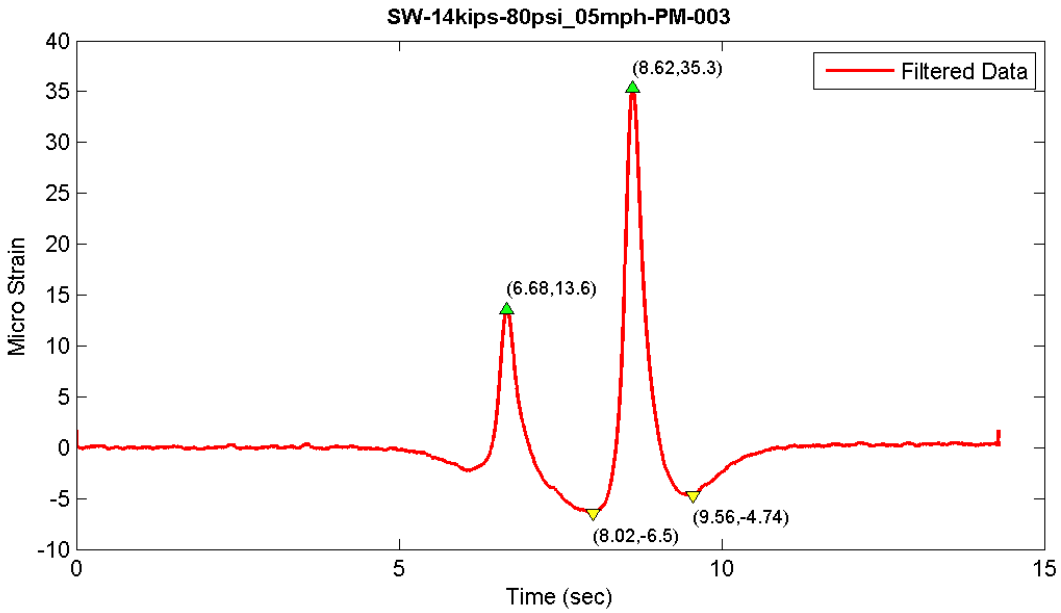

Figure 343. Graph. Ohio, driving section, strain gauge type Pm sensor 003 for single wide-base tire run No. 26.

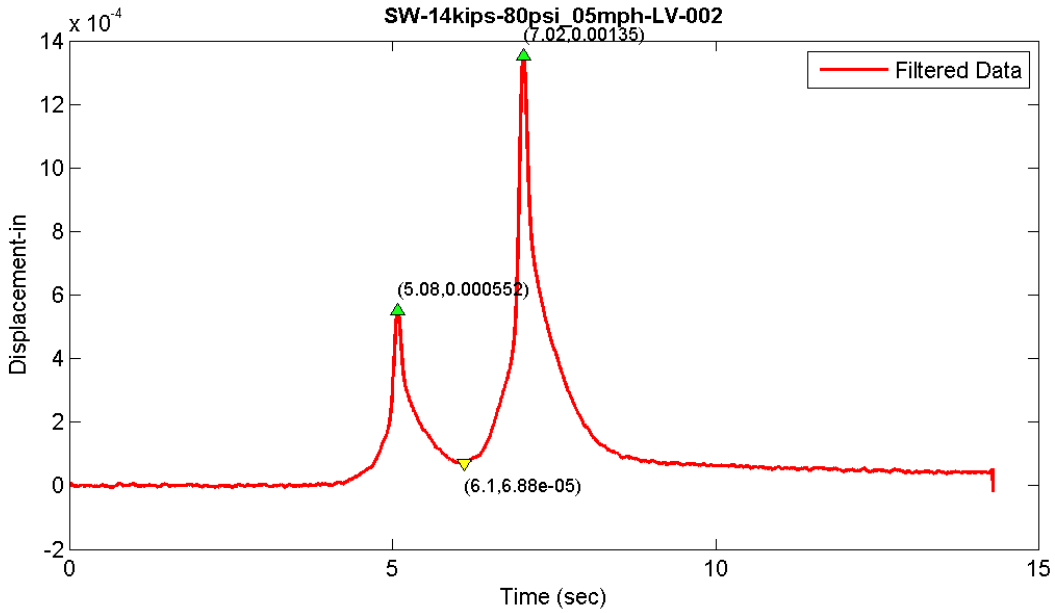

Figure 344. Graph. Ohio, driving section, linear displacement sensor 002 for single wide-base tire run No. 26.

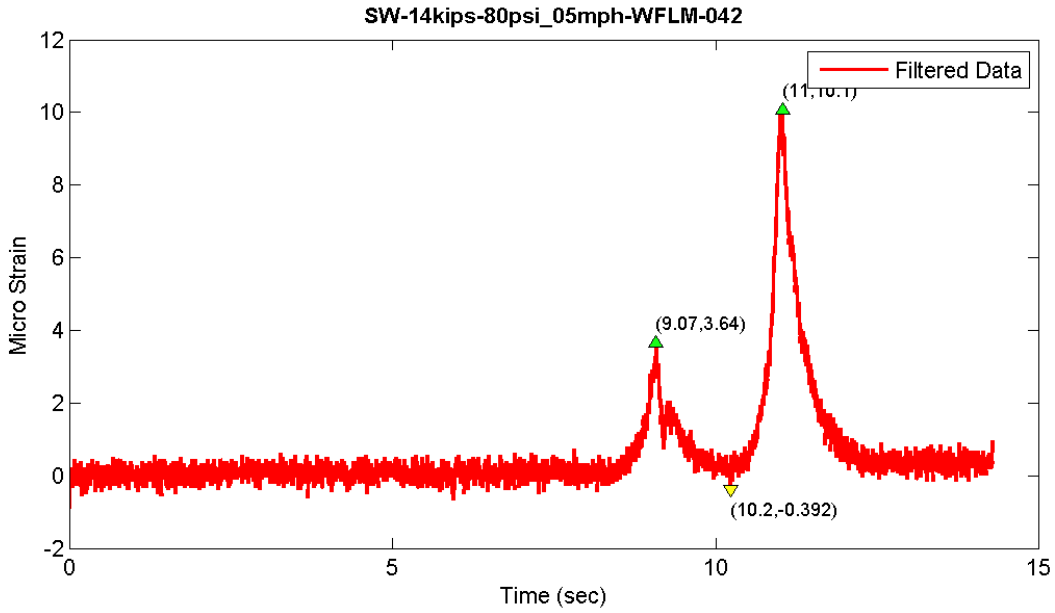

Figure 345. Graph. Ohio, driving section, shear strain gauge (Rosette) WFLM sensor 042 for single wide-base tire run No. 26.

Sample Matalb Code used for data filtering and extraction process for Florida section is provided below:

```
%% Data Management: Filtering, Peaks/Valleys Extraction Code - Florida
%
% Data Upload
% Select the folder root and then wait while data are uploaded
% automatically. You can find the data files on workspace starting with a
% character 'v'.
% Depending on the number of files this may take several minutes!
clc
clear
mfoldpath = uigetdir('','Please select tes folder containing data (Test',...
    'Pit or Test Track).'); mfoldinfo = dir(mfoldpath);
maxresp.EG=[]; maxresp.SP=[]; avgresp.EG=[]; avgresp.SP=[]; pulse=[];
maxresp.allrep_SP= []; maxresp.allrep_EG= []; avgresp.allrep_SP = [];
avgresp.allrep_EG=[];maxresp.EG=[];maxresp.SP=[];avgresp.SP=[];avgresp.EG
=[];
%% Run the code over sensor readings (files)
for nn = 3:size(mfoldinfo,1)
    try  % catches any error
    %%
    foldpath = [mfoldpath,'\',mfoldinfo(nn).name];
    cd(foldpath);foldinfo= dir([foldpath,'\*.txt']);
    %   Use for deleting current folders
            % rmdir('Filtered','s'); rmdir('plots','s');
% Data Filtering-----------------------------------------
    % Add folder root where functions are located
 addpath(['C:\Users\Mojtaba\Documents\PhD Project\' ...
    'Wide-Base Project\WB Data\New data\Matlab Codes']);
 addpath(['C:\Users\Mojtaba\Documents\PhD Project\Wide-Base Project\' ...
     'WB Data\New data\Florida Data\Mojatab files']);
 % Build an new Folder for saving filtered data
 try
     rmdir('Filtered','s'); delete('peakdet.m'); % rmdir('Plots','s')
     delete('roundsd.m'); delete('Database.mat')
 end
 mkdir([foldpath,'\Filtered\']);
 froot=regexp(foldpath,'\','split');
 froot(end)
 v = genvarname(['dbase_',froot{end-1},'_',froot{end}]);
%% For each test case
 for i=1:size(foldinfo,1);
     % Build a new folder for saving plots - delete rows with NAN
     raw = importdata(foldinfo(i).name,',',6);
     raw.data = raw.data(~any(isnan(raw.data),2),:);
     fn = strrep(strtok(foldinfo(i).name,'.txt'),'-','_');
     dbase.(fn).filt=[]; dbase.(fn).filt(:,1:2)= raw.data(:,1:2);
     % mkdir([foldpath,'\Plots\',strtok(foldinfo(i).name,'.txt')]);
     % Use when want to delete a specific folder
     %   rmdir([foldpath,'\Plots\',strtok(foldinfo(i).name,'.txt')],'s');
 %% For Each sensor reading
 for j=3:size(raw.data,2)-5
     % Define Low-pass filter parameters for each sensor (trial and error)
     if (size(foldinfo,1)>7 && i<3)
         row = 3; Fp = 0.1; Fs=0.6;
```

```
    elseif (size(foldinfo,1)<7 && i>1)
        row = 2; Fp = 0.001;Fs=0.92;
    else
        row = 2; Fp = 0.1; Fs=0.92;
    end

 raw.smth(:,j) = low_filt(raw.data(:,j),Fp,Fs,size(raw.data(:,j),1));
    % Specific sensors need different treatments
    if (size(foldinfo,1)>7 && i<3)
        dev = avg_out(raw.smth(10:40,j),1,0);
    elseif (size(foldinfo,1)<7 && i>1)
        dev = avg_out(raw.smth(40:100,j),1,0);
    else
        dev = avg_out(raw.smth(40:100,j),1,0);
    end
     dbase.(fn).filt(:,j)= raw.smth(:,j)-dev;
% Find Initial Local Extrema
      maxf = max(dbase.(fn).filt,[],1); minf = min(dbase.(fn).filt,[],1);
      rangef =(maxf(1,j)-minf(1,j)); STD = std(dbase.(fn).filt(:,j));
      delta =abs(1.5*(1.0465 - 0.8066*STD + 0.1782*rangef)) ;
      if delta<=0; delta=0.1; end;
      [maxtab, mintab] = peakdet(dbase.(fn).filt(:,j),delta, dbase.(fn). ...
          filt(:,2));
% Adjust Local extrema
     cntr = 1;
  if size(foldinfo,1)< 6
    while (i==1 && (size(maxtab,1) < 20 || size (mintab,1) < 20)) || ...
            (i~=1 && (size(maxtab,1) < 5 || size (mintab,1) < 5))
          delta = delta/1.15;
          [maxtab, mintab] = peakdet(dbase.(fn).filt(:,j),delta, ...
              dbase.(fn).filt(:,2));
          cntr = cntr + 1;
          if cntr == 10; cntr = 1; break, end
    end
    while (i==1 && (size(maxtab,1) > 20 || size (mintab,1) > 20)) || ...
            (i~=1 && (size(maxtab,1) > 5 || size (mintab,1) > 5))
          delta = delta*1.125 ;
          [maxtab, mintab] = peakdet(dbase.(fn).filt(:,j),delta, dbase. ...
              (fn).filt(:,2));
          cntr = cntr+1;
          if cntr == 10; cntr = 1; break, end
    end
  end
   if size(foldinfo,1) > 6
    while (i==1 || i==2 && (size(maxtab,1) < 50 || size (mintab,1) < ...
            50)) || (i>2 && (size(maxtab,1) < 5 || size (mintab,1) < 5))
          delta = delta/1.1;
          [maxtab, mintab] = peakdet(dbase.(fn).filt(:,j),delta, ...
              dbase.(fn).filt(:,2));
          cntr = cntr + 1;
          if cntr == 20; cntr = 1; break, end
    end
    while (i==1 || i==2 && (size(maxtab,1) > 50 || size (mintab,1) > ...
            50)) || (i>2 && (size(maxtab,1) > 5 || size (mintab,1) > 5))
          delta = delta*1.05 ;
          [maxtab, mintab] = peakdet(dbase.(fn).filt(:,j),delta, ...
              dbase.(fn).filt(:,2));
```

```
            cntr = cntr+1;
            if cntr == 20; cntr = 1; break, end
        end
    end
  % Save rut depth and local extrema and pulse duration
      %%%%%%%%%%%%%%%%%%%%%%%%%%%%%%%%%%%%%%%%%%%%%%%%%%%%%%%%%%%%%%%%%%%%%%%
      % Note: rut depth is the difference before and after wheel
      % pass over the sensor.
      dbase.(fn).Rutting(j) = avg_out(dbase.(fn).filt(end-35:end,j),1,0);
      dbase.(fn).Extrema(j) = struct('max',maxtab,'min',mintab);
      % How many pressure cells exist? %for Test Pit 4, for Test Track 2
      p = 2;
      if (i > 2 || (size(foldinfo,1)<12 && i>1)) && (j > (size(raw.data,2)...
              -5) - p); % for most of runs is 27. Some runs do not have
STG_1_3 is 26
          [puls_dur puls_dur_avg] = pulse_duration(dbase.(fn).filt(:,2),...
              dbase.(fn).filt(:,j),0.01);
          dbase.(fn).Pulse_duration(1:size(puls_dur,1)-1,j-(size...
              (raw.data,2)-5 - p)) = cell2mat(puls_dur(2:end,2));
          dbase.Respsummrary.pulse(i,j-(size(raw.data,2)-5 - p-1))...
              = num2cell(puls_dur_avg);
      end

  %% Plot Original, filtered and local extrema points
      %%%%%%%%%%%%%%%%%%%%%%%%%%%%%%%%%%%%%%%%%%%%%%%%%%%%%%%%%%%%%%%%%%%%%%%
      p = figure('visible','on');
       dev2 = avg_out(raw.data(1:35,j),1,0);
       plot(raw.data(:,2),raw.data(:,j)-dev2,'blue');
       hold on
       x = dbase.(fn).filt(:,2); y = dbase.(fn).filt(:,j);
       f = plot(x,y);set(f,'Color','red','LineWidth',1.5);xlabel('Time
(sec)');
        if j >= 27;
             ylabel('Pressure (kpa)');
        else
             ylabel('Micro Strain');
        end
       title(strcat(strtok(foldinfo(i).name,'.txt'),'_',
raw.textdata(6,j)),...
              'interpreter','none','FontWeight','bold');
       legend('Raw data (trnsfrd)','Filtered Data');
       whitebg = ([0.8 0.8 0.8]); set(gcf,'PaperPosition',[0 0 8 4])
       % Plot local extrema on the figure
     try
         plot(mintab(:,1), mintab(:,2),'kv','MarkerFaceColor',[1 1 .1]);
       for ii=1:size(mintab(:,1));
         text(mintab(ii,1),mintab(ii,2)-0.015*rangef,['(',num2str(roundsd ...
             (mintab(ii,1),3)), ',',...
         num2str(roundsd(mintab(ii,2),3)),')'],'FontSize',8) ;
       end
       for ii=1:size(maxtab(:,1));
         plot(maxtab(ii,1), maxtab(ii,2), 'k^','MarkerFaceColor',[.1 1 .1]);
         text(maxtab(ii,1),maxtab(ii,2)+0.015*rangef,['(',num2str(...
             roundsd(maxtab(ii,1),3)),',',...
          num2str(roundsd(maxtab(ii,2),3)),')'],'FontSize',8) ;
       end
     end
```

```
    hold off
   %% % Save plot
    impath=[foldpath,'\Plots\',strtok(foldinfo(i).name,'.txt')];
    imname=[num2str(j),'-',char(strcat(raw.textdata(6,j)))];
    % Choose the plot format one the  png|jpg|bmp|gif
    saveas(p, fullfile(impath, imname), 'png');
clear memory
close(p)
%}
 %% Calculate max response and pulse duration
        config = regexp(strtok(foldinfo(i).name,'.txt'),'_','split');
         if ~isempty(dbase.(fn).Extrema(j).max) && ~isempty(dbase.(fn). ...
                 Extrema(j).min)
           if i == 1 || (size(foldinfo,1)>12 && i==2)
           dbase.Respsummrary.maxresp.EG(i+1,j+5) = num2cell(max(max...
               (maxtab(:,2)),abs(min(mintab(:,2)))));
           dbase.Respsummrary.avgresp.EG(i+1,j+5) = num2cell(max...
               (avg_out(maxtab(:,2),1,1),abs(avg_out(mintab(:,2),1,-1))));
           dbase.Respsummrary.maxresp.EG(i+1,1:7) = [froot{end-1} config];
           dbase.Respsummrary.avgresp.EG(i+1,1:7) = [froot{end-1} config];
           else
           dbase.Respsummrary.maxresp.SP(i,j+5) = num2cell(max...
               (max(maxtab(:,2)),abs(min(mintab(:,2)))));
           dbase.Respsummrary.avgresp.SP(i,j+5) = num2cell(max...
               (avg_out(maxtab(:,2),1,1),abs(avg_out(mintab(:,2),1,-1))));
           dbase.Respsummrary.maxresp.SP(i,1:7) = [froot{end-1} config];
           dbase.Respsummrary.avgresp.SP(i,1:7) = [froot{end-1} config];
           end

         end
 end
 %% Add test config for each row and save filtered data in Excel
 if i == 1 || (size(foldinfo,1)>12 && i==2)
     dbase.Respsummrary.maxresp.EG(i+1,1:7) = [froot{end-1} config];
     dbase.Respsummrary.avgresp.EG(i+1,1:7) =  [froot{end-1} config];
     headerEG = [{'Section','Tire','Temp(C)','Pressure(psi)','Load(kip)'...
         ,'SensorType','Rep'}, raw.textdata(6,3:end)];
 else
     dbase.Respsummrary.pulse(i,1) = config(end);
     dbase.Respsummrary.maxresp.SP(i,1:7) = [froot{end-1} config];
     dbase.Respsummrary.avgresp.SP(i,1:7) =  [froot{end-1} config];
     headerSP = [{'Section','Tire','Temp(C)','Pressure(psi)','Load(kip)'...
         ,'SensorType','Rep'}, raw.textdata(6,3:end)];
 end
impath=[foldpath,'\Filtered\'];
dbase.(fn).filt = [raw.textdata(6,:);num2cell(dbase.(fn).filt)];
xlswrite([impath,strtok(foldinfo(i).name,'.txt')],dbase.(fn).filt);
 end
 %%
 % For Test Pit 'PG_Asph_1','PG_Asph_2','PG_Base_1','PG_Base_2'
 % For Test Track 'PG_Asph_1','PG_Asph_2'
dbase.Respsummrary.pulse(1,:) = {'repetition','PG_Asph_1','PG_Asph_2'};
dbase.Respsummrary.maxresp.EG(1,:) = headerEG; dbase.Respsummrary. ...
    maxresp.SP(1,:) = headerSP;
dbase.Respsummrary.avgresp.EG(1,:) = headerEG; dbase.Respsummrary. ...
    avgresp.SP(1,:) = headerSP;
% Replace Empty cells with zero (not needed for avg)
```

```
dbase.Respsummrary.maxresp.SP(cellfun(@isempty,dbase.Respsummrary. ...
    maxresp.SP)) = {0};
dbase.Respsummrary.maxresp.EG(cellfun(@isempty,dbase.Respsummrary. ...
    maxresp.EG)) = {0};
if nn == 3
    pulse = [headerSP(1:6),'PG_Asph_1','PG_Asph_2'];
    maxresp.allrep_EG = [headerEG(1:6),headerEG(8:end)];
    avgresp.allrep_EG = [headerEG(1:6),headerEG(8:end)];
    maxresp.allrep_SP = [headerSP(1:6),headerSP(8:end)];
    avgresp.allrep_SP = [headerSP(1:6),headerSP(8:end)];
    maxresp.SP = headerSP;   avgresp.SP = headerSP;
    maxresp.EG = headerEG;   avgresp.EG = headerEG;
end
for j = 2:size(dbase.Respsummrary.pulse,2)  % for Test Pit 2:5 for Test Track
2:3
    pulse_avg(1,j+5) = num2cell(avg_out(cell2mat(dbase.Respsummrary. ...
        pulse(2:end,j)),1,0));
end
pulse_avg(1,1:6) = dbase.Respsummrary.maxresp.SP(3,1:6);
max_allrep_SP(1,7:size(headerSP,2)-1) = num2cell(max(cell2mat(dbase. ...
    Respsummrary.maxresp.SP(2:end,8:end)),[],1));
max_allrep_SP(1,1:6) = dbase.Respsummrary.maxresp.SP(3,1:6);
max_allrep_EG(1,7:size(headerEG,2)-1) = num2cell(max(cell2mat(dbase. ...
    Respsummrary.maxresp.EG(2:end,8:end)),[],1));
max_allrep_EG(1,1:6) = dbase.Respsummrary.maxresp.EG(row,1:6);
for j=8:size(dbase.Respsummrary.avgresp.SP,2);
    avg_allrep_SP(1,j-1) = num2cell(avg_out(cell2mat(dbase.Respsummrary. ...
        avgresp.SP(2:end,j)),1,0));
end
for j=8:size(dbase.Respsummrary.avgresp.EG,2);
    avg_allrep_EG(1,j-1) = num2cell(avg_out(cell2mat(dbase.Respsummrary. ...
        avgresp.EG(2:end,j)),1,0));
end
avg_allrep_SP(1,1:6) = dbase.Respsummrary.avgresp.SP(3,1:6);
avg_allrep_EG(1,1:6) = dbase.Respsummrary.avgresp.EG(row,1:6);

pulse = vertcat(pulse,pulse_avg(1,:));
maxresp.allrep_SP = vertcat(maxresp.allrep_SP,max_allrep_SP(1,:));
avgresp.allrep_SP = vertcat(avgresp.allrep_SP,avg_allrep_SP(1,:));
maxresp.allrep_EG = vertcat(maxresp.allrep_EG,max_allrep_EG(1,:));
avgresp.allrep_EG = vertcat(avgresp.allrep_EG,avg_allrep_EG(1,:));
maxresp.SP = vertcat(maxresp.SP,dbase.Respsummrary.maxresp.SP(2:end,:));
avgresp.SP = vertcat(avgresp.SP,dbase.Respsummrary.avgresp.SP(2:end,:));
maxresp.EG = vertcat(maxresp.EG,dbase.Respsummrary.maxresp.EG(2:end,:));
avgresp.EG = vertcat(avgresp.EG,dbase.Respsummrary.avgresp.EG(2:end,:));
% Save database
save('Matlab_database', 'dbase')
%%%%%%%%%%%%%%%%%%%%%%%%%%%%%%%%%
clear dbase froot maxf minf maxx minn x y
nn
end
end
%% Save final responses for the test case
savepath = uigetdir('','Please select a folder to save the results');
answer = inputdlg('Have you ever run the script before and saved the', ...
'results? y/n');
```

```
if strcmp(answer,'n') == 1;

cell2csv([savepath,'\Pulse_Duration(sec).csv'],pulse,',');
cell2csv([savepath,'\MaxResponses_allrep_EG.csv'],maxresp.allrep_EG,',');
cell2csv([savepath,'\MaxResponses_allrep_SP.csv'],maxresp.allrep_SP,',');
cell2csv([savepath,'\AvgResponses_allrep_EG.csv'],avgresp.allrep_EG,',');
cell2csv([savepath,'\AvgResponses_allrep_SP.csv'],avgresp.allrep_SP,',');
cell2csv([savepath,'\MaxResponses_SP.csv'],maxresp.SP,',');
cell2csv([savepath,'\AvgResponses_SP.csv'],avgresp.SP,',');

else

cell2csv([savepath,'\Pulse_Duration(sec).csv'],pulse,',','a');
cell2csv([savepath,'\MaxResponses_allrep_EG.csv'],maxresp.allrep_EG,',','a');
cell2csv([savepath,'\MaxResponses_allrep_SP.csv'],maxresp.allrep_SP,',','a');
cell2csv([savepath,'\AvgResponses_allrep_EG.csv'],avgresp.allrep_EG,',','a');
cell2csv([savepath,'\AvgResponses_allrep_SP.csv'],avgresp.allrep_SP,',','a');
cell2csv([savepath,'\MaxResponses_SP.csv'],maxresp.SP,',','a');
cell2csv([savepath,'\AvgResponses_SP.csv'],avgresp.SP,',','a');

end

%------------------- END ----------------------------------------------------
```

APPENDIX H. DATABASE MANAGEMENT

OVERVIEW OF SECTIONS AND DATABASES

Different instrumented sections were built, and field and APT data were gathered. Databases from previous studies that considered NG-WBT were collected and added to the main database. The main database includes two sets: i) existing sections representing previous research, and ii) new sections, including sections built specifically for this project.

Existing Sections

The existing sections included in the database are:

- Ohio US-23 Hot Weather Test (1999)
- UC-Davis Rutting of Caltrans AC Mixes and Contact Stresses Database (2000)
- Florida Surface Strain Database (2010)
- UIUC Thin Pavement Sections (2000)
- Virginia-Tech Smart Road (2000-2002)

Ohio US-23 Hot Weather Test (1999)

The FHWA conducted controlled loading tests on U.S. Route 23 Test Road in hot weather conditions in Ohio. Testing was performed using four tire types in dual and wide-base configurations. Two pavement sections, 8 in and 4 in in thickness, were instrumented with strain gauge rosettes oriented vertically to measure strain traces induced from the passing wheel loads at three different speeds and tire inflation pressures (Xue & Weaver, 2011).

UC-Davis Rutting of Caltrans AC Mixes and Contact Stresses Database (2000)

Rutting of AC and asphalt-rubber hot-mix under different loads, tires, and temperatures was measured after APT at the Pavement Research Institute of Transportation Studies in Davis, California. The report presented the results of the APT on two overlay systems at elevated temperatures to investigate the effect of rutting in newly overlaid pavements. Two types of dual and two types of WBT were used in this study (Harvey & Popescu, 2000).

Florida Surface Strain Database (2010)

The Florida Department of Transportation investigated pavement damage potential of four tire types, including a conventional dual-tire (11R22.5), a Super Single (425/65R22.5), and two NG-WBT (445/50R22.5 and 455/55R22.5). Six test lanes were constructed considering both open- and dense-graded AC surface (Greene et al., 2010). The data include dense-graded sections. Surface strain and rutting profile were collected.

UIUC Thin Pavement Sections (2000)

To evaluate the effectiveness of geogrid on the performances of low-volume flexible pavements, nine low-volume flexible pavement sections were constructed at the Advanced Transportation Research Laboratory, University of Illinois at Urbana-Champaign. Three tire types, including dual, wide-base 425 and wide-base 455 were used in this study (Al-Qadi, Dessouky, et al., 2008).

Virginia-Tech Smart Road (2000-2002)

The pavement research component of the Smart Road Project focused on the instrumentation, evaluation, and analysis of different flexible pavement sections. The flexible pavement sections of the Smart Road had an approximate total length of 1.4 km. Twelve 100 m-long flexible pavement designs were included in this project. Different instrumentations and material characterization were used. A stand-alone software was designed as part of this research for database management purposes.

New Sections

The new sections specifically built for this project include the following:

- Delaware, Ohio
- UC-Davis
- Florida DOT

A unique test matrix was built and run for all test sections during the project as presented in Chapter 8.

PRE-PROCESSING AND FILTERING

Pre-processing data included removal of noise, smoothing, and extraction of peak points. Noise filtering and smoothing were done using the signal processing function (fdesign.lowpass/highpass) of Matlab. Smoothing is a process where important patterns in data are kept while unimportant data, such as noise, is left out. Depending on the wave form and noise characteristics, a low or high pass filter is used. Usually, a low-pass filter is needed to pass signals with a frequency lower than certain cutoff frequency and attenuate signals with frequencies higher than the cutoff frequency, thus resulting in a smooth wave.

A different Matlab code was written to extract the peak points and valleys. A sample Matlab Code is presented in Appendix G. A point is considered a maximum (or minimum) if it has the maximal (or minimal) value, and is preceded (to the left) by a value lower by a small amount of delta. Figure 343 shows the filtering data extraction flowchart. Damaged or fully noisy data were removed from the analysis. An example of filtered and extracted peak points is presented in Figure 344.

Other examples of the filtering and data extraction process are provided in Appendix G. Extracted information and filtered and raw data were stored in the database as *csv*. Interfaces were designed for each project to facilitate data access.

ONLINE USER INTERFACE

Architecture

A variety of open source technologies were used in the development of the tool:

- Java: open source object-oriented language predominantly used in server side development. Several features, such as portability, security, and ease of use, made it the first choice to write code for this tool
- MySQL: open source database
- Tomcat: application server to host web applications
- Apache: file hosting server
- JQuery: used to make web pages dynamic and interactive
- Spring: application container
- Hibernate: object relational mapping tool that helps avoid writing complex queries and treats everything as objects
- HTML: Standard Hypertext Mark-up Language for writing user interface (UI) code for browsers
- CSS: used for designing and styling the elements of web pages, such as text, tabs, menu items
- High charts: an external library used for plotting charts

A three-tier architecture model was adopted for data access. The UI does not interact directly with the database, but rather relays the command to a middle tier. The middle tier is responsible for performing business logic and directly interacts with the database. The three-tier model is very attractive because the middle tier maintains control over access and the updates that can be made to corporate data. Another advantage is that it simplifies the deployment of applications. Finally, in many cases, the three-tier architecture can provide performance advantages. Middle tier is now written in Java because of portability, speed, and security; the Java platform is fast becoming the standard platform for middle-tier development. Making use of Java's robustness, multithreading, and security features is considered a great advantage.

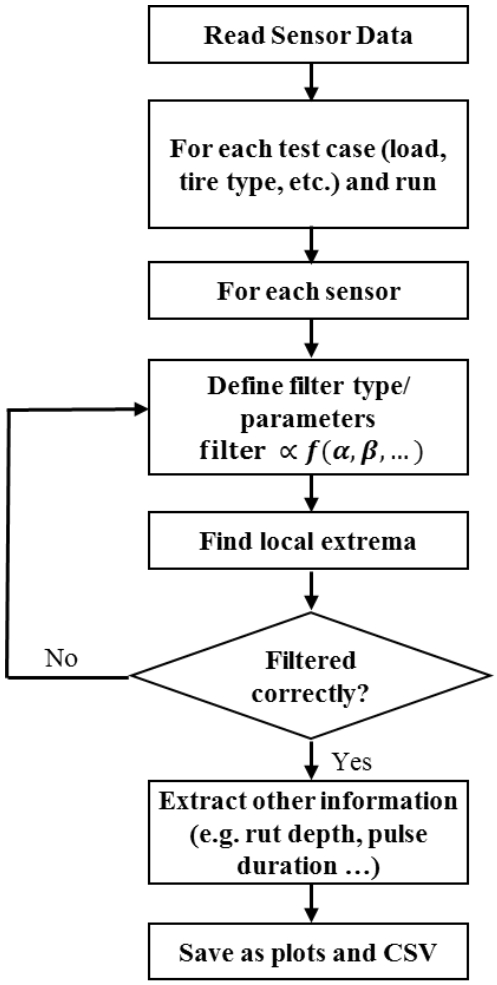

Figure 346. Illustration. Data filtering and local extrema extraction flowchart.

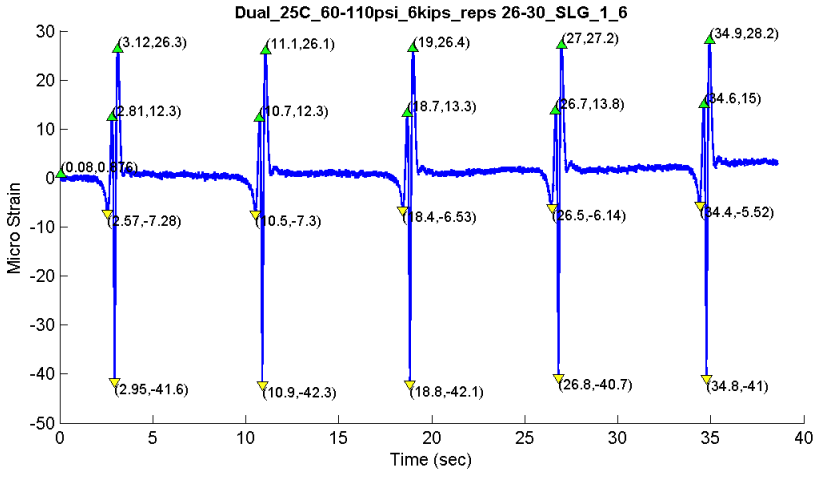

Figure 347. Graph. A sample filtered, peak points extracted case for Florida, test pit section.

Database and Management Systems

The data were stored in a structured manner maintaining relationships and dependencies. The results of various tests generated a lot of data in the form of csv, pdf, and jpeg. To visualize and access the data through a single console, Relational Database Management System (RDBMS) was used. An RDBMS provides a common storage location for all collected data. In addition, it enables the application of structured query language to retrieve data relevant to each requirement. RDBMS also facilitates visualization in the form of graphs and helps analyze data in a much better fashion.

The data of the RDBMS are structured in database tables, fields, and records. Each RDBMS table consists of database table which in its turn consists of one or more database table fields. RDBMS stores data in a collection of tables that might be related by common fields (database table columns). RDBMS also provides relational operators to manipulate the data stored into database tables. Most RDBMS use structured query language (SQL) as database query language.

RDBMS is maintained because it ensures data safety. All changes made to an RDBMS, once committed, are immune to program crashes, and hence critical data are never lost. In addition, an RDBMS allows concurrent access to entities from various sources and therefore enables collaboration while ensuring all updates are automatic. An RDBMS also supports data integrity and scalability. SQL used in an RDBMS facilitates selective access to data as well as reporting.

An ER model is typically implemented as a database. In case of a relational database, the data are stored in tables, representing the entities. Some data fields in the tables point to indexes in other tables; these pointers represent the relationships. The three-schema approach uses three levels of ER models: conceptual data, logical data, and physical data; this methodology was implemented in development of the database.

MySQL client server database was also part of the database. In client server databases, each client initiates a connection using TCP/IP. Once the connection is established, a client can send a query to server process. The server process then looks into the disk to retrieve appropriate data. A database management system was used to store data efficiently. Earlier database users were programmers and code writers. However, the need to deal with the massive amount of data using easy language to interact with databases led to the development of SQL.

Graph Features on Example Database

The project conducted in Delaware, Ohio, is used to show the capabilities of the database. This project is a field test run on the Ohio route US 23 (three sections in northbound, southbound, and ramp) using different load, tire inflation pressure and speed according to a test matrix. Response sensors include embedded strain gauges, pressure cells, MDD, and strain gauge rosettes at different depths. Data were collected for three sections: i) mainline section, driving lane, ii) ramp section, southbound, and iii) mainline section, passing lane. The database provides filtering of data based on several criteria, such as tire configuration, load, tire inflation pressure, load repetitions, and sensor type. Figure 345 shows a snapshot of filters available in the database for

data collected for the Ohio section. The data must be regularly categorized based on specific parameters; therefore, it was stored in an RDBMS.

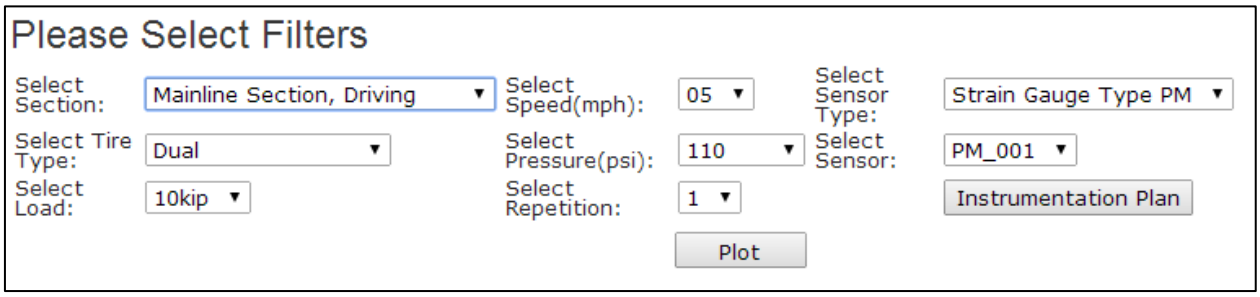

Figure 348. Illustration. Ohio section filters.

For a thorough signal analysis of a particular sensor, plot functionality was provided. The plot filters data based on the parameters selected. Figure 346 depicts a plot for the above filters. Time is plotted on the *x*-axis and strain on *y*-axis. Hovering the mouse over the graph provides the specific strain at that time. Zoom-in and zoom-out functionalities are also provided, using mouse drag. Figure 347 shows the zoom-in action, and Figure 348 provides a snapshot of the zoom-in version of the graph in Figure 346.

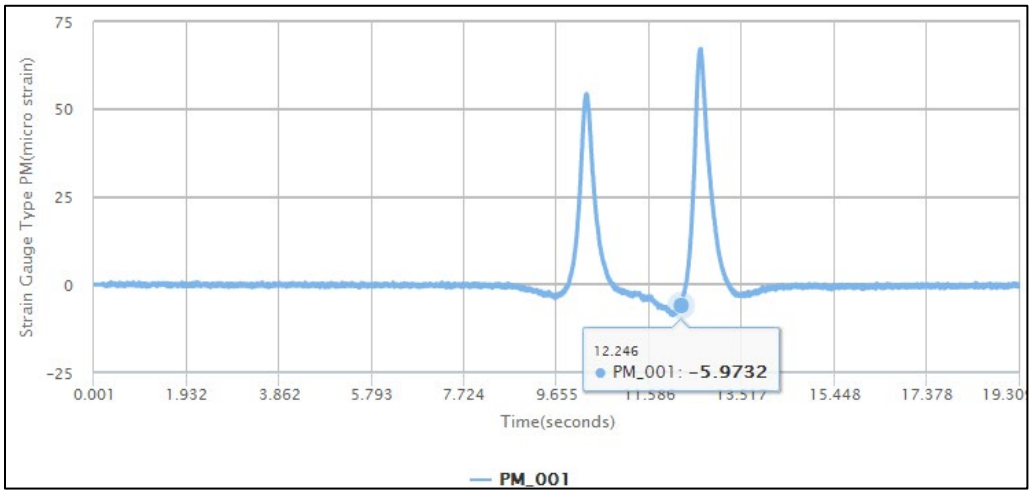

Figure 349. Graph. Snapshot of the plotted sensor reading for specified filters.

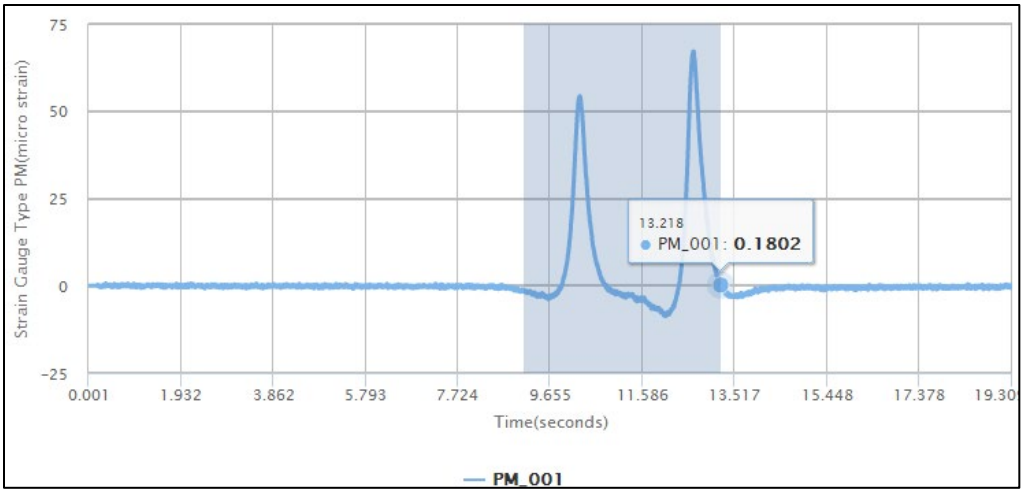

Figure 350. Graph. Zoomed-in example feature of the interface.

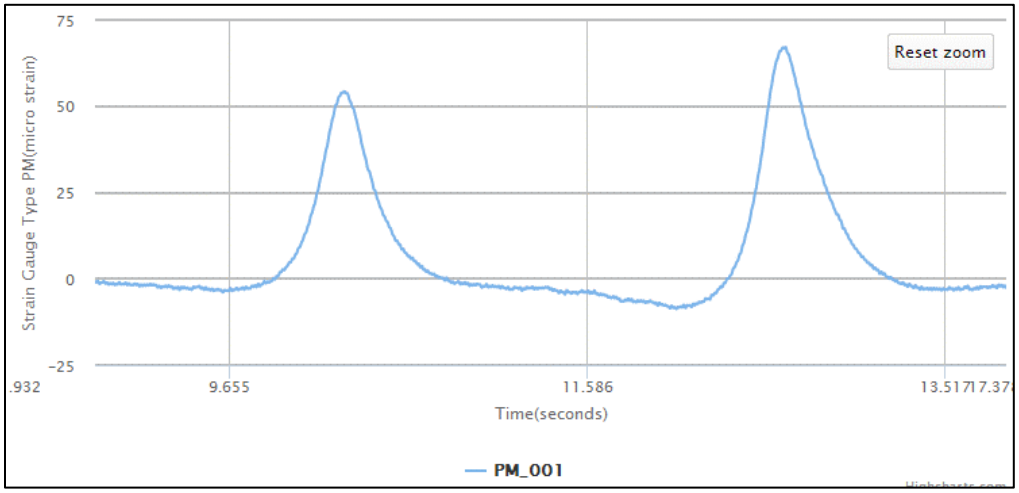

Figure 351. Graph. Zoomed-in shot of the sensor in previous example.

As presented in Figure 348, the zoom-out functionality is also provided. Clicking *Reset zoom* button will zoom out the graph, as shown in Figure 347. To enable further analysis of sensor values, downloading a copy of the graph as a *jpeg*, *svg* or *png* was also facilitated. This can be accessed using the top right button. Figure 349 explains the download functionality in greater detail.

The database also allows for the extraction of summary data on various criteria, as shown in Figure 345. Summary data can be extracted simultaneously for multiple sensor values. Further, *Download All* feature allows the user to download all the summary data, regardless of the cases for the selected sensor values. For all other sections, similar filters and plotting features are provided. This will facilitate data visualization for users. Also, the download options allow access to the filtered data for further analysis. Moreover, raw data are provided in the original format for the users interested in checking raw data.

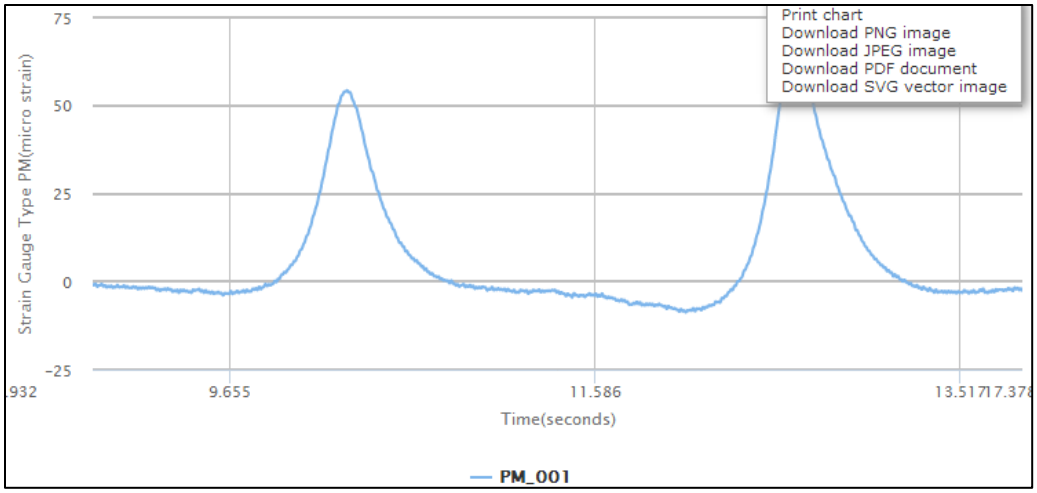

Figure 352. Graph. Download functionality of the interface.

OVERVIEW OF SOURCE CODE AND FUNCTIONALITIES

It is recommended to import the project in an IDE like Eclipse. The eclipse project file is provided. The user needs to import it as a Maven Project. The following description will provide certain snippets as to how to implement some of the core functionalities.

Source Code Structure

The package structure is divided into three parts: controller, data access objects and model classes. The controllers are basically the entry point for a *GET* and a *POST* call. Most of the business logic is written in controllers. Data access objects are responsible for inserting, querying, and deleting an object from the database. Finally, Model Classes are POJO that maps to a particular row in MySQL database.

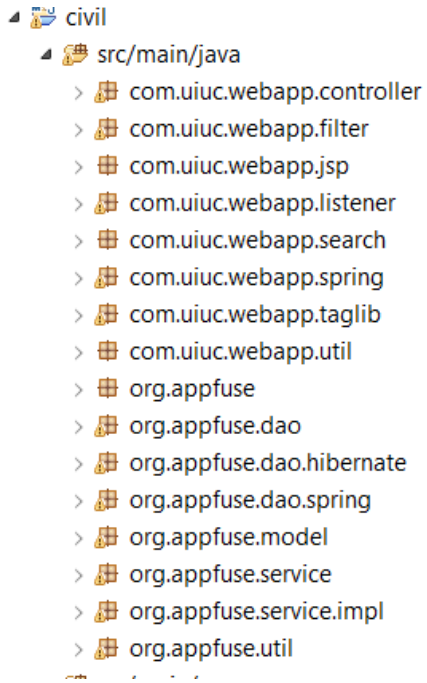

Figure 353. Illustration. Source code structure.

The steps to perform a *GET* request are presented in Figure 351.

```java
package com.uiuc.webapp.controller;

import java.io.File;

@Controller
@RequestMapping("/davis")
public class DavisController {
    @Autowired
    private IUCDavisDao davisDao;
    @Autowired
    private IDavisSummaryDao davisSummaryDao;

    @Autowired
    private PropertyPlaceholderConfigurer propertyConfigurer;
    private static final String PATH = "C:\\work\\civil_enginering\\UCDavis\\Archive
    @Autowired
    private PropertyLoaderService loaderService;

    public DavisController() {
    }

    @RequestMapping(method = RequestMethod.GET)
    public void displayCharts() {

    }

    @RequestMapping(value = "/sensorTypes", method = RequestMethod.GET)
    @ResponseBody
    List<String> getSensorType() {
        List<String> davis = davisDao.getSensorType();
        return davis;
    }

    @RequestMapping(value = "/sensorNames/{sensorType}", method = RequestMethod.GET)
```

Figure 354. Illustration. Explaining GET request.

In the Figure 351, *@Controller* and *@RequestMapping* signifies a spring controller and the URL path assigned to this controller, respectively. When *http://localhost:8080/davis* is typed, method named *display charts()* will be executed. Nothing is performed in that method; no logic will be performed and davis.jsp will be opened. If *http://localhost:8080/davis/sensorTypes* is typed, the method name *getSensorType()* is called. *DavisDAO* implementation has a method *getSensorType()*, which will return all sensor types available for Davis. Inside *DavisDAO* implementation, an interface instead of implementation was introduced.

```java
package org.appfuse.dao;

import java.util.List;

public interface IUCDavisDao extends GenericDao<UCDavis, Long> {

    List<String> getSensorType();

    List<String> getTestIds();

    List<String> getTirePressure(String testId, String sensor);

    List<String> getLoad(String testId, String sensor);

    List<String> getWheelType(String sensor, String testId, String pressure,
            String load);

    List<String> getTrafficking(String sensor, String testId, String pressure,
            String load);

    List<String> getRepetition(String sensor, String testId, String pressure,
            String load, String wheelType, String trafficking);

    List<String> getFileName(String sensor, String testId, String pressure,
            String load, String wheelType, String trafficking, String cycle);

    List<String> getDate();

    List<String> getTemp(String date);
}
```

Figure 355. Illustration. Davis section DAO Interface.

```java
@Repository
public class UCDavisDaoImpl extends GenericDaoHibernate<UCDavis, Long>
        implements IUCDavisDao {

    public UCDavisDaoImpl() {
        super(UCDavis.class);
        // TODO Auto-generated constructor stub
    }

    @SuppressWarnings("unchecked")
    public List<String> getSensorType() {
        return this.getHibernateTemplate().executeFind(
                new HibernateCallback<List<String>>() {

                    public List<String> doInHibernate(Session session)
                            throws HibernateException, SQLException {
                        List<String> query = session.createSQLQuery(
                                "SELECT DISTINCT(sensor) FROM UCDavis").list();

                        return query;
                    }
                });
    }

    @SuppressWarnings("unchecked")
    public List<String> getTestIds() {
        return this.getHibernateTemplate().executeFind(
                new HibernateCallback<List<String>>() {

                    public List<String> doInHibernate(Session session)
                            throws HibernateException, SQLException {
                        List<String> query = session.createSQLQuery(
                                "SELECT DISTINCT(testId) FROM UCDavis").list();

                        return query;
                    }
                });
    }
```

Figure 356. Illustration. Davis section DAO Implementation.

```java
@Entity
@Table
public class UCDavis implements Serializable {

    /**
     *
     */
    private static final long serialVersionUID = 4610218925220349783L;
    private String tirePressure;
    private String loadKip;
    private String testId;
    private String cycles;
    private String sensorType;
    private String sensor;
    private String trafficking;
    private String wheelType;
    private String filePath;
    private String dateTime;
    private Long id;

    @Id
    @GeneratedValue(strategy = GenerationType.AUTO)
    public Long getId() {
        return id;
    }

    public void setId(Long id) {
        this.id = id;
    }

    public String getTirePressure() {
        return tirePressure;
    }
```

Figure 357. Illustration. Davis section POJO.

Plotting Charts

A third-party library called High *Charts.js* was used to plot charts in real time. To plot line graphs is straightforward, provided all the APIs of high charts are known. For instance, to access the Florida new data page, *http://localhost:8080/florida* is typed. After selecting and plotting a case, a JavaScript function defined in *florida.jsp* is called (Figure 356). This function sends all selected parameters to *Florida Controller* and decides which data to return. *FloridaController* requests *Florida DAO* to fetch the values satisfying the given case. *Florida Controller* converts the value to *JSON* and passes it to *florida.jsp*. After calling *AJAX*, the high charts *api* is called with the given data and a chart is displayed.

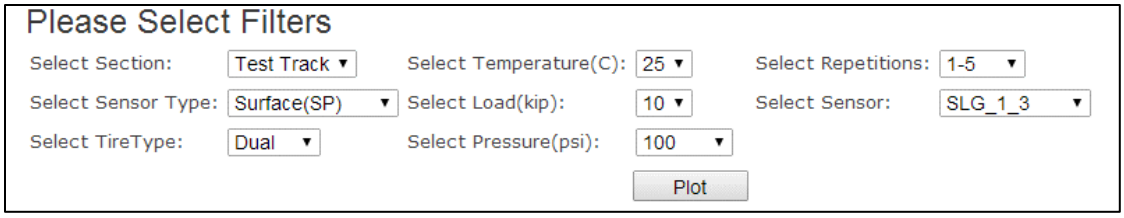

Figure 358. Illustration. Florida sensor filter.

```
function plot() {
    var url = "/florida/sensor/" + $(track).val() + "/" + $(tireType).val()
            + "/" + $(temp).val() + "/" + $(pressure).val() + "/"
            + $(code).val() + "/" + $(repetition).val() + "/"
            + $(sensor).val() + "/" + $(sensorValues).val() + "/";
    var time;
    var value;
    $
            .blockUI({
                message : '<h1>We are processing your request. Please be patient....</h1>'
            });

    $.ajax({
        url : url,
        type : "GET",
        success : function(smartphone) {

            for ( var key in smartphone) {
                time = key;
                value = smartphone[key];
            }
            var v = $(sensorValues).val();
            if (v.indexOf("SL") != -1) {
                v += "(micro strain)";
            }
            var k = tickPoint(10, eval(time).length);
            $('#container').highcharts({
                chart : {
                    borderWidth : 1,
                    zoomType : 'x'
                },
```

Figure 359. Illustration. Plot Javascript function.

File Hosting

The IP address and port number of Apache HTTP server are provided in a file called *configuration.properties*. When executing, *DconfigFile= <path of the configuration file>* needs to be passed. The content of configuration file is:

file.hosting.server=98.253.59.23
file.hosting.port=80

These values are used by the controller to pass to UI layer. The Controller layer can be seen in Figure 357.

```
@RequestMapping(value = "/download/{testId}/{sensor}/{pressure}/{load}/{wheelType}/{trafficking}/{cycle}/{date}", method = RequestMethod.GET)
@ResponseBody
public FileSystemResource download(@PathVariable String testId,
        @PathVariable String sensor, @PathVariable String pressure,
        @PathVariable String load, @PathVariable String wheelType,
        @PathVariable String trafficking, @PathVariable String cycle,
        @PathVariable String date) {
    List<String> list = null;
    if (sensor.equalsIgnoreCase("TEMP")) {
        list = davisDao.getTemp(date);
    } else {
        list = davisDao.getFileName(sensor, testId, pressure, load,
                wheelType, trafficking, cycle);
    }
    String path = PATH + list.get(0);
    return new FileSystemResource(new File(path));
}

@ModelAttribute("address")
public String getAddress() {
    String server = (String) loaderService.properties
            .get("file.hosting.server");
    String port = (String) loaderService.properties
            .get("file.hosting.port");
    return server + ":" + port;
}
```

Figure 360. Illustration. Controller Layer.

The address consists of two parts: base address and relative address. The base address represents the server address and relative address is the actual file address on the specified server. The *getAddress()* method forms an address of *Apache HTTP* server and sets it in the model attribute called address. On the UI, this base address is retrieved and appended to a particular file address. To render base address, a tree structure view an external library called *JStree* was used.

```
<div id="tabs-1">

    <div id="jstree">
        <!-- in this example the tree is populated from inline HTML -->
        <ul>
            <li>Loading History
                <ul>
                    <li><a
                        href="http://${address}\Interface-Meeting\WB Data Folder\Docs\UC Davis Data\Profile Data\504RF-WideBase_LoadingHistory_06-20-2011.csv">504RF*</a>
                    <li><a
                        href="http://${address}\Interface-Meeting\WB Data Folder\Docs\UC Davis Data\Profile Data\505RF-LoadingHistory_06-17-2011.csv">505RF</a></li>
                    <li><a
                        href="http://${address}\Interface-Meeting\WB Data Folder\Docs\UC Davis Data\Profile Data\506RF-LoadingHistory_06-20-2011.csv">506RF</a></li>
                    <li><a
                        href="http://${address}\Interface-Meeting\WB Data Folder\Docs\UC Davis Data\Profile Data\507RF-LoadingHistory_06-20-2011.csv">507RF</a></li>
                    <li><a
                        href="http://${address}\Interface-Meeting\WB Data Folder\Docs\UC Davis Data\Profile Data\508RF-LoadingHistory_06-20-2011.csv">508RF</a></li>
                    <li><a
                        href="http://${address}\Interface-Meeting\WB Data Folder\Docs\UC Davis Data\Profile Data\509RF-LoadingHistory_06-20-2011.csv">509RF</a></li>
                    <li><a
                        href="http://${address}\Interface-Meeting\WB Data Folder\Docs\UC Davis Data\Profile Data\510RF-LoadingHistory_06-20-2011.csv">510RF</a></li>
                    <li><a
                        href="http://${address}\Interface-Meeting\WB Data Folder\Docs\UC Davis Data\Profile Data\511RF-LoadingHistory_06-20-2011.csv">511RF</a></li>
                    <li><a
                        href="http://${address}\Interface-Meeting\WB Data Folder\Docs\UC Davis Data\Profile Data\512RF-LoadingHistory_06-20-2011.csv">512RF</a></li>
                    <li><a
                        href="http://${address}\Interface-Meeting\WB Data Folder\Docs\UC Davis Data\Profile Data\513RF-LoadingHistory_06-20-2011.csv">513RF</a></li>

                </ul>
            </li>
        </ul>
    </div>
```

Figure 361. Illustration. HTML snippet for specifying downloadable file.

```
$(function() {
    $("#jstree").jstree().bind("select_node.jstree", function(e, data) {
        var href = data.node.a_attr.href;
        document.location.href = href;

        //  $("#the_div").load(href);
    });
    $("#labTest").jstree().bind("select_node.jstree", function(e, data) {
        var href = data.node.a_attr.href;
        document.location.href = href;

        //  $("#the_div").load(href);
    });
    $("#tirePressure").jstree().bind("select_node.jstree",
            function(e, data) {
                var href = data.node.a_attr.href;
                document.location.href = href;

                //  $("#the_div").load(href);
            });

});
```

Figure 362. Illustration. Javascript snippet for tree type structure.

Database Schema

Figure 360 describes the names of the tables in the database, and Figure 361 shows the relationship between them.

Name	Engine	Version	Row Format	Rows	Avg Row Length	Data Length	Max Data Length	Index Length	Data Free	Auto Incre...	Create Time	U
app_user	InnoDB	10	Compact	2	8192	16384	0	32768	0	1	2013-11-02 16:1...	
davissummary	InnoDB	10	Compact	66123	278	18399232	0	0	4194304	72715	2013-12-14 12:0...	
florida_reading	InnoDB	10	Compact	13150668	38	504365056	0	1473085440	4194304	0	2014-01-19 13:1...	
floridasp	InnoDB	10	Compact	5172553	704	3643260928	0	0	7340032	5443363	2014-01-06 05:1...	
floridaspreadingtesttrack	InnoDB	10	Compact	12802235	516	6616514560	0	0	5242880	14576515	2014-01-19 13:4...	
floridaspsummary	InnoDB	10	Compact	3879	409	1589248	0	0	4194304	4269	2014-01-20 13:4...	
floridasptesttrack	InnoDB	10	Compact	1472	89	131072	0	0	0	1630	2014-01-19 19:4...	
load_ps	InnoDB	10	Compact	0	0	16384	0	81920	0	0	2013-11-02 16:1...	
loads	InnoDB	10	Compact	0	0	16384	0	0	0	1	2013-11-02 16:1...	
ohioreading	InnoDB	10	Compact	12060568	631	7614758912	0	0	5242880	12969183	2013-11-02 18:0...	
ohiosummary	InnoDB	10	Compact	1790	887	1589248	0	0	4194304	2021	2013-11-10 06:2...	
pressurespeed	InnoDB	10	Compact	0	0	16384	0	0	0	1	2013-11-02 16:1...	
psi_rep	InnoDB	10	Compact	0	0	16384	0	81920	0	0	2013-11-02 16:1...	
reading	InnoDB	10	Compact	0	0	16384	0	0	0	1	2013-11-02 16:1...	
rep_sensor	InnoDB	10	Compact	0	0	16384	0	81920	0	0	2013-11-02 16:1...	
repetition	InnoDB	10	Compact	0	0	16384	0	0	0	1	2013-11-02 16:1...	
role	InnoDB	10	Compact	2	8192	16384	0	0	0	1	2013-11-02 16:1...	
section	InnoDB	10	Compact	0	0	16384	0	0	0	1	2013-11-02 16:1...	
section_tire_types	InnoDB	10	Compact	0	0	16384	0	81920	0	0	2013-11-02 16:1...	
sensor_reading	InnoDB	10	Compact	0	0	16384	0	81920	0	0	2013-11-02 16:1...	
sensorreading	InnoDB	10	Compact	0	0	16384	0	0	0	1	2013-11-02 16:1...	
state	InnoDB	10	Compact	0	0	16384	0	0	0	1	2013-11-02 16:1...	
state_reading	InnoDB	10	Compact	12339193	38	472907776	0	1381695488	7340032	0	2013-11-02 18:0...	
state_section	InnoDB	10	Compact	0	0	16384	0	81920	0	0	2013-11-02 16:1...	
stateentity	InnoDB	10	Compact	1194	96	114688	0	0	0	1292	2013-11-02 18:0...	
tire_type_load	InnoDB	10	Compact	0	0	16384	0	81920	0	0	2013-11-02 16:1...	
tiretype	InnoDB	10	Compact	0	0	16384	0	0	0	1	2013-11-02 16:1...	
ucdavis	InnoDB	10	Compact	6190	256	1589248	0	0	4194304	6721	2013-11-25 20:3...	
user_role	InnoDB	10	Compact	2	8192	16384	0	65536	0	0	2013-11-02 16:1...	

Figure 363. Illustration. All tables.

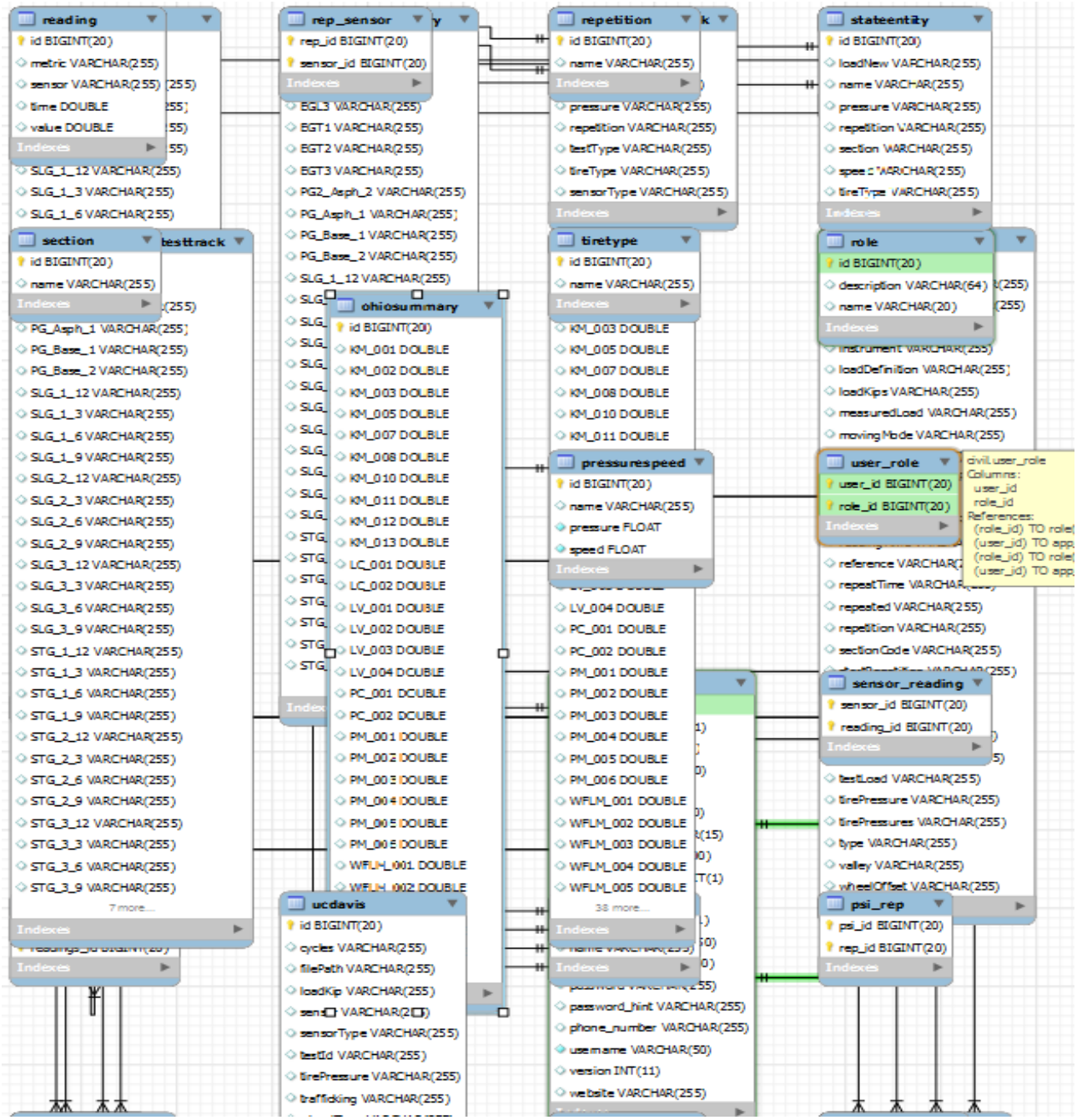

Figure 364. Illustration. ER diagram.

REFERENCES

AASHTO. (2008). “Mechanistic-Empirical Pavement Design Guide: A Manual of Practice.” Interim Edition, American Association of Highways and Transportation Officials.

Akram, T., Scullion, T., Smith, R. E., and Fernando, E. G. (1992). "Estimating Damage Effects of Dual Versus Wide Base Tires with Multidepth Deflectometers." Transportation Research Record: Journal of the Transportation Research Board, No. 1355, pp. 59-66.

Al-Qadi I.L., Dessouky S. H., Kwon J., and Tutumluer E. (2008). “Geogrid in Flexible Pavements Validated Mechanism.” Transportation Research Record: Journal of the Transportation Research Board, No. 2045, Transportation Research Board of the National Academies, Washington, DC.

Al-Qadi, I. L., Elseifi, M. A., and Yoo, P. J. (2004). “Pavement Damage due to Different Tires and Vehicle Configurations.” Virginia Tech Transportation Institute, Blacksburg, Virginia.

Al-Qadi, I. L., Elseifi, M. A., Yoo, P. J., Dessouky, S. H., Gibson, N., Harman, T., and Petros, K. (2008). “Accuracy of Current Complex Modulus Selection Procedure from Vehicular Load Pulse: NCHRP Project 1-37A Mechanistic-Empirical Pavement Design Guide.” Transportation Research Record: Journal of the Transportation Research Board, No. 2087(1), pp. 81-90.

Al-Qadi, I. L., Elseifi, M. A., Yoo, P. J., and Janajreh, I. (2005a). “Pavement Damage due to Conventional and New Generation of Wide-Base Super Single Tires.” Tire Science and Technology, 33(4), 210-226.

Al-Qadi, I. L., and Wang, H. (2009a). “Full-Depth Pavement Responses under Various Tire Configurations: Accelerated Pavement Testing and Finite Element Modeling.” Journal of the Association of Asphalt Paving Technologists, 78, 645-680.

Al-Qadi, I. L., and Wang, H. (2009b). “Evaluation of Pavement Damage due to New Tire Design.” Illinois Center for Transportation, Rantoul, IL.

Al-Qadi, I. L., and Wang, H. (2009c). “Pavement Damage due to Different Tire and Loading Configurations on Secondary Roads.” NEXTRANS University Transportation Center, West Lafayette, Indiana.

Al-Qadi, I. L., Wang, H., and Tutumluer, E. (2010). “Dynamic Analysis of Thin Asphalt Pavement by using Cross-Anisotropic Stress-Dependent Properties for Granular Layer.” Transportation Research Record: Journal of the Transportation Research Board, No. 2154, pp. 156-163.

Al-Qadi, I. L., Wang, H., Yoo, P., and Dessouky, S. (2008). “Dynamic Analysis and In Situ Validation of Perpetual Pavement Response to Vehicular Loading.” Transportation Research Record: Journal of the Transportations Research Board, No. 2087, pp. 28-39.

Al-Qadi, I. L., Xie, W., and Elseifi, M. A. (2008). “Frequency Determination from Vehicular Loading Time Pulse to Predict Appropriate Complex Modulus in MEPDG.” Journal of the Association of Asphalt Paving Technologists, 77.

Al-Qadi, I. L., Yoo, P. J., Elseifi, M. A., and Janajreh, I. (2005b). "Effects of Tire Configurations on Pavement Damage." Journal of the Association of Asphalt Paving Technologists, 84, 921-962.

Al-Qadi, I. L., and Yoo, P. J. (2007). "Effect of Surface Tangential Contact Stresses on Flexible Pavement Response (With Discussion)." Journal of the Association of Asphalt Paving Technologists, 76.

Ang-Olson, J., and Schroeer, W. (2002). Energy Efficiency Strategies for Freight Trucking: Potential Impact on Fuel Use and Greenhouse Gas Emissions. Transportation Research Record: Journal of the Transportation Research Board, No. 1815, pp. 11-18.

Asia Sustainable and Alternative Energy Program (ASTAE). (2011). "ROADEO Toolkit User Manual".

Athena Sustainable Materials Institute. (2006). "A Life Cycle Perspective on Concrete and Asphalt Roadways: Embodied Primary Energy and Global Warming Potential" <www.cement.ca/images/stories/athena%20report%20Feb.%202%202007.pdf>.

Athena Sustainable Materials Institute. (2013). Impact Estimator [software], <Athena Sustainable Materials Institute >

Bachman, L. J., Erb, A., and Bynum, C. L. (2005). "Effect of Single Wide Tires and Trailer Aerodynamics on Fuel Economy and NOx Emissions of Class 8 Line-Haul Tractor-Trailers." SAE Paper Number 05CV-45. American Society for Testing and Materials, Warrendale, PA.

Bathe, K.J. (1982). Finite Element Procedures in Engineering Analysis, Prentice-Hall, New Jersey.

Bayat, A., and Knight, M. (2012). "Field Evaluation and Analysis of Flexible Pavement Structural Responses under Dynamic Loads." Road Materials and Pavement Design, 13(1), 26-37.

Bonaquist, R. (1992). "An Assessment of the Increased Damage Potential of Wide Base Single Tires." 7th International Conference on Asphalt Pavements, Nottingham, UK, pp. 1-16.

Brock, J. D., and Richmond, J. R. (2006). "Milling and Recycling." Technical Paper T-127. An Astec Industries Company. U.S.A.

Caglar, N., M. Elmas, Z. Dere Yaman, and Saribiyik, M. (2008). "Neural Networks in 3-Dimensional Dynamic Analysis of Reinforced Concrete Buildings." Construction and Building Materials, 22, 788–800.

California Department of Transportation (Caltrans). (2011). Contract Cost Data - A Summary of Cost by Items for Highway Construction Projects. Division of Engineering Services, CA.

COST 334. (2001). "Effects of Wide Single Tires and Dual Tires, Final Report of the Action" European Cooperation in the Field of Scientific and Technical Research, Brussels, Belgium.

De Beer, M., C. Fisher, and F. J. Jooste. (1997) "Determination of Pneumatic Tyre/Pavement Interface Contact Stresses under Moving Loads and Some Effects on Pavements with Thin Asphalt Surfacing." In Proceedings of the 8th International Conference on Asphalt Pavements, Seattle, Washington. 1997, pp. 179–227.

Dessouky, S. H., Al-Qadi, I. L., and Yoo, P. J. (2014). "Full-depth Flexible Pavement Responses to Different Truck Tire Geometry Configurations." International Journal of Pavement Engineering, 15(6), 512-520.

Elseifi, M. A., Al-Qadi, I. L., and Yoo, P. J. (2006). "Viscoelastic Modeling and Field Validation of Flexible Pavements." Journal of Engineering Mechanics, 132(2), 172-178.

Emissions and Generation Resources Integrated Database (eGRID). (2012). U.S. Environmental Protection Agency. Washington, D.C.

EPA. (2008). NONROAD Model (Nonroad engines, equipment, and vehicles), NONROAD 2008a Model (Version 2008a) [software], <http://www.epa.gov/otaq/nonrdmdl.htm>.

Fakhri, M. and Ghanizadeh, A. R. (2014). "Modelling of 3D Response Pulse at the Bottom of Asphalt Layer Using a Novel Function and Artificial Neural Network." International Journal of Pavement Engineering, 15(8), 671-688.

FHWA (2012). "Long Term Pavement Performance Program Standard Data Release (SDR) 26.0". CD-ROM.

Franzese, O., Knee, H. E., and Slezak, L. (2010). "Effect of Wide-Based Single Tires on Fuel Efficiency of Class 8 Combination Trucks." Transportation Research Record, Journal of the Transportation Research Board, No. 2191, pp. 1-7.

GENIVAR Consulting Group (2005). "Economic Study Use of Supersingle Tires by Heavy Vehicles Operating in Québec." Report published by GENIVAR Consulting Group, Montreal, QC, Canada.

Gillespie, T. D., Karamihas, S. M., Sayers, M. W., Nasim, M. A., Hansen, W., Ehsan, N., and Cebon, D. (1992). "Effect of Heavy-Vehicle Characteristics on Pavement Response and Performance." Transportation Research Board, Washington, D.C.

Greenhouse Gases, Regulated Emissions, and Energy Use in Transportation (GREET) 1. (2013). Argonne National Laboratory. [Software]. Chicago, IL.

Greene, J., Toros, U., Kim, S., Byron, T., and Choubane, B. (2009). "Impact of Wide-Base Single Tires on Pavement Damage." Florida Department of Transportation.

Greene J., Toros U., Kim S., Byron T., and Choubane B., (2010). "Impact of Wide-Base Single Tires on Pavement Damage." Transportation Research Record: Journal of the Transportation Research Board, No. 2155, Transportation Research Board of the National Academies, Washington, DC.

Grellet, D., Doré, G., and Bilodeau, J. P. (2012). "Comparative Study on the Impact of Wide Base Tires and Dual Tires on the Strains occurring within Flexible Pavements Asphalt Concrete Surface Course." Canadian Journal of Civil Engineering, 39(5), 526-535.

Grellet, D., Doré, G., Bilodeau, J. P., and Gauliard, T. (2013). "Wide-base Single-tire and Dual-tire Assemblies: Comparison based on Experimental Pavement Response and

Predicted Damage." Transportation Research Record: Journal of the Transportation Research Board, No. 2369, pp. 47-56.

Hallin, J. P., Sharma, J., and Mhoney, J. P. (1983). "Development of Rigid and Flexible Pavement Load Equivalency Factors for Various Widths of Single Tires." Transportation Research Record: Journal of the Transportation Research Board, No. 949, pp. 4-13.

Harvey, J., Kendall, A., Lee, I.-S., Santero, N., Van Dam, T., and Wang, T. (2010). "Pavement Life Cycle Assessment Workshop: Discussion Summary and Guidelines." UCPRC-TM-2010-03. <www.dot.ca.gov/research/researchreports/reports/2010/2010-05_task_1897_pavement.pdf>. University of California Pavement Research Center, Davis and Berkeley, CA.

Harvey J., and Popescu, L. (2000). "Rutting of Caltrans Asphalt Concrete and Asphalt-Rubber Hot Mix under Different Wheels, Tires and Temperatures – Accelerated Pavement Testing Evaluation." Pavement Research Center Institute of Transportation Studies University of California, Berkeley

Helwany, S. (2007). Applied Soil Mechanics with ABAQUS® Applications. John Wiley & Sons, Inc, Hoboken, New Jersey.

Horvath, A. (2007). PaLATE Pavement Life Cycle Assessment Tool for Environmental and Economic Effects (ver 2.2) [software], <UC Berkeley, Pavement Life-cycle Assessment Tool for Environmental and Economic Effects>.

Huhtala, M. (1986). "The Effect of Different Trucks on Road Pavements." Proc., International Symposium on Heavy Vehicle Weights and Dimensions, Kelowna, British Columbia.

Huhtala, M., Philajamaki, J., and Pienimaki, M. (1989). "Effects of Tires and Tire Pressures on Road Pavements." Transportation Research Record: Journal of the Transportation Research Board, No. 1227, pp. 107-114.

IPCC. (2007). IPCC Fourth Assessment Report: Climate Change 2007 (AR4): The Physical Science Basis. Contribution of Working Group I to the Fourth Assessment Report of the IPCC. <www.ipcc.ch/publications_and_data/publications_ipcc_fourth_assessment_report_wg1_report_the_physical_science_basis.htm>. Cambridge University Press, Cambridge, United Kingdom and New York, NY, USA.

Kendall, A. (2007). "Concrete Infrastructure Sustainability: Life Cycle Metrics, Materials Design, and Optimized Distribution of Cement Production." Ph.D Dissertation. University of Michigan.

Kim, D., Salgado, R., and Altschaeffl, E. G. (2005). "Effects of Super-Single Tire Loadings on Pavements." Journal of Transportation Engineering, 131(10), 732-743.

Kim, M., Tutumluer, E., and Kwon, J. (2009). "Nonlinear Pavement Foundation Modeling for Three-Dimensional Finite-Element Analysis of Flexible Pavements." International Journal of Geomechanics.

Lee, I.-S. (2013). “Approaches to Life Cycle Inventory Development for Sustainable Highway Infrastructure: Protocol Development, Regionalization, and New Inventories.” Ph.D. Dissertation. University of California, Davis, Davis, CA

Lu, Q., Kohler, E., Harvey, J. T., and Ongel, A. (2009). “Investigation of Noise and Durability Performance Trends for Asphaltic Pavement Surface Types: Three-Year Results.” UCPRC-RR-2009-01. <www.ucprc.ucdavis.edu/pdf/UCPRC-RR-2009-01.pdf>. Report published by University of California Pavement Research Center, Davis and Berkeley, CA.

Maina, J. W., Ozawa, Y., and Matsui, K. (2012). “Linear Elastic Analysis of Pavement Structure under Non-circular Loading.” Road Materials and Pavement Design, 13(3), 403-421.

Markstaller, M., Pearson, A., and Janajreh, I. (2000). "On Vehicle Testing of Michelin New Wide Base Tire." Proc., SAE International Conference.

Moghaddam, F. R., Afandizadeh, S.H. and Ziyadi, M. (2011). “Prediction of Accident Severity Using Artificial Neural Networks”, International Journal of Civil Engineering, 9(1).

Motor Vehicle Emissions Simulator (MOVES) 2014 Model. (2014). U.S. Environmental Protection Agency. [Software]. Washington, D.C.

Mukherjee, A., and Cass, D. (2012). “Project Emissions Estimator Implementation of a Project-Based Framework for Monitoring the Greenhouse Gas Emissions of Pavement.” Transportation Research Record, No. 2282, pp. 91-99.

Muster, T. (2000). “Fuel Savings Potential and Costs Considerations for US Class 8 Heavy Duty Trucks through Resistance Reductions and Improved Propulsion Technologies Until 2020”, Energy Laboratory Massachusetts Institute of Technology, Cambridge, Massachusetts.

Myers, L. A., Roque, R., Ruth, B. E., and Drakos, C. (1999). “Measurement of Contact Stresses for Different Truck Tire Types to Evaluate their Influence on Near-Surface Cracking and Rutting.” Transportation Research Record: Journal of the Transportation Research Board, No. 1655, pp. 175-184.

National Cooperative Highway Research Program (NCHRP). (2004). “Guide for the Mechanistic-Empirical Design for New and Rehabilitated Pavement Structure”. 1-37A, Transportation Research Board, Washington, DC

NCHRP. (2013). “2013 Fuel Usage Factors in Highway and Bridge Construction”, NCHRP report 744, Washington, D.C.

Organization for Economic Co-Operation and Development (OECD) (1992). “OECD Report. Dynamic Loading of Pavements.” OECD, Paris, France.

Perdomo, D., and Nokes, B. (1993). "Theoretical Analysis of the Effects of Wide-Base Tires on Flexible Pavements using CIRCLY." Transportation Research Record: Journal of the Transportation Research Board, No. 1388, pp. 108-119.

Pierre, P., Dore, G., and Vagile, L. (2003). “Characterization and Evaluation of Tire-Roadway Interface Stresses.” Ministry of Transport, University of Laval, Quebec, Canada.

PRe Constultants. (2013). SimaPro8.0 [software], <SimaPro Software>.

Priest, A. L., and Timm, D. H. (2006). "Mechanistic Comparison of Wide-Base Single Versus Standard Dual Tire Configurations." Transportation Research Record: Journal of the Transportation Research Board, No. 1949(155), 163.

Romanoschi, S., and Metcalf, J. (2001). “Characterization of Asphalt Concrete Layer Interfaces.” Transportation Research Record: Journal of the Transportation Research Board, No. 1778, pp. 132–139.

Santero, N., Masanet, E., and Horvath, A. (2010). “Life Cycle Assessment of Pavements: A Critical Review of Existing Literature and Research.” <www.escholarship.org/uc/item/8632v9cc.pdf>. Portland Cement Association, Skokie, IL.

Santero, N. J., Masanet, E. and Horvath, A. (2011). “Life-cycle Assessment of Pavements. Part I: Critical Review.” Resources, Conservation and Recycling, 55(9-10), 801-809.

Schalkoff, R.J. (1997). Artificial Neural Networks. McGraw-Hill, N. Y.

Sebaaly, P. E., and Tabatabaee, N. (1992). “Effect of Tire Parameters on Pavement Damage and Load-Equivalency Factors.” Journal of Transportation Engineering, 118(6), 805-819.

Sebaaly, P. E., and Tabatabaee, N. (1989). "Effect of Tire Pressure and Type on Response of Flexible Pavement." Transportation Research Record: Journal of the Transportation Research Board, No. 1227, pp. 115-127.

Siddharthan, R. V., Krishnamenon, N., El-Mously, M., and Sebaaly, P. E. (2002). “Investigation of Tire Contact Stress Distributions on Pavement Response.” Journal of Transportation Engineering, 128(2), 136-144.

Siddharthan, R. V., Yao, J., Sebaaly, P. E. (1998). “Pavement Strain from Moving Dynamic 3D Load Distribution.” Journal of Engineering Mechanics, 124(6), 557-566.

Stripple, H. (1998). “Life Cycle Assessment of Road (Swedish).” <www.ivl.se/webdav/files/B-rapporter/B1210E.pdf>. Swedish Environmental Research Institute, Stockholm, Sweden.

Swiss Centre for Life Cycle Inventories. (2011). EcoInvent. <www.ecoinvent.org>. (Sep. 15, 2013.) Swiss Centre for Life Cycle Inventories, Dubendorf, Switzerland.

Tabatabaee, N., Ziyadi, M. and Shafahi, Y (2013). “Two-Stage Support Vector Classifier and Recurrent Neural Network Predictor for Pavement Performance Modeling.” Journal of Infrastructure Systems. 19(3), 266–274.

Tseng, E. (2012). “The Construction of Pavement Performance Models for the California Department of Transportation New Pavement Management System.” Master’s Thesis. University of California, Davis, Davis, CA.

Tutumluer, E. (2008). “State of the Art: Anisotropic Characterization of Unbound Aggregate Layers in Flexible Pavements.” Engineering Mechanics Conference. Minneapolis, MN

Tutumluer, E. and Thompson, M. (1998). “Anisotropic Modeling of Granular Bases.” Final Report for the Federal Highway Administration.

U.S. Department of Energy. (2009). Transportation Energy Data Book. 2008. U.S. Department of Transportation, National Transportation Statistics.

U.S. Energy Information Administration. (2014). Petroleum & Other Liquids. Online Database. [Jun. 2014]. <http://www.eia.gov/petroleum/>.

Wang, H. (2011). “Analysis of Tire-Pavement Interaction and Pavement Responses Using a Decoupled Modeling Approach.” PhD Dissertation. University of Illinois at Urbana-Champaign, Urbana, Illinois.

Wang, T. (2013). “Reducing Greenhouse Gas Emissions and Energy Consumption Using Pavement Maintenance and Rehabilitation: Refinement and Application of a Life Cycle Assessment Approach.” Ph.D. Dissertation. University of California, Davis, Davis, CA.

Wang, T., Lee, I.-S., Harvey, J., Kendall, A., Lee, E. B., and Kim, C. (2012). “UCPRC Life Cycle Assessment Methodology and Initial Case Studies on Energy Consumption and GHG Emissions for CAPM Treatments with Different Rolling Resistance.” UCPRC-RR-2012-02. <www.ucprc.ucdavis.edu/PDF/UCPRC-RR-2012-02.pdf>. University of California Pavement Research Center (UCPRC), Davis and Richmond, CAWSP Canada (2015). “New Generation Wide Base Single (NGWBS) Tires Study Cost-Benefit Analysis of the Removal of the Weight Limitation for NGWBS Tires Final Report.” Report published by WSP Canada, Quebec, QC, Canada.

Wang, T., Lee, I. S., Kendall, A., Harvey, J., Lee, E. B., and Kim, C. (2012). “Life Cycle Energy Consumption and GHG Emission from Pavement Rehabilitation with Different Rolling Resistance.” Journal of Cleaner Production, 33, 86-96.

Wang, D., Roesler, J. R., and Guo, D. Z. (2009). “Analytical Approach to Predicting Temperature Fields in Multilayered Pavement Systems.” Journal of Engineering Mechanics, 135(4), 334-344.

Xiao, Y., Tutumluer, E., and Siekmeier, J. (2011) “Mechanistic–Empirical Evaluation of Aggregate Base and Granular Subbase Quality Affecting Flexible Pavement Performance in Minnesota.” Transportation Research Record. No. 2227, pp. 97-106.

Xue, W., and Weaver E. (2011). “Pavement Shear Strain Response to Dual and Wide-Base Tires.” Presented in 90th Annual Meeting, Transportation Research Board of the National Academies, Washington, DC.

Xue, W., & Weaver, E. (2015). “Influence of Tire Configuration on Pavement Response and Predicted Distress.” International Journal of Pavement Engineering, 16(6), 538-548.

Yoo, P.J., and Al-Qadi, I.L. (2007). “Effect of Transient Dynamic Loading on Flexible Pavements.” Transportation Research Record: Journal of the Transportations Research Board, No. 1990, pp. 129-140.

Yoo, P. J., and I. L. Al-Qadi. (2008). “The Truth and Myth of Fatigue Cracking Potential in Hot-Mix Asphalt: Numerical Analysis and Validation.” Journal of Association of Asphalt Paving Technologists, 77, 549–590.

Yoo, P. J., Al-Qadi, I. L., Elseifi, M. A., and Janajreh, I. (2006). “Flexible Pavement Responses to Different Loading Amplitudes Considering Layer Interface Condition and Lateral Shear Forces.” The International Journal of Pavement Engineering, 7(1), 73-86.

Zhang, H., Lepech, M. D., Keoleian, G. A., Qian, S. Z., and Li, V. C. (2009). “Dynamic Life-Cycle Modeling of Pavement Overlay Systems: Capturing the Impacts of Users, Construction, and Roadway Deterioration.” Journal of Infrastructure Systems, 16(4), 299-309.